

ISSN 0377-9416



[www.pmai.in](http://www.pmai.in)

# TRANSACTIONS OF POWDER METALLURGY ASSOCIATION OF INDIA

Vol. 42 No.2, December 2016

Chief Editor - P. Ramakrishnan



ISSN 0377-9416



[www.pmai.in](http://www.pmai.in)

**Vol. 42 No.2, December 2016**

Chief Editor - P. Ramakrishnan



## **Powder Metallurgy Association of India**

### **Office Bearers**

#### **President**

Shri N. Gopinath

#### **Vice President**

Shri Deepak Grover

Shri Narendra Dhokey

Shri Rajendra Sethiya

#### **General Secretary**

Dr. Deep Prakash

#### **Hon. Treasurer**

Dr. Murli Gopal Krishnamoorthy

#### **Joint Secretary**

Shri Aniket Gore

Shri Rajat Varshney



### Chief Editor

Prof. Ramakrishnan P.

### Editorial Advisory Board

Dr. Ashok S.

Mr. Chandrachud N.L.

Dr. Rama Mohan T. R.

### Editorial Board

Dr. Appa Rao G.

Dr. Bhargava Parag

Dr. Dabhade Vikram

Dr. Deep Prakash

Dr. Dhokey N.B.

Dr. Kumar Y.V.S.

Dr. Malobika Karanjai

Dr. Murli Gopal K.

Dr. Panigrahi B.B.

Dr. Sastry I.S.R.

Dr. Tarasankar Mahata

Published by :

### Powder Metallurgy Association of India (PMAI)

1002, B-Wing, Kingston, High Street, Hiranandani Complex, Powai, Mumbai - 4000076.

Tel. : +9122 25704588

E-mail : info@pmai.in

Neither the Powder Metallurgy Association of India nor the editor assumes responsibility of opinions expressed by the authors of the papers published in this transaction.

# Editorial



Selected papers from the International PM-16, held at Hyatt Regency, Pune are included in the Trans. PMAI. Vol.42. No.2. 2016. The topics covered vary from powder preparation, modeling, characterization, metal and ceramic matrix composites, rapid prototyping sliding wear, recycling of rejected sintered nuclear fuel pellets to automation of sizing, a secondary operation of sintered bush.

The first paper is on the characterization of metal pebbles prepared by rotating electrode process is an important step since beryllium pebbles are used for tritium breeding in a thermonuclear reactor. This is followed by a paper on the dependence of the degree of oxidation of mill scale on depth of static bed and its modeling with ANSYS FLUENT soft ware. The next paper is on the effect of stirring time on the synthesis of nano crystalline magnesium aluminate spinal powder prepared by sol gel process and the processed material is used for infrared and armor widows in nuclear reactors. This is followed by a paper on the effect of nanosized materials on the dielectric and ferroelectric behavior of barium titanate which is widely used in electronics. Studies on phase evolution in dysprosium titanate based ceramics, which is used as a control rod material for thermal reactors is the subject matter of the next paper. This is followed by an article on Al-2024 metal matrix composites reinforced with ultrafine Mg-Al mechanically alloyed particles. The next paper is on the evolution of room temperature and high temperature properties of ZrB<sub>2</sub>-SiC composites. This is followed by an article entitled study of high temperature PAEK/Iron composites prepared by PM route and these materials are used in electromagnetic interface shielding, capacitors and thermal interface materials. Next paper is a comparative study on the reinforcement of Zirconium silicate and Zirconium oxide reinforcement in Al-6061 alloy. Rapid prototyping of Bronze powders using fiber laser is discussed in the next paper. This is followed by an article on the room temperature fracture toughness of refractory metal foil laminated MoSi<sub>2</sub> based composites with a view to improve the fracture toughness. Next paper is on the non-lubricating sliding wear behavior of SiC-B<sub>4</sub>C-Si ceramets fabricated by conventional and spark plasma sintering technique.

Forge ( $\delta$ ) ability of astaloy and its response to thermal processing is dealt with in the next article. The next paper describes electrochemical performance of Nd<sub>1.7</sub>Sr<sub>0.3</sub>NiO<sub>4.8</sub> as Cathode for SOFC applications. This is followed by a paper dealing with functionally graded material consisting of Iron powder and Stellite 6 powders processed by PM with improved wear resistance and shock absorbing properties. The next article is on the development of Cu/SiC, metal matrix composites by cold isostatic pressing and sintering for thermal management applications. Development of recycling process for (Th. U)O<sub>2</sub> clean rejected oxide sintered pellets is discussed in the paper and MOX is the proposed fuel for advanced Heavy water reactor. The final paper is on the automation of sintered bush a secondary operation such as sizing.

**P. Ramakrishnan**

TRANSACTIONS OF  
POWDER METALLURGY ASSOCIATION OF INDIA

Vol. 42 No.2, December 2016

CONTENTS

<b>1</b>	<b>Characterization of Metal Pebbles Prepared by Rotating Electrode Process</b> <i>T. Mohanty, B. M. Tripathi, R. K. Lenka, T. Mahata and P. K. Sinha,</i>	<b>1-6</b>
<b>2</b>	<b>Dependence of Degree of Oxidation of Mill Scale on Depth of Static Bed and its Modelling with ANSYS FLUENT</b> <i>R. Sabban, P. Tarate, N. B. Dhokey</i>	<b>7-12</b>
<b>3</b>	<b>The Effect of Stirring Time on Synthesis of Nano-Crystalline Magnesium Aluminate Spinel Powder by Sol-Gel Process</b> <i>Akash Shah, C. Jariwala, R. Pillai, S. B. Tandon, P. M. Raole and B. Sarkar</i>	<b>13-16</b>
<b>4</b>	<b>Effect of Nano Sized Starting Materials on the Dielectric and Ferroelectric Behaviour of Barium Titanate</b> <i>K. R. Kambale, A. R. Kulkarni, N. Venkataramani</i>	<b>17-30</b>
<b>5</b>	<b>Studies on Phase Evolution in Dysprosium Titanate Based ceramics</b> <i>Amit Sinha, J. Sharma and P. K. Sinha</i>	<b>31-37</b>
<b>6</b>	<b>Al-2024 Metal Matrix Composites Reinforced with Ultrafine Mg-Al Mechanically Alloyed Particles</b> <i>A. K. Chaubey and Rohit Kumar</i>	<b>38-44</b>
<b>7</b>	<b>Evaluation of Room Temperature and High Temperature Properties of ZrB<sub>2</sub>-SiC Composites</b> <i>Jiten Das, Sweety Kumari, J. Janardhana Reddy, V. VBhanu Prasad</i>	<b>45-50</b>
<b>8</b>	<b>Study on High Temperature Poly(aryletherketon) (PAEK)/Iron Composites Prepared by Powder Metallurgy (P/M) Route</b> <i>S. D. Gaikwad, P. Dhoka, R.K.Goyal</i>	<b>51-57</b>
<b>9</b>	<b>Investigation of Zirconium Silicate and Zirconium oxide reinforcement in Aluminium 6061 Metal Matrix - A Comparative Study</b> <i>Jitender Kumar Chaurasia, Paridh N. Patel, A. Muthuchamy, A. Raja Annamalai</i>	<b>58-62</b>
<b>10</b>	<b>Rapid Prototyping of Bronze Powders using Fiber Laser</b> <i>Prof. M. J. Rathod, Sumitkumar S. Bind, Tuhid M. Shaikh</i>	<b>63-69</b>
<b>11</b>	<b>Room Temperature Fracture Toughness of Refractory foil laminated MoSi<sub>2</sub> based composite</b> <i>Manoj Kumar Jain, Jiten Das, J Subrahmanyam, Subrata Ray</i>	<b>70-80</b>

<b>12 Non-lubricating Sliding Wear Behaviour Study of SiC-B<sub>4</sub>C-Si Cermets Fabricated by Conventional and Spark Plasma Sintering Techniques</b> <i>P. Sahani, S. K. Karak, D. Chaira</i>	<b>81-88</b>
<b>13 Forgeability of Astaloy and its Response to Thermal Processing</b> <i>V. T. Thavale, N. B. Dhokey, S. Dhokale, P. Ghosh</i>	<b>89-97</b>
<b>14 Electrochemical Performance Evaluation of Nd<sub>1.7</sub>Sr<sub>0.3</sub>NiO<sub>4+δ</sub> as a Cathode for IT-SOFC Applications</b> <i>Vivek Patel, R. K. Lenka, P. K. Patro, Amit Sinha, L. Muhmood, T. Mahata and P. K. Sinha</i>	<b>98-102</b>
<b>15 Dry Sliding Wear and Micro Structure of Stellite 6 Coating Processed by Powder Metallurgy</b> <i>D. Sathiya Narayanan, S. Beer Mohammed, K. Venkateswaran</i>	<b>103-107</b>
<b>16 Interfacial Design and Development of Cu/SiC MMCs for Thermal Management Applications by PM Route</b> <i>Rahul Shetty, S. Kavithaa, A. Udayakumar, S. S. Avadhani, B. Krishna Mohan, A. Murugan and S. Usha</i>	<b>108-115</b>
<b>17 Development of Dry Recycling Process for (Th,U)O<sub>2</sub> Clean Rejected Oxide Sintered Pellets</b> <i>P. M. Khot, S. K. Shotriya, K. Subbarayal, Niraj Kumar, B. Singh, B. Surendra, A. K. Mishra, P. G. Behere, Mohd Afzal</i>	<b>116-121</b>
<b>18 Automation of sintered bush secondary operation – Sizing</b> <i>Disha Nikam</i>	<b>122-127</b>

# CHARACTERIZATION OF METAL PEBBLES PREPARED BY ROTATING ELECTRODE PROCESS

T. Mohanty, B. M. Tripathi, R.K. Lenka, T. Mahata and P.K. Sinha

Powder Metallurgy Division, Bhabha Atomic Research Centre, Vashi Complex, Navi Mumbai, India

**Abstract :** Rotating Electrode Process (REP) is a centrifugal atomisation method for preparation of spherical metal pebbles by splashing out molten droplets from the tip of a rotating electrode. In this process, arc plasma is created between a rotating metal electrode and a non-consumable tungsten electrode. Intense heat is generated which melts leading edge of the metal electrode. During melting process itself, molten droplets are splashed out of the metal surface due to the centrifugal force and further solidify during travel in a chamber filled with an inert gas forming spherical pebbles. High purity argon (Ar) and helium (He) gases are used for cooling the molten metal droplets in the chamber.

The process parameters which significantly affect the pebbles size are: metal electrode diameter, metal electrode's rotational speed and physical properties of metal such as molten metal density and its surface tension. In this work stainless steel, titanium and beryllium metal pebbles were prepared under different processing parameters. Pebbles prepared by REP were seen to have spherical shape and uniform diameter. It has been observed that pebble diameter decreases with increase in rotational speed at constant anode diameter. Likewise, keeping rotational speed constant an increase in anode diameter decreases the particle diameter. Effect of process parameters on pebble characteristics, such as particle size, surface morphology and impurity content have been discussed in the present paper.

## 1. Introduction

International Thermonuclear Experimental Reactor (ITER) is a joint international research and development project constituted for demonstration of scientific as well as technological feasibility of deuterium (D)-tritium (T) nuclear fusion and thereby generating enormous energy in sustainable manner. India, among other seven participating countries is member of ITER. Unlike deuterium, tritium does not exist on earth and therefore must be bred through nuclear reaction between neutron and lithium (Li). One neutron is produced per D-T fusion which is not sufficient to achieve required tritium breeding ratio (TBR) more than unity. This is due to parasitic losses of neutrons in structural materials [1-2]. Beryllium, due to its neutron multiplying capability through  $(n, 2n)$  nuclear reaction is therefore used to compensate for neutron losses through various sources and maintain required TBR. India endeavors

to design and develop its own test blanket modules (TBM) viz. lead lithium cooled ceramic breeder (LLCB) and helium cooled solid ceramic breeder for testing in ITER. In helium cooled solid ceramic breeder (HCSB), metal beryllium/beryllide pebbles along with lithium based ceramics is used for tritium breeding [3].

Magnesium reduction and inert gas atomizing methods are standard processes for preparation of beryllium pebbles. However relatively bigger pebble size and departure from spherical shape is serious limitation of magnesium reduction method which leads to reduction in packing density and neutron multiplication [3]. In a gas atomizing process, the particle shape is spherical with fairly wide size distribution [4]. In order to overcome these problems, rotating electrode process (REP) was developed for preparation of beryllium pebbles. Beryllium pebbles prepared by REP are smaller in size, have uniform particle diameter, high purity and good sphericity [5].

# CHARACTERIZATION OF METAL PEBBLES PREPARED BY ROTATING ELECTRODE PROCESS

In REP, arc plasma is struck between a rotating metal electrode acting as anode and a tungsten electrode as cathode using inert gas atmosphere [6]. This causes melting of front edge of the anode due to high plasma temperature. The molten metal droplets experience a centrifugal force due to rotation of anode while melting and therefore, droplets are thrown out of metal electrode surface. Subsequently, the molten droplets solidify due to heat transfer while travelling in inert gas atmosphere resulting in formation of spherical pebbles.

Beryllium pebbles of diameter 0.2-2 mm are desirable for ITER application as it has improved packing density and lower thermal stress. When high energy neutrons produced in D-T fusion in ITER interact with beryllium, a large amount of helium is also formed by  $(n,\alpha)$  nuclear reaction of beryllium nuclei along with tritium. Helium condenses in the crystal lattice which induces swelling of pebbles. In order to avoid helium induced swelling and improve tritium generation, the crystal grain average diameter of beryllium pebbles should be properly controlled. The crystal grain average diameter can be tailored by proper tuning of REP process parameters [5]. Due to substantial advantages, REP has been recognized as the most appropriate technique of producing beryllium pebbles of desired properties for ITER applications.

The present paper focuses on REP process parameters affecting size of pebbles and description of REP experimental set up. Due to toxicity of beryllium initial experiments were conducted on its surrogate stainless steel (SS) and titanium (Ti) metal rods as electrode in REP [7] to validate REP for preparation of metal pebbles. Basic characterization of REP metal pebbles such as particle size distribution, density measurement, impurities study and morphology studies have been carried out.

## 2. Experimental procedure

### 2.1 Experimental setup

REP experimental set up consists of SS chamber having provision for holding the electrodes, pebbles collection port and inert gas inlet/outlet ports. A constant current DC power supply required for melting the metal electrode, rotational unit for varying the rotational speed of metal electrode and linear motion controlled unit for linear movement of anode. Fig.1 represents schematic of REP experimental set up.

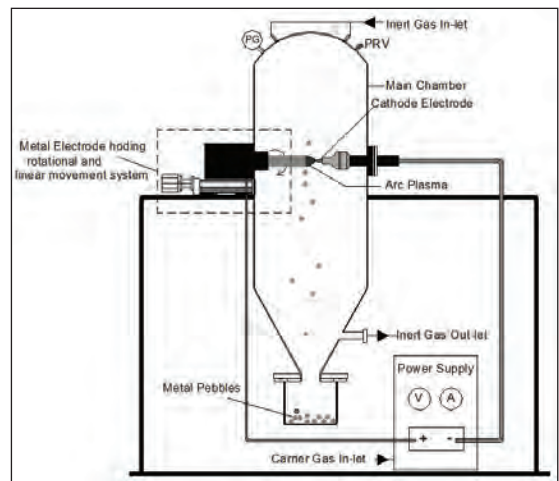


Fig. 1 Schematic of REP experimental set up

### 2.2 Preparation of metal pebbles

SS electrode of 6 mm diameter and 100 mm length was taken as anode electrode. The anode electrode was loaded into the holder arrangement attached to the SS chamber. Initial gap of 8 mm was maintained between the cathode and SS electrode. The SS chamber was filled with helium gas at 1.5 bar. Arc current was set at 40 A. the required rotational speed was adjusted by using Variable Frequency Drive. After attaining the required speed arc was generated between the SS and tungsten electrodes. During melting 8

# CHARACTERIZATION OF METAL PEBBLES PREPARED BY ROTATING ELECTRODE PROCESS

mm gap was maintained between the anode and tungsten electrode with the help of stepper motor controlled linear drive. Melting was carried out for a period of 1 minute. Metal pebbles were collected in the chamber and characterized. Same experimental procedure was repeated for the Titanium Electrode which has equal size as that of SS electrode.

## 2.3 Characterization

The pebbles prepared by REP method were characterized. The pebbles size and shape parameters were being studied by digital image analysis technique. Occhio make Zephyr LDA (Laser Diffraction Alternative) particle size and shape analyser is being used for our study. This instrument is equipped with high resolution camera with telecentric lens for taking the images of the particles with a resolution down to 10 μm / pixel. Dry static images of the pebbles have been taken and corresponding size and shape analyses were carried out with Occhio's Callisto software. Density of Titanium pebbles was measured using water displacement technique based on Archimedes' principle. The X-ray fluorescence (XRF) technique was used to determine the elemental composition of titanium rod and pebbles. The Surface morphology of Titanium pebble was observed by Scanning Electron microscope (SEM).

## 3. Results and Discussion

### 3.1 Theoretical analysis of REP

In REP, molten droplets primarily experience centrifugal force due to rotation of electrode and force due to surface tension. Droplets can splash out from the electrode surface only when centrifugal force overcomes the force due to surface tension. The following relationship is obtained by equating centrifugal force with force due to surface tension.

$$d_p = 60 * \sqrt{\frac{3\sigma_s}{D_a \rho_m}} \dots\dots\dots (1)$$

where,

- $d_p$  = particle diameter (m)
- $D_a$  = diameter of the metal electrode (m)
- $n$  = rotation of metal electrode (rpm)
- $\sigma_s$  = surface tension of molten metal (N/m)
- $\rho_m$  = density of molten metal (kg/m<sup>3</sup>)

The equation shows that metal pebbles size depends on physical properties of the metal electrode such as molten metal density and surface tension [8]. Further, the pebble size also depends on diameter and rotational speed of metal electrode.

Variation of beryllium particle diameter with beryllium anode diameter at different rotational speed (rpm) is represented in Fig. 2(a). It can be seen that particle diameter decreases with increasing anode diameter at fixed rpm and also with increasing rpm at fixed diameter of anode. This is due to increase in centrifugal force with anode diameter and rpm which imparts enough force to even smaller particles to overcome the surface tension.

Particle size have been calculated at different combination of rpm and anode diameter for SS, Ti and Be. Variation of particle diameter of beryllium, titanium and SS with anode diameter at 6000 rpm is shown in Fig.2(b). It can be inferred that particle sizes of SS and Ti produced by REP for given anode diameter and rotational speed, is smaller than beryllium particle size because of their higher molten metal density as compared to beryllium.

# CHARACTERIZATION OF METAL PEBBLES PREPARED BY ROTATING ELECTRODE PROCESS

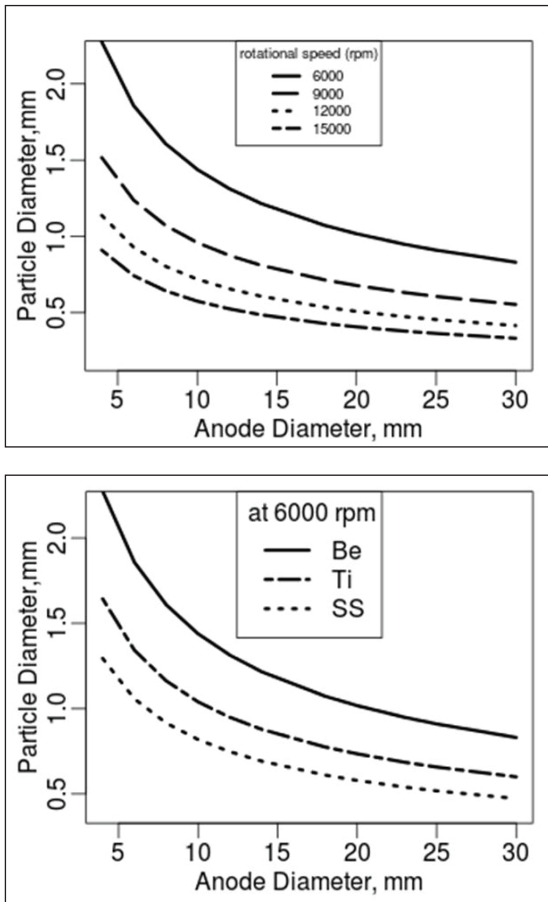


Fig. 2(a) Variation of beryllium particle diameter with beryllium anode diameter at different rotational speed, (b) Variation of particle diameter of beryllium, titanium and SS with anode diameter at 6000 rpm

### 3.2 Pebble size distribution

Size distribution of two samples of SS pebbles prepared at two different rotational speeds (3500 and 3150 rpm) is shown Fig. 3 and corresponding statistical parameters are given in Table 1. P25 value represents 25 % of the total particles have diameter less than this value. Similarly P75 value represents 75 % of the total particles have diameter less than this value. P50 is the median of the distribution. Fig.3 shows, as the rotational

speed of the electrode increases particle diameter decreases which is agreement with result predicted by theoretical analysis (Eq.1).

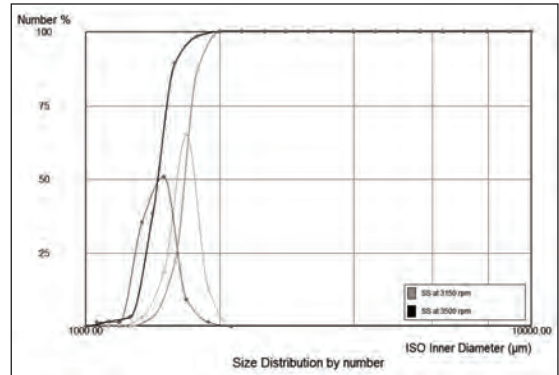


Fig.3. Particles size distribution of SS pebbles as monitored by image analysis (Zephyr LDA)

Table.1. Statistical distribution values of SS pebbles prepared by REP

Distribution Statistic	SS - 3150 rpm Value (µm)	SS - 3500 rpm Value (µm)
Mean	1662	1451
Std Dev	114.7	113.7
Min	1327	1116
P25	1588	1374
P50	1670	1455
P75	1734	1520
Max	1910	1793

Fig.4. represents particles size distribution of titanium particles at 3470 rpm and corresponding statistical parameters are given in Table 2. Median diameter of the distribution is 2074 µm with standard deviation value 128 µm. Mean and median values of particle diameter are close to each other. P75 represents 75% of the distribution is remain below 2167 µm diameter value. These values represent a narrow and symmetric distribution of particle size. It is noticeable that mean diameter of titanium

# CHARACTERIZATION OF METAL PEBBLES PREPARED BY ROTATING ELECTRODE PROCESS

pebbles is higher as compared to SS at around same rotational speed. This is due to difference in molten metal densities of Ti and SS.

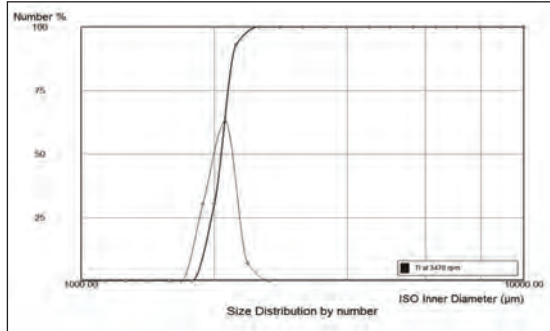


*Fig.4. Particle size distribution of titanium pebbles prepared by REP at rotational speed of 3470 rpm.*

*Table.2. Statistical distribution values of Titanium pebbles prepared by REP*

Distribution Statistics	Mean	Std Dev	Min	P25	P50	P75	Max
Value (μm)	2071	128.3	1819	1953	2074	2167	2314

Shape parameters are very important for evaluating the pebbles packing, flow and bulk properties of pebbles. Table 3 gives circularity and roundness values of the distribution monitored by image analyzer. Circularity median value is 91.22 % with standard deviation 0.815 % and roundness median value is 93.35 % with standard deviation 3.32 % which represents most of the particles are near to perfect spherical.

*Table 3. Shape parameters distribution statistic of Titanium pebbles*

Distribution Statistics	Mean	Std Dev	Min	P25	P50	P75	Max
Circularity (%)	91.13	0.815	88.5	90.66	91.22	91.64	92.7
Roundness (%)	92.8	3.32	84.17	90.49	93.35	95.54	97.15

### 3.3 Chemical composition of Ti pebbles

Table 4 represents the chemical composition of Titanium samples obtained by XRF

technique. The results of the XRF analyses show significantly low level of impurities in Ti pebbles as compared to corresponding electrode. Low impurity content in pebbles may be attributed to vaporization of some of the impurities having low melting points.

*Table 4. Chemical composition of Titanium Electrode and pebbles*

Element (wt%)	Ti	Al	Si	Other Impurities
Ti electrode	95.63	2.61	0.97	< 0.77
Ti pebbles	99.35	0.47	0.17	< 0.01

### 3.4 Surface morphology

Density of titanium pebbles obtained was about 93% TD of titanium. General morphology is depicted in SEM micrographs of Titanium pebbles (Fig. 5(a) and (b)). Fig.5 (a) shows good sphericity of Ti pebbles having diameter around 2 mm. The higher magnification SEM image (Fig. 5b) exhibits smooth surface of Ti pebble without any visible porosity.

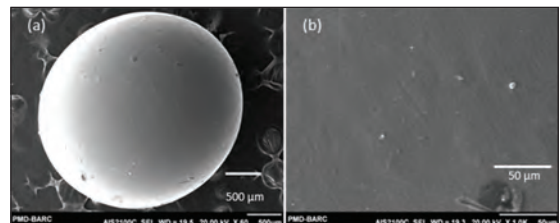


*Fig.5 SEM micrographs of Titanium pebbles prepared by REP*

### 4. Conclusions

Pebbles of stainless steel and titanium were prepared by REP under different processing parameters. It has been observed that process parameters which significantly affect the pebbles size are: metal electrode diameter, metal electrode's rotational speed and physical properties of metal such as molten metal density

## CHARACTERIZATION OF METAL PEBBLES PREPARED BY ROTATING ELECTRODE PROCESS

---

and its surface tension. Diameter of pebbles decreases with increase in rotational speed at constant anode diameter. At constant rotational speed, an increase in anode diameter decreases the particle diameter. Pebbles prepared by REP were seen to have good spherical shape with narrow and symmetric particle size distribution. Metal pebbles exhibit smooth surface morphology and have no visible open porosities. Low impurity content of pebbles as compared to parent electrode dictates possibility of vaporization of some impurity elements having low melting point.

### References

- [1] A. Khomutov, V. Barabash, V. Chakin, V. Chernov, D. Davydov, V. Gorokhov, H. Kawamura, B. kolbasov, I.Kupriyanov,G.longhurst, F. scaffidi-argentina, V. Shestakov.[Beryllium for fusion application-recent results] *Journal of Nuclear Materials*. **307-311**, pp. 630-637, (2002).
- [2] Dakshinamoorthy Sathiyamoorthy, S.J. Ghanwat , B.M. Tripathi , Chandan Danani. Novel mixed-oxide ceramic for neutron multiplication and tritium generation. *Journal of Nuclear Materials*. 417 (1-3), 775-779, (2011)
- [3] D.D. Thorat, B.M. Tripathi, D. Sathiyamoorthy. (2011, Sep). Extraction of beryllium from Indian beryl by ammonium hydrofluoride. *Journal of Hydrometallurgy*.109(1-2), pp.18-22.
- [4] FENG Yongjin , FENG Kaiming , CAO Qixiang , ZHANG Jianli, HU Jin Mar. 2013. Current Status of the Fabrication of Li<sub>4</sub>SiO<sub>4</sub> and Beryllium Pebbles for CN HCCB TBM in SWIP. *Plasma Science and Technology*, 15(3), pp.291-2914
- [5] Etsuo Ishitsuka, Hiroshi Kawamura, Naoki Sakamoto, Kiyotoshi Nishida, "Process for preparing Metallic Beryllium Pebbles" , US Patent no:5,958,105, Sep 28 (1999)
- [6] B. champagne, R. anders. Fabrication of powders by the Rotating Electrode Process.(1980). *International Journal of Powder Metallurgy & Powder Technology*. 16(4), pp. 359-367.
- [7] Mohanty, T. , Tripathi, B.M. , Mahata, T., Sinha, P.K. (2014, Nov). Arc plasma assisted rotating electrode process for preparation of metal pebbles. *Proceedings - International Symposium on Discharges and Electrical Insulation in Vacuum*, ISDEIV Article number 6961789, pp. 741-744
- [8] D. Sathiyamoorthy, Mohanty T, Srinivas K, Selvaraj D, Thorat D D.(2012, Feb.). Beryllium pebbles preparation and modeling of Rotating Electrode Process. *Fusion Science and Technology*. 61 (2), pp. 159-166.

# DEPENDENCE OF DEGREE OF OXIDATION OF MILL SCALE ON DEPTH OF STATIC BED AND ITS MODELLING WITH ANSYS FLUENT

R. Sabban, P. Tarate, N. B. Dhokey

Department of Metallurgical Engineering, Govt. College of Engineering, Pune, India

**Abstract :** Conversion of multi-oxide mill Scale to single highest oxide i.e.  $\text{Fe}_2\text{O}_3$  by oxygen blowing is most studied topic as  $\text{Fe}_2\text{O}_3$  powder has applications in many sectors like Soft and Hard ferrites, paint, tiles, ceramic colours, Cancer treatment etc. The present study focuses upon the conceptualization, design aspects of the process of oxidation of mill scale to  $\text{Fe}_2\text{O}_3$  and the formulation of model of the complete process considering the effect of different parameters like temperature, time of oxygen blowing, average particle size of mill scale, Oxygen flow rate, surface area of sample exposed to the flow, diffusivity of oxygen, chemical kinetics, dimensional parameters etc. on degree of oxidation of mill scale. Also, industrially attractive designs of the complete process of oxidation of mill scale were shaped in software like PRO-E. The formulation of mathematical model is carried out with approach of solving the basic equations of fluid flow with Computational Fluid Dynamics (CFD) algorithms. Analytical tool like ANSYS Fluent software is used for the modeling.

**Keywords:** Mill Scale,  $\text{Fe}_2\text{O}_3$ , design, Mathematical model, ANSYS FLUENT

## 1. Introduction

Mill scale basically is a combination of different oxides like Hematite ( $\text{Fe}_2\text{O}_3$ ), Magnetite ( $\text{Fe}_3\text{O}_4$ ) and Wustite ( $\text{FeO}$ ) etc [1]. Conversion of this multi oxide mill scale into single oxide ( $\text{Fe}_2\text{O}_3$ ) is the best suited route for turning out to be an industrially attractive process for gas sensing applications, thermite welding, surface temperature measurement, float-sink processing of ) etc [2,3,4]. This is economically can be carried out with increasing the kinetics of the reaction which again depends upon several experimental factors and nature of initial mill scale. The whole oxidation process can be modelled in static manner [ref]. Better design of the process will lead to enhancement in the degree of oxidation of mill scale.

ANSYS Fluent is the most powerful computational fluid dynamics (CFD) software tool used, so as to optimize the experimentation

conditions to get maximum output [8,9]. Fluent includes well-validated physical modeling capabilities to model flow, turbulence, heat transfer, and reactions for the application of oxygen flow in a furnace over the porous powder material i.e. mill scale in this case [7].

In this paper, in static modelling, the area of focus is the effect of depth of mill scale bed on degree of oxidation of mill scale with the help of ANSYS FLUENT software. In this model the depth upto which the oxygen in controlled flow will diffuse is calculated with the help of well equipped software tooling that will help in considering optimum combination of input variables corresponding to the desired output of maximum degree of oxidation of mill scale without carrying out repeated experiments. To support the optimum depth result the corresponding experimentation is also carried out at varying depth of static mill scale powder [5,6].

## DEPENDENCE OF DEGREE OF OXIDATION OF MILL SCALE ON DEPTH OF STATIC BED AND ITS MODELLING WITH ANSYS FLUENT

### Experimentation

Mill scale powder having chemical composition as presented in Table 1 is generally produced hot rolling operation.

*Table 1. Chemical composition of mill scale*

Compound	Fe <sub>Total</sub>	FeO	CaO	SiO <sub>2</sub>	MnO
Wt%	72.13	56.70	0.42	0.14	0.37

Coarse mill scale powder was procured and 100 grams of this mill scale was milled in a laboratory attritor mill for 6 hours. The rotating speed of ball mill bowl was adjusted to the 350 RPM. The ball to powder ratio was maintained at 10:1 by weight. The average particle size is found to be 7.16 mm with the help of LASER Particle Analyzer.

The blended mill scale sample weighing 20 grams was taken in a sample boat and placed in a MoSi<sub>2</sub> furnace as shown in Fig. 1 for Oxygen blowing with flow rate of 2 lit/min to get maximum yield of Fe<sub>2</sub>O<sub>3</sub>.

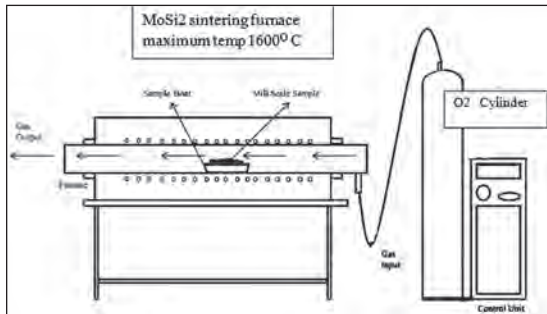


*Fig.1. MoSi<sub>2</sub> Furnace setup for oxygen blowing of mill scale at 1100° C*

The first set of experiments, the mill scale powder with mechanical attrition was heated to 1100°C and kept in the flow of pure oxygen for variable time from one hour, 2 hours and 3 hours. These set of experiments helped in the determination of optimum time (t) required for the complete oxidation to occur.

In the next set of experiments, after getting the optimum time (t), the sample were kept in the same furnace for time 't' at fixed temperature of 1100°C but with varying depth of mill scale in the tray by changing the weight of mill scale and its effect on degree of oxidation is determined. Potassium Dichromate test is carried out to determine Fe<sub>2</sub>O<sub>3</sub> and Fe total actual values so that we can modify out oxygen blowing parameters to get highest degree of oxidation of mill scale.

### Ansys Fluent Modelling

The fluid mechanics based system adopted here by choosing the process parameters of mill scale oxidation like depth of mill scale bed, temperature, and flow rate of oxygen blowing to get required degree of oxidation. Initially to start with the domain of the oxidation of mill scale is shaped in the PRO-E software as shown in Fig. 2.

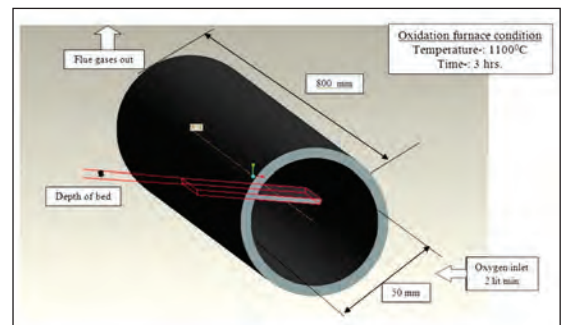


*Fig. 2. ANSYS FLUENT modeling domain for oxygen blowing of mill scale at 1100°C*

This PRO-E file is imported in the Geometry option in the ANSYS Fluent Workbench for editing it further. Then next stage is Meshing the domain. First of all the boundaries should be labeled as input, output, wall and porous media etc. Very fine meshing is done with

Minimum size = 0.00007 m, Maximum face size = 0.007 m, Maximum size = 0.04 m

Now next steps are to be done in SETUP. In model, multiphase volume of fluid is

## DEPENDENCE OF DEGREE OF OXIDATION OF MILL SCALE ON DEPTH OF STATIC BED AND ITS MODELLING WITH ANSYS FLUENT

selected. The System under consideration is time dependent so equations can be solved in transient mode. The tube under consideration is horizontal so gravity effect is neglected.

In the material selection option, oxygen gas is selected as one material and the values of viscosity and density at 1100°C are entered and mill scale powder is selected as porous media with porosity of 0.7 and density of 5.3 g/cc are entered.

Before any oxygen blowing there is presence of air inside the tube so air is taken as phase 1 and oxygen gas is taken as phase 2.

During entering the boundary conditions, the velocity at the inlet can be calculated as given in eq. (1)

$$\text{Velocity of flow} = \frac{\text{volume flow rate}}{\text{cross sectional area of the tube}} \dots\dots\dots(1)$$

Volume fraction of second phase is taken as 1 as pure oxygen gas is entering. Frequency is set as 5 activities in the calculation activities. We initialized the solution from inlet side; we need to make sure that all the area inside the tube is filled with air only so in Adopt by selecting area we can make the volume fraction of oxygen gas as zero.

In run calculation, the step size set is 0.02 and the number of iterations need to be done is 200. K-epsilon model is used to simulate the problem in which turbulent viscosity is assumed to be constant. The contours of movement of oxygen gas inside the tube are viewed in result part.

The affecting parameters on the degree of oxidation that are considered in the ANSYS FLUENT modelling are listed in following Fig. 3.

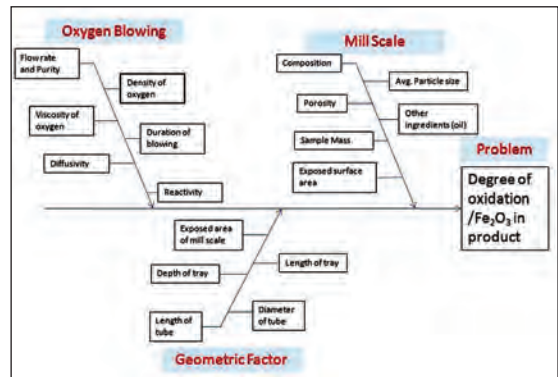


Fig. 3. Fishbone diagram comprising of process parameters used in FLUENT modelling

### Results and Discussion

#### 1) Experimental results

LASER Particle size analysis of 7 hrs Attritor milled powder

Fig. 4 shows the grading curve obtained on conducting Particle size distribution on Microtrac S3500 machine.

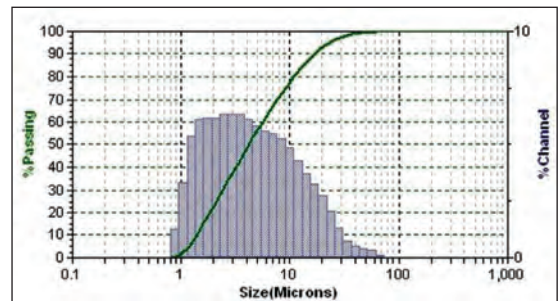


Fig. 4. Grading curve of Particle size distribution in LASER Particle Analyzer

The overall particle size distribution is given in Table 2 which represents the spread of the reading from average value. With the help of statistics the value of Mean or average particle size is found out on which the kinetics of oxidation is strongly dependent [10].

## DEPENDENCE OF DEGREE OF OXIDATION OF MILL SCALE ON DEPTH OF STATIC BED AND ITS MODELLING WITH ANSYS FLUENT

*Table 2 .particle size distribution of 7 hrs Attritor milled powder*

Particle Size Distribution,( $\mu\text{m}$ )			Mean Size ( $\mu\text{m}$ )
D10	D50	D90	
1.377	4.17	16.79	7.16

### XRD data analysis of optimum oxygen blowing time of 3 h

As shown in Fig. 5, XRD peaks indicate that there are nearly all peaks of higher oxide i.e.  $\text{Fe}_2\text{O}_3$ . Qualitatively, we can say that absence of any lower oxide peaks indicates that degree of oxidation is higher than in the case of the lower oxygen blowing time of powder.

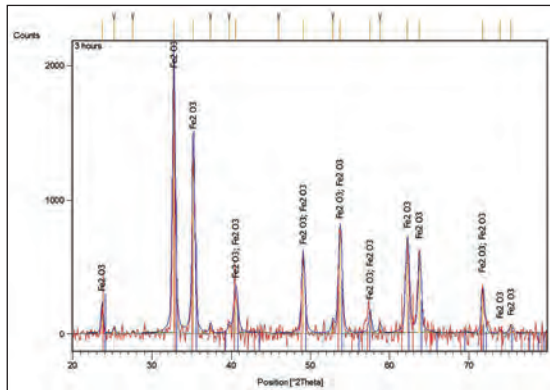


*Fig. 5. XRD of Oxygen blown powder for 3 hrs. at 1100°C showing nearly all peaks of  $\text{Fe}_2\text{O}_3$*

Fig. 6 shows the variation of wt %  $\text{Fe}_2\text{O}_3$  Vs. depth of mill scale bed used for oxidation. The difference between the readings relates directly to the diffusivity of oxygen into the porous bed of mill scale depending upon the particle size and subsequently reaction of diffused oxygen and the mill scale powder particle surface. Here the surface energy plays an important role. Focussing upon diffusion of oxygen into mill scale bed, initially oxygen gas will form stagnant layer on the porous surface of bed, this condition is known as No slip condition and then oxygen gas will diffuse inside the bed. So to have

maximum efficiency of the process bed depth should be optimum. Maximum yield of  $\text{Fe}_2\text{O}_3$  is obtained at 10 mm bed depth. So this is the Optimum bed depth for given set of conditions.

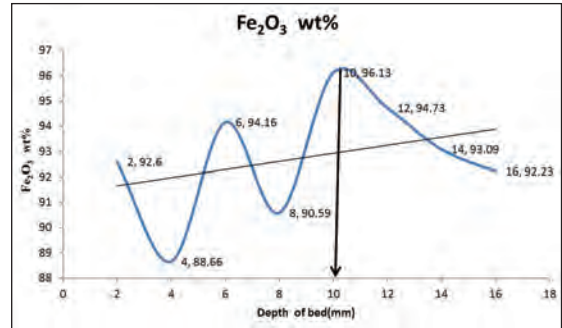


*Fig. 6. The variation of wt %  $\text{Fe}_2\text{O}_3$  Vs. depth of mill scale bed used for oxidation at 1100°C*

Similarly, Fig. 7 projects the variation of wt % Fe total Vs. depth of mill scale bed in similar manner as in Fig 4. The diffusion of oxygen gas through open porosity is the only culprit here.

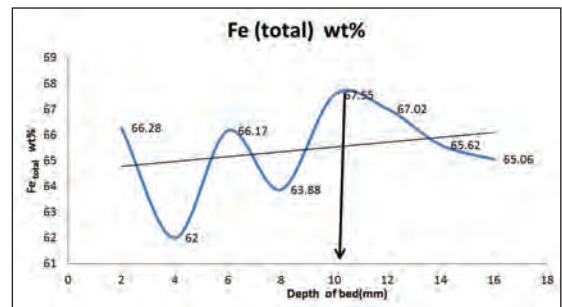


*Fig. 7. The variation of wt % Fe total Vs. depth of mill scale bed used for oxidation at 1100°C*

## 2) Ansys Fluent Results

Very fine meshing as described in the experimental procedure is shown in Fig. 8. This fine meshing is done to get exact volume fraction of oxygen gas in the tube so that optimum depth can be determined.

# DEPENDENCE OF DEGREE OF OXIDATION OF MILL SCALE ON DEPTH OF STATIC BED AND ITS MODELLING WITH ANSYS FLUENT

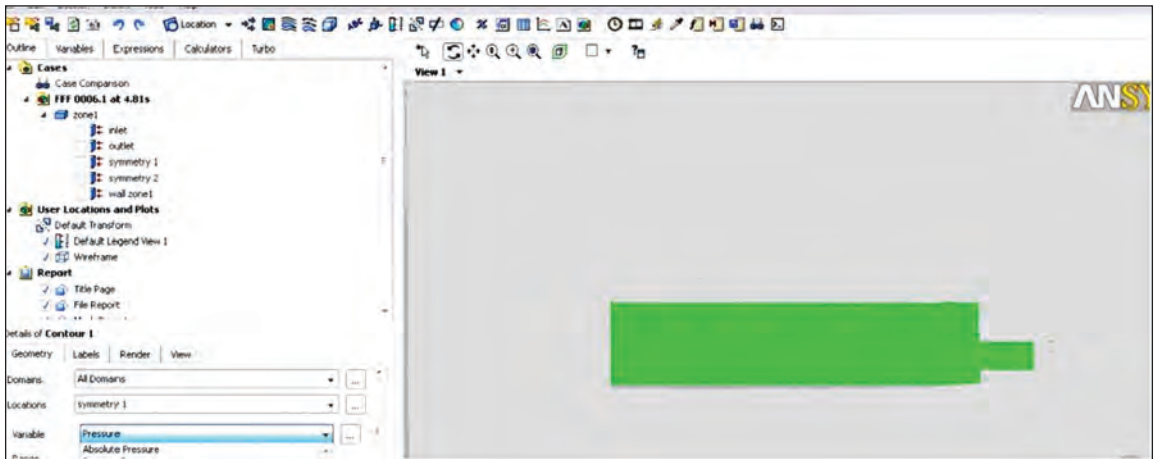


*Fig. 8. Very fine mesh size shaped in mesh editor in ANSYS FLUENT Modulator*

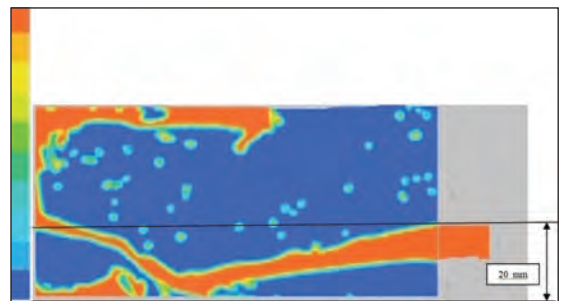
## Different stages during the oxygen blowing

Fig. 9 - Fig. 12 shows the photographs taken at different timings with an interval of 1 h.

With increase in time the diffusion of oxygen increases at constant temperature of 1100°C across the porous layer as it is a transient process. But we optimised the oxygen blowing time as 3 hrs so for 3 hrs oxygen blowing we need to optimise depth of mill scale bed so as shown in Fig.10 most of the volume is occupied by oxygen gas below 11.2 mm. so with the help of modelling we can predict the optimum depth of the mill scale bed and this value is near to the experimentally found value.



*Fig. 9. At t=0 volume distribution of two phases in the tube(Air is completely filled in tube)*



*Fig. 10. At t=1 hr volume distribution of two phases in the tube(smaller diffusion of oxygen across the porous layer)*

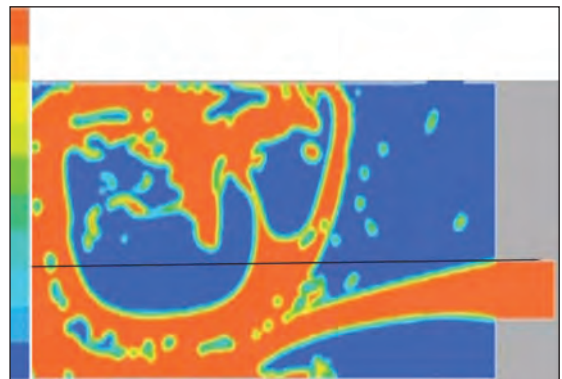


*Fig. 11. At t=2 hr volume distribution of two phases in the tube(more diffusion of oxygen across the porous layer)*

## DEPENDENCE OF DEGREE OF OXIDATION OF MILL SCALE ON DEPTH OF STATIC BED AND ITS MODELLING WITH ANSYS FLUENT

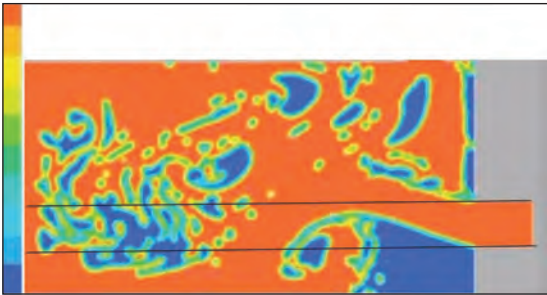


Fig. 12. At  $t=3h$  volume distribution of two phases in the tube (most of the diffusion of oxygen across the porous layer is possible)

### Conclusions

Depending upon the above mentioned analysis of effect of depth of mill scale bed on degree of oxidation of mill scale with both experimental results and supporting ANSYS FLUENT modelling the following conclusions can be drawn-

1. The experimental and modelling results are nearly same.
2. The accuracy of the predicted optimum mill scale depth obtained from the modelling is 92 %
3. This little variation can be caused due to fact that we assumed the particles are spherical in nature but practically there are small fraction of irregular particles depending upon prior history and these irregular particles decreases the porosity level and subsequently the diffusion of oxygen in the mill scale bed.

### References

- [1] N. M. Gaballah et al., A. F. Zikry1 "Production of Iron from Mill Scale Industrial Waste via Hydrogen" Open Journal of Inorganic Non-Metallic Materials, 3, 23-28, (2013)
- [2] R. Nowosielski, R.Babilas, "Structure and properties of barium ferrite powders prepared by milling and annealing" Archives of Materials Science and Engineering
- [3] Zviad Kovziridze, Paata Khorava, Nunu Mitskevich "Controlled Local Hyperthermia and Magnetic Hyperthermia of Surface (Skin) Cancer Diseases" Journal of Cancer Therapy, 2013, 4, 1262-1271 Published Online September 2013
- [4] J. MERIKHI, C. FELDMANN Philips Research Laboratories, "Homogeneous coatings of nanosized  $Fe_2O_3$  particles on  $Y_2O_3:S:Eu$ ," "JOURNAL OF MATERIALS SCIENCE" 35 (2000) 3959 - 3961"
- [5] Vandna Luthraa,1, Keith F.E. Pratt a, "Fabrication and characterization of  $Fe_{1.90}Ti_{0.10}O_3$  gas sensitive resistors for carbon monoxide" Sensors and Actuators B: Chemical Volume 135, Issue 2, 15 January 2009,
- [6] R.M. Cornell, U.Schwertmann The iron oxide: Structure, properties, reactions, occurrence and uses 2003 WILEY -VCH verlag GmbH
- [7] Mir Esmaeil Masoumi and Zahra Izakmehri "Improving of Refinery Furnaces Efficiency Using Mathematical Modeling" International Journal of Modeling and Optimization, Vol. 1, No. 1, April 2011
- [8] Chunfeng Yue ; Grad. Sch. of Eng., Kagawa Univ., Kagawa, Japan ANSYS FLUENT-based modeling and hydrodynamic analysis for a spherical underwater robot
- [9] S.A. Hosseini, H. Vahedi Tafreshi Modeling particle-loaded single fiber efficiency and fiber drag using ANSYS-Fluent CFD code Computers & Fluids Volume 66, 15 August 2012, Pages 157-166
- [10] Wahyu Kuntjoro, Aidah Jumahat, "Computational Simulation of Boil-Off Gas Formation inside Liquefied Natural Gas Tank Using Evaporation Model in ANSYS Fluent" 10.4028/www.scientific.net/AMM.393.839

# THE EFFECT OF STIRRING TIME ON SYNTHESIS OF NANO-CRYSTALLINE MAGNESIUM ALUMINATE SPINEL POWDER BY Sol-Gel PROCESS

Akash Shah<sup>1,2</sup>, C. Jariwala<sup>1</sup>, R. Pillai<sup>1</sup>, S.B.Tandon<sup>2</sup>, P.M. Raole<sup>1</sup> and B. Sarkar<sup>1</sup>

<sup>1</sup>Fusion Reactor Materials Development and Characterization Division, Institute for Plasma Research, Gandhinagar, India

<sup>2</sup>Department of Metallurgical and Materials Engineering, Indus University Ahmedabad, India

**Abstract :** Magnesium Aluminate ( $MgAl_2O_4$ ) is considered as high performance ceramic material, which retains its strength at elevated temperature. Further it has excellent thermal shock resistance, high resistance to chemical degradation, good optical and dielectric properties. It exhibits great structural stability under neutron irradiation environment. Owing to these unique combination of properties,  $MgAl_2O_4$  is widely used as highly effective transparent ceramic materials for infrared and armor windows used in nuclear reactors. It also has great potential for variety of applications as functional material in nuclear technology, nano fillers as reinforcement, ceramic pigments, and humidity sensors.  $MgAl_2O_4$  spinel powder is prepared by various synthetic methods such as: Precipitation route, Aerosol method, Citric-nitric route, Sol-Gel method, Spray drying, Freeze drying, and Solid state sintering. Conventionally,  $MgAl_2O_4$  powder is prepared by solid state reaction (SSR) route using high purity metal oxides at temperature above  $1600^\circ C$ . However, high purity and fine  $MgAl_2O_4$  powder is difficult to produce using solid state route due to contamination from inclusion during grinding step and abnormal grain growth during calcination at high temperature. Therefore, it is imperative to look for alternate processing method that will produce high purity  $MgAl_2O_4$  powder without adverse grain growth. In the present study,  $MgAl_2O_4$  nano powder is produced by Sol-Gel process. Sol-Gel is a chemical process consisting of formation of Sol and Gel via controlled reaction rate. The reaction rate is controlled by controlling the pH of Sol, temperature, stirring rate, precursor agents etc. In this study, the effect of Sol-Gel process parameters on particle size, size distribution and morphology of  $MgAl_2O_4$  nano powder is studied. The Sol-Gel process is optimized for producing  $MgAl_2O_4$  powder of size of about 220nm.

**Keywords:** Sol-Gel, Nano Particle, Magnesium Aluminate, Stirring time

## Introduction:

Nano materials with crystal sizes of about few nanometers have drawn significant attention among researchers around the world due to their unique properties. Nano materials have high strength; improved ductility/toughness, reduced elastic modulus. The extraordinary physical properties of nano materials are due to their relatively high volume fraction of grain boundaries. The volume fraction of grain boundaries can be as high as ~40%. Nano materials have huge application

potential in the field of sensors, structural ceramics, magnetic materials, fuel cells etc. where conventional microcrystalline materials fail to achieve desired combination of physical properties. Over the last few decades significant efforts are made to produce nano materials by several methods to produce nano materials with uniform crystal size and produce consistent properties. However, the true technological benefits of nano materials are yet to fully realize in commercial scale because of relatively high

## THE EFFECT OF STIRRING TIME ON SYNTHESIS OF NANO-CRYSTALLINE MAGNESIUM ALUMINATE SPINEL POWDER BY Sol-Gel PROCESS

cost of production and lack of guidelines and standards on handling of nano materials.

Magnesium Aluminate ( $\text{MgAl}_2\text{O}_4$ ) has long been known as a high performance ceramic material for structural applications because of its unique ability to develop high strength at both elevated and normal temperature. It has excellent thermal stability as it does not undergo any phase transformation up to its melting point. High structural stability at elevated temperature makes  $\text{MgAl}_2\text{O}_4$  a very promising material for use as refractory material. In addition,  $\text{MgAl}_2\text{O}_4$  spinel offers very good thermal shock resistance and high resistance to acidic and alkaline attack, which makes it a candidate material for use in chemical, electrochemical, and metallurgical industries.  $\text{MgAl}_2\text{O}_4$  spinel is also being considered for use in nuclear industries due to its high resistance to radiation damage [1]. Some of the other industries where  $\text{MgAl}_2\text{O}_4$  spinel may find applications to provide structural support are: dentistry, sensor manufacturers, and catalyst supports etc. Recently, the use of  $\text{MgAl}_2\text{O}_4$  in the development of transparent ceramic materials for infrared and armor windows in nuclear reactors is also being explored. Despite of high potential usage of  $\text{MgAl}_2\text{O}_4$  spinel, its commercial market is limited due to high cost of production. High cost required for producing superior quality  $\text{MgAl}_2\text{O}_4$  spinel with uniform nano-sized crystals is primarily due to tight process control and long process time.

Magnesium aluminate ( $\text{MgAl}_2\text{O}_4$ ) spinel are produced by various synthetic methods such as: precipitation route, aerosol method, citric-nitric route, sol-gel method, spray drying, freeze drying, and solid state sintering [2]. Conventionally,  $\text{MgAl}_2\text{O}_4$  powders are prepared by solid solution reaction (SSR) route using high purity metal oxides at temperature above  $1600^\circ\text{C}$ . However, the high purity and fine

$\text{MgAl}_2\text{O}_4$  powders are difficult to obtain due to contamination. In addition, calcination at high temperature results in abnormal grain growth during SSR processing route [3]. The  $\text{MgAl}_2\text{O}_4$  spinel produced via SSR route results in the formation of microcrystalline material instead of nano materials owing to high processing temperature. Therefore it is a prerequisite to lower the processing temperature to produce nano crystalline  $\text{MgAl}_2\text{O}_4$  spinel and maintaining chemical homogeneity. Sol-gel method provides an alternate method for producing uniformly sized nano crystalline  $\text{MgAl}_2\text{O}_4$  spinel without adversely affecting chemical homogeneity. Therefore, in the present study, an effort is made to produce magnesium aluminate ( $\text{MgAl}_2\text{O}_4$ ) nano powders through sol-gel process due to its unique ability to precisely control the particle size, size distribution, and morphology through systematic monitoring of reaction parameters. The effect of processing parameters on particle size distribution and phase evolution is discussed in this article.

### Experimental procedure:

Sol-Gel method for the preparation of  $\text{MgAl}_2\text{O}_4$  nano powder consists of preparation of Sol and Gel, followed by calcination of Gel at various temperatures. Precursor materials used for the preparation of  $\text{MgAl}_2\text{O}_4$  spinel were Aluminum Nitrate Nona-Hydrate [ $\text{Al}(\text{NO}_3)_3 \cdot 9\text{H}_2\text{O}$ ], Magnesium Nitrate Hexa-Hydrate [ $\text{Mg}(\text{NO}_3)_2 \cdot 6\text{H}_2\text{O}$ ] and Ammonium Hydroxide [ $\text{NH}_4\text{OH}$ ]. The calculated amount of Aluminum Nitrate Nona-Hydrate and Magnesium Nitrate Hexa-Hydrate solution in the molar ratio of 2:1 were slowly mixed while continuously stirred for 1 hour. On hour of stirring was required to ensure uniform mixing and get pH value of the solution to a desired level. After 1 hour of mixing, Ammonium Hydroxide [ $\text{NH}_4\text{OH}$ ] solution was added drop by drop to the

# THE EFFECT OF STIRRING TIME ON SYNTHESIS OF NANO-CRYSTALLINE MAGNESIUM ALUMINATE SPINEL POWDER BY Sol-Gel PROCESS

solution of Aluminum Nitrate Nona-Hydrate and Magnesium Nitrate Hexa-Hydrate under continuous stirring till the pH of the solution is brought to the desired level of 3. Through extensive experimentation, it was noted that the Sol pH level of 3 is optimum for preparation of fine nano sized  $MgAl_2O_4$  powder. The prepared solution was stirred for following durations: 24, 48, 72, 84, and 96 hours. The duration of stirring significantly affected particle size and its size distribution. Subsequent to stirring operation of Sol for various intervals, solution was dried in an oven drying at  $110^\circ C$  for 48 hours. After drying, each sample was heated to  $500^\circ C$ ,  $1000^\circ C$ , and  $1500^\circ C$  at the heating rate of 0.6/minute for calcination. The calcined sample was ground to produce powder. The process flow chart for the preparation of  $MgAl_2O_4$  powder is shown in Fig. 1. The crystal size of calcined powder and phase formed after calcination was identified using X-Ray diffraction (XRD). In addition, calcined powder was characterized by Scanning electron microscope (SEM), and particle size analyzer.

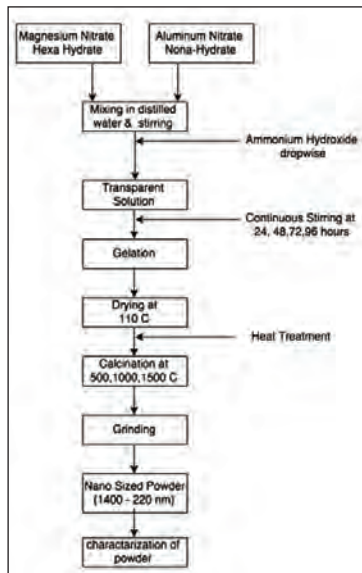


Fig. 1. Typical flowchart of the preparation of Magnesium Aluminate

## Results and Discussion:

### 1. X-Ray Diffraction (XRD) Analysis:

The XRD patterns of samples processed at various temperatures are shown in Fig. 2. The XRD analysis confirms the formation of magnesium aluminate spinel phase in sample calcined at  $1500^\circ C$  for different stirring time. On contrary, the powder calcined at  $500^\circ C$  shows very low intensity and broad peaks due to amorphous like nature of powder. As expected, on increasing the calcination temperature from  $500^\circ C$  to  $1500^\circ C$ , the intensity of XRD peak increases and their corresponding peak width at half maxima decreases. This is due to the crystallization of  $MgAl_2O_4$  powder from amorphous state. This shows that the powder formed during sol-gel method is in amorphous state. Further XRD analysis using "Debye Scherer" formula [cite reference] shows that the size of  $MgAl_2O_4$  powder crystal is in the range of 84- 103 nm.

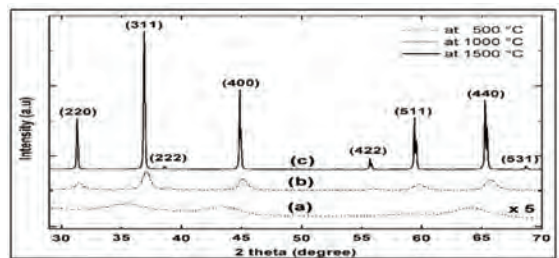


Fig. 2. XRD spectra for Magnesium Aluminate powder processed at (a)  $500^\circ C$  (data amplified with the factor of  $\times 5$ ) (b)  $1000^\circ C$  (c)  $1500^\circ C$

### 2. Scanning Electron Microscope (SEM):

Scanning electron micrographs of  $MgAl_2O_4$  powder calcined at  $1500^\circ C$  for different stirring times are shown in Fig. 3A-D. Scanning electron microscopic (SEM) observation showed that particles were of uneven shape and formed clusters during calcinations. These agglomerates were ground to produce fine powder.

# THE EFFECT OF STIRRING TIME ON SYNTHESIS OF NANO-CRYSTALLINE MAGNESIUM ALUMINATE SPINEL POWDER BY Sol-Gel PROCESS

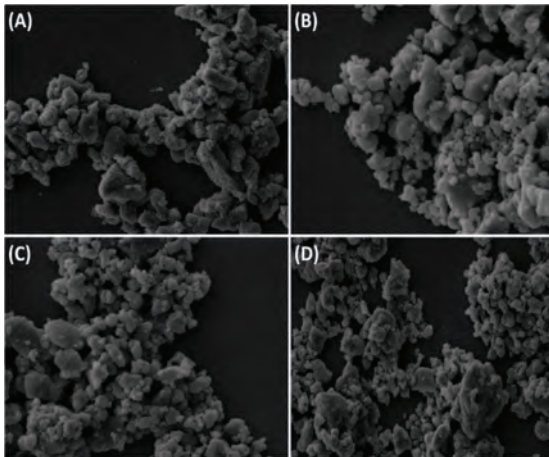


Fig. 3. Scanning electron micrographs of powder calcined at 1500°C for following stirring times: (A) 24 hrs (B) 48 hrs (C) 72 hrs (D) 96 hrs.

### 3. Particle Size analyzer:

The particle analyzer was used to determine the size and size distribution of Magnesium Aluminate powder. The effect of stirring time on particle size of MgAl<sub>2</sub>O<sub>4</sub> powder is shown in Fig. 4. It shows that particle size of MgAl<sub>2</sub>O<sub>4</sub> powder decreases with the increasing of stirring time up to 72 hours; beyond which the particle size increases when the stirring time was increased to 96 hours. This is attributed to the increase in viscosity of the solution with the increase in stirring time up to a threshold time of 72 hours. This also explains the reason for the formation of agglomerates with the solution during sol-gel process.

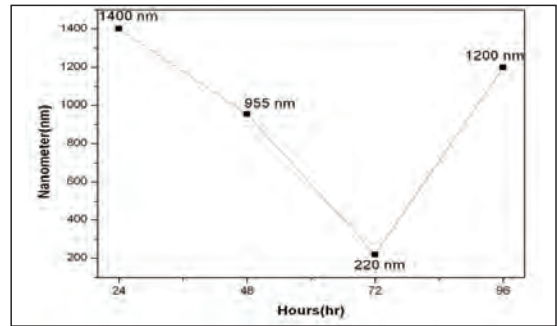


Fig. 4. Plot showing the variation of particle size of MgAl<sub>2</sub>O<sub>4</sub> powder vs. stirring time

### Conclusions:

Nano crystalline MgAl<sub>2</sub>O<sub>4</sub> spinel powder was successfully produced by Sol-Gel process. The XRD analysis confirmed the formation of MgAl<sub>2</sub>O<sub>4</sub> powder in sample calcined at 1500°C. The optimum stirring time required producing MgAl<sub>2</sub>O<sub>4</sub> powder of 220 nm size was 72 hours and calcination temperature required for the same was 1500°C. During calcination, agglomerates of MgAl<sub>2</sub>O<sub>4</sub> particles formed and the particle morphology was unevenly spherical.

### References:

1. F. Tavangarian and R. Emadi, Journal of Alloys and Compounds, 489 (2010), p. 600-604
2. Milan Kantinaskar and Minati Chatterjee, Journal of the American Ceramic Society, 88(1), (2015), p. 38-44
3. Li-Zhaipei, Wan-Yun Yin, Ji-Fen Wang, Junchen, Chuan-Gang Fan, Qian-Fengzhang, Materials Research, 13, (2010), p. 339-343.

# EFFECT OF NANO SIZED STARTING MATERIALS ON THE DIELECTRIC AND FERROELECTRIC BEHAVIOUR OF BARIUM TITANATE

K. R. Kambale<sup>1</sup>, A. R. Kulkarni<sup>2</sup>, N. Venkataramani<sup>2</sup>

<sup>1</sup> Department of Metallurgy and Materials Science, College of Engineering Pune, India

<sup>2</sup> Department of Metallurgical Engineering and Materials Science, Indian Institute of Technology Bombay, Mumbai, India.

**Abstract :** Barium titanate is a ceramic widely used in electronic industry because of its high dielectric constant and low tangent losses. Barium titanate used in electronic circuits is not in powder form but it is a sintered product with shape formed as per component design. Thus, it becomes important to study sintering characteristics of barium titanate. The main objective of this research work was to synthesize barium titanate from micron sized barium carbonate and titanium oxide having different particle size (0.7  $\mu\text{m}$ , 50 – 60 nm and 80 – 90 nm) and study the effect of particle size on sintering characteristics and dielectric and ferroelectric properties of barium titanate. The calcination temperature of barium titanate was 1150 °C when micro sized barium carbonate and titanium oxide were used as starting materials. However, calcination temperature decreased to 900 and 950 °C when micro sized barium carbonate and nano titanium oxide with particle size 50 – 60 nm and 80 – 90 nm were used respectively. Peak dielectric constant was reduced and transition temperature was enhanced in case of barium titanate synthesized from nano sized starting materials. Ferroelectric parameters were also reduced in case of barium titanate synthesized from nano sized starting materials. Fatigue characterization of ceramics caused 3 – 5% reduction in spontaneous polarization on application of  $10^7$  cycles. Leakage current in sintered ceramics varied from  $10^{-6}$  to  $10^{-10}$  A. Leakage current in ceramics sintered using spray dried powders were an order less than ceramics sintered using non spray dried powders.

**Keywords:** Barium titanate, particle size, sintering, dielectric, ferroelectric, fatigue and leakage current

## Introduction

Barium titanate is a ceramic widely used in electronic industry because of its high dielectric constant and low tangent losses. It is often used as basic ferroelectric material in electronic components such as multilayer ceramic capacitors (MLCC), positive temperature coefficient thermistors (PTC), electro-optic devices, memory applications, sensors and actuators etc. High purity barium titanate powder is reported to be an important component of new barium titanate capacitor energy storage systems for use in electric vehicles [1].

Barium titanate exhibits cubic perovskite structure ( $a = 4.09$  a.u.) above its Curie

temperature ( $T_c \sim 120$  °C). This cubic structure is stable up to 1460 °C. Below  $T_c$  the structure slightly distorts due to displacement of  $\text{Ti}^{4+}$  cations (11 pm),  $\text{Ba}^{2+}$  cations (6 pm) and oxygen sublattice (3 pm) and becomes tetragonal ( $a = 3.992$  a.u.  $c = 4.035$  a.u.). Traditionally,  $\text{BaTiO}_3$  is prepared using a high-temperature (>1100 °C) solid-state reaction between  $\text{BaCO}_3$  and  $\text{TiO}_2$  which yields large crystal grains (>3  $\mu\text{m}$ ) with a wide range of shape and size. Moreover, these powders result in less chemical homogeneity. Even if the ratio of  $\text{BaCO}_3/\text{TiO}_2$  is one it may result in intermediate phases which are retained in end product. However, wet chemistry methods such as co precipitation, hydrothermal, micro emulsion and sol gel process offer advantages in terms of

## EFFECT OF NANO SIZED STARTING MATERIALS ON THE DIELECTRIC AND FERROELECTRIC BEHAVIOUR OF BARIUM TITANATE

processibility, phase purity, homogeneity and controlled stoichiometry but still these methods also pose serious problems. For example, first three methods have complicated washing conditions which are difficult to control. Sol-gel process requires precursors that are highly expensive and are not commonly available. Thus, despite several drawbacks of solid state reaction method, it becomes necessary to study some new aspects of this method. It is difficult to develop a dielectric layer of less than 10  $\mu\text{m}$  for increased capacitance, which is a major requirement for miniaturization of next generation of electronic/microelectronic devices and the MLCC industries. To meet these requirements, the synthesis of  $\text{BaTiO}_3$  nanopowders having particle size less than 100 nm and a high dielectric constant is needed for further miniaturization of electronic circuits [2-3].

Barium titanate used in electronic circuits is not in powder form but it is a sintered product with shape formed as per component design. Thus, it becomes important to study sintering characteristics of barium titanate than merely studying synthesis of barium titanate powders. Though many research articles are available in literature on the synthesis of barium titanate, very few discuss about sintering and sintering kinetics of barium titanate. Nikolic et. al. have studied sintering characteristics of submicron sized barium titanate powder and found that maximum density achieved was 88% of theoretical density. Recently, sintering studies on nano sized barium titanate powder synthesized by hydrothermal, sol-gel route etc. have revealed that maximum density achieved is greater than 95% of theoretical density. However, none of these studies elaborate on the effect of particle size on sintering kinetics and dielectric behaviour of barium titanate [3-5].

In view of the above discussion, the main objective of this research was to synthesize barium titanate using micron sized barium carbonate and nano

sized titania of different particle size by solid state reaction route and study the effect of particle size on sintering characteristics and dielectric and ferroelectric properties.

### Experimental Work

To synthesize barium titanate by solid state reaction method micron sized barium carbonate (mean particle size = 2  $\mu\text{m}$ ) and titanium oxide (mean particle size = 0.7  $\mu\text{m}$ ) were purchased from Sigma Aldrich chemical Company. Nano sized titania (particle size = 50 - 60 nm and 70 - 80 nm) powders were purchased from Tiona and Degussa chemical companies respectively. Fig. 1 (a) and (b) show SEM images of micro

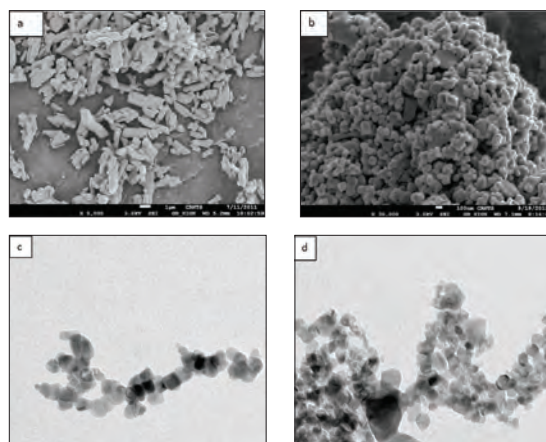


Fig. 1 SEM images of micro - sized (a)  $\text{BaCO}_3$  (b)  $\text{TiO}_2$  and TEM images of nano sized  $\text{TiO}_2$  purchased from (c) Tiona (d) Degussa

sized  $\text{BaCO}_3$  and  $\text{TiO}_2$  while (c) and (d) show TEM images of nano sized  $\text{TiO}_2$ . Fig. 2 (a) - (c) show Thermogravimetric analysis (TGA) curves for micro - sized  $\text{BaCO}_3$  and Tiona  $\text{TiO}_2$  and Degussa  $\text{TiO}_2$  to incorporate weight loss/gain in batch calculation and decide the calcination temperature.

## EFFECT OF NANO SIZED STARTING MATERIALS ON THE DIELECTRIC AND FERROELECTRIC BEHAVIOUR OF BARIUM TITANATE

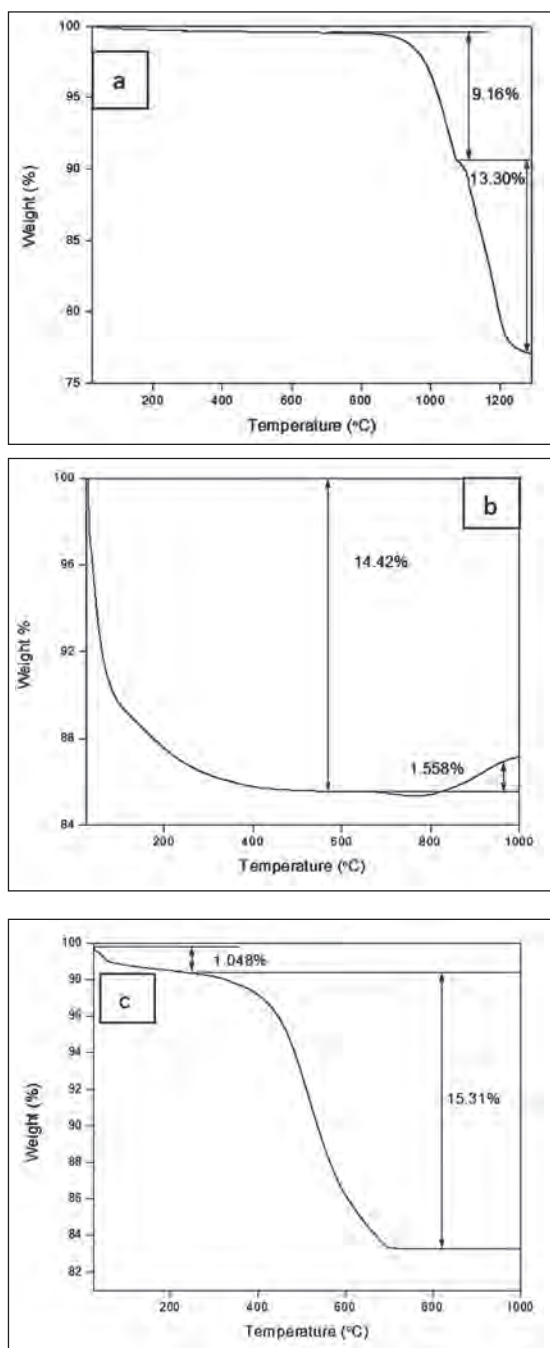


Fig. 2 TGA curves for (a) micro - BaCO<sub>3</sub> (b) Tiona TiO<sub>2</sub> (c) Degussa TiO<sub>2</sub>

In order to synthesize barium titanate, micro - sized starting materials were first mixed in methanol to make slurry and yttria stabilized zirconia balls were added to mixture so as to ball mill the mixture. Ball/powder ratio was 5:1 and the mixture was ball milled for 48 hours. After taking away the slurry from the ball mill, it was washed with methanol to take out the balls and slurry was kept in an oven at 80°C to evaporate methanol. The dry mass was crushed in agate mortar and pestle to make a fine powder. This powder was calcined at 1150°C for 4 hours. Same procedure was repeated for micro BaCO<sub>3</sub> - Tiona TiO<sub>2</sub> and micro - BaCO<sub>3</sub> - Degussa TiO<sub>2</sub> in the temperature range 750 - 900°C and 750-950°C respectively. Spray drying of powders was carried out using BUCHI mini spray dryer B-290 with inlet temperature of 190°C and outlet temperature of 75°C. Ammonium poly-acrylate was used as dispersant for slurry used to prepare spray dried powder and 1 wt% poly vinyl alcohol (PVA) was used as a binder in a slurry. Green pellets were prepared from non spray dried as well as spray dried BaTiO<sub>3</sub> powders using uniaxial pressing at 250 MPa. 3 wt% PVA was used as a binder for non - spray dried powders. Solid state sintering was carried out at 1200°C for 2, 4 and 6 hours in a muffle furnace.

To identify the structure of calcined powder, X- ray diffraction was carried out using X-ray diffractometer (PANalytical X-ray diffractometer PW 3040/60) in the 2θ range of 5-90°. X-ray source was Cu-ka with the wavelength of 1.54 angstrom. Generator voltage and tube current were 40 kV and 30 mA respectively. Room temperature XRD data was collected with a step size of 0.016 and 24.765 second time per step. Density of pellets was determined using Archimedes' principle [6]. Scanning electron microscopy (SEM) (JEOL JFC-1600 FESEM Oxford Instruments) was carried out to study the morphology of barium titanate ceramics powders as well as sintered

## EFFECT OF NANO SIZED STARTING MATERIALS ON THE DIELECTRIC AND FERROELECTRIC BEHAVIOUR OF BARIUM TITANATE

pellets. Dielectric properties of sintered pellets were measured in the temperature range -10 to 180°C in the frequency range 0.1 Hz to 1 MHz using Novocontrol alpha dielectric alpha analyzer at 0.1 V RMS, with 10 frequency steps per decade spaced equally on a logarithmic scale. Differential scanning calorimetric studies were performed in order to confirm the transition temperature of barium titanate using (NETZSCH DSC 200 PC). The heating rate employed was 5°C/min and the temperature range was 30 to 200 °C. The ferroelectric properties of sintered samples were measured using (TF analyzer 2000 FE Module aixACCT). The field applied was about 15 kV/cm. P-E loop measurements were carried out at frequencies 1, 10, 50 and 100 Hz respectively. The measurements were made in a temperature range of 30 to 180° C. Leakage current experiments were carried out with amplitude of 450 V. Fatigue experiments were carried out at fatigue frequency of 1kHz and fatigue amplitude of 3V. The electric field applied for fatigue experiments was 15 kV/cm and frequency of 10 HZ.

### Results and Discussion

XRD pattern of BaTiO<sub>3</sub> powder synthesized from BaCO<sub>3</sub> and micro TiO<sub>2</sub> is shown in Fig. 3. Formation of barium titanate was confirmed with JCPDS database (reference code: 01-079-2264 and ICSD collection code: 067519). The crystal structure of barium titanate powder is tetragonal. Fig. 4 shows XRD patterns for calcination of BaCO<sub>3</sub> and TIONA TiO<sub>2</sub> calcined at temperatures from 750 to 900°C, i.e. at 50°C intervals and held for 4 hours at each temperature. Complete phase formation takes place at 900°C. Similarly, Fig. 5 shows XRD patterns for calcination of BaCO<sub>3</sub> and Degussa TiO<sub>2</sub> at temperatures 750 to 950°C, i.e. at 50°C intervals and held for 4 hours at each temperature. Phase pure barium titanate gets formed after recalcination at 950°C. Fig. 6 shows

XRD patterns for spray dried powders. Table 1 shows comparison between the calculated and standard parameters of barium titanate powder P1. It can be seen that actual lattice parameters are in excellent agreement with theoretical lattice parameters and hence, it confirms the formation of tetragonal BaTiO<sub>3</sub> powder synthesized using micro - sized BaCO<sub>3</sub> and TiO<sub>2</sub>. Similar kind of agreement in lattice parameters was obtained for other BaTiO<sub>3</sub> powders.

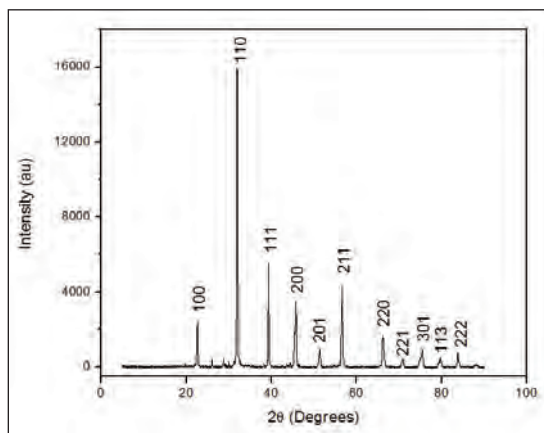


Fig. 3 XRD pattern for calcined BaTiO<sub>3</sub> powder synthesized from micro - sized BaCO<sub>3</sub> and TiO<sub>2</sub>

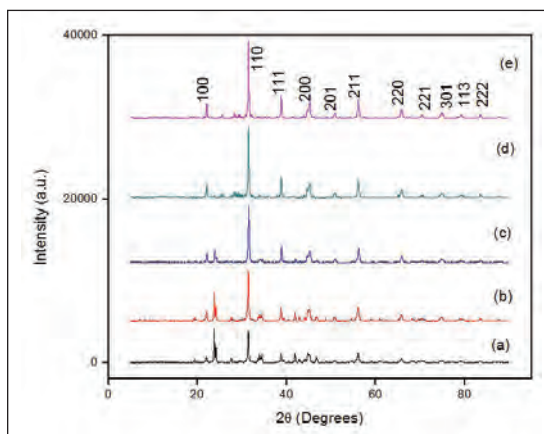


Fig. 4 XRD patterns for calcination of BaCO<sub>3</sub> and TIONA TiO<sub>2</sub> at (a) 750 °C for 4 hours (b) 800 °C for 4 hours (c) 850 °C for 4 hours (d) 900 °C for 4 hours (e) recalcination at 900 °C for 4 hours

# EFFECT OF NANO SIZED STARTING MATERIALS ON THE DIELECTRIC AND FERROELECTRIC BEHAVIOUR OF BARIUM TITANATE

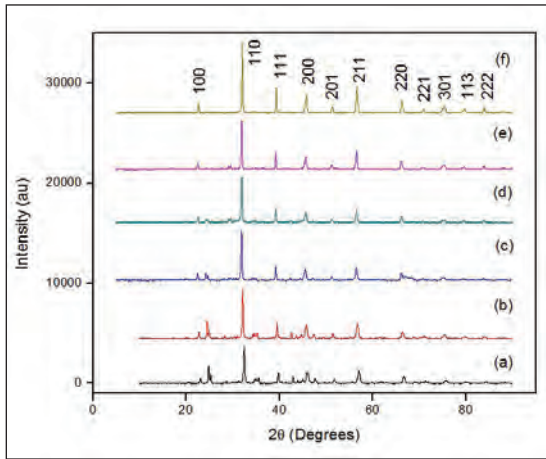


Fig. 5 XRD patterns for calcination of BaCO<sub>3</sub> and Degussa TiO<sub>2</sub> at (a) 750°C for 4 hours (b) 800°C for 4 hours (c) 850°C for 4 hours (d) 900°C for 4 hours (e) 950°C for 4 hours (f) Recalcination at 950°C for 4 hours

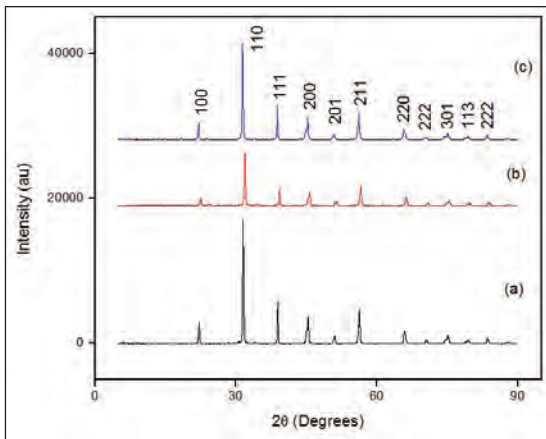


Fig. 6 XRD patterns for spray dried BaTiO<sub>3</sub> powders synthesized from (a) BaCO<sub>3</sub> and micro TiO<sub>2</sub> (b) BaCO<sub>3</sub> and TIONA nano TiO<sub>2</sub> (c) BaCO<sub>3</sub> and Degussa nano TiO<sub>2</sub>

Table 1 Comparison of lattice parameters of calcined BaTiO<sub>3</sub> powder with standard values of lattice parameters of BaTiO<sub>3</sub>

Sample	Calculated	Standard	Percentage Change
BaTiO <sub>3</sub> powder synthesized from BaCO <sub>3</sub> and micro TiO <sub>2</sub>	a = 3.983Å	a = 3.9998 Å	0.42
	b = 3.983Å	b = 3.9998 Å	0.42
	c = 4.020 Å	c = 4.0180 Å	0.0497
	α = β = γ = 90°	α = β = γ = 90°	0
	V = 63.78Å <sup>3</sup>	V = 64.28 Å <sup>3</sup>	0.7778

Table 2 shows meaning of sample codes used for BaTiO<sub>3</sub> powders and ceramics prepared using different starting materials and processes.

Table 2 Sample codes for different BaTiO<sub>3</sub> powders and sintered ceramics

Sample Code	Description
P1	BaTiO <sub>3</sub> powder synthesized from micro BaCO <sub>3</sub> and micro TiO <sub>2</sub>
P2	BaTiO <sub>3</sub> powder synthesized from micro BaCO <sub>3</sub> and TIONA TiO <sub>2</sub>
P3	BaTiO <sub>3</sub> powder synthesized from micro BaCO <sub>3</sub> and Degussa TiO <sub>2</sub>
P4	Spray dried BaTiO <sub>3</sub> powder synthesized from micro BaCO <sub>3</sub> and micro TiO <sub>2</sub>
P5	Spray dried BaTiO <sub>3</sub> powder synthesized from micro BaCO <sub>3</sub> and TIONA TiO <sub>2</sub>
P6	Spray dried BaTiO <sub>3</sub> powder synthesized from micro BaCO <sub>3</sub> and Degussa TiO <sub>2</sub>
S1	Ceramic sintered using powder 1
S2	Ceramic sintered using powder 2
S3	Ceramic sintered using powder 3
S4	Ceramic sintered using powder 4
S5	Ceramic sintered using powder 5
S6	Ceramic sintered using powder 6

Fig. 7 shows relative density of BaTiO<sub>3</sub> powders prepared using micro - sized and nano sized TiO<sub>2</sub> powders via conventional and spray drying process and subsequently sintered at 1200°C for 6 hours. It can be seen that for ceramics sintered using nano TiO<sub>2</sub> powders in non spray dried condition relative density was marginally lower than that obtained with micro sized TiO<sub>2</sub>. However, after spray drying the powders improvement in the density was obtained.

## EFFECT OF NANO SIZED STARTING MATERIALS ON THE DIELECTRIC AND FERROELECTRIC BEHAVIOUR OF BARIUM TITANATE

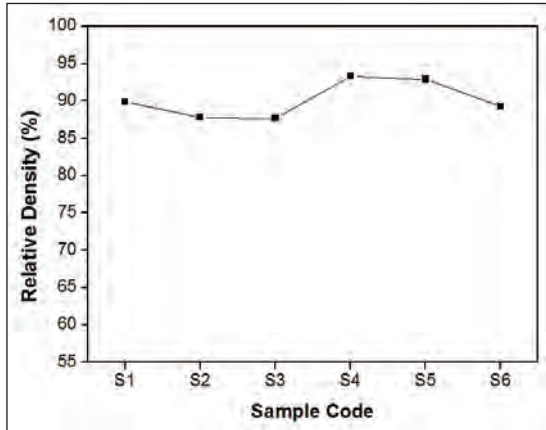


Fig. 7 Relative density of various BaTiO<sub>3</sub> ceramics prepared from different powders

Fig. 8 (a - f) shows morphology of barium titanate powder synthesized from BaCO<sub>3</sub> and micro TiO<sub>2</sub>, BaCO<sub>3</sub> and TIONA nano TiO<sub>2</sub> and BaCO<sub>3</sub> and Degussa nano TiO<sub>2</sub> without spray drying and with spray drying respectively. It can be observed that barium titanate powder particles are nearly spherical similar to titania particles. The particle size of powders is in the range 0.5-0.7 μm which is in good agreement with the particle size determined using particle size analyzer. Fig. 9 shows SEM images of sintered BaTiO<sub>3</sub> ceramics S1 - S6. Average grain size of S1 ceramics is about 10 μm while that of ceramics S2 - S6 is about 1 μm which can be effect of nano TiO<sub>2</sub> and/or spray drying process. Fig. 10 shows EDS spectrum of sintered BaTiO<sub>3</sub> (S1) sample. The average Ti/Ba ratio was calculated to be 1.04 and there is small deviation from stoichiometry. This can be attributed to the intrinsic drawback of solid state reaction in which close control of stoichiometry is not possible [1, 7]. Table 3 shows wt % of each element in barium titanate as observed in EDS chemical analysis. From Table 4 it is clear that amount of element in each grain slightly deviates from its theoretical value. Similar kind of marginal deviation in stoichiometry was observed in ceramics S2 - S5.

Table 3 Elemental analysis of S1 barium titanate ceramic

Spectrum	Actual Content Calculated from ED S (wt %)			Theoretical Content Calculated from formula weight (wt %)			Total
	O	Ti	Ba	O	Ti	Ba	
1	22.18	19.79	58.03	20.58	20.53	58.89	100
2	17.47	20.26	62.27	20.58	20.53	58.89	100
3	17.02	20.85	62.13	20.58	20.53	58.89	100

Fig. 11 shows room temperature variation of dielectric constant of ceramics S1, S2 and S3 as a function of frequency in the range of 0.1 Hz to 1 MHz. The room temperature dielectric constant of ceramic S1 at 1 kHz frequency is about 1522 while those of S2 and S3 are 870 and 1140. These values of dielectric constant are in good agreement with those reported in literature [7 - 8]. It is interesting to note that dielectric constant of BaTiO<sub>3</sub> synthesized from TIONA TiO<sub>2</sub> is having minimum dielectric constant at room temperature and 1 kHz frequency. At low frequencies dielectric constant of BaTiO<sub>3</sub> synthesized from Degussa TiO<sub>2</sub> is as high as 80000 but reduces drastically above 10 Hz frequency. Fig. 12 shows variation of dielectric constant versus frequency of ceramics S4, S5 and S6. It can be seen that dielectric constant values got reversed on spray drying. At all frequencies dielectric constant of S5 is greater than that of S4 and S6. At 1 kHz frequency, dielectric constant of S5 is as high as 2600 and that of S4 is about 2000 but dielectric constant of S6 is only about 925. Dielectric constant for S4, S5 was significantly improved on spray drying but reduced in the case of S6. Fig. 13 shows variation of tan δ versus frequency at room temperature for ceramics S1, S2 and S3. It can be seen that tan δ value for S3 is as high as 20 at low frequencies but reduces drastically below 10 Hz and then becomes comparable with S1 and S2. It can also be seen from inset that tan δ of S2 is slightly greater than that of S1 at all frequencies. Fig. 14 shows variation of tan δ versus frequency for ceramics S4, S5 and S6. At all frequencies value of tan δ is minimum for S6 ceramic. Values of tan δ are comparable beyond 100 Hz for S4 and S5 ceramics.

EFFECT OF NANO SIZED STARTING MATERIALS ON THE DIELECTRIC AND FERROELECTRIC BEHAVIOUR OF BARIUM TITANATE

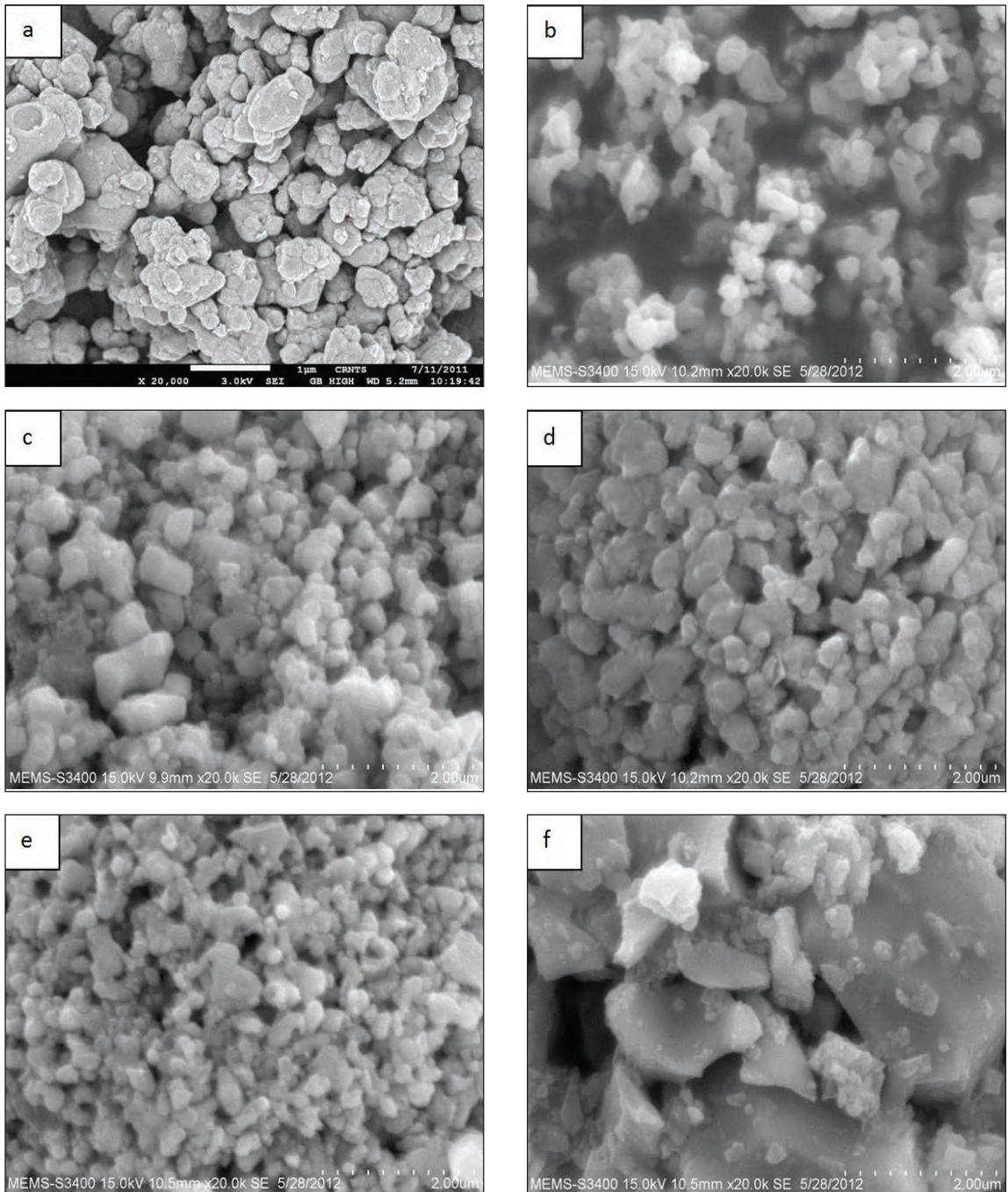
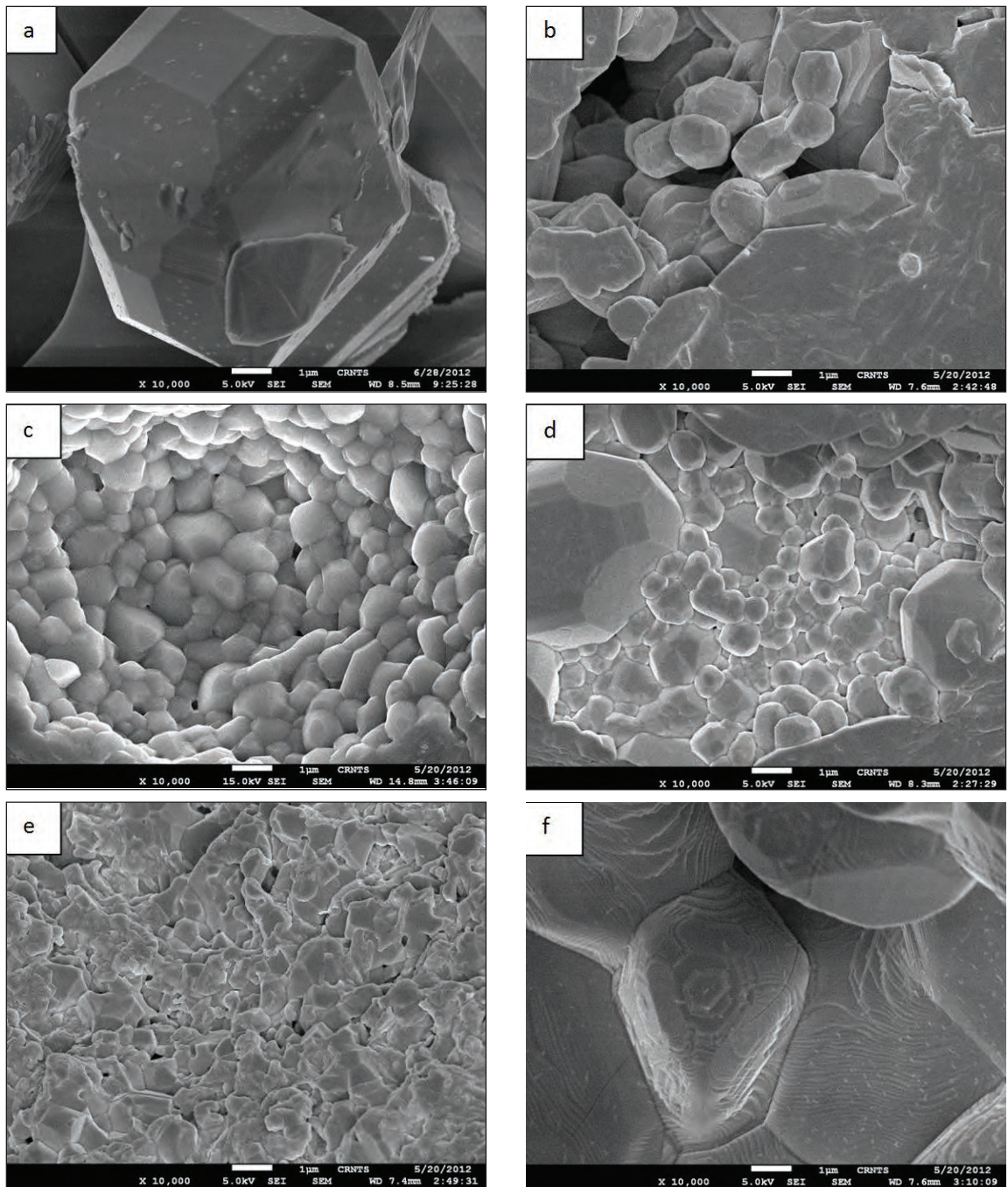


Fig. 8 SEM images of BaTiO<sub>3</sub> powders (a) P1 (b) P2 (c) P3 (d) P4 (e) P5 (f) P6 at a magnification of 20000X

## EFFECT OF NANO SIZED STARTING MATERIALS ON THE DIELECTRIC AND FERROELECTRIC BEHAVIOUR OF BARIUM TITANATE



*Fig. 9 SEM images showing fractured surfaces of sintered BaTiO<sub>3</sub> pellets (a) S1 (b) S2 (c) S3 (d) S4 (e) S5 and (f) S6 at a magnification of 10,000X*

# EFFECT OF NANO SIZED STARTING MATERIALS ON THE DIELECTRIC AND FERROELECTRIC BEHAVIOUR OF BARIUM TITANATE

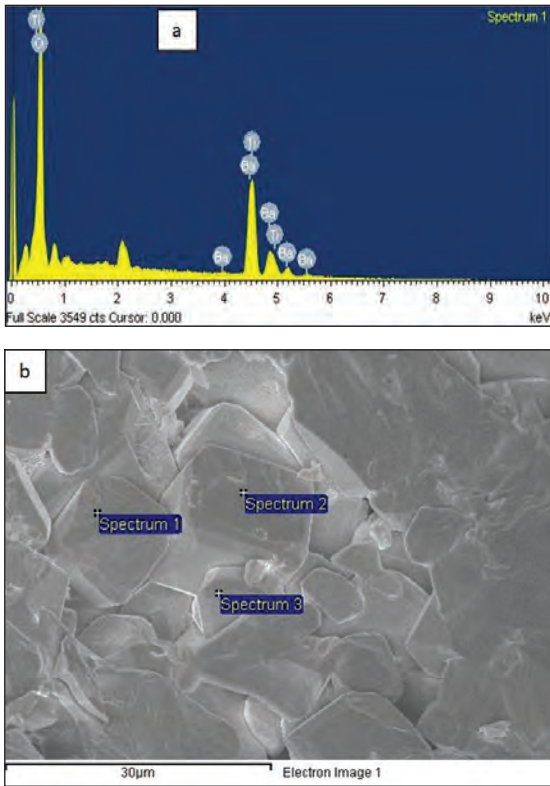


Fig. 10 EDS chemical analysis on sample S1 (a) EDS chemical spectrum (b) Corresponding region from which spectrum was taken

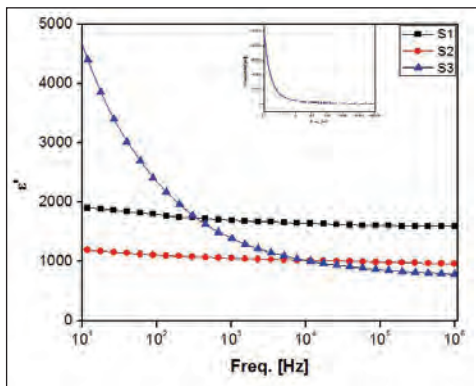


Fig. 11 Variation of dielectric constant for ceramics S1, S2 and S3 as a function of frequency at room temperature

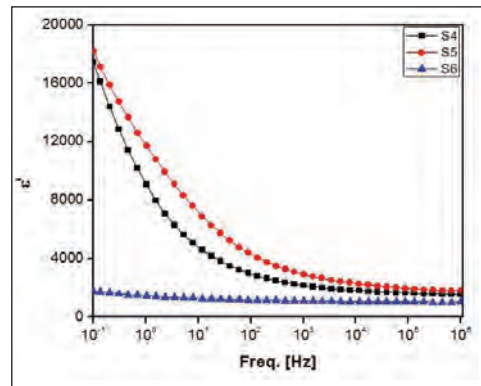


Fig. 12 Variation of dielectric constants for ceramics S4, S5 and S6 as a function of frequency at room temperature

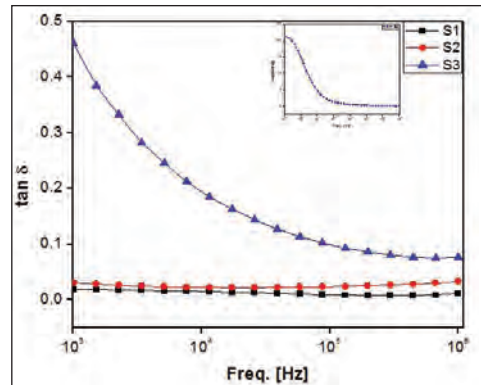


Fig. 13 Variation of  $\tan \delta$  versus frequency for S1, S2 and S3 at room temperature

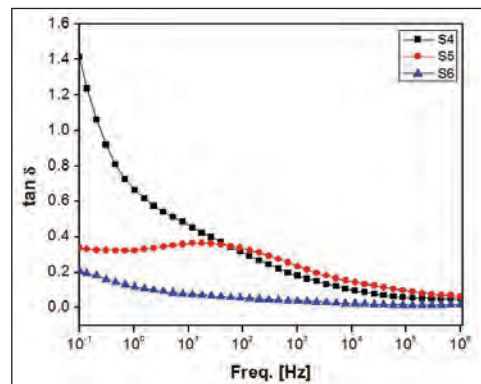


Fig. 14 Variation of  $\tan \delta$  versus frequency for S4, S5 and S6 at room temperature

## EFFECT OF NANO SIZED STARTING MATERIALS ON THE DIELECTRIC AND FERROELECTRIC BEHAVIOUR OF BARIUM TITANATE

**Table 4 Comparison of transition temperatures obtained from dielectric studies and DSC**

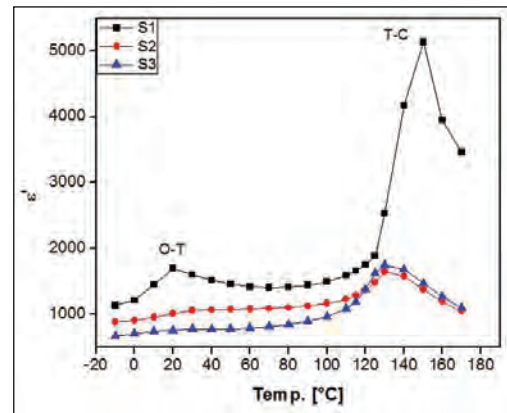
Sample	T <sub>c</sub> (°C) from dielectric studies	Sample	T <sub>c</sub> (°C) from DSC
S1	120	P1	119
S2	128	P2	130
S3	126	P3	127
S4	125	P4	125
S5	130	P5	130
S6	127	P6	127

Fig. 15 shows variation of dielectric constant for ceramics S1, S2 and S3 as a function of temperature at 1 kHz and Fig. 16 shows dielectric constant for ceramics S4, S5 and S6 as a function of temperature at 1 kHz. The peak dielectric constant for S1 is about 4500. This value is in good agreement with the value reported by Sharma et. al [8]. However, it is significantly lower than the value reported by Gao et. al [9]. This can be attributed to comparatively large grain size ~ 10µm in present experiment while the grain size was controlled up to 0.5 µm in the experiments carried out by Gao et.al. It is also very obvious that peak dielectric constant is lower with respect to nanocrystalline BaTiO<sub>3</sub> ceramics synthesized by various methods [10-11]. It has been reported in literature that reducing grain size of barium titanate from 50 µm to 1 µm increases dielectric constant from 2000 to 10000 [12].

However, peak dielectric constants for S2 and S3 are only about 1500. The grain size of these ceramics is about 1-2 µm. Still reduction in grain size has not caused any improvement in dielectric constant. However, these results are in accordance with the results of Jonker et. al (1962) who proposed that maximum in dielectric constant decreases with decrease in grain size because of suppression in spontaneous polarization. Micheron (1972) also predicted theoretically and proved experimentally that value of maximum dielectric constant  $\epsilon'_{max}$  increases with increase in grain size. Berton and Roelandt also found the same behaviour in Ba-

Sr titanates. From literature it can be concluded that on increasing grain size,  $\epsilon'_{max}$  increases and T<sub>c</sub> decreases. The increase in T<sub>c</sub> with decrease in grain size of ceramics S2 and S3 exactly agrees with what has been said in the literature [13].

As shown in Fig. 16 the peak dielectric constant for ceramic S4 is about 12000 while that for S5 and S6 is about 3000-4000. It can be noted that spray drying caused significant improvement in peak dielectric constant of all the ceramics with respect to their counterparts which were sintered using non spray dried powders. Though grain sizes of ceramics S4, S5 and S6 are nearly same, the particle size of their starting materials is different. Starting materials for S4 were BaCO<sub>3</sub> and TiO<sub>2</sub> (both micro sized) while those for S5 and S6 were micro sized BaCO<sub>3</sub> and nano TiO<sub>2</sub>. Thus, it can be said that not only decreased grain size but also decreased particle size of starting materials can reduce  $\epsilon'_{max}$  and increase T<sub>c</sub>. This gets proved in case of ceramics S4, S5 and S6 where  $\epsilon'_{max}$  of S5 and S6 are lesser than that of S4 and T<sub>c</sub> of S5 and S6 is greater than that of S4.



**Fig. 15 Variation of dielectric constant versus temperature of ceramics S1, S2 and S3 at 1 kHz frequency**

## EFFECT OF NANO SIZED STARTING MATERIALS ON THE DIELECTRIC AND FERROELECTRIC BEHAVIOUR OF BARIUM TITANATE

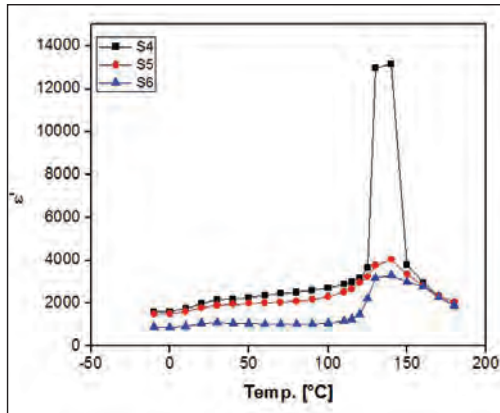


Fig. 16 Variation of dielectric constant versus temperature for ceramics S4, S5 and S6 at 1 kHz frequency

Curie temperatures ( $T_c$ ) of ceramics were determined by plotting  $1/\epsilon'$  versus temperature and then extrapolating that graph to x - axis as shown in Fig. 17.  $T_c$  obtained from dielectric measurements were confirmed by DSC measurements for S1 - S6 ceramics as shown in Fig. 18 and 19. The shift of  $T_c$  to higher temperature in case of ceramics S2-S6 is in accordance with the experimental findings of previous researchers [13]. Table 4 shows  $T_c$  obtained for these ceramics from dielectric measurements and DSC analysis which are in excellent agreement with each other.

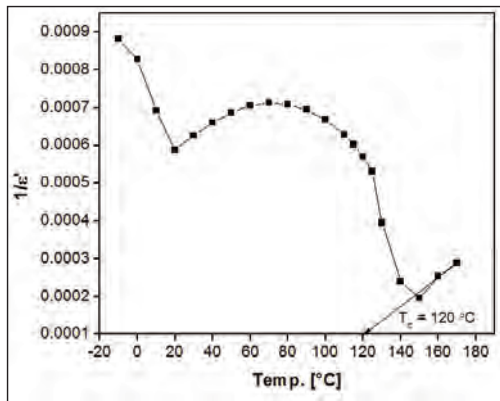


Fig. 17 Variation of  $1/\epsilon'$  versus temperature for ceramic S1

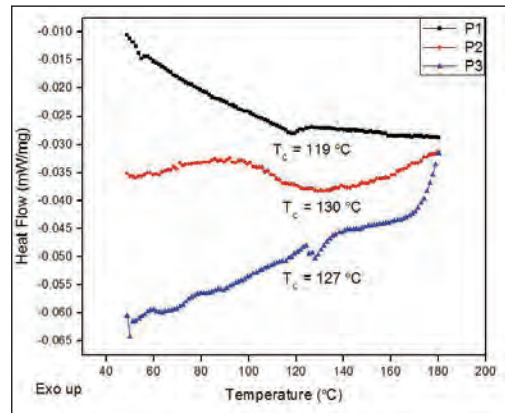


Fig. 18 Variation of heat flow as a function of temperature for  $\text{BaTiO}_3$  non spray dried powders P1, P2 and P3

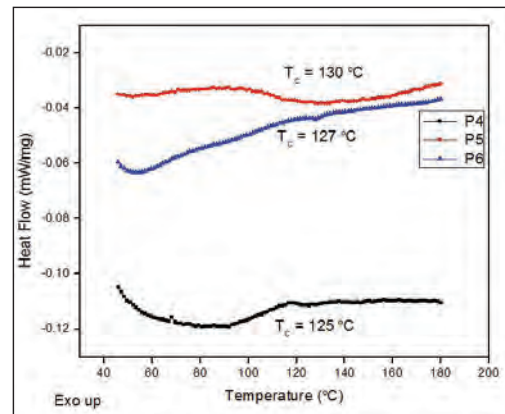


Fig. 19 Variation of heat flow as a function of temperature for  $\text{BaTiO}_3$  spray dried powders P4, P5 and P6

Ferroelectric hysteresis measurements were carried out on sintered ceramics to study polarization behaviour of these ceramics. It was observed that polarization values increase with decrease in frequency of applied electric field. As the frequency increases, the dipoles/ domains get lesser time to orient in the direction of applied field. On the contrary at lower frequency, domains get sufficient time to align themselves in the direction of applied field.

Maximum polarization values vary in case of ceramics made from non spray dried ceramics in

## EFFECT OF NANO SIZED STARTING MATERIALS ON THE DIELECTRIC AND FERROELECTRIC BEHAVIOUR OF BARIUM TITANATE

the order  $(P_s)_{S1} > (P_s)_{S3} > (P_s)_{S2}$ . It should be noted that loops of S2 and S3 are narrower than those of S1 indicating reduced energy loss in hysteresis. In case of ceramics sintered using spray dried powders  $P_s$  values are still lesser than ceramics sintered using non spray dried ceramics except for ceramic S5. For ceramic S5, Saturation polarization value is about  $25 \mu\text{C}/\text{cm}^2$ . Table 5 indicates values of ferroelectric parameter of these ceramics at 10 Hz frequency. From this table it can be seen that all the ferroelectric parameters, viz.,  $P_s$ ,  $P_r$ ,  $V_c$  and energy loss have lower values than S1.

Ferroelectric properties of ceramic S1 are in good agreement with those reported in literature with same route of synthesis and having similar grain sizes [13 - 14, 15 -18]. Reduction in polarization values of ceramics S2-S6 is also similar to the ferroelectric behaviour reported by Tura et. al. Ceramics S2-S6 show grain sizes of the order of 1-2  $\mu\text{m}$ . In case of research carried out by Tura et. al. effect of decreasing grain size on ferroelectric properties of barium titanate was studied which is on the parallel lines of the study carried out in this research work. Reduction in ferroelectric parameters can be attributed to increased defects like grain boundary (area) on reducing grain size of  $\text{BaTiO}_3$  ceramic [19]. The ferroelectric properties/parameters of ceramics S1-S6 possess higher values than those reported in literature for nanocrystalline  $\text{BaTiO}_3$  ceramics [20 - 21].

**Table 5 Ferroelectric parameters (from P-E loop) values of the sintered ceramics S1-S6**

Sample	$P_s$ ( $\mu\text{C}/\text{cm}^2$ )	$P_r$ ( $\mu\text{C}/\text{cm}^2$ )	$-P_r$ ( $\mu\text{C}/\text{cm}^2$ )	$V_c$ (volt)	$-V_c$ (volt)	Energy loss ( $\mu\text{J}/\text{cm}^2$ )
S1	6.5427	2.6119	-1.6580	1023.42	-1798.32	27607.8
S2	2.4787	0.3189	-0.2862	488.148	-502.573	3388.25
S3	4.5674	1.4096	-1.41308	751.235	-716.098	8227.58
S4	5.3483	1.5244	-0.5470	238.083	-766.646	7427.6
S5	4.8806	1.6377	-0.9919	377.317	-723.634	7202.76
S6	2.16627	0.0234	-0.2434	281.996	-24.7818	890.017

Fatigue characterization was carried out to study the effect of switching cycles on polarization. Fig. 20 shows variation of spontaneous polarization as a function of number of switching cycles for ceramics S1-S3. Polarization values remain

constant for these ceramics up to  $10^6$  cycles and at the end of  $10^7$  cycles these ceramics show 3-5% reduction in spontaneous polarization values. The general mechanism for fatigue in ferroelectric materials is explained on the basis of electrical stress which causes creation or redistribution of imperfection in a ferroelectric material which in turn affect switchable polarization. The results for ceramics S1, S2 and S3 are consistent with the results of Lu et. al. In their case also, there was no significant reduction in polarization up to  $10^6$  cycles for  $\text{BaTiO}_3$  ceramics sintered at different temperatures and isothermal holding durations. Similar results were obtained for ceramics S4- S6. These ceramics also suffered only 3-5% loss in spontaneous polarization value on the application of  $10^7$  switching electrical cycles making them potential candidate for actuator applications [18, 22].

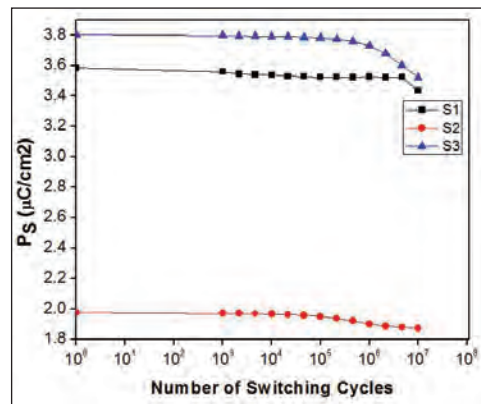


**Fig. 20 Variation of spontaneous polarization as a function of number of switching cycles for ceramics S1, S2 and S3**

Leakage current test was carried using electrical fields in the range 1.5-4 kV/cm on ceramics S1-S6. It was observed that current in these ceramics vary in between  $10^{-6}$ -  $10^{-10}$  A and current through ceramics S4, S5 and S6 is nearly one order less than through S1, S2 and S3 respectively. This can be attributed to higher density of S4, S5 and S6 ceramics. Values of leakage current observed

## EFFECT OF NANO SIZED STARTING MATERIALS ON THE DIELECTRIC AND FERROELECTRIC BEHAVIOUR OF BARIUM TITANATE

in this study fall in the same range reported by other researchers working in the same area [23-24].

### Conclusions

Barium titanate was synthesized using conventional solid state reaction with  $\text{BaCO}_3$  and  $\text{TiO}_2$  as starting materials and also using two different types of nano  $\text{TiO}_2$ . Calcination temperature for formation of barium titanate powder was  $1150^\circ\text{C}$  for conventional reaction while calcination temperature was reduced to  $950^\circ\text{C}$  and  $900^\circ\text{C}$  by use of Degussa nano  $\text{TiO}_2$  (particle size  $\sim 80$  nm) and TIONA nano  $\text{TiO}_2$  (particle size  $\sim 50$  nm) and XRD confirmed the formation of tetragonal barium titanate powder. SEM micrographs of barium titanate ceramic revealed that the grain size is of order of  $10\ \mu\text{m}$  and porosity were observed in sintered ceramics made by conventional route while grain sizes of ceramics made from nano sized starting materials were  $1\text{-}2\ \mu\text{m}$ . Dielectric properties of barium titanate ceramic were measured. The room temperature dielectric constant was about 1100 at 1 kHz frequency and  $\tan \delta$  was 0.025 at 1 kHz frequency. However, decrease in peak dielectric constant and increase in transition temperature was observed with reduced grain size. Transition temperature of barium titanate ceramics was confirmed using DSC. Decrease in grain size of ceramics made by new route caused decrease in ferroelectric parameters values. Fatigue characterization of all the ceramics revealed that only 3-5% loss in spontaneous polarization would occur on the application of  $10^7$  switching cycles. Leakage currents in the ceramics ranged between  $10^{-10}$  to  $10^{-6}$  A and leakage current in ceramics made from spray dried powders is an order less than other ceramics.

### References

- [1] M. M. Vijatović, D. Bobić and B. D. Stojanović. "History and challenges of barium titanate: part I" *Science of Sintering* 2008; 40: 155-165.
- [2] A.K. Jha and K. Prasad. "Ferroelectric  $\text{BaTiO}_3$  nanoparticles: biosynthesis and characterization" *Colloids and Interfaces B: Biointerfaces* 2010; 75: 330-334.
- [3] P. Yu, X. Wang and B. Cui. "Preparation and characterization of  $\text{BaTiO}_3$  powders and ceramics by the sol-gel process using organic monoacid as surfactant" *Scripta Materialia* 2007; 57: 623-626.
- [4] M.V. Nikolic, V.P. Pavlovic, V.B. Pavlovic, N. Labus and B. Stojanovic. "Application of master sintering curve theory to non- isothermal sintering of  $\text{BaTiO}_3$  ceramics" *Materials Science Forum* 2005; 494: 417-422.
- [5] H. Xu and L. Gao. "Hydrothermal synthesis of high purity  $\text{BaTiO}_3$  powders: control of powder phase and size, sintering density and dielectric properties" *Materials Letters* 2004; 58: 1582-1586.
- [6] ASTM C 373-88 "Standard test method for water absorption, bulk density, apparent porosity and apparent specific gravity of fired whiteware products" *ASTM International* (1988) 1-2.
- [7] C.Y. Chang, C.Y. Huang, Y.C. Wu, C.Y. Su and C.L. Huang. "Synthesis of submicron  $\text{BaTiO}_3$  particles by modified solid state reaction" *Journal of alloys and Compounds* 2010; 495: 108-112.
- [8] H.B. Sharma, H.N.K. Sarma and A. Mansingh. "Ferroelectric and dielectric properties of sol-gel processed barium titanate ceramics and thin films" *Journal of Materials Science* 1999; 34: 1385-1390.
- [9] L.J. Gao, X.L. Liu, J.Q. Zhang, S.Q. Wang and J.F. Chen. "Grain controlled barium titanate ceramics prepared from high gravity reactive precipitation process powder" *Materials Chemistry and Physics* 2004; 88:27-31.

## EFFECT OF NANO SIZED STARTING MATERIALS ON THE DIELECTRIC AND FERROELECTRIC BEHAVIOUR OF BARIUM TITANATE

---

- [10] B. Cui, P. Yu and X. Wang. "Preparation and characterization of BaTiO<sub>3</sub> powders and ceramics by sol-gel process using decanedioic acid" *Journal of Alloys and Compounds* 2008; 459: 489-493.
- [11] L. Wu, M.C. Chure, K.K. Wu, W.C. Chang, M.J. Yang, W.K. Liu and M.J. Wu. "Dielectric properties of barium titanate ceramics with different materials powder size" *Ceramics International* 2009; 35: 957-960.
- [12] K. Kinoshita and A. Yamaji. "The effect of grain size on the permittivity of BaTiO<sub>3</sub> ceramics" 1976; 47: 365-374.
- [13] H.T. Martirena and J.C. Butterfoot. "Grain size effects on properties of some ferroelectric ceramics" *Journal of Physics C: Solid State Physics* 1974; 7: 3182-3192
- [14] W. Li, Z. Xu, R. Chu, P. Fu and J. Hao. "Structure and electrical properties of BaTiO<sub>3</sub> prepared by sol-gel process" *Journal of Alloys and Compounds* 2009; 482: 137-140.
- [15] Y. Li, H. Liu, Z. Yao, J. Xu, Y. Cui, H. Hao, M. Cao and Z. Yu. "Characterization and energy storage density of BaTiO<sub>3</sub> - Ba(Mg<sub>1/3</sub>Nb<sub>2/3</sub>)O<sub>3</sub> ceramics" *Materials Science Forum* 2010; 654-656: 2045-2048.
- [16] G.A. Schneider and V. Heyer. "Influence of the electric field on Vickers indentation crack growth in BaTiO<sub>3</sub>" *Journal of European Ceramic Society* 1999; 19: 1299-1306.
- [17] V. Tura, L. Mitoseriu, C. Papusoi, T. Osaka and M. Okuyama. "Ferroelectric - to - paraelectric phase transition in barium titanate ceramics by pyrocharge measurement techniques" *Journal of Electroceramics* 1998; 2-3: 163-169.
- [18] S.C. Lu, Y.H. Chen, W.H. Tuan, J. Sheih and C.Y. Chen. "Effect of microstructure on dielectric and fatigue strengths of BaTiO<sub>3</sub>" *Journal of European Ceramic Society* 2010; 30: 2569-2576.
- [19] A.J. Moulson and J.M. Herbert. *Electroceramics* 2nd Edition Wiley and Sons, New York (2003) 78-79.
- [20] X. Deng, X. Wang, H. Wen, L. Chen and L. Li. "Ferroelectric properties of nanocrystalline barium titanate ceramics" *Applied Physics Letters* 2006; 88: 1-3.
- [21] C.J. Xiao, Z.H. Chi, W.W. Zhang, F.Y. Li, S.M. Feng, C.Q. Jin, X.H. Wang, X.Y. Deng and L.T. Li. "The phase transitions and ferroelectric behaviour of dense nanocrystalline BaTiO<sub>3</sub> ceramics fabricated by pressure assisted sintering" *Journal of Physics and Chemistry of Solids* 2007; 68: 311-314.
- [22] M. Ozgul. "Polarization switching and fatigue anisotropy in relaxor lead titanate ferroelectric single crystals" A PhD Thesis, Pennsylvania state university (2003) 25-40.
- [23] I.R. Abothu, P.M. Raj, J.H. Hwang, M. Kumar, M. Iyer, H. Yamamoto and R. Tummala. "Processing, properties and electrical reliability of embedded ultra thin film ceramic capacitors in organic packages" *Electronic Components and Technology Conference* 2007; 1014-1018.
- [24] Y.H. Lee, M.H. Oh and C.Y. Park. "Study on dielectric reliability of the multilayered barium titanate" *Journal of Korean Physical Society* 1998; 32: 330-333.

# STUDIES ON PHASE EVOLUTION IN DYSPROSIUM TITANATE BASED CERAMICS

Amit Sinha, J. Sharma and P. K. Sinha

Powder Metallurgy Division, BARC, Navi Mumbai, India

**Abstract :** Dysprosium titanate based ceramic is one of the control rod materials for thermal reactors. This ceramic was prepared by conventional mixing and calcination technique starting with dysprosium oxide and hydrated titanium dioxide powders. The binary system of  $Dy_2O_3$  and  $TiO_2$  exhibits two stable line compounds -  $Dy_2TiO_5$  and  $Dy_2Ti_2O_7$ . The  $Dy_2TiO_5$  phase has three polymorphs (orthorhombic, hexagonal and fluorite). The low temperature orthorhombic phase transforms into hexagonal phase at a temperature of  $\sim 1350^\circ C$ , which on subsequent heating converts into fluorite phase at  $\sim 1680^\circ C$ . The fluorite phase of  $Dy_2TiO_5$  is reported to have lowest in-service irradiation swelling characteristics when used as control rod elements in thermal reactors.  $Dy_2Ti_2O_7$  has a pyrochlore structure, which is reported to transmute, under irradiation, into fluorite structure. The objective of the present study was to stabilize the high temperature fluorite polymorph of  $DyTi_2O_5$  at room temperature. Phase evolution of pure dysprosium titanate based ceramics was studied by reaction-sintering the compacts of  $Dy_2O_3$  and  $TiO_2$  under different temperatures. The formation of  $Dy_2TiO_5$  phase from the  $Dy_2O_3$  -  $TiO_2$  starting mixture was found to be a two-step process. In order to stabilize the high temperature fluorite phase of  $Dy_2TiO_5$ , the powder was doped with aliovalent dopants. The effects of vacuum and microwave sintering conditions on the stabilization of higher temperature polymorph of  $DyTi_2O_5$  have been studied in the present investigation.

**Keywords:** Dysprosium titanate;  $Dy_2Ti_2O_7$ ; XRD; Phase transformation.

## Introduction

Elements with large thermal neutron absorption cross-sections such as cadmium, boron, hafnium, iridium and their compounds find applications as control rod elements in a nuclear reactor. Boron in the form of boron carbide ( $B_4C$ ) is one of the popular control rod materials; the major advantages of  $B_4C$  carbide are the relatively high neutron absorption cross-section of boron, high thermal stability as well as commercial availability. However, boron based control elements suffers from irradiation induced damages due to (n,a) reaction that results in formation of helium bubbles causing swelling and cracking of the control rod elements and thus limits the life time of the control rod [1-2]. To circumvent these problems, one can make use of the (n,g) by utilizing lanthanide elements such

as dysprosium or gadolinium which exhibits large thermal neutron absorption cross-sections. Among the lanthanides based compounds, dysprosium mono-titanate ( $Dy_2TiO_5$ ) is an attractive control rod material both in the form of powder (density of 4-5 g/cm<sup>3</sup>) or pellets (density of 6 g/cm<sup>3</sup> and more) for thermal neutron reactors [2]. The major advantages of  $Dy_2TiO_5$  based control rod material over  $B_4C$  are the higher neutron absorption crosssection, lower irradiation induced swelling, high melting points (2143 K), good mechanical properties, thermo-chemical stability with the cladding materials and finally ease of fabrication [3].

The binary system of  $Dy_2O_3$  and  $TiO_2$  exhibits two stable line compounds -  $Dy_2TiO_5$  and  $Dy_2Ti_2O_7$ . The  $Dy_2TiO_5$  phase has three polymorphs (orthorhombic, hexagonal and fluorite). The low

temperature orthorhombic phase transforms into hexagonal phase at a temperature of  $\sim 1350^\circ\text{C}$ . The hexagonal phase on subsequent heating converts into fluorite phase at  $\sim 1680^\circ\text{C}$ . The fluorite phase of  $\text{Dy}_2\text{TiO}_5$  is reported to have lowest inservice irradiation swelling characteristics when used as control rod elements in thermal reactors [3-4].  $\text{Dy}_2\text{Ti}_2\text{O}_7$  has a pyrochlore structure, which is reported to transmute, under irradiation, into fluorite structure. The objective of the present study was to stabilize the high temperature fluorite polymorph of  $\text{Dy}_2\text{TiO}_5$  at room temperature through heat treatment and control of composition [4]. Phase evolution of pure dysprosium titanate based ceramics was studied by reactionsintering the compacts of  $\text{Dy}_2\text{O}_3$  and  $\text{TiO}_2$  under different temperatures. In order to stabilize the high temperature fluorite phase of  $\text{Dy}_2\text{TiO}_5$ , the powder was doped with aliovalent dopants. In the present investigation, effects of microwave sintering and sintering under reducing environment on the phase stability and microstructures of dysprosium titanate based ceramics were also studied.

### Experimental

Dysprosium titanate based ceramic was prepared starting from  $\text{Dy}_2\text{O}_3$  and  $\text{TiO}_2$  powders through conventional mixing and calcination technique. High purity (99.9% pure)  $\text{Dy}_2\text{O}_3$  (Indian Rare Earth, India) and uncalcined pure hydrated  $\text{TiO}_2$  (M/s Travankore Titanium Products Ltd., India) were taken as starting materials. For preparation of  $\text{Dy}_2\text{TiO}_5$  samples containing molybdenum trioxide as dopant,  $\text{MoO}_3$  powder (AR Grade, M/s Thomas Baker, India) was added to the starting powder mix. The powders were mixed by wet-ball milling, with alumina balls under acetone for 36 h. The slurry obtained after mixing was dried under infrared lamp. The dried powder mixture was compacted into pellets of 14 mm diameter and 5 mm thickness using unidirectional hydraulic press at a

pressure of 100 MPa. The green compacts were then calcined at  $600^\circ\text{C}$  for 14 h. For studying the evolution of phases, the calcined compacts were further heated at different temperatures ranging from  $700^\circ$  to  $1550^\circ\text{C}$  for specific period of time. The calcined compacts that were heat treated up to  $800^\circ\text{C}$  were taken for sintering study. The sintering of the samples was carried out at a temperature of  $1600^\circ\text{C}$  for 4 h under air. The phase analysis of the calcined as well as heat treated samples was carried out by X-ray diffraction (Philips Analytical, Model PW1710). The XRD patterns were recorded at a scan rate of  $0.025^\circ/\text{s}$  using  $\text{CuK}\alpha$  radiation. To identify the presence of any minor second phase in the structure, XRD patterns were taken at a slow scan rate of  $0.002^\circ/\text{s}$ . The microstructural analysis of the sintered samples was carried out using light optical microscopy. For microstructural study, the sintered samples were polished followed by thermal etching at  $1500^\circ\text{C}$  for 15 minutes.

The identification of different phases present in the microstructure was carried out by Electron Probe Micro Analyzer (CAMECA-SX 100). The grain size was measured by linear intercept method. The density of the sintered samples was measured by Archimedes principle of water displacement as well as by dimensional measurements. To confirm the effect of molybdenum in stabilizing high temperature fluorite phase of  $\text{Dy}_2\text{TiO}_5$ , samples were also prepared without using  $\text{MoO}_3$  in the starting mixture. The phase evolution study of the calcined as well as heat treated samples was carried out by X-ray diffraction. In order to study the effect of reducing environment, the calcined compacts of undoped composition were also sintered under vacuum at  $1600^\circ\text{C}$  for 4 h. The compacts were also sintered under microwave conditions at  $1550^\circ\text{C}$  for 2 h using an industrial microwave furnace.

Results and Discussions

For the control rod application, the composition of dysprosium titanate is richer in titanium content as compared to stoichiometric  $Dy_2TiO_5$  in order to ensure absence of  $Dy_2O_3$  in the final microstructure of the control element. Thus the dysprosium deficient composition ultimately results in formation of  $Dy_2TiO_5$  and  $Dy_2Ti_2O_7$ , the presence of which is not considered harmful for control rod application as it converts into fluorite phase under irradiation [2]. The XRD patterns of the starting powders are shown in Fig. 1. The XRD pattern of hydrated  $TiO_2$  could be assigned to anatase phase of  $TiO_2$  (ICDD PDF 84-1286) while the pattern of dysprosium oxide corresponds to cubic phase of  $Dy_2O_3$  (ICDD PDF 86-1327). The XRD pattern of  $MoO_3$  powder could be assigned to orthorhombic phase of  $MoO_3$  (ICDD PDF 35-0609).

The density of the green compacts was 3.33 g/cc which is equivalent to 50.3 %T.D. of the powder composition under investigation. The heating schedule for the green compacts was largely governed by the dissolution of  $MoO_3$  in the starting mixture.  $MoO_3$  melts at 795°C and boils at 1155°C. It also forms a low temperature eutectic with  $Dy_2O_3$  (10-mol%) having a melting point of 725°C. [5] To avoid any intermittent melting due to formation of low temperature eutectic of  $MoO_3$  and  $Dy_2O_3$ , the samples were calcined at 600°C for 14 h. This thermal treatment is also needed to prevent the loss of  $MoO_3$  through volatilization.

The XRD pattern of the sample calcined at 600°C is shown in Fig. 2. The pattern exhibits the peaks corresponding to  $Dy_2O_3$  and anatase  $TiO_2$ . The absence of any peak corresponding to either  $Dy_2TiO_5$  or  $Dy_2Ti_2O_7$  in the XRD pattern indicates that the formation of titanate from the reacting mixture does not start 600°C.

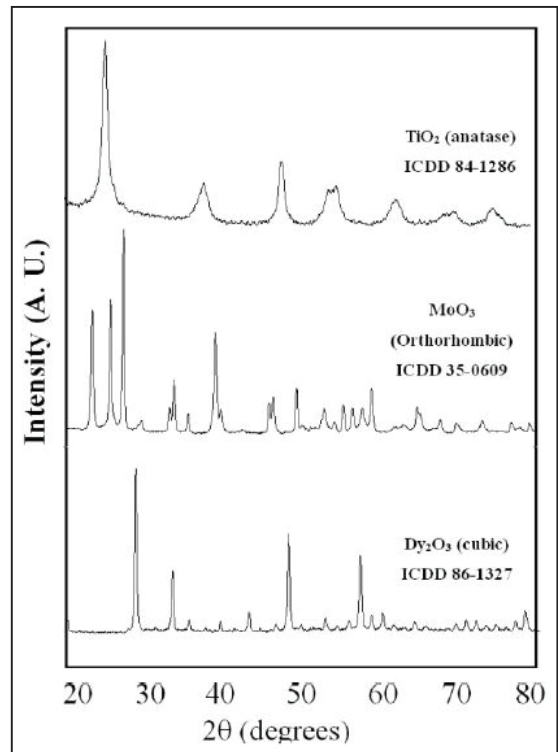


Fig. 1. XRD patterns of the constituent oxides

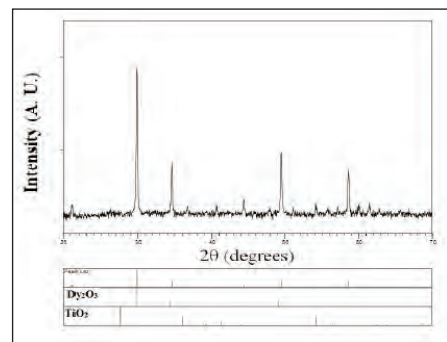


Fig. 2. XRD pattern of the mixture calcined at 600°C.

The XRD pattern of the sample calcined to 700°C as shown in Fig. 3a, exhibits the peaks corresponding to  $Dy_2O_3$ ,  $Dy_2Ti_2O_7$  and  $TiO_2$  (anatase). This result suggests that the formation of  $Dy_2TiO_5$  does not take place by direct reaction

between  $Dy_2O_3$  and  $TiO_2$ . Dysprosium ditanate ( $Dy_2Ti_2O_7$ ) is the phase that forms first. The XRD pattern of sample heated up to  $1050^\circ C$  (Fig. 3b) shows the presence of  $Dy_2Ti_2O_7$  and  $Dy_2O_3$ . Even under slow scan, the pattern did not resolve the presence of  $TiO_2$ . This confirms that almost all  $TiO_2$  present in the system has reacted with  $Dy_2O_3$  to form  $Dy_2Ti_2O_7$ . The formation of  $Dy_2TiO_5$  is likely to take place by the reaction of  $Dy_2Ti_2O_7$  and  $Dy_2O_3$  remaining in the reacting powder mixture.

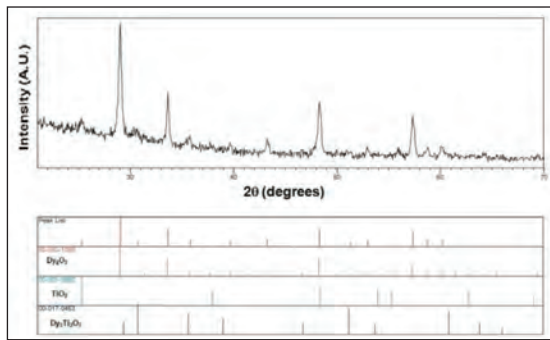


Fig 3a. XRD pattern of the mixture calcined at  $700^\circ C$ .

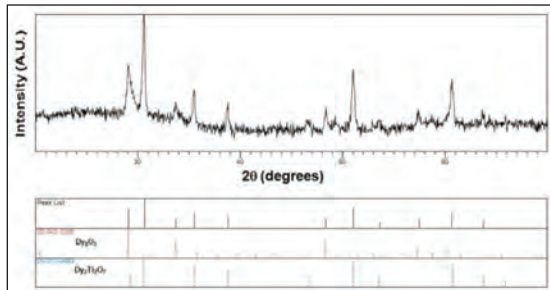


Fig 3b. XRD pattern of the mixture calcined at  $1050^\circ C$ .

The formation of  $Dy_2TiO_5$ , as evidenced by XRD, does not start up to  $1050^\circ C$ . At  $1250^\circ C$ , peaks corresponding to cubic polymorph of  $Dy_2TiO_5$  appear in XRD (Fig. 4). The equilibrium formation temperature of fluorite phase, as dictated by phase diagram of  $Dy_2O_3 - TiO_2$  is  $1680^\circ C$ . The lowering of formation temperature of fluorite phase of  $Dy_2TiO_5$  as well as its stabilization

to room temperature may be attributed to the presence of  $MoO_3$  dopant. To study the effect of temperature on the formation of  $Dy_2TiO_5$ , intensity ratios of XRD peaks corresponding to (222) planes of  $Dy_2TiO_5$  (fluorite) and  $Dy_2Ti_2O_7$  were plotted against the temperature. Fig. 5. shows that with increase in temperature, there is a continuous increase in formation of  $Dy_2TiO_5$  phase from the  $Dy_2Ti_2O_7$  and  $Dy_2O_3$ . The formation of cubic  $Dy_2TiO_5$  goes to completion at a temperature of  $1450^\circ C$ .

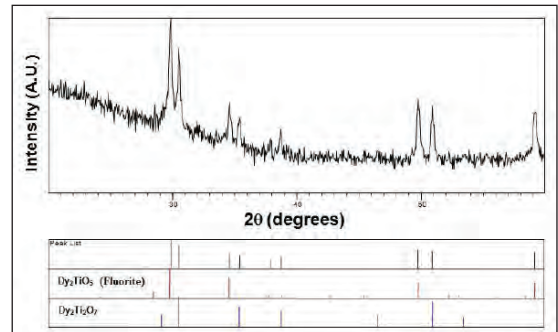


Fig 4. XRD pattern of the mixture calcined at  $1250^\circ C$

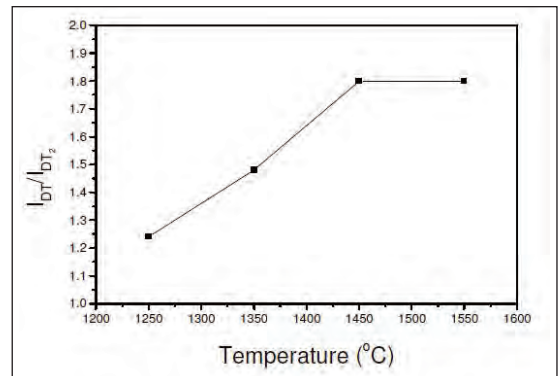


Fig 5. intensity ratios of XRD peaks corresponding to (222) planes of  $Dy_2TiO_5$  (fluorite) and  $Dy_2Ti_2O_7$  as a function of calcination temperature

From the above it may be concluded that the synthesis reaction of  $Dy_2TiO_5$  from a powder mixture of  $Dy_2O_3$  and  $TiO_2$  may be broken to two steps:



### Sintering Study

The XRD pattern of the sintered pellet reveals the presence of two phases (fluorite polymorph of  $\text{Dy}_2\text{TiO}_5$  and  $\text{Dy}_2\text{Ti}_2\text{O}_7$ ). The sintering of dysprosium titanate based ceramic at  $1600^\circ\text{C}$  for 4 h yields an average density of  $\sim 7.01$  g/cc. This is approximately 97.5% of T.D. The optical photomicrograph of the thermally etched pellets sintered at  $1600^\circ\text{C}$  for 4 h is shown in Fig. 6. The micrograph reveals two different grain structures – bright grains and grains with very fine serrations. The average grain size of the sample is  $5 \mu\text{m}$ . The grain size distribution is found to be uniform throughout the microstructure. To identify the two phases ( $\text{Dy}_2\text{TiO}_5$  and  $\text{Dy}_2\text{Ti}_2\text{O}_7$ ) present in the microstructure, EPMA study was carried out. Backscattered electron image (Z contrast) of the sample (Fig. 7.) exhibits the presence of three phases: a) dark phase, b) bright phase and c) a mixture of dark and bright phase. Electron beam scan of Dy, Ti, and O indicates that the dark phase is  $\text{Dy}_2\text{Ti}_2\text{O}_7$ , while the bright phase is  $\text{Dy}_2\text{TiO}_5$ . The electron beam scan for molybdenum showed uniform distribution of the element in the three phases.

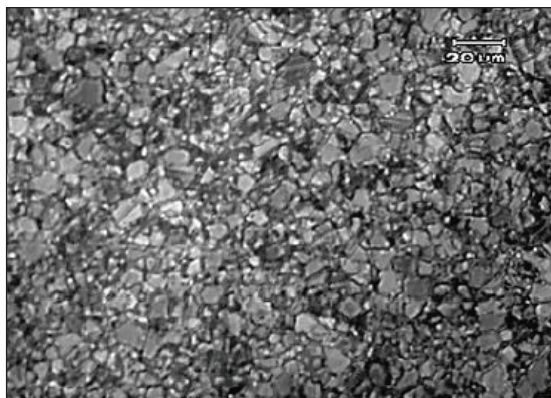


Fig. 6. Optical micrograph of thermally etched sample of dysprosium titanate reaction sintered at  $1600^\circ\text{C}$  for 4h

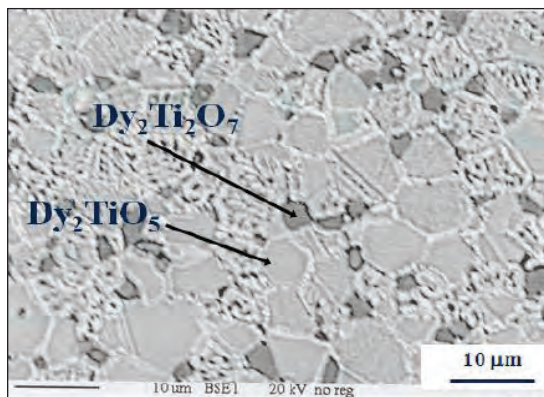


Fig. 7. Backscattered electron image (of the thermally etched pellet of dysprosium titanate sintered at  $1600^\circ\text{C}$  for 4 h

### Effect of $\text{MoO}_3$ on phase formation

To study the effect of  $\text{MoO}_3$  on stabilizing the cubic phase of  $\text{Dy}_2\text{TiO}_5$ , samples were prepared without adding  $\text{MoO}_3$  in the starting mixture. Though the starting mixture did not contain  $\text{MoO}_3$ , the mixture was subjected to a heat treatment step at  $800^\circ\text{C}$ . This was carried out to provide an identical thermal treatment as compared to that of  $\text{MoO}_3$  containing samples. Fig. 8a. shows the XRD pattern of the molybdenum free  $\text{Dy}_2\text{O}_3$ - $\text{TiO}_2$  mixture heat treated at  $800^\circ\text{C}$  for 12 h. Though the starting mixture corresponds to the phase of  $\text{Dy}_2\text{TiO}_5$ , it is the  $\text{Dy}_2\text{Ti}_2\text{O}_7$  phase that forms first when a mixture of  $\text{Dy}_2\text{O}_3$  and  $\text{TiO}_2$  is heated. The XRD pattern of the mixture calcined at  $1050^\circ\text{C}$  (Fig. 8b.) reveals the peaks corresponding to  $\text{Dy}_2\text{O}_3$  and  $\text{Dy}_2\text{Ti}_2\text{O}_7$  only. The absence of any peak corresponding to  $\text{TiO}_2$  confirms that the reaction (1) is almost complete at  $1050^\circ\text{C}$ .

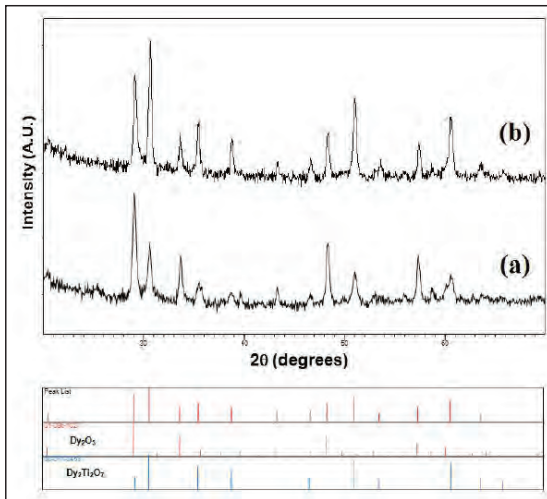


Fig 8. XRD pattern of the molybdenum free Dy<sub>2</sub>O<sub>3</sub>-TiO<sub>2</sub> mixture heat treated at (a) 800°C and 1050°C respectively.

The XRD pattern of the sample calcined at 1250°C (Fig. 9.) shows the presence of Dy<sub>2</sub>TiO<sub>5</sub> (orthorhombic) and Dy<sub>2</sub>Ti<sub>2</sub>O<sub>7</sub>. The XRD pattern of the sample (Fig. 10.) calcined at 1450°C exhibits the two polymorphs of Dy<sub>2</sub>TiO<sub>5</sub> i.e. hexagonal and orthorhombic. The XRD patterns of the samples calcined at higher temperatures exhibited only the peak corresponding to hexagonal Dy<sub>2</sub>TiO<sub>5</sub>. The XRD results suggest that high temperature hexagonal phase is stabilized during cooling to room temperature.

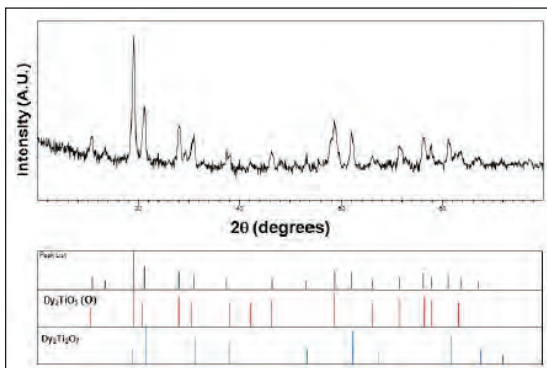


Fig 9. XRD pattern of the molybdenum free Dy<sub>2</sub>O<sub>3</sub>-TiO<sub>2</sub> mixture heat treated at 1250°C

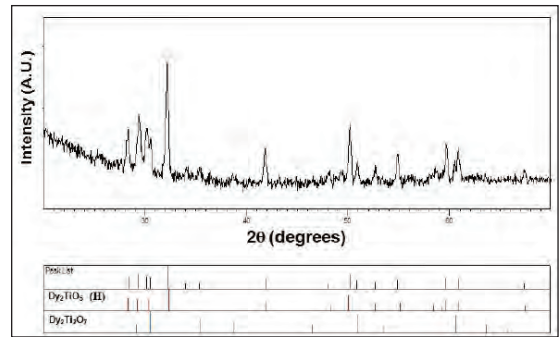


Fig 10. XRD pattern of the molybdenum free Dy<sub>2</sub>O<sub>3</sub>-TiO<sub>2</sub> mixture heat treated at 1450°C

Effect of Vacuum and Microwave Sintering To study the effect of reducing environment on the stability of phases in the dysprosium titanate system, the Dy<sub>2</sub>O<sub>3</sub>-TiO<sub>2</sub> mixture without any dopant was reaction sintered under vacuum at 1600°C for 2 h. The XRD pattern of the sample obtained after vacuum sintering is shown in Fig 11. The pattern exhibits all reflections corresponding to the hexagonal polymorph of Dy<sub>2</sub>TiO<sub>5</sub> along with the peaks of Dy<sub>2</sub>Ti<sub>2</sub>O<sub>7</sub> phase. The above result suggests that cubic phase of Dy<sub>2</sub>TiO<sub>5</sub> cannot be stabilized by vacuum sintering. Similar effect was also observed when the Dy<sub>2</sub>O<sub>3</sub>-TiO<sub>2</sub> mixture was sintered in the presence of microwave. Only hexagonal phase of Dy<sub>2</sub>TiO<sub>5</sub> could be stabilized through microwave sintering.

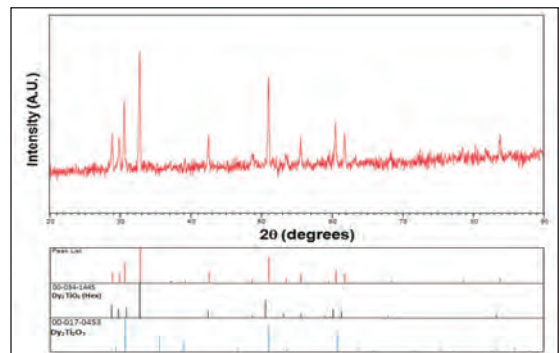


Fig 11. XRD Pattern of dysprosium titanate sintered under vacuum at 1600°C

### Conclusions

Dysprosium titanate based ceramics was prepared by conventional solid-state technique using fine  $Dy_2O_3$  and hydrated titanium dioxide. The formation of  $Dy_2TiO_5$  phase does not take place directly from the  $Dy_2O_3$ - $TiO_2$  mixture. During calcination of the mixture,  $Dy_2Ti_2O_7$  is the phase that forms first.  $Dy_2Ti_2O_7$  on subsequent high temperature treatment reacts with remaining  $Dy_2O_3$  present in the mixture and forms  $Dy_2TiO_5$ . It has been demonstrated that doping with  $MoO_3$  helps in stabilization of high temperature fluorite phase of  $Dy_2TiO_5$ . In the presence of  $MoO_3$ ,  $Dy_2TiO_5$  (fluorite) forms at a relatively lower temperature than dictated by phase diagram. The vacuum sintering as well as sintering in the presence of microwave conditions could stabilize the hexagonal polymorph of dysprosium titanate phase.

### References

- [1] F. The´venot, J. Eur. Ceram.Soc., 6 [4] 205–25 (1990)
- [2] V. D. Risovany, E. P. Klochkov, and E. E. Varlashova, "Atomic Energy, 81 [5] 764–9 (1996).
- [3] V. D. Risovany, E. E. Varlashova, and D. N. Suslov, J. Nuclear Mater., 281, 84–9 (2000).
- [4] V. D. Risovaniy, A V. Zaharov, E. P. Klochkov, E. E. Varlashova, and D. N. Suslov, "Dysprosium and Hafnium Base Absorbers for Advanced WWER Control Rods;" pp. 91–102 in Proceedings of a Technical Committee meeting on Control Assembly materials for Water Reactors: Experience, Performance and Perspectives, International Atomic Energy Agency, Vienna (Austria), IAEATECHDOC- 1132, February 2000.
- [5] G. V. Shamraj, R. L. Magunov, I. V. Stasenko, and A. P. Zhirnova, "Dy<sub>2</sub>O<sub>3</sub>-TiO<sub>2</sub> system," Izv. Akad. Nauk SSSR. Neog. Mater., 25 [2] 273–5 (1989); Inorg. Mater. (Engl. Transl.) 25 [2] 233–5 (1989).

# Al-2024 METAL MATRIX COMPOSITES REINFORCED WITH ULTRAFINE Mg-Al MECHANICALLY ALLOYED PARTICLES.

A. K. Chaubey and Rohit Kumar

Institute of Minerals and Materials Technology (IMMT), Bhubaneswar, India

**Abstract :** Al-2024 metal matrix composites (MMCs) reinforced with Mg-Al mechanically milled particles (MAPs) were prepared by powder metallurgical process. In order to produce the composite the Al-2024 powder was mechanically mixed with 10 and 20 vol. % of Mg-Al MAPs. The composite powders were consolidated by hot pressing followed by hot extrusion process at 623 K and 400 MPa under a vacuum of  $10^{-4}$  mbar. This gives rise to highly dense bulk sample with a relative density of about 99.78 % of theoretical density and remarkably improves the mechanical properties. The yield strength increases from 202 MPa for unreinforced alloy matrix to about 246 and 275 MPa for the samples having 10 and 20 vol.% of reinforcement, respectively, while retaining appreciable plastic deformation ranging between 3 and 6 %. Furthermore, the addition of the low-density Mg-7.6% Al particles, which transform to  $\beta$ - $\text{Al}_3\text{Mg}_2$  phase during compaction decreases the density of the materials below that of the unreinforced 2024 matrix and considerably increasing the specific strength of the composites. This behavior is linked to the reduced matrix ligament size characterizing the milled composites.

## 1. Introduction

Among the advanced engineering materials, Al-based metal matrix composites matrix composite (MMCs) exhibits a large potential to further improve the performances of Al-2024 alloy due to their excellent properties, such as high strength-to-weight ratio, elevated service temperature, and good wear resistance and fatigue [1-3]. Particulate-reinforced MMCs are especially attractive among various developed types of composites thanks to their easier and less expensive processing, isotropic properties and multiple viable processing techniques, such as forging, rolling and extrusion [4]. The powder metallurgy (PM) method has been successfully applied to prepare the particulate-reinforced MMCs. Compared with other conventional methods, PM has many advantages, such as development of novel matrix materials outside the compositional limits dictated by equilibrium thermodynamics, controlling the porosity, producing fine and isotropic structures, etc [5,6]. Mechanical alloying have proved to be a process that eliminates some drawbacks that occurred

in composites when are produced by liquid processes such as for example segregation phenomena typical of the casting processes [7]. Segregation always causes that distribution of the alloy elements do not be homogenous affecting by this way the resulting mechanical properties. Also, when liquid process are used, density differences between matrix and reinforcement particles does not allow to distribute homogenously the latter, using mechanical alloying lead to better homogenous distribution of reinforcement.

Apart from conventional reinforcements, such as  $\text{Al}_2\text{O}_3$  and SiC [8,9], metallic glasses [10-13] and quasicrystals [14,15] have already been successfully used as reinforcing agents in MMCs. MMCs reinforced with ceramic particles have extensively been used for several light weight and wear resistance applications [16-18]. However, owing to the high abrasiveness, brittleness and wettability of ceramics [18-21] in recent years, intermetallics as reinforcements in MMCs have emerged as possible substitutes for ceramic reinforcements [22-25]. This appears

to be a highly promising option in view of high hardness of intermetallics and their compatibility with the metal matrix. In addition, thermal expansion coefficients of intermetallics are much closer to the metals than those of ceramic reinforcements.

Accordingly, in this work Al 2024 matrix composites reinforced with different volume fractions (10 and 20 vol.%) of mechanically alloyed Mg-7.4%Al particles were prepared by PM. The effects of the reinforcement on the mechanical as well as on the structural properties of the composites were systematically investigated. The Mg-Al reinforcement was selected because of its attractive properties, including low density ( $\sim 1.79 \text{ g/cm}^3$ ), high room temperature strength ( $\sim 700 \text{ MPa}$ ) and high hardness (170Hv) [26].

## 2. Experimental

Mg-7.4%Al (wt.%) powder was produced by mechanical alloying of elemental Mg and Al powders in a planetary ball mill for 100h room temperature followed by 3h cryo-milling. The detailed production and characterization of the Mg-7.4%Al powder has been reported elsewhere [26]. In order to produce Al-based MMCs, the pure Al powder was mechanically mixed by ball milling with 10 and 20 vol.% Mg-7.4%Al particles using a Retsch PM400 planetary ball mill. The composite powders were consolidated by hot pressing followed by hot extrusion at 673 K and 400 MPa. Structural characterization was performed by X-ray diffraction (XRD) using a Philips PW 1050 diffractometer (CoK $\alpha$  radiation;  $\lambda = 0.17889 \text{ nm}$ ) and by scanning electron microscopy (SEM) using a Gemini 1530 microscope. The density of the bulk samples was measured using Archimedes principle. Hardness measurements were done using a computer-

controlled Struers Duramin 5 Vickers hardness tester. The device is equipped with a typical diamond indenter in the form of a pyramid with square base and an angle of  $136^\circ$  between the opposite faces. Indentations were carried out with an applied load of 0.01 kg and a dwell time of 10 s. Cylinders having a length/diameter ratio of 2.0 (6 mm length and 3 mm diameter) were prepared from the hot consolidated samples in accordance with the ASTM standard for compression testing [27]. The specimens were tested at room temperature using universal testing machine (Instron 8562) under quasistatic compressive loading (strain rate  $\sim 1 \times 10^{-4} \text{ s}^{-1}$ ).

## 3. Result and discussion

### 3.1 Characterization of mechanically alloyed Mg-7.4%Al powder

The Mg-7.4%Al reinforcement was produced by MA of elemental powder mixtures with composition Mg-7.4%Al. The structure of the Mg-7.4%Al powders prepared by MA usually consists of a nanostructured supersaturated Al(Mg) solid solution and  $\gamma\text{-Al}_{12}\text{Mg}_{17}$  [28].

The particle size and the particle size distribution of the reinforcement are among the fundamental factors influencing the strengthening of composites [28]. After sieving the as-milled powders to  $-64 \mu\text{m}$ , their morphology and size distribution were analyzed using SEM. The SEM image of the as-milled Mg-7.4%Al powders is shown in Fig.1. The particles display a rather spherical shape. In order to have a quantitative analysis of the particle size distribution, the size of the particles lying on diagonal lines of the SEM image shown in Fig. 1 were measured. All particles were regarded as spherical to simplify the measurement. The results are illustrated in Fig. 2 (accuracy of  $0.01 \mu\text{m}$ ) and the corresponding particle size distribution of is displayed in Fig.3.

# Al-2024 METAL MATRIX COMPOSITES REINFORCED WITH ULTRAFINE Mg-Al MECHANICALLY ALLOYED PARTICLES.

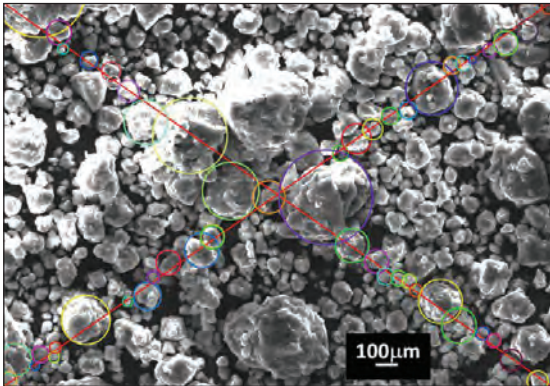


Fig. 1 SEM image of the as-milled Mg-7.4%Al powder.

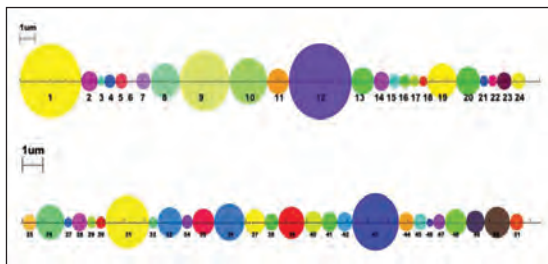


Fig. 2 Sizes of the Mg-7.4%Al powder particles along the diagonal lines of SEM image shown in Fig. 1.

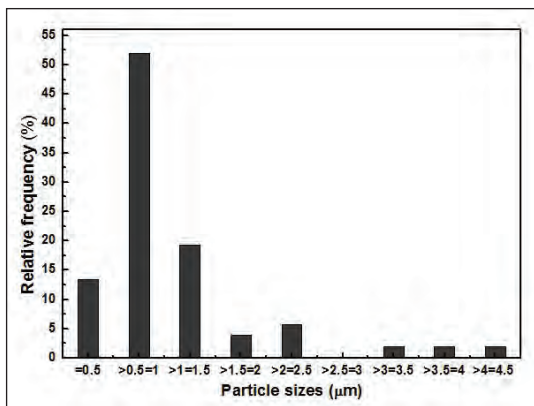


Fig. 3 Particle size distribution of the as-milled Mg-7.4%Al powders after sieving to -64 μm.

About 52 % of the particles are in the size ranging from 0.5 to 1 μm. Particles with size smaller than 0.5 μm has a relative frequency of 13.5%, while particles with size between 1 and 1.5μm account for 19.2 %. Only 15.3 % of the measured particles are larger than 1.5 μm. These results indicate that the main size of the particles after ball-milling and sieving is around 1 μm.

### 3.2 Microstructural analysis

Fig. 4 shows the XRD patterns (Co Kα radiation) of the as-extruded pure Al 2024 matrix ( $V = 0$ ) and composites with 10 and 20 vol.% Mg-7.4%Al mechanically milled particles. All the patterns display strong diffraction peaks which belong to face-centered cubic (fcc) Al. In addition, the diffraction peaks of  $Al_2CuMg$  can be observed, which is the secondary phase most often observed in the Al 2024 alloy [29,30]. With the increasing volume fraction of the Mg-7.4%Al particles, the intensity of the peaks belonging to the  $\beta-Al_3Mg_2$  phase considerably increases whereas the intensity of the peaks belonging to  $Al_2CuMg$  decreases.

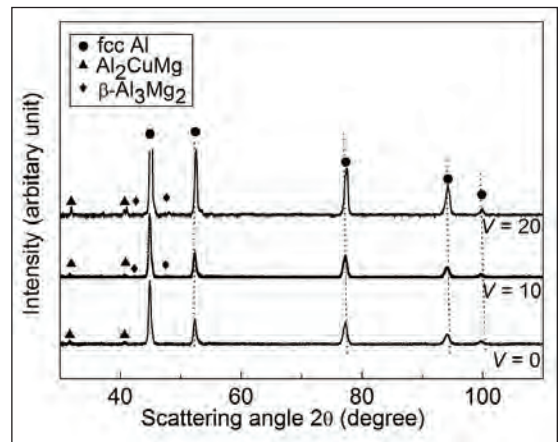


Fig. 4. XRD patterns (Co Kα radiation) for the as-extruded unreinforced Al-2024 matrix ( $V = 0$ ) and composites with 10, and 20 vol.% Mg-7.4%Al particles.

## Al-2024 METAL MATRIX COMPOSITES REINFORCED WITH ULTRAFINE Mg-Al MECHANICALLY ALLOYED PARTICLES.

No additional diffraction peaks due to other phases, such as  $\text{Al}_2\text{Cu}$  and  $\text{Al-Fe-Cu-Mn-Si}$  [30], can be detected, presumably because of the limited dimension and/or small content of these phases. The detection of the  $\beta\text{-Al}_3\text{Mg}_2$  phase implies that a phase transformation takes place during the consolidation process. The formation of the  $\beta\text{-Al}_3\text{Mg}_2$  phase can be understood by considering the Al-Mg phase diagram. According to the phase diagram [31] pure Al and the Mg-rich Mg-7.4%Al do not coexist at the equilibrium. It is thus possible to conclude that the solid state diffusion between Al matrix and the reinforcing Mg-7.4%Al particles can lead to the formation of the equilibrium  $\beta\text{-Al}_3\text{Mg}_2$  phase during powder consolidation

The SEM micrographs taken from the cross-section of the consolidated composites are shown in Fig. 5. Fig.5(a) shows the micrographs of unreinforced Al 2024 matrix consists of small bright particles ( $\text{Al}_2\text{CuMg}$ ) with size of about 200 – 500 nm homogeneously dispersed in a continuous gray matrix. The composite samples with 10 vol.% reinforcement (Fig. 5(b)) shows the homogeneous distribution of the Mg-7.4%Al particles (dark contrast) in the Al matrix (gray regions). As the volume percentage increases to 20 %, the microstructure shows clusters of agglomerated particles (Fig. 5(c)). The microstructure also shows a few pores at the particle-matrix interface, as usually interfaces are most preferred site for the porosity [32]. The electron probe microanalysis (EPMA) of the 20% reinforced sample shown in the Fig.6 also corroborates uniform distribution of the reinforcement in the matrix.

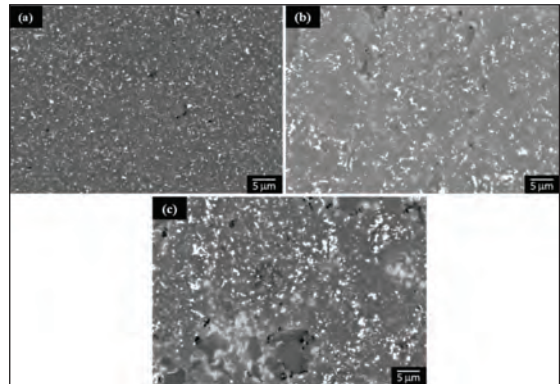


Fig. 5 SEM micrographs for the as-extruded (a) Al 2024 matrix unreinforced and (b) composite with 10 vol.% reinforcement (c) composite with 20 vol.% reinforcement.

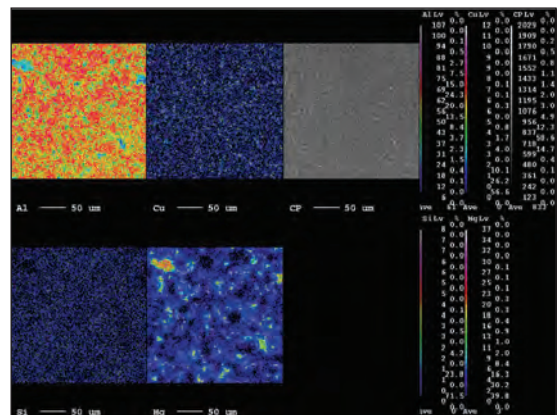


Fig. 6 EPMA of the Al 2024 composite reinforced with 20 vol.% MMPs.

The density of the as-extruded 2024-matrix composites reinforced with various volume fractions of mechanically milled Mg-7.4%Al particles are shown in Fig. 7. The density decreases linearly from 2.78 g/cm<sup>3</sup> for the pure Al 2024 (V = 0) to 2.52 g/cm<sup>3</sup> for the composite with 20 vol. % Mg-7.4%Al particles. This leads to a reduction of density of about 0.46 % for each vol.% of Mg-7.4%Al particles added.

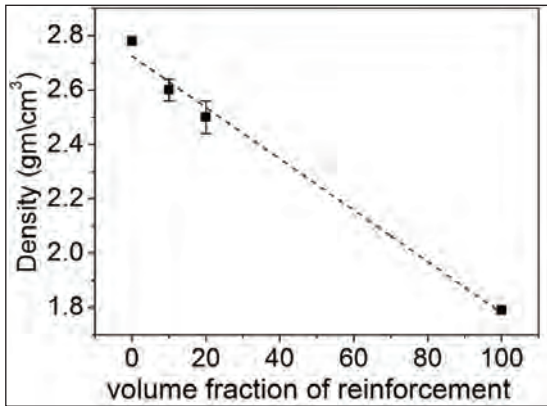


Fig. 7 Density of the as-extruded composites as a function of the volume fraction of Mg-7.4%Al mechanically milled particles.

### 3.3 Mechanical properties

#### 3.3.1 Hardness

Fig.8 shows the effect of the volume fraction of Mg-7.4%Al particles on the microhardness of the as-extruded composites. The hardness increases considerably with the increasing volume fraction of the reinforcement from 81.6 HV for the pure Al 2024 ( $V = 0$ ) to 120 HV for the composite with 20 vol.% Mg-7.4%Al particles

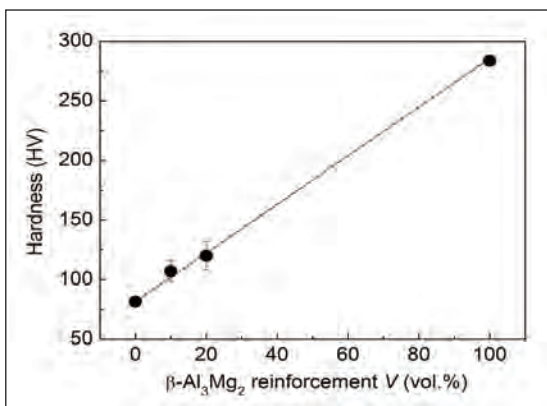


Fig. 8 Microhardness of the as-extruded composites as a function of the volume fraction of Mg-7.4%Al mechanically milled particles.

#### 3.3.2 Mechanical deformation

The room temperature tensile stress-strain curves of the composites and unreinforced Al-2024 matrix are shown in Fig. 9. The addition of the Mg-7.4%Al particles to the Al-2024 matrix increases the strength of the samples remarkably. The composite with  $V = 10$  exhibits yield strength of  $202 \pm 3$  MPa and tensile strength of  $331 \pm 2$  MPa along with plastic strain exceeding 6%. This increase in compressive strength could be attributed to well-known factors (pertaining to reinforcement) such as: (i) the dislocation strengthening in the matrix, which is related to the nucleation of additional dislocations in the matrix due to the introduction of the reinforcement [33,34], (ii) Orowan strengthening mechanism [35], and (iii) load transfer from the matrix to reinforcement [34]. Increasing the reinforcement content to 20 vol.% raises the yield to about 246, while reducing the tensile strength by 3% and plastic deformation to about 50%. This can be attributed to the observed particle agglomeration and clustering and to the increase of effective vol.% of the reinforcement due to the transformation of the Mg-7.4%Al particles to the  $\beta$ -Al<sub>3</sub>Mg<sub>2</sub> phase (see Fig. 1), which may on one side provide additional strengthening to the material but it also may favor the brittle behavior in the composites with larger reinforcement content [35].

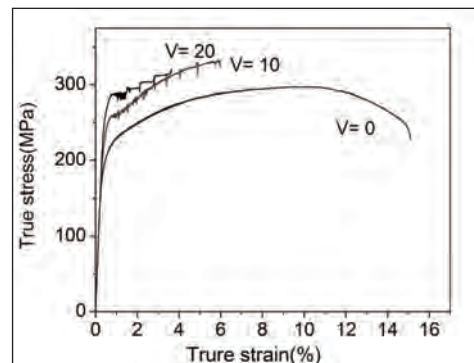


Fig. 9 Room temperature compression stress-strain curves for the as-extruded Al 2024 matrix composites with 10 and 20 vol.% of Mg-7.4%Al mechanically milled particles.

# Al-2024 METAL MATRIX COMPOSITES REINFORCED WITH ULTRAFINE Mg-Al MECHANICALLY ALLOYED PARTICLES.

## 4. Conclusions

Al-2024 matrix reinforced with different volume fractions of mechanically milled Mg-7.4%Al particles have been produced by powder metallurgy, and their mechanical properties have been investigated under tensile loading. The results reveal encouraging room temperature mechanical properties with respect to the unreinforced Al-2024 matrix. Yield and tensile strength have increased from 202 and 297 MPa for unreinforced alloy matrix to about 246 and 331MPa for the composite reinforced with 10 vol.% mechanically milled Mg-7.4%Al particles respectively, while retaining appreciable plastic deformation. Furthermore, the addition of low-density Mg-7.4%Al particles reduces the tensile strength as well as the plastic strain but significantly decreased the density of the composites.

## References

1. Mousavi Abarghouie, S., and Reihani, S. (2010) *Materials & Design* 31, 2368-2374
2. Kainer, K. U. (2006) *Metal matrix composites*, Wiley-VCH Weinheim
3. Clyne, T., and Withers, P. (1993) *An introduction to metal matrix composites*, Cambridge University Press
4. O'Donnell, G., and Looney, L. (2001) *Materials Science and Engineering A* 303, 292-301
5. Kang, S. J. L. (2005) *Sintering: densification, grain growth, and microstructure*, Butterworth-Heinemann
6. Lloyd, D. (1994) *International Materials Reviews* 39, 1-23
7. Suryanarayana, C., (2000) *Mechanical alloying*, *Prog. Mat. Sci.* 46, 15-30.
8. Tan, M. J., and Zhang, X. (1998) *Materials Science and Engineering: A* 244, 80-85
9. Slipenyuk, A., Kuprin, V., Milman, Y., Goncharuk, V., and Eckert, J. (2006) *Acta Materialia* 54, 157-166
10. Scudino, S., Liu, G., Prashanth, K. G., Bartusch, B., Surreddi, K. B., Murty, B. S., and Eckert, J. (2009) *Acta Materialia* 57, 2029-2039
11. Scudino, S., Surreddi, K., Sager, S., Sakaliyska, M., Kim, J., L ser, W., and Eckert, J. (2008) *Journal of Materials Science* 43, 4518-4526
12. Lee, M. H., Kim, J. H., Park, J. S., Kim, J. C., Kim, W. T., and Kim, D. H. (2004) *Scripta materialia* 50, 1367-1371
13. 15. Yu, P., Kim, K. B., Das, J., Baier, F., Xu, W., and Eckert, J. (2006) *Scripta materialia* 54, 1445-1450 .
14. Kabir, El, Joulain, T., Gauthier, A., Dubois, V. J., Bonneville, S., and Bertheau, D. (2008) *Journal of Materials Research* 23, 904-910.
15. Schurack, F., Eckert, J., and Schultz, L. (2003) *Philosophical Magazine* 83, 807-825.
16. Lim, Y.H., Lim, S.C., and Gupta, M.(2003) *J. Wear* 225, 629-637.
17. Huang, Z., Yu, S.,and Li, M., (2010) *Trans. Nonferr. Met. Soc. China* 20, 458-462
18. Munitz, A., Jo I., Nuechterlein, J., Garrett, W., Moore, J.J., and Kaufman M.J., (2012) *Int. J. Mater. Sci.* 2, 15-19 .
19. Jayalakshmi, S., Kailas, S.V., and Seshan, S., (2002) *Composites Part A. Appl. Sci. Manuf. A* 33, 1135-1140.
20. Chen, L.Q., Dong, Q., Zhao, M.J., Bi J.,and Kanetake, N., (2005) *Mater. Sci. Eng. A* 408, 125 -130.
21. Zheng, M.Y., Wu, K., Kamado, S., and Kojima, Y. (2003) *Mater. Sci. Eng. A* 348, 67-75.
22. Lee, J.M., Kang, S.B., Sato, T., and Tezuka, H., Kamio, A.(2003) *Mater. Sci. Eng. A* 343, 199-209.
23. Muñoz-Morris, M.A., Rexach, J.I., and Liebllich, M., (2005) *Intermetallics* 13, 141-149.
24. Torralba, J.M., Velasco, F., Costa, C.E, Vergara, I.,and Cáceres D.(2002) *Composites A* 33, 427-434
25. Velasco, F., Lima, W.M., Antón, N., Abenójar, J., and Torralba, J.M., (2003) *Tribol. Int.* 36, 547-551.

## Al-2024 METAL MATRIX COMPOSITES REINFORCED WITH ULTRAFINE Mg-Al MECHANICALLY ALLOYED PARTICLES.

---

26. Chaubey, A.K., Scudino, S., Khoshkhoo, M. Sama, di., Prashanth, K.G., Mukhopadhyay, N.K., Mishra, B.K., and Eckert, J.(2013) *Metals* 3, 58- 68.
27. ASTM E9-89a, Standard test methods for compression testing of metallic materials at room temperature, West Conshohocken, 2000.
28. Wang, Z., Song, M., Sun, C., Xiao, D., and He, Y. (2010) *Materials Science and Engineering: A* 528.1131-1137.
29. Mousavi Abarghouie, S., and Reihani, S. (2010) *Materials & Design* 31, 2368-2374.
30. Buchheit, R., Grant, R., Hlava, P., McKenzie, B., and Zender, G. (1997) *Journal of the Electrochemical Society* 144, 2621-2627.
31. Hugh Baker: *ASM Handbook, Alloy phase diagrams*, ASM International, third edition, 1997.
32. Saha, R., Morris, E., and Chawla ,N.(2002) *J. Mater. Sci. Lett.* 21, 337-339.
33. Hassan, S.F, and Gupta, M. J., (2006) *Mater. Sci.* 41, 2229-2236
34. Shi ,N., Wilner, B., and Arsenault, R.J., *Acta. Metall. Mater.* 40, (1992) 2841-2854
35. Szaraz, Z., Trojanova, Z., Cabbibo, M.,and Evangelist, E. (2007) *Mater. Sci. Eng. A* 462, 225-229.

# EVALUATION OF ROOM TEMPERATURE AND HIGH TEMPERATURE PROPERTIES OF ZrB<sub>2</sub>-SiC COMPOSITES

Jiten Das, Sweety Kumari, J. Janardhana Reddy, V. V. Bhanu Prasad

Defence Metallurgical Research Laboratory, Hyderabad, India

**Abstract :** Low density and high melting point of ZrB<sub>2</sub> has made it attractive for structural application at ultra-high temperatures. To improve its strength, fracture toughness and oxidation resistance, SiC is added to it. In order to assess the suitability of ZrB<sub>2</sub>-SiC composite for ultra-high temperature structural application, room temperature as well as high temperature flexural strength of the composite was evaluated. Flexural strength of the composite at room temperature was found to vary in between 281 to 658 MPa and the flexural strength value was not deteriorated significantly at elevated temperatures (>1400°C). Microstructural study and fractography of these room temperature flexural tested samples were also carried out in order to find the reason for scattering value of flexural strength. Samples were exposed to oxygen rich oxy-acetylene flame (flame temperature >1600 °C, 3s) as well as IR heating (heating rate 10 °C/s up to 1500 °C). In both the cases, no significant weight gain was observed in the sample. Samples did not also show any visible crack after these tests. Surface of the exposed layers were analyzed by XRD and SEM and reported in this study.

## Introduction

Both HfB<sub>2</sub> and ZrB<sub>2</sub> finds potential application in ultra-high temperature because of their very high melting temperature (3245°C), strength retention at high temperature, and reasonably good oxidation resistance at high temperature [1]. ZrB<sub>2</sub> is contemplated to be the better candidate for hypersonic vehicles, because of its lower price and density as compared to HfB<sub>2</sub>. However, ZrB<sub>2</sub> has moderate thermal shock and oxidation resistance. It is also difficult to obtain full density ZrB<sub>2</sub> by conventional sintering. SiC addition to ZrB<sub>2</sub> has been proved to be beneficial since, SiC improves flexural strength, fracture toughness and oxidation resistance of ZrB<sub>2</sub> [2]. Prior investigation by several researchers proved that the optimum properties are obtained with 20 vol.% of SiC addition to ZrB<sub>2</sub> [3]. In this investigation, Hot pressing technique was used to obtain full density ZrB<sub>2</sub>-20 vol.% SiC composite. Flexural strengths were evaluated at room and elevated temperature to assess the suitability of this composite at high temperature. Thermal shock resistance of this material has been evaluated by heating this material at 10°C/s

using IR lamps. Few samples were exposed to oxygen rich oxy-acetylene flame to evaluate its oxidation resistance at elevated temperature. Thermal conductivity, thermal diffusivity and specific heat of this material were also measured at different temperatures.

## Experimental

ZrB<sub>2</sub>-20 vol.% SiC composites used in the present study were prepared from the powders of ZrB<sub>2</sub>, SiC. 1wt.% B<sub>4</sub>C powder was also added as a sintering additive to improve the sinterability. ZrB<sub>2</sub>, SiC and B<sub>4</sub>C powders for this investigation was obtained from H.C. Starck, Germany. The average particle sizes of these powders were 2-6 μm, <1 μm and 4-8 μm respectively. First, SPEX milling of SiC powders were carried out for 3 h to reduce the SiC particle size further. These powders were then mixed with ZrB<sub>2</sub> and B<sub>4</sub>C powders in appropriate proportion and high energy planetary ball milled for 10 h at 150 rpm with ball to powder ratio of 2:1. The tungsten carbide grinding media were used for high energy milling. Powders were wet milled with acetone and subsequently dried in open air.

## EVALUATION OF ROOM TEMPERATURE AND HIGH TEMPERATURE PROPERTIES OF ZrB<sub>2</sub>-SiC COMPOSITES

The blended powders were then vacuum hot pressed to consolidate. Vacuum hot pressing was carried out at 1900 °C with 30 MPa pressure with a vacuum level of 10<sup>-5</sup> m-bar. Graphite dies were used for Hot Pressing operation.

Hot pressed Disc of size 100mm diameterX5mm thickness was sand blasted to remove graphite layer. Grinding and polishing of both the flat surfaces of the Disc were carried out with a diamond grinder to a final thickness of 3 mm. Flexural test samples of size 50mm(L)X4mm(W) X3mm(T), oxidation test coupon of size 30mmX30mmX3mm and Thermal conductivity test coupon of size 12.5mm diameterX3mm thickness were extracted by wire cutting from the disc. The disc was also exposed to IR heating. Few samples from different areas of the disc were also metallographically polished for metallographic examination by SEM attached with EDS system.

3 point bend test with 40 mm span was carried out to determine flexural strength of the sample using INSTRON machine at a cross head speed of 0.5mm/min. Fracture surface of the tested samples were examined by SEM in order to find out the origin and cause of failure.

Thermal conductivity, thermal diffusivity and specific heat of the samples were measured using LFA- 427 Model-Netzsch, Germany. IR heating of the samples were carried out up to a temperature of 1500 °C with a heating rate of 10 °C/s using IR heating device (M/s Litel IR System, Pune). Samples were kept at 1500°C for 5 minutes. Samples were also exposed to oxygen rich oxyacetylene flame for 3 minutes. Samples surface after oxy-acetylene test and IR heating were examined by XRD in order to know the phases formed after high temperature exposure.

### Results and Discussion

Evaluation of room temperature Flexural Strength (FS) Flexural strength of the ZrB<sub>2</sub>+SiC composite were recorded and tabulated in

Table 1. The flexural strength values are ranging from 281MPa to 658 MPa which is similar to the values reported in the literature [3]. Weibull plot of Flexural strength of the composite is shown in Fig. 1. FS values are very much scattered which is also reflected by a low R2 value of 0.77 and a weibull modulus value of 4.1. In order to find out the reason for this scattering, selected samples having minimum (sample No. 4) and maximum (sample No. 10) FS value were characterized by examining their microstructures using SEM attached with EDS system. SEM image of sample No. 4 and 10 are shown in Fig. 2. Both the samples look similar in respect of distribution of ZrB<sub>2</sub> and SiC phase and their grain size. Carbon and oxygen analysis of both the samples were carried out and shown in Fig. 3. C and O level of both the samples are seemed to be similar.

*Table 1: Flexural strength of the sample taken out from different locations.*

Sample Number	Flexural Strength (FS), MPa
1	407.0
2	391.5
3	435.7
4	281.1
5	430.0
6	404.3
7	351.3
8	374.2
9	390.2
10	658.0

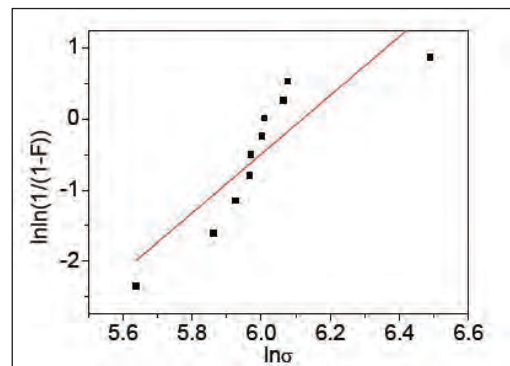
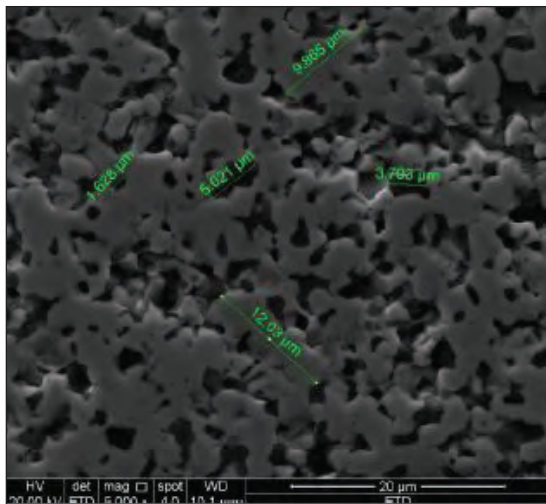
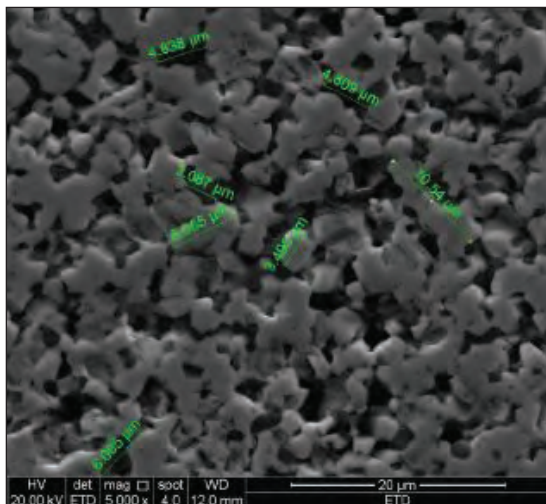


*Fig. 1: Weibull plot of flexural strengths of the samples extracted from different locations*

EVALUATION OF ROOM TEMPERATURE AND HIGH TEMPERATURE PROPERTIES OF  $ZrB_2$ -SiC COMPOSITES

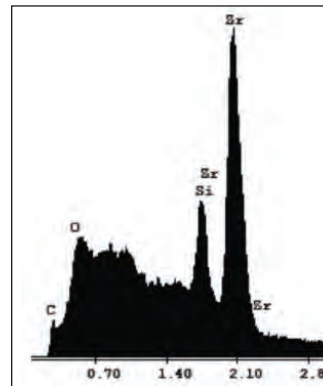


(a)

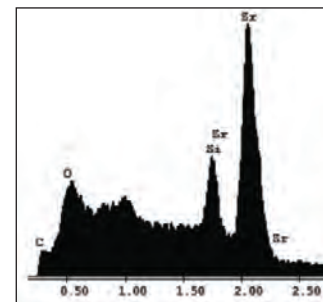


(b)

Fig. 2 : SEM image of (a) sample No. 4 having FS value of 281.1 MPa and (b) sample No. 10 having FS value of 658.0 MPa. Both the samples look similar in respect of distribution of  $ZrB_2$  and SiC phase and their grain size.



(a)



(b)

Fig. 3 : EDS of (a) sample No. 4 having FS value of 281.1 MPa and (b) sample No. 10 having FS value of 658 MPa. Oxygen level of both the sample looks similar.

Fractography of samples having lowest, intermediate and high flexural strength values were carried out using SEM and are shown in Fig. 4. The origin of the crack initiation is also shown in the fractographs by arrow. Cracks are originated mainly from the surface which is subjected to tensile stress during 3 point bend test. Crack is observed to be originated from a defect concentration sites located at the tensile stressed surface in case of sample with lowest Flexural strength. This is not the case for the other two samples having intermediate and high FS value. For these later two samples no visible defects concentration is observed at the origin of crack.

EVALUATION OF ROOM TEMPERATURE AND HIGH TEMPERATURE PROPERTIES  
OF ZrB<sub>2</sub>-SiC COMPOSITES

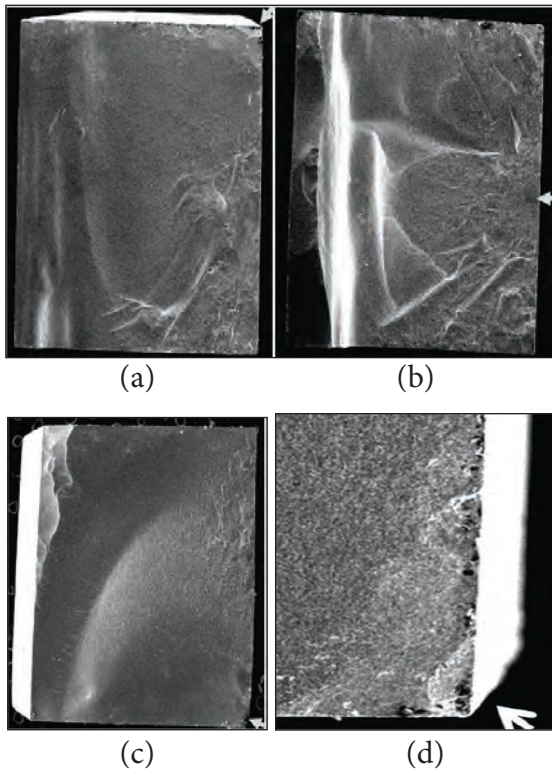


*Fig. 4 : SEM fractographs of 3 point bend tested samples : (a) sample No. 4 with FS 281.1 MPa (b) Sample No. 3 with FS 435.7 MPa and (c) Sample No. 10 with FS 658.0MPa. The origin of the cracks are shown by arrow. (d) Magnified image of crack origin of (a) showing concentration of defects at the origin of the crack.*

From this it may be said that lowest value of flexural strength of sample 4 is due to defect concentration at the surface subjected to tensile stress during 3 point bend test. This is further substantiated by the fact that SEM images and oxygen level of samples having lowest and highest FS are almost similar. More over fractographs of lowest and highest FS samples at higher magnification look alike (Fig. 5). Therefore, sample preparation rather than inherent material properties may be said to have caused the failure of sample 4 at lower FS value.

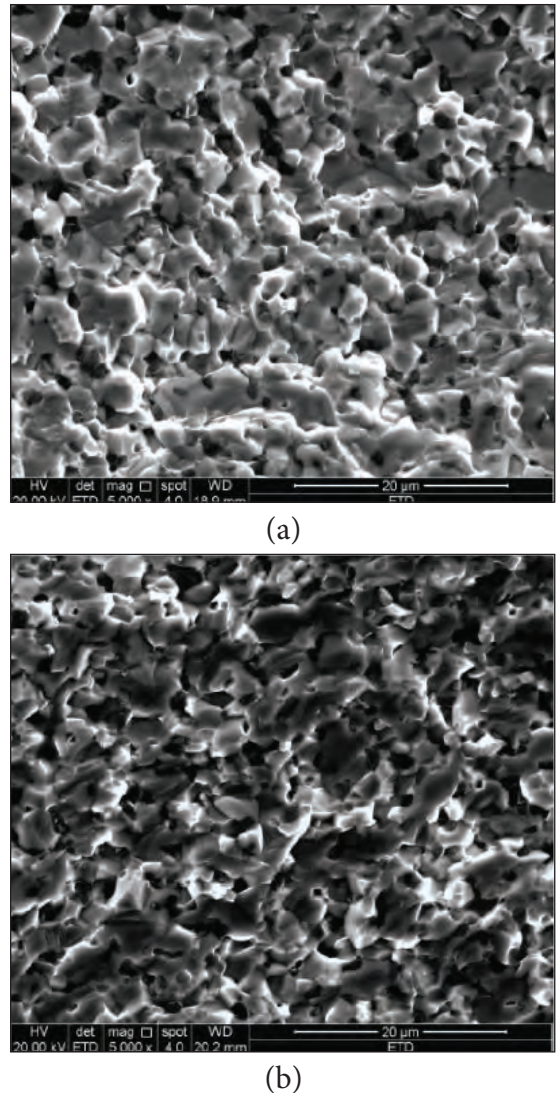


*Fig. 5 : SEM fractographs of 3 point bend tested samples : (a) sample No. 4 with FS 281.1 MPa (b) Sample No. 10 with FS 658.0MPa. Fractographs look similar in both (a) and (b)*

### Evaluation of elevated temperature properties

#### Flexural strength

Flexural strength of few samples were carried out at 1400 and 1450 °C, in order to find out the

## EVALUATION OF ROOM TEMPERATURE AND HIGH TEMPERATURE PROPERTIES OF ZrB<sub>2</sub>-SiC COMPOSITES

strength of the ZrB<sub>2</sub>-SiC composite at elevated temperature since this composite is contemplated to be used at elevated temperature. The FS values of the samples are recorded in Table 2. No significant deterioration of FS value is observed in this study at elevated temperature.

*Table 2 : FS of the sample as a function of test temperature.*

Temperature of test, °C	FS, MPa
1400	314
1450	383

Thermal conductivity, thermal diffusivity and specific heat Thermal conductivity, thermal diffusivity and specific heat of the samples are recorded up to 1000 °C at a temperature interval of 100 °C and shown in Table 3.

*Table 3: Thermal conductivity, thermal diffusivity and specific heat of the samples at different temperatures.*

	Thermal Diffusivity mm <sup>2</sup> /S	Thermal Conductivity W/(m*K)	Specific Heat J/g/K
50°C	26.2	114.4	0.8
100°C	24.2	116.0	0.9
200°C	21.5	115.6	1.0
300°C	20.0	114.6	1.1
400°C	18.9	113.2	1.1
500°C	17.9	110.3	1.2
600°C	17.4	109.0	1.2
700°C	17.1	108.9	1.2
800°C	18.2	117.3	1.2
900°C	12.8	84.4	1.2
1000°C	19.3	127.0	1.3

Whereas, thermal diffusivity value of the samples decreases with the temperature, minor increase in thermal conductivity and specific heat of the sample is observed with increase of temperature. The thermal conductivity value of ZrB<sub>2</sub>-20vol.%SiC is found to be better than the thermal conductivity of ZrB<sub>2</sub> (57.9 Wm<sup>-1</sup>K<sup>-1</sup>) reported in the literature [4].

### Oxidation and thermal shock resistance

In order to observe the behavior of the material at high temperature, the material was subjected to oxygen-rich oxy-acetylene flame at a temperature above 1600 °C for 180 s. The exposed sample is shown in Fig. 6.



*Fig. 6: Image of sample after exposure of Oxygen rich Oxyacetylene flame for 180 s.*

No visible cracks, oxide scale and weight gain were observed on the sample. X-ray diffraction pattern of sample exposed at oxygen-rich oxy-acetylene flame is shown in Fig. 7. Only prominent ZrB<sub>2</sub> and SiC peaks are seen. A few low intensity ZrO<sub>2</sub> and SiO<sub>2</sub> peaks are also seen. From this we can say that very less oxidation of the sample occurs after exposing the sample at Oxygen-rich Oxy-acetylene flame. This may be due to very short exposure time.

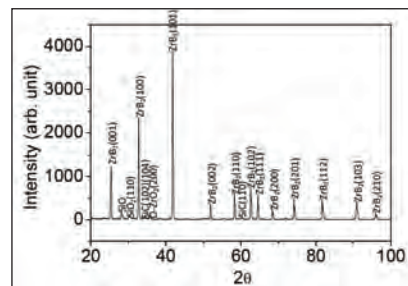


*Fig. 7: XRD plot of sample exposed at oxygen rich oxy-acetylene flame for 180 s. Sample shows prominent ZrB<sub>2</sub> peaks with SiC peaks along with a few ZrO<sub>2</sub> peaks of very low intensities.*



# STUDY ON HIGH TEMPERATURE POLY(ARYLEETHERKETON) (PAEK)/IRON COMPOSITES PREPARED BY POWDER ETALLURGY (P/M) ROUTE

S. D. Gaikwad<sup>1</sup>, P. Dhoka<sup>2</sup>, R. K.Goyal<sup>1</sup>

<sup>1</sup>Department of Metallurgy and Materials Science, College of Engineering, Pune, India

<sup>2</sup>Industrial Metal Powders (I) Pvt. Ltd., Shirur, Pune, India

**Abstract :** Electrolytic grade iron (Fe) powder filled high performance poly(aryletherketon) (PAEK) based composites were prepared using planetary ball mill followed by compaction for the electronic applications. It was found that the experimental density of the composites was very close to those of theoretical density. Scanning electron microscopy showed excellent dispersion of Fe particles in the matrix. Thermogravimetry analyzer (TGA) showed that the thermal stability of the composites is more than 550 °C. Vickers microhardness of the composites increased with increasing Fe content in the matrix. For a given volume fraction of Fe particle, the microhardness was increased with increasing ball milling time. The dielectric constants of the composites increased significantly with low dissipation factor compared to those of pure PAEK.

**Keywords:** Iron, high performance polymer, ball mill, hardness, electrical properties.

## 1. Introduction

Polymer matrix composites containing electrically conductive particles (or fillers) are widely used for the applications like electronic embedded system, electromagnetic interference (EMI) shielding, capacitors, and thermal interface materials. The electrical property of polymer composites depends upon types, size, shape and volume fraction of fillers, dispersion of filler in the matrix, crystallinity of polymer, processing methods, and the interface between matrix and filler. In recent years, polyethylene (PE), polyoxymethylene (POM), polyamide (PA), PE/POM [1,2], polystyrene [3], low density polyethylene (LDPE) and high density polyethylene (HDPE) [4], epoxy [5] polymers as matrices and iron as filler have been studied for the dielectric properties. Moreover, poly(aryletherketone) (PAEK)/ZnO [6], polypropylene (PP)/silver (Ag) [7], poly(etheretherketone) (PEEK)/barium titanate [8], poly(phenylene sulphide) (PPS)/copper [9], PAEK/Ti<sub>3</sub>SiC<sub>2</sub> [10], epoxy/cobalt [11], epoxy/aluminium [12], silicone, polyamide,

polynorborene, benzocyclobutene/aluminium [12], polyarylenethernitrile (PEN)/Al<sub>2</sub>O<sub>3</sub>/Multiwalled carbon nanotubes [13], PPS/molybdenum oxide [14], epoxy/iron [15], PEN/graphene oxide [16] composites have also been studied for their electrical and thermal properties. Some of their applications have been suggested for the embedded capacitors which require high dielectric constant and low dielectric loss.

Polymers are known for their excellent flexibility, low density and easy processability. One of the high performance polymers, i.e., poly(aryletherketone) (PAEK) is a semi-crystalline thermoplastic polymer which has high melting temperature (~ 360 °C) and glass transition temperature (~154 °C). It also exhibits high fatigue strength, good impact strength at low temperature, very low tendency to creep and good wear resistant. In view of this, the PAEK/electrolytic grade iron (Fe) powder composites were prepared using planetary ball mill followed by hot pressing. The electrical, thermal and mechanical properties of the composites were discussed. Moreover, effect of ball milling time

# STUDY ON HIGH TEMPERATURE POLY(ARYLETHERKETON) (PAEK)/IRON COMPOSITES PREPARED BY POWDER ETALLURGY (P/M) ROUTE

on microhardness of the composites was also discussed.

## 2. Experimental procedure

### 2.1 Materials

Commercial PAEK (1100PF graded) powder donated by Gharda Chemicals Ltd., Thane (Mumbai), India, was used as matrix. The electrolytic grade Fe powder manufactured by M/s Industrial metal powders (I) Pvt. Ltd. Pune India was used as filler. According to manufacturer particle size of Fe powder is # 325 mesh. Fig 1 shows the SEM image of Fe powder. It has irregular shaped particle with aspect ratio more than 1. The differential particle size distribution of Fe powder was determined using Laser Distribution Particle Size Analyzer, Microtrac S3500 USA. Figure 2 shows the particle size distribution of Fe powder. The particle size varies from 5 to 100  $\mu\text{m}$  and its median particle is 30  $\mu\text{m}$ .

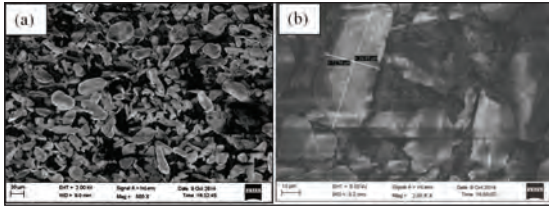


Fig. 1 SEM image of pure Fe powder before milling at a magnification of (a) 500X and (b) 2000X

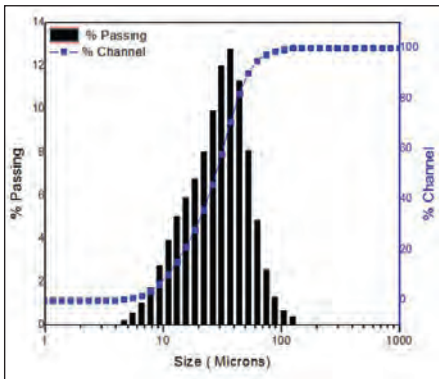


Fig. 2 Particle size distribution of Fe powder.

### 2.2 Preparation of PAEK/Fe composites

The PAEK and Fe powders were mixed and milled in a planetary ball mill (Retsch Technology, Germany, PM 200). Four compositions of PAEK/Fe mixtures with Fe contents varying from 0 to 50 wt.% (14.4 vol.%) were prepared. The rotation speed of vials was 250 rpm. The milling time was 5 h. The composites were fabricated using 15 T hot compaction machine (M/s Kimaya Engineering, Thane, India). Then the samples were heated to 380°C with heating rate of ~10°C/min at 60 MPa with dwell time of 20 min. Finally, samples were cooled naturally. The prepared samples were coded by MC-X, where X indicates weight % of Fe powder in the matrix, as shown in Table 1.

Table 1 Compositions of PAEK/Fe composites

Notation	Percentage of Iron in PAEK matrix	
	Wt.%	Vol.%
MC-00	0	0
MC-10	10	1.84
MC-30	30	6.76
MC-50	50	14.4

### 2.3 Characterization

#### 2.3.1 Density Measurement

The theoretical density ( $\rho_{th}$ ) of the composites was calculated using rule of mixture as shown in equation (1). The densities of Fe ( $\rho_f$ ) and PAEK ( $\rho_m$ ) were considered as 7.8 g/cc and 1.32 g/cc, respectively.

$$\rho_{th} = \rho_f \cdot V_f + \rho_m \cdot V_m \quad (1)$$

Where,  $V_m$  and  $V_f$  are the volume fraction of the matrix and the filler, respectively. The experimental density ( $\rho_{ex}$ ) was determined by Archimedes Principle using equation (2).

$$\rho_{exp} = \frac{W_{air}}{W_{air} - W_{liq}} \times \rho_{liq} \quad (2)$$

Where,  $W_{air}$  and  $W_{liq}$  are the weight of samples in air and liquid (ethanol) medium, respectively. The density of ethanol ( $\rho_{liq}$ ) is (0.79 g/cc).

# STUDY ON HIGH TEMPERATURE POLY(ARYLEETHERKETON) (PAEK)/IRON COMPOSITES PREPARED BY POWDER ETALLURGY (P/M) ROUTE

## 2.3.2 Microhardness

The microhardness of well polished samples was determined using Vickers hardness tester (Future-Tech Corp FM-700, Tokyo, Japan) at a constant load of 100 g and dwell time of 15 s. Average values of five readings were reported as the microhardness of the samples.

## 2.3.3 Scanning electron microscopy (SEM)

The distribution and morphology of Fe particles in the PAEK matrix were observed using field emission scanning electron microscope (ZEISS: SIGMA) operated at 5 to 20 kV. The surface of the well polished samples was coated with a thin layer of Au-Pd alloy using sputter coater (QUORUM, UK) and mounted on metal stub which was grounded with adhesive conductive tape to minimize charging effects.

## 2.3.4 Thermal properties

The thermal stability of the composites was investigated using TGA (TGA 4000, Perkin Elmer, USA). The samples were heated from ambient temperature to 900 °C at a heating rate of 10°C/min in N<sub>2</sub> atmosphere. Degradation temperature (T<sub>10</sub>) was taken as the temperature corresponding to 10 wt.% weight loss. The maximum decomposition temperature (T<sub>max</sub>) was taken as the temperature corresponding to maximum of the peak obtained by first order derivative curve of TGA (DTG). The melting and non-isothermal crystallization behaviour of composites was performed using DSC (MDSC-Q20, TA Instruments, USA) under nitrogen atmosphere. The samples placed in an aluminium pan were first heated from 30°C to 400°C at a heating rate of 10°C/min in order to erase thermal history of the polymer. The cooling rate was 10°C/min. The second heating was considered for data analysis. The heating rate was 10°C/min and temperature range 30°C to 400°C. The broad exothermic peak

indicates crystallization temperature (T<sub>cr</sub>) and endothermic peak indicates melting temperature (T<sub>m</sub>). The data of second heating and first cooling curves were discussed.

## 2.3.5 Electrical Properties

Dielectric measurements were carried out using a precision impedance analyser (Wayne Kerr Electronics 6515B, UK). The capacitance, dissipation factor and impedance were obtained from the instrument in a frequency range of 20 Hz to 15 MHz at ambient temperature. Dielectric constant was calculated by using equation (3).

$$\epsilon = \frac{(C \times t)}{(\epsilon_0 \times A)} \quad (4)$$

Where, C is the measured capacitance of the sample, t is the thickness of the sample, A is the surface area of the sample and  $\epsilon_0$  is the permittivity of free space. The volume resistance ( $\rho$ ) of samples was measured using an electrometer (Keithley 6517-B). The D.C. resistivity was calculated from equation (4).

$$\rho = \frac{R.A}{t} \quad (4)$$

Where, R is the resistance of the sample

## 3. Results and Discussion

### 3.1 Density

Theoretical and experimental density of the samples is shown in Fig. 3. It can be seen that the experimental density of the composites increased with increasing Fe content. This is due to higher density of Fe (7.8 g/cc) as compared to that of the PAEK matrix (1.32 g/cc). Experimental density of the composites is very close to that of theoretical density indicating that the composites were almost porosity free.

# STUDY ON HIGH TEMPERATURE POLY(ARYLETHERKETON) (PAEK)/IRON COMPOSITES PREPARED BY POWDER ETALLURGY (P/M) ROUTE

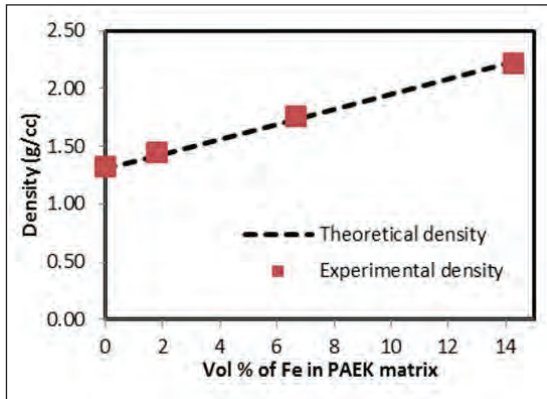


Fig. 3 Experimental and theoretical density of the PAEK/Fe composites

### 3.2 Scanning electron microscopy (SEM)

Fig. 4a and b show SEM images of the MC-30 and MC-50 composites, respectively. The Fe particles are almost uniformly distributed in the PAEK matrix.

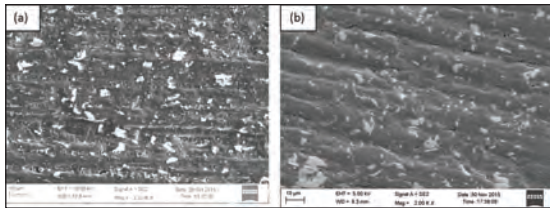


Fig. 4 SEM images of (a) MC-30 and (b) MC-50 composites at (a) 2000X and (b) 5000X.

### 3.3 Microhardness

The microhardness of the composites PAEK/Fe as a function of Fe particles in the PAEK matrix is shown in Fig. 5a. The hardness of composite increased from 30 kg/mm<sup>2</sup> for the pure matrix to 36 kg/mm<sup>2</sup> for MC-50. The uniform dispersion of Fe particle in the matrix increases the resistance to the indentation of the indenter. As shown in Fig. 5b, for a constant weight % (i.e. 50 wt%) of Fe, the microhardness of the composite increases with increasing ball milling time. It is due to

increase in number of Fe particles with increasing ball milling time which increases the interfacial volume fraction dramatically compared to the composites containing 0 h milled Fe powder.

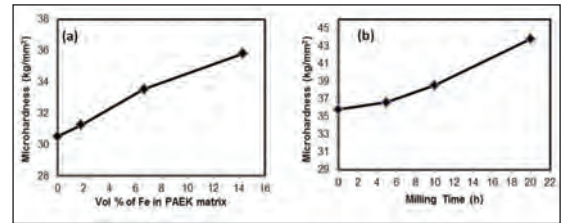


Fig. 5 Microhardness of PAEK/Fe composite as a function of (a) volume % of Fe and (b) milling time for MC-50

### 3.4 Thermogravimetry analysis (TGA)

Fig. 6a shows the residual weight of the composites as a function of temperature. It is observed that pure PAEK has a degradation temperature ( $T_{10}$ ) of 561°C. The  $T_{10}$  decreased with increasing Fe content in the composites by 10°C, i.e., thermal stability of the composites decreased slightly. This may be attributed to the breakage of inter-chain bonds of the polymer due to incorporation of Fe particles. Fig. 6b shows DTG traces of the composites. When major weight loss begins, there is a sharp increase in the derivative which then reaches a maximum rate of weight loss. It shows that the maximum decomposition of the composites decreases from 578 °C for the pure matrix to 535 °C for MC-50.

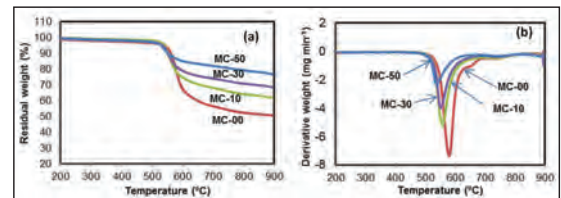


Fig. 6 Thermogravimetric analysis of nanocomposites with varying Fe content (a) TGA curve and (b) DTG curve

# STUDY ON HIGH TEMPERATURE POLY(ARYLETHERKETON) (PAEK)/IRON COMPOSITES PREPARED BY POWDER ETALLURGY (P/M) ROUTE

## 3.5 Differential Scanning Calorimeter (DSC)

The DSC heating curves of the PAEK/Fe composites are shown in Fig. 7a. It was observed that the peak melting temperature of the composites decreases slightly with increasing Fe content. The onset of melting temperature for pure PAEK is about 348.6°C which is decreased to 337.0°C for 50 wt.% Fe (MC-50) composite. However, the melting temperature is affected slightly. Figure 7b shows DSC cooling curves. It was found that the peak crystallization temperature of the composites is decreased by 13.5°C compared to that of pure PAEK. Crystallinity of the PAEK/Fe composites decreases from 25.26 % for pure matrix to 18.4% for 50 wt.% Fe composite indicating that the presence of Fe particles impede the crystallization process of the matrix [4].

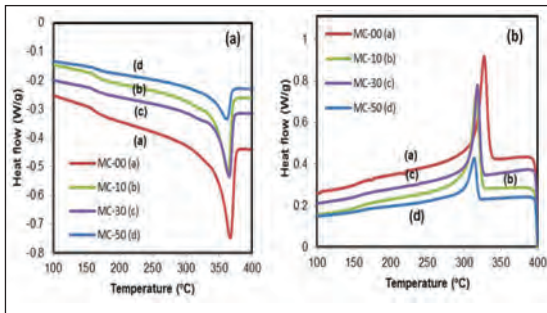


Fig. 7 DSC curves during (a) heating cycle and (b) cooling cycle for PAEK/Fe composites

## 3.6 Dielectric Properties

Fig. 8a shows dielectric behaviour of the PAEK/Fe composites studied as a function of frequency (1 kHz to 15 MHz) and volume fraction of Fe content at room temperature. It can be seen that the dielectric constant of composites remains almost stable with varying frequencies. For a given frequency, the dielectric constant increases with increasing volume fraction of Fe in the polymer matrix, e.g., at 1 kHz the dielectric constant increases from 4.6 for pure

PAEK to 13.9 for MC-50. The increased dielectric constant of the composites may be attributed to the polarization associated with the charges induced on Fe particle surfaces and at the interface. The higher dielectric constant for the PAEK/Fe composites with low Fe content (i.e. 14.4 vol%) with lower dissipation may be due to the presence of thin oxide layer on Fe particles [5,9]. The dielectric constant of MC-50 composite becomes slightly frequency dependent.

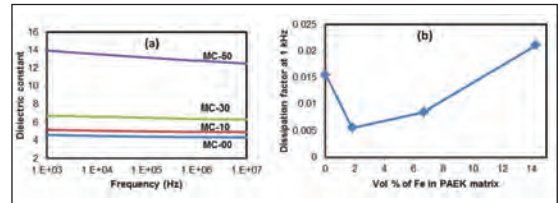


Fig. 8 (a) Dielectric constant versus frequency and (b) dissipation factor (at 1 kHz) versus vol% Fe for the PAEK/Fe composites.

Fig. 8b shows variation of dissipation factor at 1 kHz as a function of vol.% of Fe particle. It can be seen that the dissipation factor decreases up to 1.84 vol.% Fe and thereafter it increases on further increasing Fe content. The lower dissipation factor for the composites at lower Fe loading may be due to the formation of oxide layer around Fe particles during processing and post processing which restrict the transfer of charge between the Fe particles.

## 3.7 DC and AC Conductivity

AC and DC conductivities of the composites as a function of vol.% of Fe is shown in Figure 9. Both AC and DC conductivities increase slightly with increasing Fe content in the PAEK matrix. The order of magnitude, i.e., 10<sup>-12</sup> and 10<sup>-9</sup> for the DC and AC conductivity remains same as compared to pure matrix, respectively, indicating that composites are insulating. This may be due to larger inter-particles distances between Fe particles in PAEK matrix and the presence of an oxide layer on the surface of Fe particles [7].

# STUDY ON HIGH TEMPERATURE POLY(ARYLETHETERKETON) (PAEK)/IRON COMPOSITES PREPARED BY POWDER ETALLURGY (P/M) ROUTE

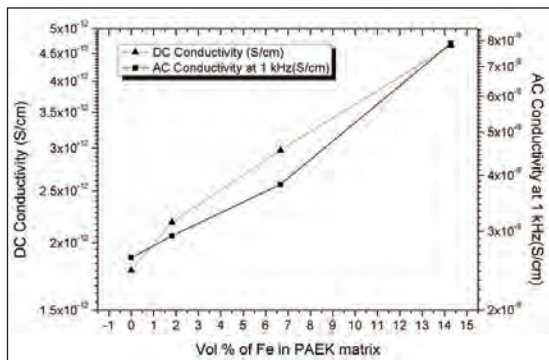


Fig.9 DC and AC Conductivity of the PAEK/Fe composites as a function of frequency.

## 4. Conclusions

PAEK/Fe composites containing 0 to 50 wt. % (14.4 vol %) Fe particles were successfully fabricated using planetary ball mill (for blending) followed by hot pressing. Experimental density of the composites is very close to those of theoretical density. SEM revealed a good dispersion of Fe particles in the matrix. Dielectric constant of the composites increased with increasing Fe content. The low value ( $< 0.02$ ) of dissipation factor is an important achievement of this study. AC and DC conductivities of the composites slightly increases with increasing Fe content. The presence of Fe particles decreases the peak crystallization temperature significantly but affects melting temperature slightly. The % crystallinity of the composites is decrease with increasing Fe content. Thermal stability of the composites slightly decreases with increasing Fe content in the matrix. Microhardness of the composites increased with increasing Fe particles and milling time for a given composition.

## Acknowledgement

RKG and SDG acknowledge to M/s Industrial Metals Powder Pvt. Ltd., Pune, India and M/s Gharda Chemical Ltd., Thane, India for providing electrolytic grade Fe powder and PAEK powder, respectively, for this research.

SDG also acknowledges the Director, College of Engineering Pune for encouraging him for the research

## References

- [1] H. Zois, L. Apekis, Y. P. Mamunya, Dielectric properties and morphology of polymer composites filled with dispersed iron, *J. Appl. Polym. Sci.* 88 (2003) 3013-20.
- [2] Y. P. Mamunya, Y. V. Muzychenko, P. Pissis, E. V. Lebedev, M. I. Shut, Percolation phenomena in polymers containing dispersed iron, *Polym. Eng. Sci.* 42 (2002) 90-100.
- [3] F.S. Al-Aqrabawi, A.M. Zihlif, Z.M. Elimat, G. Ragosta, Effect of partial size on the AC electrical behaviour of iron/polystyrene composites, *J. Mater. Sci.: Mater. Electr.* 24 (2013) 1690-1695.
- [4] Y.J. Li, M. Xu, J.Q. Feng, X.L. Cao, Y.F. Yu, Z.M. Dang, Effect of the matrix crystallinity on the percolation threshold and dielectric behaviour in percolative composites, *J Appl. Polym. Sci.* 106 (2007) 3359-3365.
- [5] H. Sharma, S. Jain, P.M. Raj, K.P. Murli, R. Tummala, Magnetic and dielectric property studies in Fe and NiFe-based polymer nanocomposites, *J. Electr. Mater.* 44 (2015) 3819-3826.
- [6] R.K. Goyal, D. Vaishnav, Thermal and dielectric properties of high performance polymer/ZnO nanocomposites, *IOP Conf. Series: Mater. Sci. Eng.* 64 (2014) 012016.
- [7] M. Karttunen, P. Ruuskanen, V. Pitkanen, W. M. Albers, Electrically conductive metal polymer nanocomposites for electronic applications, *J. Electr. Mater.* 37 (2008) 951-954.
- [8] R.K. Goyal, V.V. Madan, P.R. Pakankar, S.P. Butee, Fabrication and properties of novel polyetheretherketone/barium titanate composites with low dielectric loss, *J. Electr. Mater.* 40 (2011) 2240-2247.
- [9] R.K. Goyal, K.R. Kambale, S.S. Nene, B.S. Selukar, S. Arbut, U.P. Mulik, Fabrication, thermal and electrical properties of polyphenylene sulphide/copper composites, *Mater. Chem. Phys.* 128 (2011) 114-120.

## STUDY ON HIGH TEMPERATURE POLY(ARYLETHETERKETON) (PAEK)/IRON COMPOSITES PREPARED BY POWDER ETALLURGY (P/M) ROUTE

---

- [10] K.V. Mahesh, S. Balanand, R. Raimond, A. P. Mohamad, S. Ananthakumar, Polyarylrtherketone polymer nanocomposites engineered with nanolaminated  $Ti_3SiC_2$  ceramic fillers, *Mater. Design* 63(2014)360-367.
- [11] P.M. Raj, H. Sharma, G.P.Reddy, N.Altunyurt, M.Swaminathan, R. Timmala, V. Nair, Cobalt-polymer nanocompositedielectrics for miniaturized antennas, *J. Electr. Mater.* 43 (2014) 1097-1106.
- [12] J.Xu, C.P.Wong, Effect of polymer matrices on the dielectric behaviour of a percolative high-k polymer composites for embedded capacitor application, *J. Electr. Mater.* 35 (2006) 1087-1094.
- [13] M.Feng, X.Huang, Z.Pu, X.Liu, Dielectric and mechanical properties of three-component  $Al_2O_3/MWCNTs/polyarylene$  ether nitrile micro-nanocomposite, *J. Mater. Sci: Mater. Electr.* 25 (2014) 1393-1399.
- [14] N.Qureshi, M.Shinde, R.Ratheesh, A.Bhalerao, B.Kale, U.Mulik, D.P.Amalnerkar, Superior Dielectric performance of engineering thermoplastic as a result of In Situ embedding of nanoscale mixed phase molybdenum oxide, *J. Electr. Mater.* 44 (2015) 2269-2275.
- [15] G.C.Psarras, E.Manolakaki, G.M.Tsangaris, Dielectric dispersion and ac conductivity in Iron particles loaded polymer composites, *Compos: Part B* 34 (2003) 1187-1198.
- [16] J.Li, Z.Pu, Z.Wang, Y.Long, K.Jia, X.Liu, High dielectric constants of composites of fiber like copper phthaloyanine coated graphene oxide embedded in poly(arylene ther nitriles), *J. Electr. Mater.* 44 (2015) 2378-23

# INVESTIGATION OF ZIRCONIUM SILICATE AND ZIRCONIUM OXIDE REINFORCEMENT IN ALUMINIUM 6061 METAL MATRIX - A COMPARATIVE STUDY

Jitender Kumar Chaurasia, Paridh N. Patel, A. Muthuchamy, A. Raja Annamalai

School of Mechanical Engineering, VIT University, Vellore, Tamilnadu, India

**Abstract :** In the present study, a comparative investigation was done to study the influence of reinforcing Zirconium Silicate ( $ZrSiO_4$ ) and Zirconium oxide ( $ZrO_2$ ) in pre-alloyed Al 6061 powder through powder metallurgy route. Pre-alloyed Al 6061 powder, with average particle size of 20 microns, was used. Commercially available Zirconium Silicate and Zirconium oxide with different weight percentage (5%, 10%, 15% and 20%) were reinforced in Al 6061 matrix. Densification behaviour after cold compaction and sintering were studied. Maximum sintered density of 96% and 92% of theoretical density has been achieved in Al-5ZrSiO<sub>4</sub> and Al-5ZrO<sub>2</sub>, respectively. Optical microscopy was done to investigate the particle-matrix interface and microstructure. Hardness test was also done to investigate the overall hardness of the matrix.

**Keywords :** Powder metallurgy, Al 6061, Zirconium Silicate, Zirconium oxide, Densification

## 1. Introduction

Use of materials reinforced with ceramics and their production has improved significantly in the recent decades. Industries like automobile and marine require materials with high strength, low cost and low density. Aluminium 6061 is amongst the most extensively used alloys of its family. With its excellent corrosion resistance, Al 6061, particularly, finds its application in marine fittings, tank fitting and heavy duty structures such as components and equipments of the off-shore platforms and oil rigs. It is a heat treatable alloy and can be hardened by solution heat treatment. Combined with both solution treatment and artificial aging its hardness and strength can be taken up to the level of T6 temper [1]. However, even with these properties, Al 6061 lacks in delivering good mechanical properties such as tensile strength and wear resistance. Advancements in metal matrix composites have helped to enhance thermal stability, high specific modulus, strength, workability, and creep resistance [2]. To fabricate metal matrix, Powder metallurgy is one the various manufacturing process. Powder metallurgy

has its own advantages such as Near Net shape forming, less residual voids and good interface between inclusion and metal matrix [3-5]. Powder metallurgy provides a great distribution of reinforcement into the matrix as compared to any other process like stir casting [6]. Particle size is an another importance parameter for achieving good sinter density and mechanical property [3].

Particulate reinforcement is a method by which one can combine metals and ceramics in a predetermined composition to enhance material properties like hardness and tensile test [7-8]. However, the elongation property of the material get reduces, which is due to high availability of nucleation site to form crack in the metal matrix [9]. Ceramic-reinforced Aluminium metal matrix composites, prepared by means of particulate reinforcements, are one of the greatest substitutes for these kinds of applications. Ceramics such as Alumina, Silicon Carbide and fly ash are amongst the most used reinforcement for aluminium metal matrix. In the present study, a comparison between reinforcement of  $ZrSiO_4$  and  $ZrO_2$  with varying

# INVESTIGATION OF ZIRCONIUM SILICATE AND ZIRCONIUM OXIDE REINFORCEMENT IN ALUMINIUM 6061 METAL MATRIX - A COMPARATIVE STUDY

weight% in Al6061 has been done. Zirconium diboride and Zirconium Silicate are the materials of particular interest due their high melting point, high electrical and thermal conductivity, and chemical inertness [10,11].

## 2. Experimental Details

### 2.1 Powder Preparations

Pre alloyed Aluminium 6061 powder of average particle size of 20  $\mu\text{m}$  (Material Vendor: NB Enterprises, India) was used as matrix. Varying weight percentages (5%, 10%, 15% and 20%) of Zirconium silicate( $\text{ZrSiO}_4$ ) and Zirconium oxide ( $\text{ZrO}_2$ ) were mixed manually with Al 6061 powder, each for about an hour to ensure proper mixing of the reinforcements in Al 6061 powder. For powder morphology SEM images (Model: ZEISS EVO-18 Research) of the as received powder was also taken. Fig. 1 shows the SEM morphology of the as received Al 6061 powder. SEM morphology reveals that the particles of aluminium powder are random in shape.

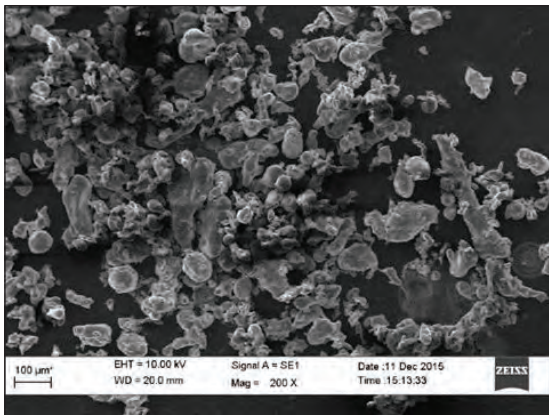


Fig. 1: SEM morphology of the as received Al 6061 powder

### 2.2 Compaction and Sintering

The mixed powders were cold compacted using a hydraulic press at three different pressure 300, 400 and 500 MPa. A die with circular cross-section, having diameter of 16mm, was used to

compact samples from the prepared powder compositions. Zinc stearate was applied on punch and die for lubrication and to reduce the die wall friction effect and to allow the punch to move freely in the die. Eight different samples with 5, 10, 15 and 20 weight percentage of  $\text{ZrSiO}_4$  and  $\text{ZrO}_2$ , mixed with Al 6061, were compacted, each having height of  $7\pm 1$  mm. After compaction, the green samples were conventionally sintered in a tubular furnace (Model: VB Ceramics-1200 Tubular Furnace) at  $550^\circ\text{C}$  with a heat rate of  $5^\circ\text{C}/\text{min}$ . After reaching the required temperature, samples were quenched in water for solution heat treatment.

### 2.3 Microstructural Characterisation

For microstructure analysis the samples were prepared conventionally i.e. first polished using Silicon carbide abrasive sheet of grit size 220, 400, 600, 800, 1000, 1200, 1500 and 2000 and followed by Disc polishing with Alumina and Water. After polishing, the samples were cleaned. To view the microstructure, all the samples were etched using Keller's reagent (as per ASTM E407 Standards). Microstructure structure analysis of the composite was done using a ZEISS light optical microscope.

### 2.4 Mechanical Property Characterisation

Vickers micro-hardness test was performed with indenter load of 100g and dwell time 10s for all the prepared sample using a Vickers Hardness Tester (Model: Economet VH-1MD). All the readings were taken close to the reinforcement to ensure the proper hardness value of the metal matrix. Ten readings from each sample were taken and arithmetic mean with standard deviation was calculated.

## 3. Results

### 3.1 Density Measurement

Fig. 2 shows the green density achieved by the different samples at different compaction

# INVESTIGATION OF ZIRCONIUM SILICATE AND ZIRCONIUM OXIDE REINFORCEMENT IN ALUMINIUM 6061 METAL MATRIX - A COMPARATIVE STUDY

pressure. It has been observed that densification is enhanced with increasing pressure, keeping other parameters constant.  $ZrSiO_4$  reinforced samples have yielded better densification as compared to samples reinforced with  $ZrO_2$ , which is close to the theoretical density (96%) of the composite. Increase in the density has been observed with the decrease in weight% of reinforcement. Minimum density has been achieved with the maximum reinforcement percentage in both the cases. For sintering, the samples with higher green density (samples compacted at 500 MPa) were selected. Fig. 3 shows the densification achieved by Al 6061 reinforced with  $ZrSiO_4$  and  $ZrO_2$  and compacted at 500 MPa. Maximum density in case of Al 6061- $ZrSiO_4$  was found to be 96% of theoretical density, similarly, 92.75% for Al 6061- $ZrO_2$ .

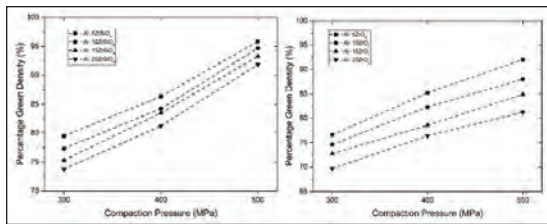


Fig. 2: Percentage green density of the Al with different weight% of  $ZrSiO_4$  and  $ZrO_2$  at 300, 400, 500 MPa compaction pressure

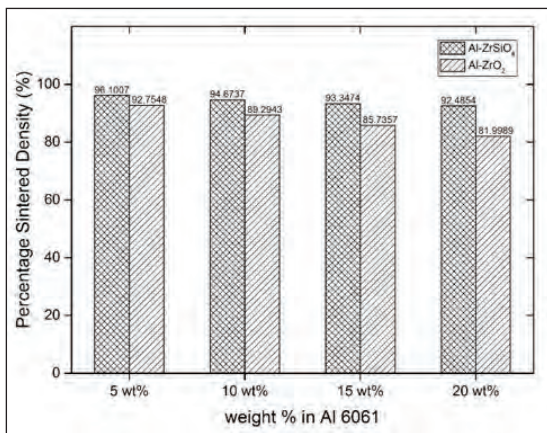


Fig. 3: Percentage sintered density of Al with different weight% of  $ZrSiO_4$  and  $ZrO_2$

## 3.2 Material Characterisation

Fig. 4 shows optical micrographs of all the prepared composition of Al 6061- $ZrSiO_4$  and Al 6061- $ZrO_2$ . Micrographs, reveal the random mixing of the reinforcement in the matrix. The reinforcement phase is clearly visible in the metal matrix. Increases in porosity has been observed with the increase of reinforcement percentage. Al 6061 reinforced with  $ZrO_2$  has more porosity than the samples reinforced with  $ZrSiO_4$ . Proper compaction is achieved in case of Al 6061- $ZrSiO_4$  which is due to the random shape of particles of  $ZrSiO_4$  and Al 6061 powders. Vickers micro hardness was performed to check the hardness of the sintered composites. Fig. 5 shows the hardness values of Al 6061- $ZrSiO_4$  and Al 6061-

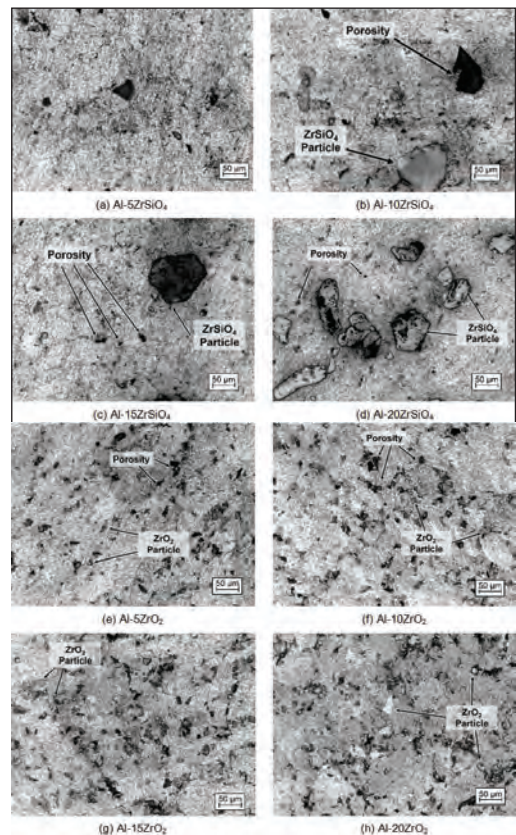


Fig. 4: Micrographs of Al- $ZrSiO_4$  and Al- $ZrO_2$  with different weight % of reinforcement

# INVESTIGATION OF ZIRCONIUM SILICATE AND ZIRCONIUM OXIDE REINFORCEMENT IN ALUMINIUM 6061 METAL MATRIX - A COMPARATIVE STUDY

ZrO<sub>2</sub> with different weight % (5%, 10%, 15%, 20%) of reinforcement. Results conclude that the increase in reinforcement weight% increases the hardness value. Maximum hardness values of 93.11 HV and 90.1 HV have been achieved in Al 6061-20ZrSiO<sub>4</sub> and Al 6061-20ZrO<sub>2</sub>, respectively. Hardness values of the sintered samples show a linear trend with the increase in reinforcement weight% in the Al 6061 matrix. About 30% increase in the hardness value has been observed as the weight% of ZrSiO<sub>4</sub> increased from 5 to 20% within the metal matrix, whereas only 19.13% increase in the hardness value has observed as the weight% of ZrO<sub>2</sub> in the Al 6061 metal matrix increases from 5 to 20%.

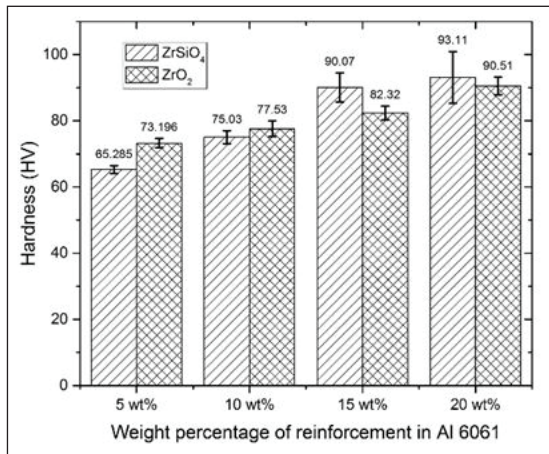


Fig. 5: Hardness value of Al-ZrSiO<sub>4</sub> and Al-ZrSiO<sub>2</sub> with different weight % of reinforcement

## 4. Discussion

After compacting all the sample with varying weight% of reinforcements, at pressures of 300, 400 and 500 MPa, maximum densification of the green compacts was found to be around 95.83% of theoretical density at a pressure of 500MPa for the composition Al 6061-5ZrSiO<sub>4</sub>. A similar trend in density was also observed by N. Showaiter et. al. [12]. The reason for good densification of all the samples is due to the fine particles size of the base powder, which helps in filling up the voids completely which may be produced by

coarser particles. Since, the material, in its green state, has already attained 95% density, very less change has been observed after sintering. It has been observed that the increase in the weight% of the reinforcement decreases the overall density of the composite. More density has been achieved with ZrSiO<sub>4</sub> as compared to ZrO<sub>2</sub>. Comparing the volume of green compacts with sintered samples, a maximum of 1.4% of volume shrinkage has been observed. Microstructure images shows that the reinforcement particles are evenly distributed over the entire Al 6061 matrix. Fine grain structure of the matrix phase has been observed. No plastic deformation of the reinforcement particles is observed at a pressure of 500 MPa. As it is known that hardness is the measure of indentation, the increase in hardness is quite obvious with the increasing weight% of ZrSiO<sub>4</sub> and ZrO<sub>2</sub>. The increased hardness value is completely attributed to the hard reinforcement phase (ZrSiO<sub>4</sub> and ZrO<sub>2</sub>) in the metal matrix, which has reduced the movement of dislocation with in the matrix. More hardness has been observed in the Al-ZrSiO<sub>4</sub> samples as compared to Al-ZrO<sub>2</sub> sample. Similar hardness trend for the particulate reinforced samples has been reported by other authors as well [13-14].

## 5. Conclusion

In the present work, a comparison between ZrSiO<sub>4</sub> and ZrO<sub>2</sub> reinforcement in the Al 6061 metal matrix, has been done. The study reveals that the Al 6061 matrix reinforced with ZrSiO<sub>4</sub> resulted in more densification as compared to ZrO<sub>2</sub> reinforcement. Green, as well as, the sintered densities were found to be increasing with the increasing weight% of reinforcement in both the cases. Fine grain structure has been observed in the both Al-ZrSiO<sub>4</sub> and Al-ZrO<sub>2</sub>, which is a required property in Aluminium for its structural application. Reinforcement of the ZrSiO<sub>4</sub> and ZrO<sub>2</sub> in the Al 6061 matrix has shown a significant improvement in hardness, with the maximum hardness achieved in the case of Al-ZrSiO<sub>4</sub>.

# INVESTIGATION OF ZIRCONIUM SILICATE AND ZIRCONIUM OXIDE REINFORCEMENT IN ALUMINIUM 6061 METAL MATRIX - A COMPARATIVE STUDY

## 6. References

- [1] Aluminium: Properties and Physical Metallurgy, ed. J. E. Hatch, American Society for Metals, 1984
- [2] J.V. Foltz, C.M. Blackmon, "Metal matrix composites", *Advanced Materials and Process* Vol-154/6, 1998, p19-23
- [3] M. Kok, Production and mechanical properties of Al<sub>2</sub>O<sub>3</sub> particle reinforced 2024 aluminium alloy composites, *Journal of Materials Processing Technology* 161 (2005) 381-387
- [4] A. Gökçe, F. Findik, Mechanical and physical properties of sintered aluminium powders, *Journal of Achievements in Materials and Manufacturing Engineering*, Vol:30, Issue-2, 2008, p157-164
- [5] J. B. Fogagnolo, M. H. Robert, E. M. Ruiz-Navas, "6061 Al Reinforced with Zirconium Diboride Particles Processed by Conventional Powder Metallurgy and Mechanical Alloying", *Journal of Materials Science* Vol-39 2004 p127 - 132
- [6] K.T. Kim, S.C. Lee, H.S. Ryu, "Densification behavior of aluminum alloy powder mixed with zirconia powder inclusion under cold compaction", *Materials Science and Engineering* Vol-A340, 2003, p41- 48
- [7] Hossein Abdizadeh, Mohammad Amin Baghchesara, "Investigation on mechanical properties and fracture behavior of A356 aluminum alloy based ZrO<sub>2</sub> particle reinforced metal-matrix composites" *Ceramic International*, Vol-39, 2013, p2045-2050
- [8] Joaõ B. Fogagnolo, Elisa M. Ruiz-Navas, Maria H. Robert, Jose M. Torralba, "The effects of mechanical alloying on the compressibility of aluminium matrix composite powder" *Material Science and Engineering*, A355, 2003, p50-55
- [9] V. Amigo, J.L. Ortiz, M.D. Salvador, "Microstructure and mechanical behaviour of 6061 Al reinforced with Silicon Nitride Particles, processed by Powder Metallurgy", *Scripta mater*, Vol-42, 2000, p383-388
- [10] S. K. M. Pathak, S. Das, S. K. Das and P. Ramachandrarao, "Sintering studies on ultrafine ZrB<sub>2</sub> powder produced by a self-propagating high-temperature synthesis process", *Journal of Materials Research*, Vol-15, 2000, p2499-2504.
- [11] F. Monteverde, S. Guicciardi, A. Bellosi, "Advances in microstructure and mechanical properties of ZrB<sub>2</sub> based ceramics", *Material Science and Engineering*, A 346/1-2, 2003, p310-319
- [12] N. Showaiter, M. Youseffi, "Compaction, sintering and mechanical properties of elemental 6061 Al powder with and without sintering aids", *Materials and Design* Vol-29, 2008, p752-762
- [13] S.C. Sharma, B.M. Girish, D.R. Somashekar, Rathnakar Kamath, B.M. Satish, "Mechanical properties and fractography of zircon-particle-reinforced ZA-27 alloy composite materials", *Composites Science and Technology*, Vol-59, 1999, p1805-1812
- [14] K. S. Chan, "Fracture Mechanisms and Properties of Metal-Matrix Composites", *Key Engineering Materials*, Vols, 104-107, 1995, p791-798

# RAPID PROTOTYPING OF BRONZE POWDERS USING FIBER LASER

M. J. Rathod, Sumitkumar S. Bind, Tuhid M. Shaikh

Department of Metallurgy and Materials Science, College of Engineering, Pune, India

**Abstract:** Selective laser sintering of metal powder produces complex three-dimensional parts directly by providing two-dimensional data using computer-aided design. In this work, Laser sintering of tin-bronze metal powder was done by using 400W pulsed fiber laser. The objective of the experiment was to investigate the effect of power density and interaction time on the microstructural changes, mechanical properties and surface roughness of the sintered specimen. Seven mixtures of tin-bronze powders with varying average particle size ( $D_{50}$ ) from 22 to 29  $\mu\text{m}$  were laser-sintered. Laser sintering setup consisted of fiber laser source, CNC table and chiller. Laser source was a fiber laser with maximum power 400W. For laser-sintering, laser power density was varied from 455 to 1365  $\text{W}/\text{mm}^2$  and interaction time was varied from 14 to 56 ms. The parameters that did not vary were - powder layer thickness ( $w$ ), scan line spacing ( $h$ ). Pulsed laser beam was used with constant frequency, pulse width, duty cycle and beam diameter.

**Keywords:** Rapid Prototyping, Selective laser sintering

## 1. Introduction

There are number of manufacturing processes used in industries such as casting, cold and hot mechanical working, and powder metallurgical route. Powder metallurgical route requires tooling for powder compaction and sintering furnace with controlled atmosphere for achieving metallic bonding. Hence, its production rate is slow. To reduce the time of manufacturing, rapid prototyping of metallic powder is coming up in industries. The advantages of using rapid prototyping of metallic powder are - tooling cost is reduced as no dies are required, faster production rate as compaction and sintering do not need extra time, also design correction can be made in software directly giving high flexibility [1-5].

Laser sintering is one of the rapid prototyping techniques that uses high power laser beam as heat source to sinter virtually all types materials - polymers, metallic alloys, ceramic/glass powders and their hybrids. It involves layer-by-layer deposition to produce the desired

three-dimensional shape. Laser beam follows the predefined path given by CAD data in a predefined space and fuses the powder particles in a layer by scanning the surface of a powder bed [1]. After each layer is scanned, the powder bed is lowered by one layer thickness and a new layer of powder material is spread on the top. This sequence is repeated to generate the designed three-dimensional component. Limitations of laser sintering are - relatively costly laser beam source combined with CNC system and porous structure due to absence of powder compaction. The process is generally useful for small batch of components. The parameters that decide the product quality are grouped as laser parameters, material parameters and process parameters [2]. Laser parameters are energy density or power density, wavelength, plasma and thermal effects. Material parameters involve particle size distribution, particle shape and thermal properties like thermal expansion, thermal conductivity. Process parameters are interaction time, scan spacing, scan length, layer thickness and travel speed.

## RAPID PROTOTYPING OF BRONZE POWDERS USING FIBER LASER

For this study, experimental setup has been designed and developed for laser sintering with 400 W Fiber laser to produce complex 3D objects from powder mixtures of tin-bronze. The particle size distribution ( $S_w$ ) was varied to investigate the effect of power density ( $P_d$ ) and interaction time ( $t$ ) on surface roughness, sintered density, secondary dendritic arm spacing (SDAS) and mechanical properties such hardness and tensile strength.

### 2. Experimental Procedure

Laser machine used was fiber laser with maximum power 400 W. Due to interaction of laser beam energy with powder bed there is formation of plasma 'plume' above the laser-irradiated spot. This plasma affects in two ways – absorption of laser power reducing the heat source efficiency and there is excessive heat generation in plasma leading to oxidation of metal powder. Therefore, to remove the plasma during laser sintering, it was decided to provide a continuous inert gas flow across the laser beam with a protective inert gas chamber as shown in Fig. 1. Argon gas was used in this work to protect powder from oxidation and removal of plasma. Flow rate of argon gas was 30 liter/min.

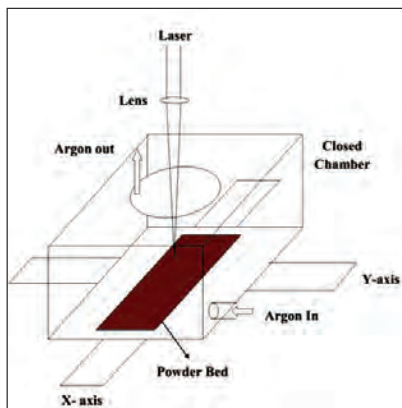


Fig. 1. Schematic of Inert gas chamber fabricated for laser sintering

Powder mixtures were made by mixing commercially available powders to achieve their statistical average particle size ( $D_{50}$ ) and size distribution ( $S_w$ ) as shown in Table 1. The seven powder mixtures were predominantly consisting of finer particles than  $37\ \mu\text{m}$  and coarser particles in the range of  $53\text{--}66\ \mu\text{m}$ , making them as double peak mixtures. To keep clarity of data, the trends have been shown in this work are for the three representative powder mixtures with average particle size ( $D_{50}$ ) 22, 25 and  $29\ \mu\text{m}$ .

Table.1 Bronze powder mixtures used for laser sintering with particle size distribution ( $S_w$ ) and average particle sizes ( $D_{50}$ )

Powder Mixture No.	Particle size distribution ( $S_w$ )	Av. Particle size ( $D_{50}$ )
I	1.316	22
II	1.335	23
III	1.354	24
IV	1.373	25
V	1.37	27
VI	1.368	28
VII	1.357	29

Power density ( $P_d$ ) of the laser beam is laser power ( $P_l$ ) per unit area of laser beam on the surface of powder bed. Beam:material interaction time ( $t$ ) depends on scanning speed ( $V_s$ ) and laser beam diameter ( $d$ ). In laser sintering experiments, beam diameter ( $d$ ) was kept constant at  $0.28\ \text{mm}$ . Therefore, by varying laser power ( $P_l$ ) the power density ( $P_d$ ) of laser beam was changed as 455, 910 and  $1365\ \text{W}/\text{mm}^2$ . The interaction times ( $t$ ) were changed as 14, 28 and 56 ms by varying scanning speeds ( $V_s$ ).

Laser-sintered ring shaped specimens were used for hardness measurement, microstructure observation, determination of SDAS and surface roughness ( $R_a$ ) values. Tensile test was performed on the rectangular bar specimens.

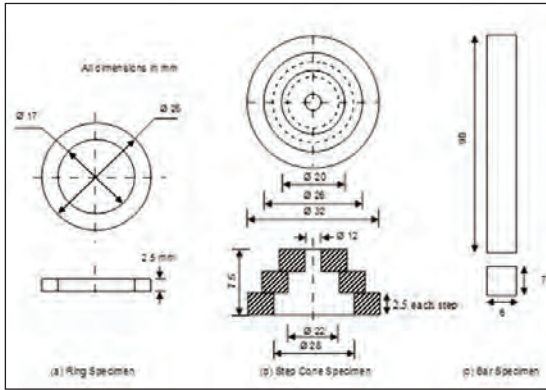


Fig. 2. Geometries of specimens fabricated by laser sintering

### 3. Result and Discussion

#### 3.1 Surface Roughness

As shown in Fig. 3, surface roughness for all powder mixtures increases from 19.69 to 29.5  $\mu\text{m}$  with the increase in both interaction time as well as power density. With longer interaction time and increased power density, heat input to the powder bed increases. This causes formation of coarser particles and splashing of the liquid metal droplets and hence the surface roughness increases. Surface roughness is also deteriorating due to melting of more particles and increase in the width of the irradiated line since total energy added is increased. Some of the lines were found to be broken due to surface tension further affecting the surface roughness. In contrast, when scanning speed is increased ( $V_s$ ), the beam:material interaction time ( $t$ ) decreases. Hence, small agglomerates are formed with minimum surface tension giving low surface roughness value resulting in better surface quality [2].

#### 3.2 Sintered Density

When laser sintering of powder mixture with finer particle size ( $D_{50}$ ) of 22  $\mu\text{m}$  was performed with high energy per unit length ( $P/V$  ratio) of

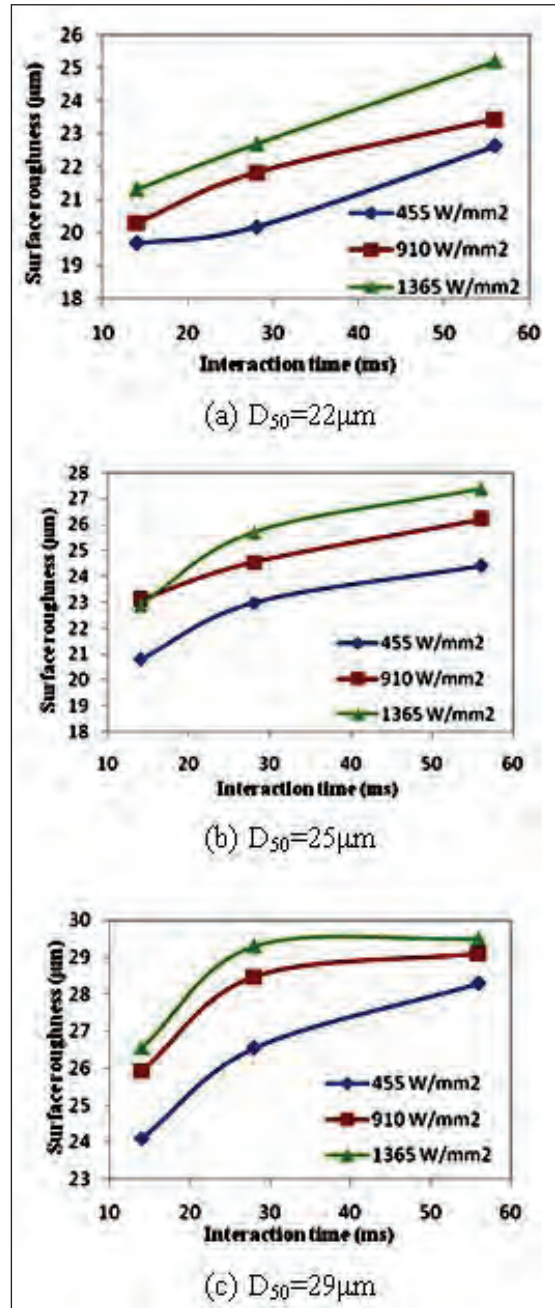


Fig. 3. Effect of power density and interaction time on average particle size (a)  $D_{50}=22\mu\text{m}$  (b)  $D_{50}=25\mu\text{m}$  and (c)  $D_{50}=29\mu\text{m}$

16.8 J/mm, the resultant sintered density was 87.2% (Fig.4). For the same energy per unit length on the coarser powder mixture of  $D_{50}$  of 29  $\mu\text{m}$ , the sintered density reduced to 75.23%. Same trend is observed for reduced energy per unit length (5.6 and 11.2 J/mm) with each powder mixture. For all powder mixtures, the reduction in energy per unit length resulted in decreased sintered density. When the amount of coarser particles is large ( $D_{50}$  of 29  $\mu\text{m}$ ), the number of contact points is reduced between neighboring particles effectively decreasing the thermal conductivity. Therefore, poor heat transfer from particle to particle results in incomplete melting increasing the porous structure [3].

The effect of power density and interaction time (t) on the sintered density of powder mixtures of varying average particle size ( $D_{50}$ ) is shown

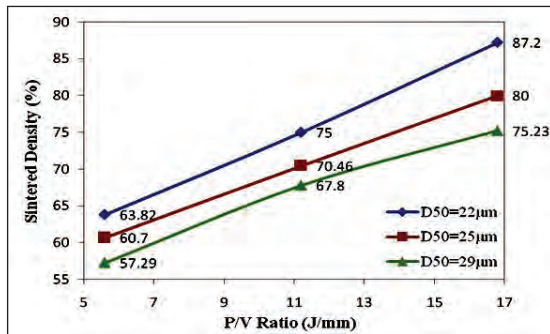


Fig. 4. Effect of energy per unit length (P/V Ratio) on sintered density (%) of laser sintered bronze powder mixtures with Interaction time of 56 ms.

in Fig.5. It can be noted that for all the powder mixtures, increase in power density and longer interaction times result in increased sintered density values. For the finest powder mixture of  $D_{50}$  22  $\mu\text{m}$ , the highest sintered density of 87.2% was achieved when power density 1365 W/mm<sup>2</sup> and interaction time of 56 ms were used. This condition shows increased energy input per unit length to the powder bed and hence results in complete melting of the powder particles

causing improvement in sintered density. Whereas for same powder mixture of  $D_{50}$  22  $\mu\text{m}$ , when low power density 455 W/mm<sup>2</sup> of laser beam was used without changing the interaction

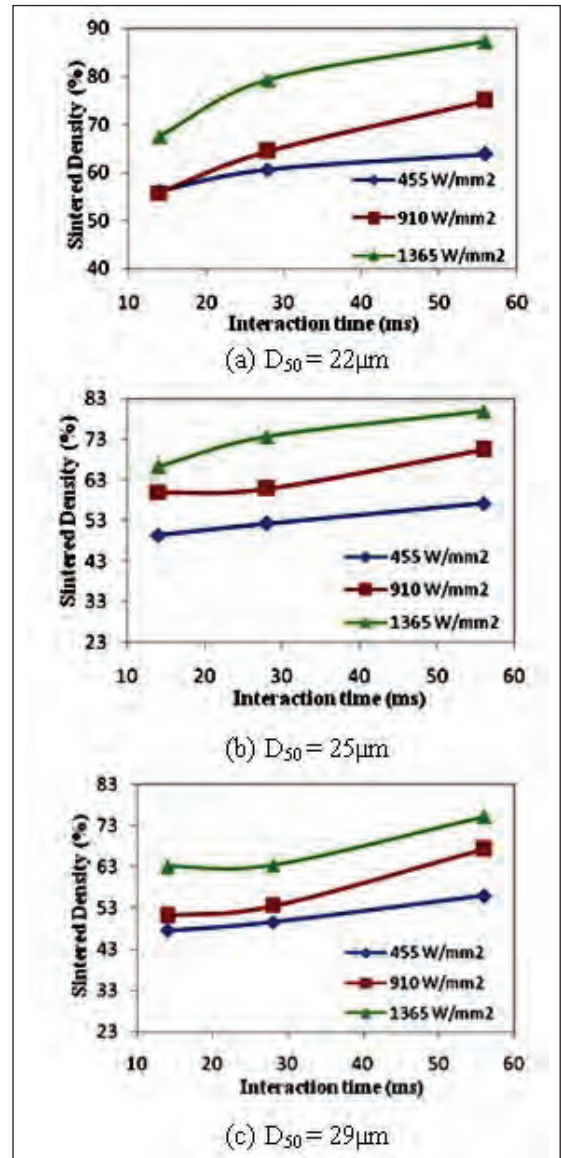


Fig. 5. Effect of Power density and Interaction time on sintered density with average particle size of (a)  $D_{50} = 22\mu\text{m}$  (b)  $D_{50} = 25\mu\text{m}$  and (c)  $D_{50} = 29\mu\text{m}$ .

time, the sintered density reduced to 63.82%. The coarser powder mixtures resulted in lower sintered density than those with finer particle size; this can be attributed to the reduced thermal conductivity in coarser powders and complete melting of fine powders due to their increased surface energy [4]. As the scanning speed increases, the interaction time of laser beam with powder surface decreases. This results in reduced energy input resulting in incomplete melting of the powder bed increasing the porosity.

### 3.2 Hardness

High power density, slow scan speed, that is, short time for beam:material interaction means large amount of energy to the powder bed. This causes increase in volume of molten powder giving high density of the sintered specimen and reduced porosity. This also causes good sintering between top layer and the layers beneath it [5]. Therefore, high hardness values are obvious when melting is near to complete due to increased energy in the powder bed (Fig.6). The specimen resulted in maximum sintered density (87.2%) was the hardest of all (96.3 HRH). Whereas low hardness of 93 HRH was noted for the condition of the lowest power density (455 W/mm<sup>2</sup>) and shortest interaction time (14 ms) having sintered density of 56.1%.

### 3.3 Tensile strength

The trend for tensile strength was similar to that of hardness for all the conditions of laser beam and powder particle size. With low laser power density of 455 W/mm<sup>2</sup> and short interaction time of 14 ms, all the powder mixtures resulted in poor tensile strength values between 1.11 to 1.16 MPa. Sintering conditions of high power density 1365 W/mm<sup>2</sup> and longer interaction time 56 ms produced the specimens with higher tensile strength in the range of 4.68 to 4.86 MPa. The increased density - hence reduced porosity - and tensile strength indicate strong metallic bonding between the neighboring particles [4].

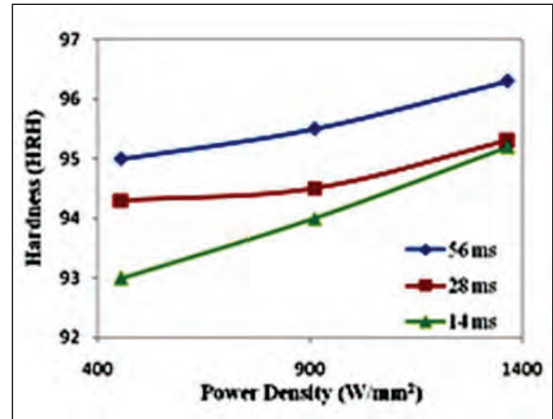


Fig. 6. Effects of Power density and Interaction time on Hardness of sintered specimen with average powder particle size 22 $\mu$ m.

### 3.4 Secondary Dendritic Arm Spacing (SDAS)

The microstructures of laser-sintered specimens typically showed dendrites of varying secondary dendritic arm spacing (Fig.7) as a function of laser energy addition per unit length. When low power density 455 W/mm<sup>2</sup> and short interaction time 14 ms were used to sinter the finest powder mixture of D<sub>50</sub> 22  $\mu$ m, due to rapid cooling fine SDAS dendrites of 3.45  $\mu$ m were formed. Due to fast interaction time and hence fast cooling rate there was no time for growth of the dendrites, which resulted in fine SDAS values. However, for the same powder mixture with high power density 1365 W/mm<sup>2</sup> and longest interaction time 56 ms, the cooling rate is slow to cause coarsening of dendrites with SDAS of 6.0  $\mu$ m. The effect of increasing interaction time on the SDAS of the dendrite solidified is shown in Fig.8 [6]. This mechanism might have been prevalent during the laser sintering of the bronze powders. The effect of product of temperature gradient (G) and growth rate (R) is evident in achieving variation in fineness of SDAS in the laser-sintered specimens of all powder mixtures.

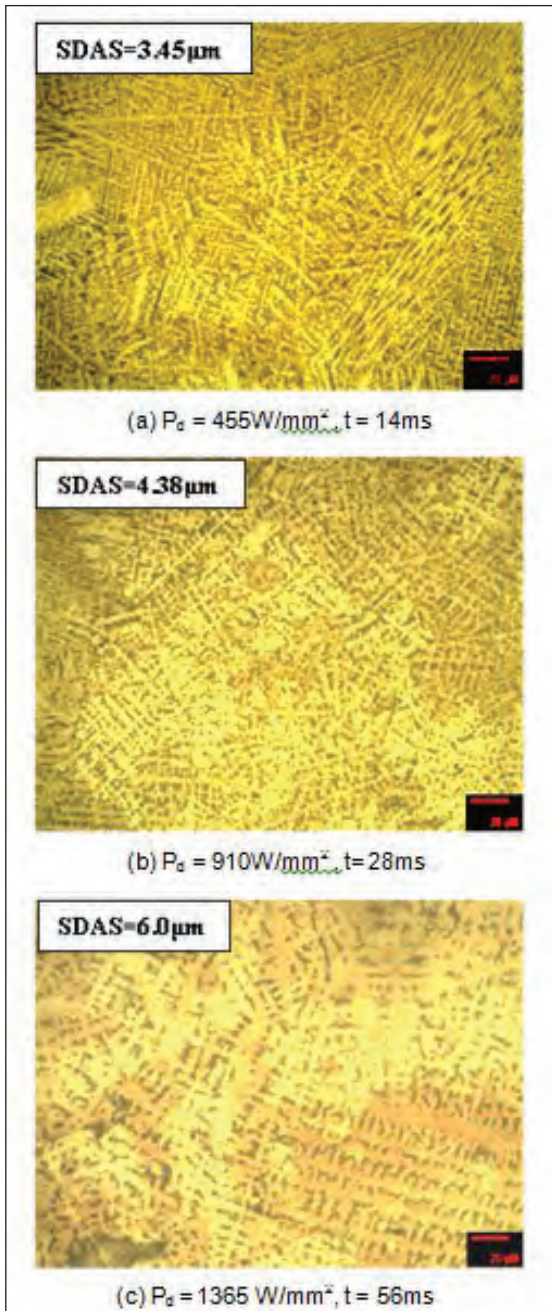


Fig. 7. Variation in SDAS of laser-sintered powder with particle size  $D_{50}=22\mu\text{m}$ .

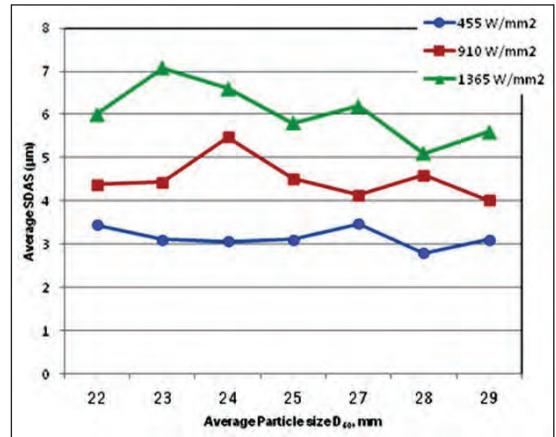


Fig. 8. Effect of powder density of laser beam and particle size of powder on fineness of dendrites SDAS

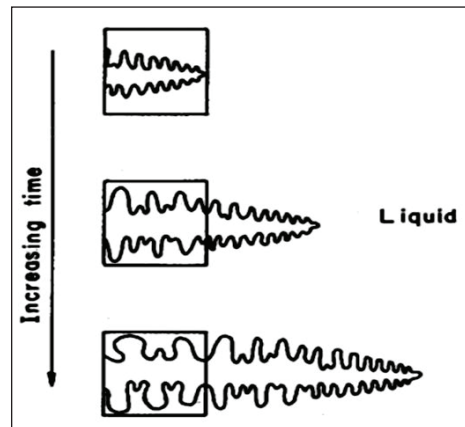


Fig. 9. Schematic showing dendritic growth of an alloy at a fixed position at various stages of solidification. Note that several smaller arms disappear while larger ones grow [6].

#### 4. Conclusion

1. By using pulsed fiber laser, laser sintering was successfully carried out on tin-bronze powders. The difficulty of oxidation due to plasma during sintering with side nozzle was eliminated by providing the closed inert chamber of continuous argon supply.

2. Surface roughness of the laser-sintered bronze specimens was becoming poor, when laser power density and interaction time were on higher side and the powder mixture was coarser. This may be attributed to line widening and formation of coarser molten globules.
3. For all powder mixtures, the reduction in energy per unit length resulted in decreased sintered density. When the amount of coarser particles was large, the number of contact points reduced between neighboring particles. This effectively decreased the thermal conductivity resulting in incomplete melting and increasing the porous structure. Sintered density was increased when energy addition was large giving complete melting of particles.
4. High sintered density conditions resulted in high hardness and tensile strength due to complete melting and strong bonding between the layers being sintered and already sintered.
5. The fineness of dendrites as measured by SDAS value was affected by the power density and interaction time.

### Acknowledgment

Authors are thankful to the grant support from AICTE under the RPS scheme. For their wholehearted support, we also thank Prof. A.D. Sahasrabudhe, Chairman AICTE, Prof. B.B. Ahuja, Director, College of Engineering Pune and Prof. Ms. A.V. Mulay of Department of Production Engineering and Engineering Management, College of Engineering Pune.

### References

- 1) K. Murali, A.N. Chatterjee, P. Saha, R. Palai, S. Kumar, S.K. Roy, P.K. Mishra, A. Roy Choudhury, Direct selective laser sintering of iron-graphite powder mixture, *Journal of Materials Processing Technology*, 136 (2003) 179-185.
- 2) Wilfried Koenig, Experimental Study of the Basic Process Mechanism for Direct Selective Laser Sintering of Low-Melting Metallic Powder, *Manufacturing Technology*, 46 (1997) 127-130.
- 3) Y. Tang, H.T. Loh, Y.S. Wong, J.Y.H. Fuh, L.Lu, X.Wang, Direct laser sintering of a copper-based alloy for creating three-dimensional metal parts, *Journal of Materials Processing Technology*, 140 (2003) 368-372
- 4) A. Simchi, Direct laser sintering of metal powders: Mechanism, kinetics and microstructural features, *Materials Science and Engineering A*, 428 (2006) 148-158.
- 5) A.N. Chatterjee, Sanjay Kumar, P. Saha, P.K. Mishra, A. Roy Choudhury, An experimental design approach to selective laser sintering of low carbon steel, *Journal of Materials Processing Technology*, 136 (2003) 151-157.
- 6) Sindo Kou, *Welding Metallurgy*, Second Edition, Wiley Interscience, 2003, pp 158-166.

# ROOM TEMPERATURE FRACTURE TOUGHNESS OF REFRACTORY FOIL LAMINATED MoSi<sub>2</sub> BASED COMPOSITE

Manoj Kumar Jain<sup>1</sup>, Jiten Das<sup>1</sup>, J. Subrahmanyam<sup>1</sup>, Subrata Ray<sup>2</sup>

<sup>1</sup> Defence Metallurgical Research Laboratory, Hyderabad, India

<sup>2</sup> Indian Institute of Technology, Roorkee, India

**Abstract:** MoSi<sub>2</sub> based materials have gained momentum in recent years for various high temperature structural applications such as Aircraft engine hot-section components, Turbine blades and Vanes etc. For elevated temperature structural applications, it is necessary to improve both, its high temperature strength and creep resistance as well as its room temperature fracture toughness. In the present work, an attempt has been made to understand the role of various ductile refractory metals in toughening of MoSi<sub>2</sub> matrix. Different ductile refractory metals like molybdenum, tantalum and niobium are selected (in foil form) as the reinforcements to carry out a comparative study of their compatibility with MoSi<sub>2</sub> and their effect on its room temperature mechanical behaviour. The composites were prepared by reinforcing the matrix with Ta, Mo, and Nb foils (laminated approach). The MoSi<sub>2</sub> matrix was also modified by 20 vol% SiC<sub>p</sub> (hybrid composites) to obtain tailored microstructures and optimized mechanical properties.

At high processing temperatures, chemical interactions between MoSi<sub>2</sub>-SiC<sub>p</sub> layer and refractory metal foils result in interfacial reaction layers of varying thickness. The Ta foil laminated composite exhibited a minimum reaction zone thickness of only 10 μm suggesting that the Ta has better chemical compatibility with MoSi<sub>2</sub> as compared to Mo and Nb. In Mo, Ta and Nb foil reinforced ((MoSi<sub>2</sub> + 20 vol% SiC<sub>p</sub>) matrix laminated composites tested in crack arrester mode, there is significant improvement in room temperature fracture toughness over that in monolithic MoSi<sub>2</sub>, which could be attributed to the combined effects of crack bridging by ductile metal foils and a high degree of constraint imposed by the brittle MoSi<sub>2</sub>-SiC matrix on the ductile foils. The highest improvement in room temperature fracture toughness is observed in case of Ta foil laminated composite.

**Keywords:** Fracture Toughness, Refractory Foil, MoSi<sub>2</sub> based composite

## Introduction

Ceramic reinforcements have been successfully used to improve the high temperature strength and creep resistance of MoSi<sub>2</sub> [1-11]. However, the various studies on addition of ceramic reinforcements in MoSi<sub>2</sub> matrix revealed that the brittle ceramic reinforcements did not result in significant improvement in room temperature fracture toughness of MoSi<sub>2</sub>. Their effect on improving the room temperature fracture toughness was found to be very marginal. Only moderate room temperature toughening effects have been derived with the addition of brittle ceramic particles and whiskers. Toughening

levels achieved by these reinforcements were similar to those observed in ceramic matrix composites, and are associated with mechanisms such as crack deflection / crack branching.

The room temperature fracture toughness (KIC) of MoSi<sub>2</sub> has been reported to be in the range of 3-4 MPa√m [12-13]. Since a fracture toughness level of 12 to 15 MPa√m is desirable for possible structural applications, other types of reinforcements, e.g., ductile phases have also been explored. However, the literature review revealed that there were very limited studies on the use of ductile reinforcements in MoSi<sub>2</sub> matrix. Most of the work reported till date is

## ROOM TEMPERATURE FRACTURE TOUGHNESS OF REFRACTORY FOIL LAMINATED MoSi<sub>2</sub> BASED COMPOSITE

only on the use of Nb as a ductile reinforcement in MoSi<sub>2</sub> [14]. The other candidate ductile reinforcements could be refractory metals like Ta, Mo and W. However, the data available in the literature on the use of ductile reinforcements other than Nb in MoSi<sub>2</sub> was scanty. The success achieved in improving the room temperature fracture toughness of MoSi<sub>2</sub> by incorporating Nb motivates further studies on understanding the effect of other ductile reinforcements on microstructure and properties of MoSi<sub>2</sub>.

In the present work, an attempt has been made to understand the role of various ductile refractory metals in toughening of MoSi<sub>2</sub> matrix. Different ductile refractory metals like molybdenum, tantalum and niobium are selected (in foil form) as the reinforcements to carry out a comparative study of their compatibility with MoSi<sub>2</sub> and their effect on its room temperature mechanical behaviour. The MoSi<sub>2</sub> matrix was also modified by additions of SiC particles to obtain the synergistic effects with ductile reinforcements as well as to improve the thermal compatibility between MoSi<sub>2</sub> and the various ductile phases.

### Experimental

To improve thermal compatibility between MoSi<sub>2</sub> and the refractory metal foils, it was decided to add 20 vol% of SiC particles in MoSi<sub>2</sub> matrix layer in the development of laminated composites. SiC was chosen as it is not only thermodynamically stable with MoSi<sub>2</sub> but reinforcement of MoSi<sub>2</sub> with SiC<sub>p</sub> also provides improved high temperature mechanical properties in comparison to pure MoSi<sub>2</sub>. The size of SiC phase was kept small, so as to eliminate thermally induced cracking.

Processing of these hybrid composites (with brittle ceramic particles as well as ductile metal foils) is extremely challenging. The component material layers are stacked together in a vacuum

hot press and heated to a high temperature with simultaneous application of pressure to facilitate diffusion bonding between the various layers. Three different refractory metal foils Mo, Ta and Nb were used to make different composites. A single refractory metal foil was sandwiched in between two layers of MoSi<sub>2</sub> + 20 vol% SiC<sub>p</sub> blended powder in an appropriate thickness ratio.

The as-polished specimens were observed under an optical microscope. The X-ray diffraction (XRD) analysis was carried out using the Cu K $\alpha$  ( $\lambda = 15.4056$  nm) radiation to analyse the nature of phases formed during processing in different composites. Qualitative and quantitative chemical information about the material can be obtained by the analysis of energy / wave length and intensity of the X-ray emission from the material. In the present investigation, CAMEBAX microprobe equipment, controlled by a CAMECA system was used. A Leo 440i scanning electron microscope equipped with secondary and back scattered electron detectors as well as energy dispersive spectrometer (EDS) was used to study the microstructure and fractographs of the specimens.

All the composite materials prepared in the present study were evaluated for their room temperature mechanical properties including flexural strength and fracture toughness. The flexural strength and fracture toughness were measured in crack arrester as well as in crack divider modes. Apart from the stress intensity factor based fracture toughness, energy driven fracture toughness in terms of 'work of fracture' was also evaluated. In the present investigation, room temperature flexural strength of various monolithic and composite materials were evaluated by a three-point bend test using equation: 
$$S = \frac{3}{2} \frac{PL}{bd^2}$$
 Where,  $P$  is the peak

## ROOM TEMPERATURE FRACTURE TOUGHNESS OF REFRACTORY FOIL LAMINATED MoSi<sub>2</sub> BASED COMPOSITE

or breaking load.  $P$  is the load at which fracture occurs. Fracture was identified by the breakage of the test bar into two or more pieces or the load drop by at least 20 % from the maximum load without the sample clearly separating.

The fracture toughness of the composites was also evaluated by single edge notched beam (SENB) test method using a three-point bend test specimen of the following dimensions: span ( $S$ ) = 40 mm, width ( $W$ ) = 5 mm and thickness ( $B$ ) = 5 mm. The minimum length of the specimen was kept as 45 mm. The toughness was measured in crack arrester as well as crack divider modes.

The fracture toughness,  $K_{Ic}$  is given by:

$$K_{Ic} = \frac{P_{max}}{BW^{\frac{3}{2}}} \frac{S}{W} f(\alpha) = \frac{P_{max}}{BW^{\frac{3}{2}}} Y(\alpha)$$

$$Y(\alpha) = \frac{S}{W} f(\alpha)$$

where

$$f(\alpha) = \frac{3(\pi\alpha)^{\frac{1}{2}}}{2} (1.107 - 1.552\alpha + 7.71\alpha^2 - 13.55\alpha^3 + 14.25\alpha^4)$$

Various processes for toughening brittle ceramics resulted in extremely complex fracture processes and mechanisms. As a consequence, differences in the conventional fracture mechanics test methods (stress intensity factor based) might yield significant differences in the experimentally determined fracture toughness values,  $K_{Ic}$ . The work of fracture of the composite

was determined using

$$\gamma_{WOF} = \frac{W_{WOF}}{2S}$$

Where,  $W_{WOF}$  is the total work done on the test specimen to break it into two pieces and  $2S$  is the resultant total fracture surface area [15, 16]. In the present investigation, the work of fracture of the composites was calculated from the area measured under the load-displacement curves.

### Results and discussion

MoSi<sub>2</sub> has a higher coefficient of thermal

expansion than most of the refractory metals. In laminated composites, large thermal expansion mismatch between the layers of pure MoSi<sub>2</sub> and refractory metal foils may give rise to residual thermal stresses in the composites during cooling from processing temperature to the room temperature. To improve the thermal compatibility between MoSi<sub>2</sub> and the refractory metal foils, 20 vol% SiC particles (SiC<sub>p</sub>) were added in MoSi<sub>2</sub> matrix.

### Microstructure

The microstructures of MoSi<sub>2</sub> + 20 vol% SiC<sub>p</sub> monolithic material taken under ordinary light are shown in Fig. 1. The microstructures reveal that SiC particles were uniformly distributed in MoSi<sub>2</sub> matrix. A uniform distribution of SiC particles results in better mechanical properties in the composite. The microstructures also reveal the presence of small and rounded particles distributed randomly throughout the matrix. These were identified as SiO<sub>2</sub> particles by EPMA studies. The average grain size of MoSi<sub>2</sub> was found to be in the range of 5 – 8 μm as measured from the optical micrographs taken with polarized light (not shown here).

The microstructures of (MoSi<sub>2</sub> + 20 vol% SiC<sub>p</sub>) + Mo foil laminated composite using polarized light, SEM and EPMA are shown in Fig. 2. Figure 2a exhibits the interfacial reaction zone between MoSi<sub>2</sub> based matrix and Mo. SiC particles are uniformly distributed in MoSi<sub>2</sub> matrix. Fig. 2a reveals the MoSi<sub>2</sub> grains with a grain size in the range of 5 – 8 μm. The interfacial reaction layer is indicated by the arrow marks. SiO<sub>2</sub> particles are also present distributed throughout the microstructure (Fig. 2c).

**ROOM TEMPERATURE FRACTURE TOUGHNESS OF REFRACTORY FOIL LAMINATED  
MoSi<sub>2</sub> BASED COMPOSITE**

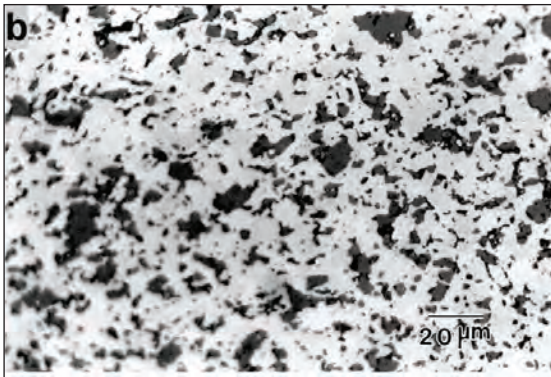


**Fig. 1.** Microstructures of MoSi<sub>2</sub> reinforced with 20 vol% SiC particles.

The EDS analysis identifies the presence of Mo<sub>5</sub>Si<sub>3</sub> and Mo<sub>2</sub>C phases in the interfacial reaction layer (Fig 2b). The formation of Mo<sub>2</sub>C phase in the reaction zone was probably due to the reaction between SiC and pure Mo. The thickness of the interfacial reaction layer was measured to be approximately 50 μm. The x-ray diffraction pattern of (MoSi<sub>2</sub> + 20 vol% SiC<sub>p</sub>) + Mo foil laminated composite (not shown here), reveals the peaks of MoSi<sub>2</sub>, SiC and pure Mo. X-ray diffraction data suggests that the interfacial reaction layer consisted of mainly Mo<sub>5</sub>Si<sub>3</sub> phase. Si diffused from MoSi<sub>2</sub> and reacted with pure Mo to form Mo<sub>5</sub>Si<sub>3</sub> at the interface.

Fig. 2c shows an SEM back scattered electron image of (MoSi<sub>2</sub> + 20 vol% SiC<sub>p</sub>) + Mo foil laminated composite along with EDS analysis revealing the SiC, SiO<sub>2</sub> and Mo<sub>5</sub>Si<sub>3</sub> phases inside the MoSi<sub>2</sub> matrix layer. The chemical composition obtained by EDS analysis has confirmed the SiC, SiO<sub>2</sub> and Mo<sub>5</sub>Si<sub>3</sub> phases marked as C, D and E, in the SEM micrograph, respectively. SiC particles were irregular in shape while most of the SiO<sub>2</sub> particles were globular. The BSE image along with the EDS analysis reveals that the Mo<sub>5</sub>Si<sub>3</sub> phase, which forms mainly at the interface in the form of a continuous layer, is also present as

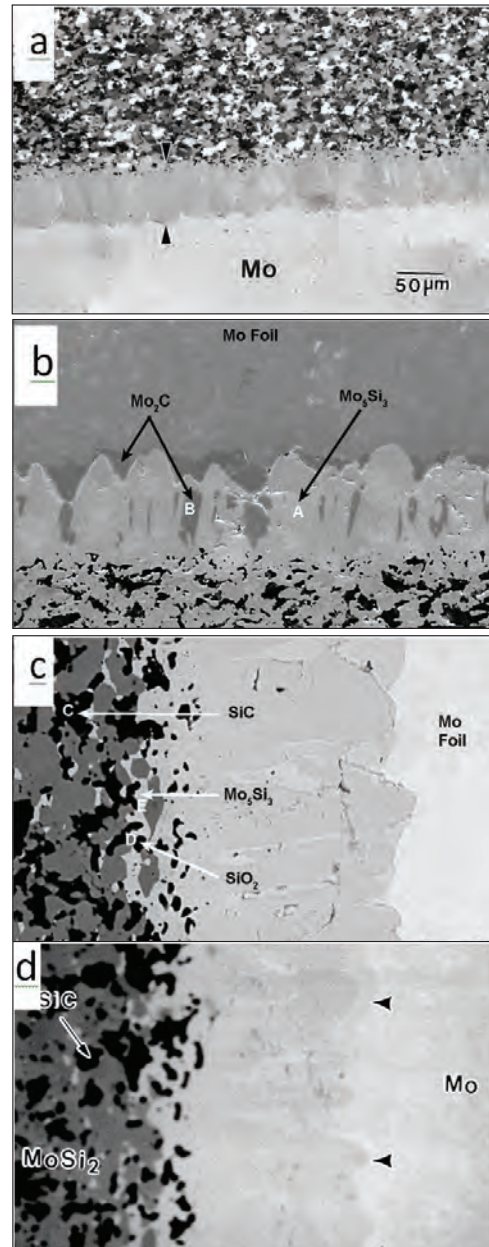


**Fig. 2.** (a) Polarized light optical microstructures (b-c) SEM back scattered electron image and (d) EMPA back scattered electron image of (MoSi<sub>2</sub> + 20 vol% SiC<sub>p</sub>) + Mo foil laminated composite showing interfacial reaction zone at different magnifications.

## ROOM TEMPERATURE FRACTURE TOUGHNESS OF REFRACTORY FOIL LAMINATED MoSi<sub>2</sub> BASED COMPOSITE

discrete particles along with SiC particles within the MoSi<sub>2</sub> matrix. In addition to SiO<sub>2</sub>, commercial MoSi<sub>2</sub> powders are likely to contain some Mo<sub>5</sub>Si<sub>3</sub> also. SiO<sub>2</sub> forms due to the oxidation of the surfaces of MoSi<sub>2</sub> particles during exposure to air or storage. The formation of significant quantity of SiO<sub>2</sub> leads to depletion of Si in MoSi<sub>2</sub>, shifting the composition towards the Mo rich side of the Mo - Si binary phase diagram. This possibly leads to the formation of Mo<sub>5</sub>Si<sub>3</sub>. The EPMA images of (MoSi<sub>2</sub> + 20 vol% SiC<sub>p</sub>) + Mo foil laminated composite are shown in Fig. 2d.

The microstructures of (MoSi<sub>2</sub> + 20 vol% SiC<sub>p</sub>) + Ta foil laminated composite using polarized light, SEM and EPMA are shown in Fig. 3. The microstructure reveals a uniform distribution of SiC particles and SiO<sub>2</sub> particles distributed as usual. The MoSi<sub>2</sub> grain size, which was found to be in the range of 5 – 8 μm (Fig. 3 a). The interfacial reaction layer is indicated by the arrow marks. The x-ray diffraction pattern of (MoSi<sub>2</sub> + 20 vol% SiC<sub>p</sub>) + Ta foil laminated composite is (not shown here) exhibits the peaks of MoSi<sub>2</sub>, SiC and pure Ta. A few peaks of Ta<sub>5</sub>Si<sub>3</sub> and Ta<sub>2</sub>Si are also detected but most of the Ta<sub>5</sub>Si<sub>3</sub> and Ta<sub>2</sub>Si peaks were either too small or overlapped with the peaks of the other phases. The x-ray diffraction data suggested that the reaction products formed at the interface are Ta<sub>5</sub>Si<sub>3</sub> and Ta<sub>2</sub>Si due to Si diffusion across the interface.

The thickness of the interfacial reaction layer in (MoSi<sub>2</sub> + 20 vol% SiC<sub>p</sub>) + Ta foil laminated composite was found to be approximately 10 μm which is much smaller than the thickness of the reaction layer in (MoSi<sub>2</sub> + 20 vol% SiC<sub>p</sub>) + Mo foil laminated composite. This suggests that the diffusivity of Si in Ta and Ta<sub>5</sub>Si<sub>3</sub> layers is smaller than the diffusivity of Si in Mo and Mo<sub>5</sub>Si<sub>3</sub> layers.

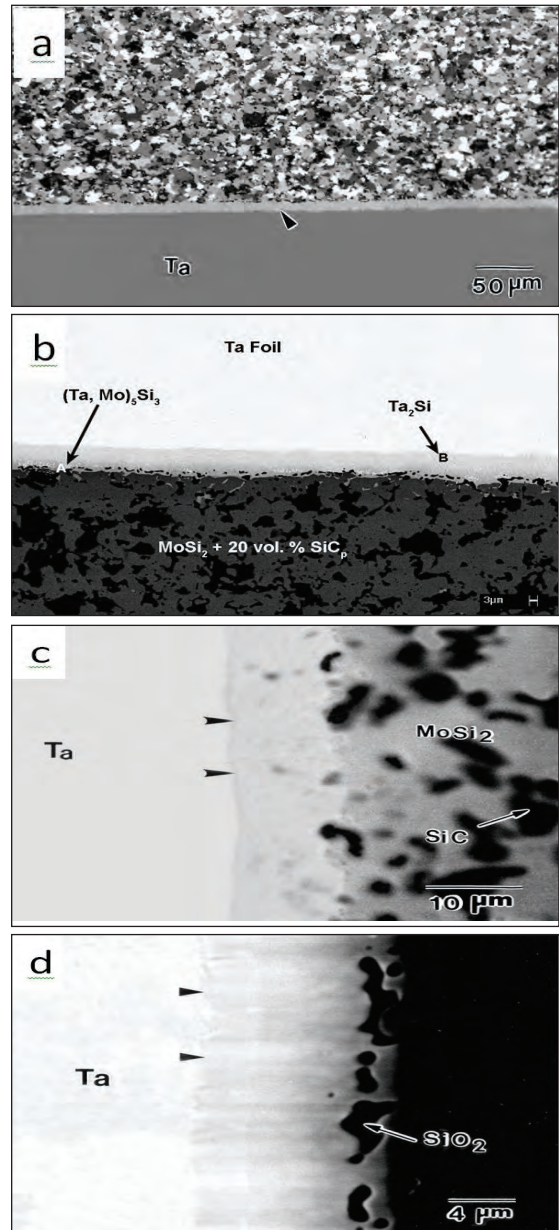


*Fig. 3. (a) Polarized light optical microstructures, (b) SEM back scattered electron image and (c-d) EMPA back scattered electron image of (MoSi<sub>2</sub> + 20 vol% SiC<sub>p</sub>) + Ta foil laminated composite showing interfacial reaction zone at different magnifications.*

## ROOM TEMPERATURE FRACTURE TOUGHNESS OF REFRACTORY FOIL LAMINATED MoSi<sub>2</sub> BASED COMPOSITE

EDS analysis revealed the presence of Ta<sub>5</sub>Si<sub>3</sub> and Ta<sub>2</sub>Si phases at the locations marked as A and B in Fig. 3 b. The back scattered electron image could not resolve Ta<sub>5</sub>Si<sub>3</sub> and Ta<sub>2</sub>Si phases clearly owing to their similar average atomic numbers as described earlier. Apart from Si diffusion from MoSi<sub>2</sub>, some Mo and Ta have also diffused across the interface. Mo dissolved in newly formed Ta<sub>5</sub>Si<sub>3</sub> phase forming (Ta, Mo)<sub>5</sub>Si<sub>3</sub> while Ta dissolved in Mo<sub>5</sub>Si<sub>3</sub> phase formed as a result of Si depletion within MoSi<sub>2</sub> region. The EPMA back scattered electron image of (MoSi<sub>2</sub> + 20 vol% SiC<sub>p</sub>) + Ta foil laminated composite are shown in Fig. 3c. The x-ray mapping and the line scan of Si could not clearly resolve Ta<sub>5</sub>Si<sub>3</sub> and Ta<sub>2</sub>Si phases separately. The interfacial reaction layer grows on both sides i.e., towards the Ta foil as well as towards MoSi<sub>2</sub> layer. This is evidenced by the presence of SiO<sub>2</sub> particles within the reaction zone adjacent to the MoSi<sub>2</sub> layer as depicted in Fig. 3d.

The microstructures of (MoSi<sub>2</sub> + 20 vol% SiC<sub>p</sub>) + Nb foil laminated composite using polarized light, SEM and EPMA are shown in Fig. 4. The optical as well as SEM microstructures exhibit more or less a uniform distribution of SiC particles. The average grain size of MoSi<sub>2</sub> was measured from the microstructure observed under polarized light and was found to be ~ 6μm. The optical microstructures reveal the presence of an interfacial reaction layer between MoSi<sub>2</sub> based matrix and Nb foil reinforcement as indicated by the arrow marks in Fig. 4a. The reaction zone is more clearly visible in back scattered electron image (Fig. 4b), the thickness of which was measured to be approximately 20μm. The main reaction product between MoSi<sub>2</sub> and Nb is identified as Nb<sub>5</sub>Si<sub>3</sub> by quantitative electron probe micro analysis. The x-ray diffraction data (not shown here) does not reveal any Nb<sub>5</sub>Si<sub>3</sub> peaks although the peaks of

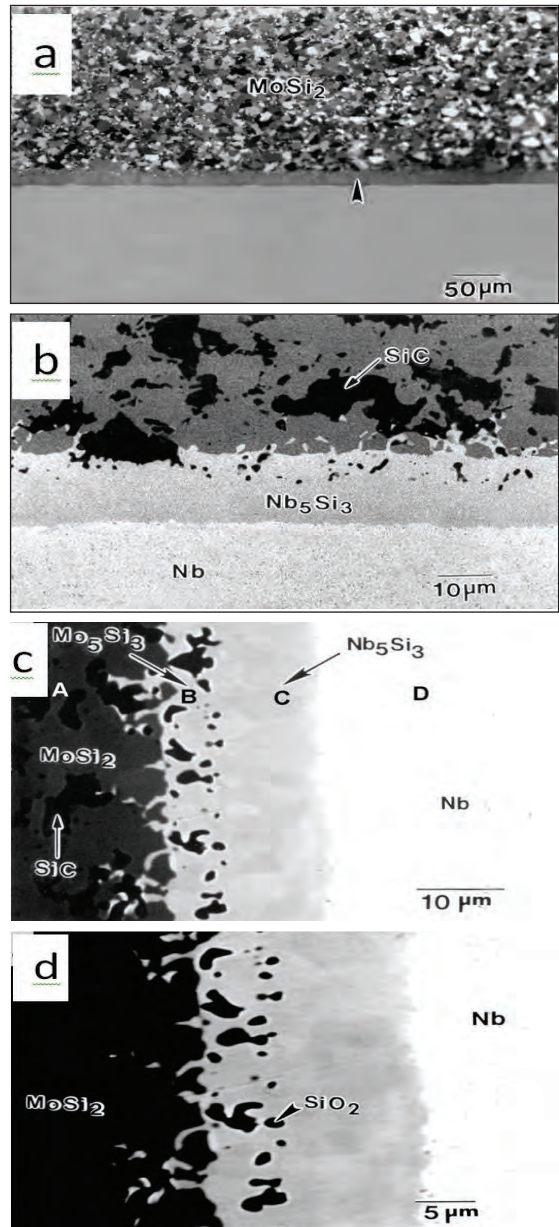


**Fig. 4:** (a) Polarized light optical microstructures, (b) SEM back scattered electron image and (c-d) EMPA back scattered electron image of (MoSi<sub>2</sub> + 20 vol% SiC<sub>p</sub>) + Nb foil laminated composite showing interfacial reaction zone at different magnifications.

## ROOM TEMPERATURE FRACTURE TOUGHNESS OF REFRACTORY FOIL LAMINATED MoSi<sub>2</sub> BASED COMPOSITE

MoSi<sub>2</sub>, SiC and pure Nb are clearly identified. This could be due to only a small amount of Nb<sub>5</sub>Si<sub>3</sub> present in the microstructure, which was not enough to be detected by x-ray diffraction analysis. Fig. 4c is a back scattered electron (BSE) image using EPMA for (MoSi<sub>2</sub> + 20 vol% SiC<sub>p</sub>) + Nb foil composite. The typical microprobe data obtained at locations indicated by A, B, C and D in Fig. 4c correspond to MoSi<sub>2</sub>, Mo<sub>5</sub>Si<sub>3</sub> (with Nb in solid solution), Nb<sub>5</sub>Si<sub>3</sub> (with Mo in solid solution) and pure Nb phases, respectively.

The relatively large and irregular shaped dark particles present in MoSi<sub>2</sub> are of SiC while smaller and rounded dark particles are of SiO<sub>2</sub>. The SiC and SiO<sub>2</sub> particles are present inside the reaction zone close to the MoSi<sub>2</sub>. This suggests that the interfacial reaction layer has grown inside both MoSi<sub>2</sub> based matrix and the Nb foil. The block arrow indicates the probable original interface between MoSi<sub>2</sub> based matrix and the Nb foil prior to any chemical interaction. The reaction layer towards the Nb foil is much thicker than that towards the matrix. The line scans of Mo and Nb of Figs. 4d reveal the SiO<sub>2</sub> particles at the interface.

### Mechanical Properties

The room temperature mechanical properties of MoSi<sub>2</sub> + 20 vol% SiC<sub>p</sub> monolithic, (MoSi<sub>2</sub> + 20 vol% SiC<sub>p</sub>) + Mo foil, (MoSi<sub>2</sub> + 20 vol% SiC<sub>p</sub>) + Ta foil and (MoSi<sub>2</sub> + 20 vol% SiC<sub>p</sub>) + Nb foil laminated composites are presented in Fig.5. Each data point in Fig. 5 is an average of 4 to 5 tests.

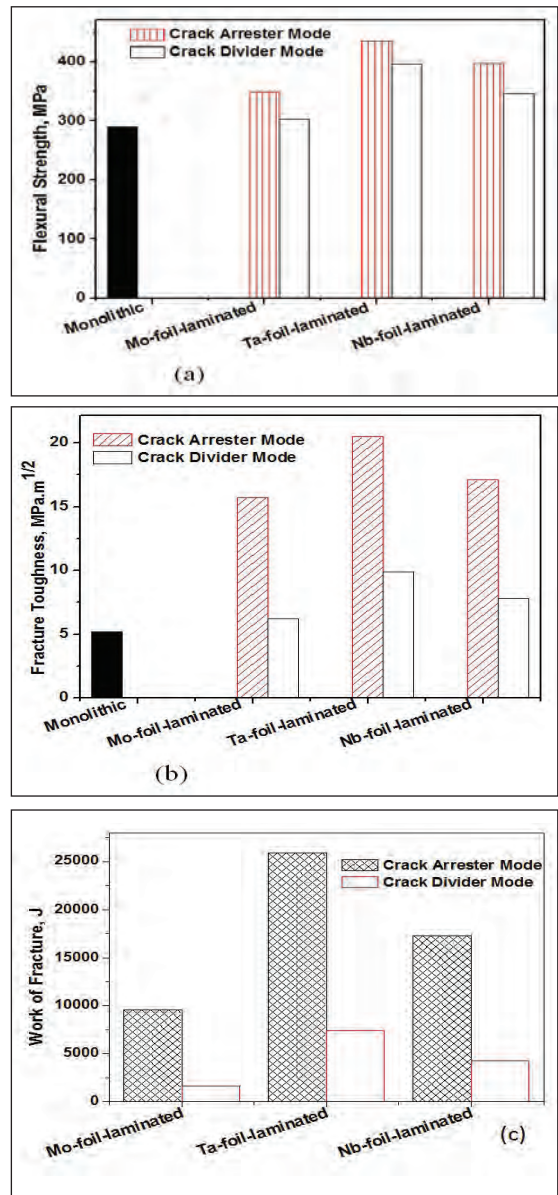


Figure 5: (a) flexural strength, (b) Fracture toughness and (c) Work of fracture of Mo, Ta and Nb reinforced MoSi<sub>2</sub> + 20 vol% SiC<sub>p</sub> matrix composite tested in crack arrester and crack divider mode. The flexural strength and fracture toughness value (solid column) of the MoSi<sub>2</sub> + 20 vol.% SiC<sub>p</sub> matrix is superimposed in (a) and (b) for comparison.

## ROOM TEMPERATURE FRACTURE TOUGHNESS OF REFRACTORY FOIL LAMINATED $\text{MoSi}_2$ BASED COMPOSITE

The room temperature flexural strength of  $\text{MoSi}_2 + 20 \text{ vol\% SiC}_p$  monolithic material was measured as 290 MPa, which was remarkably higher than flexural strength of pure  $\text{MoSi}_2$  as reported by Mitra et al. [17]. The improvement in flexural strength could be attributed to the strengthening effect of SiC reinforcements, as observed in other  $\text{MoSi}_2$  matrix composites reinforced with brittle ceramic particles. In addition, the grain growth in  $\text{MoSi}_2$  is also inhibited by fine SiC particles during high temperature processing. The moderate increase in fracture toughness by addition of SiC particles in  $\text{MoSi}_2$  matrix could be attributed to grain growth inhibition and crack deflection processes by SiC particles.

In case of  $(\text{MoSi}_2 + 20 \text{ vol\% SiC}_p) +$  refractory metal foil laminated composites, the strength and toughness values obtained from three-point bend tests as presented in Fig.5 are for comparative purposes only and should not be treated as absolute values for these properties. The fracture toughness value calculated is called "damage tolerance" and is designated as  $K_{max}$  rather than  $K_{IC}$ , since it is calculated from the peak load. Xiao and Abbaschian [18, 19] have argued that the value calculated from the peak load of a bending test was actually a reflection of the bridging capability of the ductile phases and could be interpreted as an indicator of the damage tolerance of the composite.

There is a very significant improvement in flexural strength as well as fracture toughness of  $(\text{MoSi}_2 + 20 \text{ vol\% SiC}_p) + \text{Mo}$  foil,  $(\text{MoSi}_2 + 20 \text{ vol\% SiC}_p) + \text{Ta}$  foil and  $(\text{MoSi}_2 + 20 \text{ vol\% SiC}_p) + \text{Nb}$  foil laminated composites. In case of Ta foil laminated composite, the increase in flexural strength is 50 % while the toughness improved by almost a factor of four measured in crack arrester mode as compared to the  $\text{MoSi}_2 + 20 \text{ vol\% SiC}_p$  monolithic material. However, lamination with Mo foil results in relatively lower improvement

in flexural strength and fracture toughness of the laminated composite as compared to the lamination with Ta and Nb foils. The flexural strength and fracture toughness values of  $(\text{MoSi}_2 + 20 \text{ vol\% SiC}_p) + \text{Nb}$  foil laminated composite are slightly lower than the values obtained for  $(\text{MoSi}_2 + 20 \text{ vol\% SiC}_p) + \text{Ta}$  foil composite.

The strength and toughness of the laminated composites have been calculated from the peak load obtained in three point bend tests. The strength and toughness of  $(\text{MoSi}_2 + 20 \text{ vol\% SiC}_p) + \text{Mo}$  foil composite is found to be the minimum among all the three  $\text{MoSi}_2\text{-SiC}_p$  matrix laminated composite systems. The peak load obtained in a bending test conducted on a laminated composite specimen is governed by the strength of the refractory metal foil as well as the interfacial bonding. A strong interfacial bond between  $\text{MoSi}_2$  based matrix and the metal foil would result in a higher constraint by the elastic matrix on the metal foil. The load carried by the ductile metal foil is expected to be higher with a high degree of constraint imposed on it. In the case of Mo foil laminated composite, the thermal expansion mismatch between Mo foil and  $\text{MoSi}_2\text{-SiC}_p$  matrix is larger than thermal expansion mismatch between Ta / Nb foils and  $\text{MoSi}_2\text{-SiC}_p$  matrix. This results in a higher residual tensile hoop stress in the matrix near the Mo foil. The residual tensile stresses have been estimated as 201 MPa, 59 MPa and 14 MPa in Mo, Ta and Nb foil laminated composites, respectively. The residual stress cannot only result in weak interfacial bonding but also increases the stress intensity in the composite. Therefore, a reduced peak load ( $P_{max}$ ) in Mo foil laminated composite could be attributed to higher residual stresses in spite of the fact that as received Mo foil has much higher strength than Ta and Nb foils. Contribution of yield strength to fracture toughness was mainly to increase the maximum stress reached by the

## ROOM TEMPERATURE FRACTURE TOUGHNESS OF REFRACTORY FOIL LAMINATED MoSi<sub>2</sub> BASED COMPOSITE

constrained ductile reinforcement. However, in the present case of (MoSi<sub>2</sub> + 20 vol% SiC<sub>p</sub>) + Mo foil laminated composite, the poor interfacial bonding seems to have more pronounced effect on the peak load reached than the strength of the foil.

However, the improvements in fracture toughness of the laminated composites tested in crack divider mode were moderate. Only a limited load transfer from matrix to the foil occurs since the primary crack could propagate continuously within the MoSi<sub>2</sub>-SiC<sub>p</sub> brittle matrix without encountering any obstacle in the form of a ductile metal foil. Only a small segment of the crack front propagates through the ductile foil and resists the unstable crack propagation through the MoSi<sub>2</sub>-SiC<sub>p</sub> layers.

In many of the advanced ceramic matrix composites, linear elastic behavior is violated for common test specimens. Consequently, nonlinear approaches are needed to characterize the material behaviour [20]. The concept of work of fracture has been widely applied to characterize the crack growth resistance for extremely complicated non-linear fracture processes [15-16, 21-22]. At elevated temperatures, the fracture of pure MoSi<sub>2</sub> is also not linear elastic. Therefore, the fracture toughness of MoSi<sub>2</sub> at elevated temperatures is measured as "work of fracture" and not as K<sub>IC</sub>.

A work of fracture value of 25,920 J/m<sup>2</sup> was obtained in case of laminated composite with Ta foil as compared to a value of 9,570 J/m<sup>2</sup> in laminated composite with Mo foil. The lower work of fracture obtained in (MoSi<sub>2</sub> + 20 vol% SiC<sub>p</sub>) + Mo foil laminated composite could be attributed to a much lower ductility of as received Mo foil used in synthesizing the laminated composite. The work of fracture in crack divider mode was lower than the work of fracture measured in crack arrester mode.

Similarly, the work of fracture measured in case of Nb foil laminated composite was lower than the work of fracture obtained in case of Ta foil reinforced laminated composite. The work of fracture in a bending test on a laminated composite specimen is a function of strain hardening coefficient and ductility of the metal foil as well as the degree of interfacial debonding. A higher degree of constraint on Nb foil (due to lower residual thermal stresses) is expected to result in a relatively reduced interfacial debonding allowing less Nb to undergo plastic deformation and necking.

Gac and Petrovic [7] have observed that a flexural strength value of 310 MPa was within an acceptable use regime for structural applications of MoSi<sub>2</sub> based materials. Petrovic and Vasudevan [23] have proposed that industrial applications of MoSi<sub>2</sub> would typically require a K<sub>IC</sub> value of 10 MPa√m while a K<sub>IC</sub> value of 15 MPa√m at room temperature would be acceptable for aerospace applications of MoSi<sub>2</sub>. These proposed target properties have been met or exceeded in the present work by ductile phase toughening of MoSi<sub>2</sub> and designing the MoSi<sub>2</sub> based composites in the laminated form consisting of alternate layers of MoSi<sub>2</sub> based matrix and the ductile refractory metal foils. Addition of SiC particles in MoSi<sub>2</sub> matrix not only results in improved thermal compatibility between MoSi<sub>2</sub> and refractory metal foils but also is expected to impart improved high temperature strength and creep resistance to MoSi<sub>2</sub>.

### Conclusions :

- ✓ Reinforcement of MoSi<sub>2</sub>-SiC<sub>p</sub> matrix with Ta foil resulted in a higher value of fracture toughness than that obtained for MoSi<sub>2</sub>-SiC<sub>p</sub> monolithic material. Ta was also found to be thermodynamically more stable with MoSi<sub>2</sub> than Mo and Nb resulting in a lower thickness of the interfacial reaction zone.

## ROOM TEMPERATURE FRACTURE TOUGHNESS OF REFRACTORY FOIL LAMINATED MoSi<sub>2</sub> BASED COMPOSITE

- ✓ In the crack divider orientation, improvement in fracture toughness of MoSi<sub>2</sub>-SiC<sub>p</sub> matrix reinforced with Ta foil relative to un-laminated system is modest.
- ✓ Further improvements in the toughness in the crack divider orientation are desirable as this is often the key orientation for many structural applications. It is envisaged that a multi-layer laminated composite consisting of several alternate layers of MoSi<sub>2</sub> based matrix and the ductile refractory metal foils would result in acceptable levels of fracture toughness in crack divider mode.

### Acknowledgement

The authors are thankful to Director, DMRL for his encouragement and DRDO for the financial support to carry out this investigation

### References:

1. Petrovic J.J. and Honnell R.E. (1990a), "SiC Reinforced MoSi<sub>2</sub>/WSi<sub>2</sub> Alloy Matrix Composites", Ceramic Engineering and Science Proceedings, Vol. 11, p. 734.
2. Petrovic J.J. and Honnell R.E. (1990b), "Partially Stabilized ZrO<sub>2</sub> Particle - MoSi<sub>2</sub> Matrix Composites", Journal of Materials Science, Vol. 25, pp. 4453-4456.
3. Petrovic J.J. and Honnell R.E. (1991), "SiC Reinforced MoSi<sub>2</sub> Based Matrix Composites", in Ceramic Transactions, Vol. 19, Advanced Composite Materials, Ed. Sacks M.D., American Ceramic Society, Westerville, OH, pp. 817-830.
4. Gibbs W.S., Petrovic J.J. and Honnell R.E. (1987), "SiC Whisker-MoSi<sub>2</sub> Matrix Composites", Ceramic Engineering and Science Proceedings, Vol. 8, pp. 645-648.
5. Bhattacharya A.K. and Petrovic J.J. (1991), "Hardness and Fracture Toughness of SiC Particle Reinforced MoSi<sub>2</sub> Composites", Journal of American Ceramic Society, Vol. 74, pp. 2700-2703.
6. Yang J.M., Kai W. and Jeng S.M. (1989), Scripta Metallurgica, Vol. 23, p. 1953.
7. Gac F.D. and Petrovic J. J. (1985), "Feasibility of a Composite of SiC Whiskers in an MoSi<sub>2</sub> Matrix", Journal of American Ceramic Society, Vol. 68, pp. C200-C201.
8. Hebsur M.G. (1994), "Pest Resistant and Low CTE MoSi<sub>2</sub> Matrix for High Temperature Structural Applications", Proceedings Materials Research Society Symposium, Vol. 350, pp. 177-182.
9. Tuffe S.C., Plucknett K.P. and Wilkinson D.S. (1993), "Processing and Mechanical Properties of Alumina Platelet Reinforced Molybdenum Disilicide Laminates", Ceramic Engineering and Science Proceedings, Vol. 14, pp. 1199-1208.
10. Sadananda K., Jones H., Feng J., Petrovic J.J. and Vasudevan A.K. (1991), "Creep of Monolithic and SiC Whisker Reinforced MoSi<sub>2</sub>", Ceramic Engineering and Science Proceedings, Vol. 12, pp. 1671-1678.
11. Sadananda K., Feng C.R., Jones H.N. and Petrovic J.J. (1993), "Creep of Intermetallic Composites", in Proceedings International Symposium on Structural Intermetallics, Seven Springs, 26-30 September.
12. Xiao L., Kim Y.S. and Abbaschian R. (1990), "Ductile Phase Toughening of MoSi<sub>2</sub> - Chemical Compatibility and Fracture toughness", Intermetallic Matrix Composites, Proceedings Materials Research Society Symposium, Vol. 194, pp. 399-404.
13. Xiao L., Kim Y.S., Abbaschian R. and Hecht R.J. (1991), "Processing and Mechanical Properties of Nb Reinforced MoSi<sub>2</sub> Composites", Materials Science and Engineering, Vol. A144, pp. 277-285.
14. Badrinarayanan K., Mckelvey A.L., Venkateswara Rao K.T. and Ritchie R.O. (1996), "Fracture and Fatigue Crack Growth Behaviour in Ductile Phase Toughened MoSi<sub>2</sub>: Effects of Nb Wire vs. Particulate Reinforcements", Metallurgical and Materials Transactions A, Vol. 27A, pp. 3781-3792.
15. Nakayama J. (1965), "Direct Measurement of Fracture Energies of Brittle Heterogeneous Materials", Journal of American Ceramic Society, Vol. 48, pp. 583-587.
16. Tattersall H.G. and Tappin G. (1966), Journal of Material Science, Vol. 1, p. 296.

## ROOM TEMPERATURE FRACTURE TOUGHNESS OF REFRACTORY FOIL LAMINATED MoSi<sub>2</sub> BASED COMPOSITE

---

17. Mitra R., Prasad N.E., Rao A. Venugopal and Mahajan Y.R. (1997), "Mo and Ti Silicide Based Composites and Alloys", Structural Intermetallics 1997, Eds. Nathal M.V., Darolia R., Liu C.T., Martin P.L., Miracle D.B., Wagner R. and Yamaguchi M., The Minerals, Metals and Materials Society, pp. 959-968.
18. Xiao L. and Abbaschian R. (1992), "Interfacial Modification in Nb / MoSi<sub>2</sub> Composites and its Effects on Fracture Toughness", Materials Science and Engineering, Vol. A155, pp. 135-145.
19. Xiao L. and Abbaschian R. (1992), "Role of Matrix / Reinforcement Interfaces in the Fracture Toughness of Brittle Materials Toughened by Ductile Reinforcements", Metallurgical Transactions A, Vol. 23A, pp. 2863-2872.
20. Evans A.G. (1990), "Perspective on the Development of High Toughness Ceramics", Journal of American Ceramic Society, Vol. 73, pp. 187-206.
21. Sakai M. and Ichikawa H. (1992), "Work-of-Fracture of Brittle Materials with Microcracking and Crack Bridging", International Journal of Fracture, Vol. 55, pp. 65-79.
22. Sakai M. and Bradt R.C. (1993), "Fracture Toughness Testing of Brittle Materials", International Materials Review, Vol. 38, pp. 53-78.
23. Petrovic J.J. and Vasudevan A.K. (1999), "Key Developments in High Temperature Structural Silicides", Materials Science and Engineering, Vol. A261, pp. 1-5.

# NON-LUBRICATING SLIDING WEAR BEHAVIOUR STUDY OF SiC-B<sub>4</sub>C-Si CERMETS FABRICATED BY CONVENTIONAL AND SPARK PLASMA SINTERING TECHNIQUES

P. Sahani, S. K. Karak, D. Chaira

Department of Metallurgical and Materials Engineering, National Institute of Technology, Rourkela, India

**Abstract :** This paper investigates the non-lubricated sliding wear behaviour of SiC-B<sub>4</sub>C-Si cermets against a diamond indenter. SiC-B<sub>4</sub>C-Si cermets containing 2, 5, 10 and 20 wt. % of Si were fabricated by both pressure-less sintering and spark plasma sintering (SPS) techniques to study the density, hardness and wear behaviour. The wear behaviour was studied using sliding wear test at 20, 40, 60 and 80N load for SPS samples, whereas 20 and 40N loads were applied for conventional sintered samples. The wear depth versus sliding distance as a function of loads were recorded and wear tracks were investigated using scanning electron microscopy (SEM). A density value of around 97% with maximum micro-hardness of ~27 GPa was obtained for SiC-B<sub>4</sub>C-Si (10 wt. %) cermet consolidated by SPS process. On the other hand, density of 92% and micro-hardness of 18 GPa were achieved for conventional sintered sample. A general observation from this study is that wear depth increases with increasing load and minimum wear depth is obtained for cermet containing 10 wt. % Si. It has also been found that SiC-B<sub>4</sub>C exhibits maximum wear depth for both cases. Cermet samples sintered by SPS process possess maximum wear resistance than the conventional sintered samples. This is due to the increased density, hardness and decreased porosity ratios for SPS samples. With increase in applied load the impact of wear is severe due to severity in plastic deformation, surface de-lamination, formation of cavities and grooves on the damaged surface.

## 1. Introduction

The components used in aero engines and turbo pumps are operated at high speed which experience higher pressure and temperature. Thus, improved mechanical properties like high strength, hardness, toughness with oxidation and wear resistance are required for the materials [1-3]. It has been found that compared to other carbide materials, boron carbide (B<sub>4</sub>C) and silicon carbide (SiC) possesses excellent high hardness, wear resistance, high melting point, high oxidation resistance, good chemical stability and low density [4-6]. Components made of B<sub>4</sub>C and SiC ceramics have been used extensively in abrasive media for grinding and lapping, polishing media for hard materials, wear resistance components as blast nozzles and wheels dressing tools, valve components and bearings, seal rings, high speed machining

operations, cutting tools at high temperatures, aerospace industry, heat exchangers, heat engine parts, fusion reactors and armour plates etc [7-12]. The mixture of SiC and B<sub>4</sub>C offer a better combination of light weight materials with high hardness, strength and high temperature resistance. Unfortunately, the processing of B<sub>4</sub>C and SiC is very difficult due to their covalent bond, low plasticity and very low fracture toughness (2-4 MPa m<sup>1/2</sup>), limits their application as structural material [13-15]. To improve the fracture toughness and ductility of SiC-B<sub>4</sub>C based cermets; Si has been added separately into SiC-B<sub>4</sub>C cermets. It is proposed that Si acts as a binder and imparts a certain degree of toughness into the ceramic materials without impairing the hardness of the matrix. Si addition in the B<sub>4</sub>C and SiC is very useful in improving the sinterability and properties of sintered products [16]. Boron carbide can act as an alternative source of carbon

# NON-LUBRICATING SLIDING WEAR BEHAVIOUR STUDY OF SiC-B<sub>4</sub>C-Si CERMETS FABRICATED BY CONVENTIONAL AND SPARK PLASMA SINTERING TECHNIQUES

in the presence of Si to form secondary SiC particles and was beneficial for the improvement in properties [16-19]. It was not able to achieve the theoretical density more than 85% for the cermets fabricated by conventional pressureless sintering. But on other hand, all the compositions were successfully sintered by SPS with higher than 98% of the theoretical density [20].

There are relatively very few studies on wear behaviour of SiC-B<sub>4</sub>C-Si cermets fabricated by pressure-less sintering and also by spark plasma sintering (SPS) techniques. We have prepared SiC-B<sub>4</sub>C based cermets with varying amount of Si (2, 5, 10 and 20 wt. %) by using planetary milling and followed by pressure-less sintering at 2223 K. In another set of experiments, sintering was carried out by SPS at 1623 K. The hardness and non-lubricated sliding wear behaviour of the composites under various applied loads have been evaluated in detail. The possible wear mechanisms and morphology of wear debris were also studied.

## 2. Experimental

The elemental powders of SiC, B<sub>4</sub>C, and Si (purity >99%, and an initial average particle size <40 μm) were selected as starting materials. The raw materials were Analar grade with high purity (impurity <1 %). The different amount of Si (2, 5, 10 and 20 wt. %) were added to the base SiC-B<sub>4</sub>C materials. The powders were blended to obtain nominal compositions of 60SiC40B<sub>4</sub>C, 60SiC38B<sub>4</sub>C2Si, 60SiC35B<sub>4</sub>C5Si, 60SiC30B<sub>4</sub>C10Si and 60SiC20B<sub>4</sub>C20Si (in wt. %). These compositions were milled in a Fritsch planetary (P5) mill at a speed of 300 rpm for 10 h with ball to powder weight ratio of 6:1 and milling was carried out under toluene to prevent oxidation. The milled powders were sintered by both conventional sintering at 2223 K for 30 min in argon atmosphere and spark plasma

sintering at 1623 K with a heating rate of 100 K / min and held for 5 min under 50 MPa pressure. The phase evolutions of the milled powder as well as sintered pellets were analyzed by X-ray diffractometer (XRD) using Cu-Kα (λ=1.54059Å) radiation. For structural and morphological analysis, scanning electron microscopy (SEM) was used. Micro-hardness of sintered samples was measured by Vickers microhardness tester. Ball-On-Plate wear tester TR-208-M1 was used to investigate the non-lubricated sliding wear behaviour of sintered samples against a Rockwell diamond indenter. The wear test was carried out with normal loads of 20N, 40N, 60N and 80N. Uni-directional sliding between test samples and indenter take place with a speed of 6.28 mm sec<sup>-1</sup> where sliding distance of 3.77 m was covered in 10 min. Depth of worn surface was measured by stylus surface profilometer (Veeco Dektak 150).

## 3. Results and discussion

### 3.1 Density and micro-hardness study

Density and microhardness were measured for all the conventional and spark plasma sintered samples. Fig. 1 (a) shows the bar diagram of all the compositions versus relative density at different temperatures. For all the compositions, sintered density for SPS samples is higher than conventional sintered samples. Maximum relative density of 94.6% was obtained for SiC-B<sub>4</sub>C-2 wt. % Si composites sintered by SPS at 1623 K. Relative density of 94% was measured for SiC-B<sub>4</sub>C sample without metal addition when SPS was conducted at 1623 K. The relative density was below 90% for all the samples sintered by conventional sintering technique. Conventional sintering uses only heat energy. It has been found that low temperature SPS processed samples exhibit higher density and hardness than conventionally consolidated samples due to simultaneous application of heat

# NON-LUBRICATING SLIDING WEAR BEHAVIOUR STUDY OF SiC-B<sub>4</sub>C-Si CERMETS FABRICATED BY CONVENTIONAL AND SPARK PLASMA SINTERING TECHNIQUES

and pressure. The densities of sintered samples increases with increasing Si up to 10 wt. % and then slightly decreased with the further addition of Si (20 wt. %) for both cases. The highest density was obtained for samples (10 wt. % Si addition) sintered by conventional (92%) as well as SPS (98%).

Fig. 1 (b) shows the bar diagram which represents Vickers's microhardness for all samples at different temperatures. It is to be noted that the hardness of SiC-B<sub>4</sub>C sintered conventionally at 2223 K was 20 GPa. Whereas, the hardness value of SiC-B<sub>4</sub>C was found to be 28 GPa consolidated by SPS at 1873 K. The hardness was less in conventional sintered samples possibly due to low sintered density and coarsening of grains. It may be also noted that addition of 2 wt. % of Si into SiC-B<sub>4</sub>C, decreased the hardness values. Micro-hardness of 22 GPa was obtained for SiC-B<sub>4</sub>C-2 wt. % Si samples sintered by SPS. The hardness of the cermets is directly related to the addition of Si in the main constituent and distribution of SiC, B<sub>4</sub>C, and Si phases. It may be pointed out that B<sub>4</sub>C is harder than SiC and Si. Increasing Si (softer phase) leads to the reduction in the proportion of B<sub>4</sub>C. To be more precise, the micro-hardness value of conventional pressureless sintered samples varies from 16 GPa to 18 GPa with increasing Si content from 5 wt. % to 10 wt. %, but decreased to 15 GPa in the case of Si 20 wt. %. While samples prepared by SPS at 1623 K (1350 °C), the hardness varied from 24.42 GPa in case of 5 wt. % Si addition to maximum microhardness value of 27.80 GPa for 10 wt. % of Si addition. But lower microhardness value of 23.95 GPa was obtained for 20 wt. % of Si sample, because of the increase in SiC content and residual Si in the product phase for Si (20 wt. %) cermet.

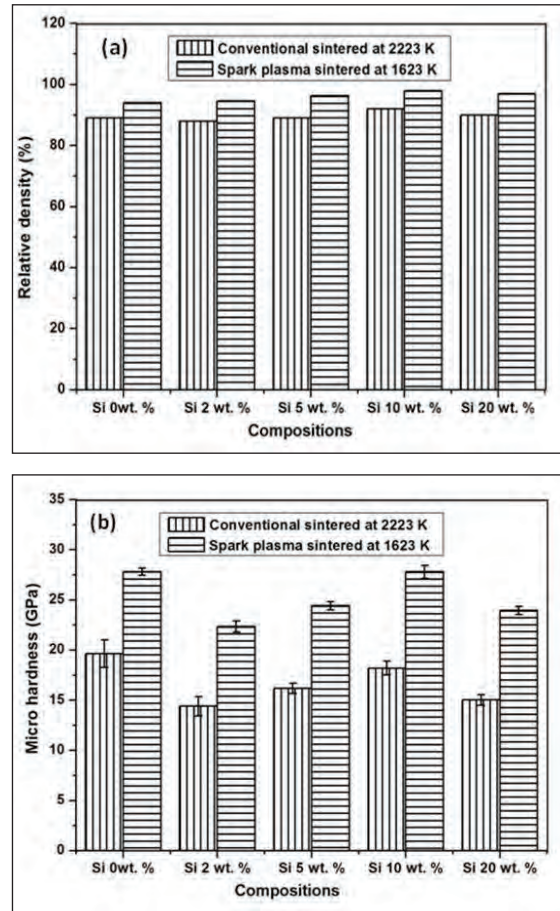
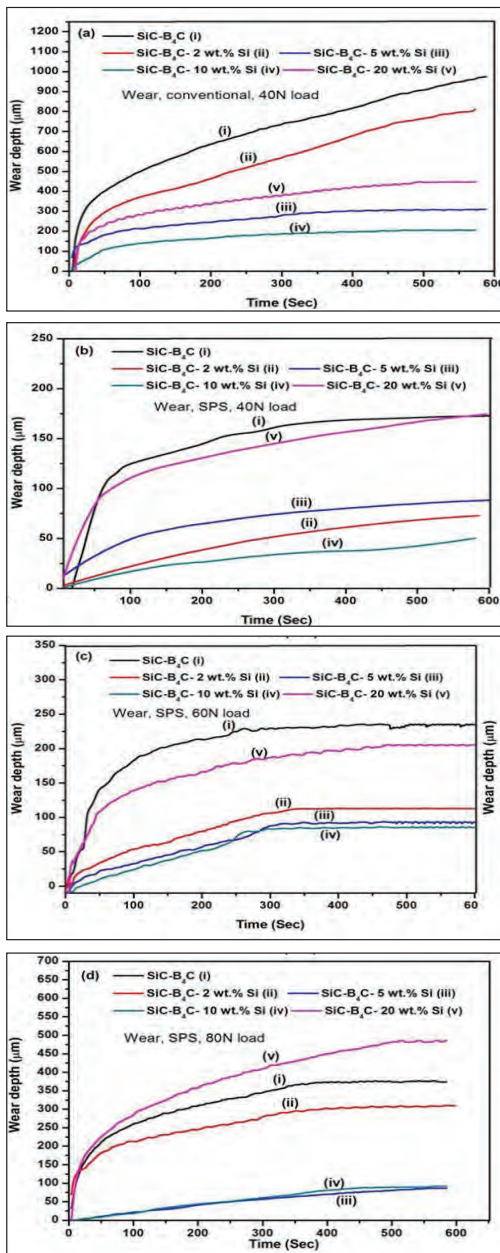


Fig. 1 (a) shows the bar diagram of the relative sintered density of various compositions sintered by pressureless sintering and SPS, and (b) bar chart showing micro-hardness of pressureless sintered and spark plasma sintered SiC-B<sub>4</sub>C based cermets (Si varies from 0–20 wt. %).

### 3.2 Wear depth study

The variation of wear depth with sliding time for all the compositions consolidated by conventional sintering and SPS process are shown in Fig. 2 (a–d). The wear depth of all the SPS samples at 40N, 60N, and 80N applied load are shown in Fig. 2 (a–c) and for conventional sintered samples at 40N applied load is shown

# NON-LUBRICATING SLIDING WEAR BEHAVIOUR STUDY OF SiC-B<sub>4</sub>C-Si CERMETS FABRICATED BY CONVENTIONAL AND SPARK PLASMA SINTERING TECHNIQUES



*Fig. 2 (a-c) Wear depth ( $\mu\text{m}$ ) vs. Time (sec) plot for the SPS samples at 40, 60, and 80N loading condition and (d) conventional sintered samples at 40N loading condition.*

in Fig. 2 (d) respectively. The wear depth of the SPS samples containing 0, 2, 5, 10, and 20 wt. % Si at 40N applied load is measured to be 162, 52, 74, 33, and 145  $\mu\text{m}$  respectively. Similarly, the wear depth is found to be 230, 104, 87, 83, and 188  $\mu\text{m}$  respectively tested at 60N applied load. Whereas, for conventional sintered samples wear depth is 742, 568, 281, 145, and 377  $\mu\text{m}$  respectively when tested at 40N applied load. Cermet samples sintered by SPS process possess maximum wear resistance than the conventional sintered samples. This is due to the increased density, hardness and decreased porosity ratios for SPS samples. The wear resistance increases with Si content up to 10 wt. % and minimum wear depth of 87  $\mu\text{m}$  is obtained at 10 wt. % Si when tested at 60 N. However, wear resistance decreases with increase in Si content at 20 wt. %. A wear depth of 188  $\mu\text{m}$  was obtained for SiC-B<sub>4</sub>C-Si (20 wt. %), whereas wear depth of 230  $\mu\text{m}$  was obtained for SiC-B<sub>4</sub>C sample when both were consolidated by SPS and subsequently tested at 60N applied load.

Fig. 3 shows a typical front view of the depth of the worn region of the sample containing 10 wt. % of Si observed by stylus surface profilometer. Here a diamond stylus is moved vertically in contact with sample and moved laterally across the sample for a specified distance and specified contact force. Here, the stylus tracking force was fixed to 1mg. The wear depth of conventional sintered sample containing Si 10 wt. % measured from surface profilometer is 128  $\mu\text{m}$  (Fig. 3a). This value is in good agreement with the wear depth measured from graph of wear depth vs. sliding time as shown in Fig. 2 (a). From surface profilometer study, the wear depth of 10 wt. % Si consolidated by SPS is found to be around 68  $\mu\text{m}$  for 80N applied load as shown in Fig. 3 (b). From wear depth vs. Sliding time plot of 10

# NON-LUBRICATING SLIDING WEAR BEHAVIOUR STUDY OF SiC-B<sub>4</sub>C-Si CERMETS FABRICATED BY CONVENTIONAL AND SPARK PLASMA SINTERING TECHNIQUES

wt. % Si sample it was found to be 60 μm. This value is corroborated with the wear depth vs. Sliding time plot in Fig. 2 (d).

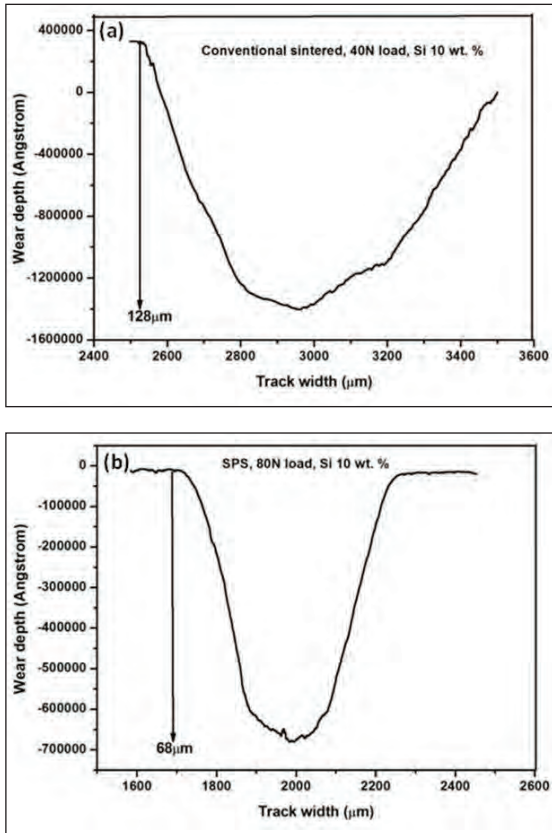


Fig.3 Surface profilometer data of depth of the worn region of (a) conventional sintered sample containing 10 wt. % Si using 40N applied load and (b) SPS sample using 80N applied load.

### 3.3 Effect of compositions (Si content)

Fig. 4 (a–d) represents the SEM images of worn surface of SPS samples containing 2, 5, 10, and 20 wt. % Si tested at 60N applied load. In Fig. 4 (a), the wear track and the magnified image of wear track is shown for Si 2 wt. %, which illustrate the micro cracks that exist on the surface of the wear track under the applied load of 60N. The

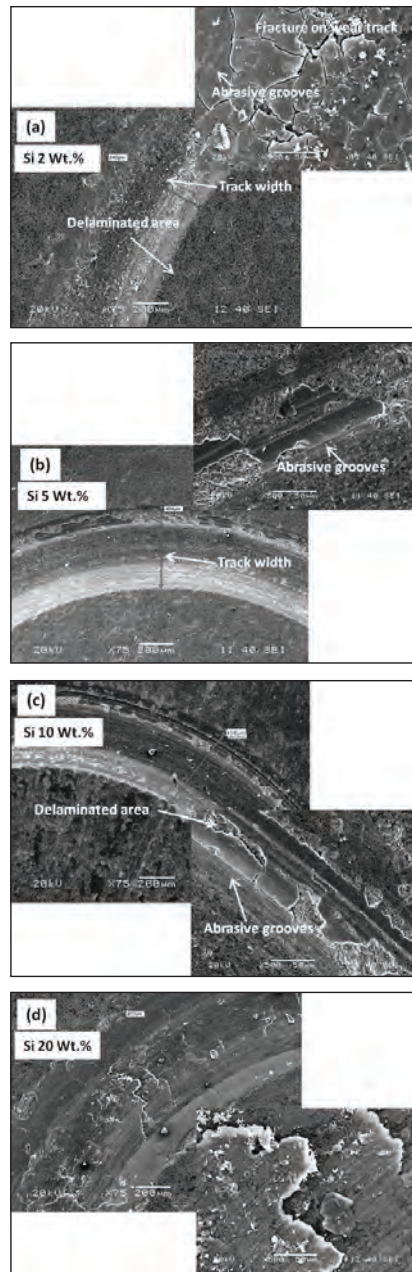


Fig. 4 SEM micrographs of worn surfaces of SPS samples of 60SiC38B<sub>4</sub>C<sub>2</sub>Si, 60SiC35B<sub>4</sub>C<sub>5</sub>Si, 60SiC30B<sub>4</sub>C<sub>10</sub>Si and 60SiC20B<sub>4</sub>C<sub>20</sub>Si compositions after wear test at 60N load.

# NON-LUBRICATING SLIDING WEAR BEHAVIOUR STUDY OF SiC-B<sub>4</sub>C-Si CERMETS FABRICATED BY CONVENTIONAL AND SPARK PLASMA SINTERING TECHNIQUES

surface cracks are believed to be caused by surface fatigue. This is called as fatigue cracks on the intergranular boundaries which are followed by removal of carbide grains from the matrix [21]. As the bonding of covalent and brittle SiC-B<sub>4</sub>C for 2 wt. % Si addition is poor, the applied repeated load creates cracks on the surface. With increasing Si content in the composition as it act as binder in SiC-B<sub>4</sub>C based cermets, the bulk hardness and density of the composites increases and as a result wear resistance increased. But with increasing applied load from 20N to 80N the impact of wear increases for all the compositions. It is observed that the failure is severe in 60 and 80N applied load than 20 and 40N load due to higher frictional force as shown in Fig. 5. From the SEM microstructures of the worn surface it is found that all the compositions follow the abrasive wear mark along the sliding direction with ploughing mode (abrasive grooves). The degree of ploughing (grooves) depends on the strength of the materials. Stronger materials have lower ploughing mode of impression. It also depends on the amount of applied load, as load increases the grooves formed are also deeper as shown in Fig. 5. As Si 20 wt. % composition

have comparatively lower strength, it undergoes severe ploughing compared to 5 and 10 wt. % of Si added materials. Due to the harder nature of 5 and 10 wt. % of Si samples it undergoes mild ploughing impression.

### 3.4 Effects of load

The impact of wear is comparatively less for Si 10 wt. % compositions under repeated loading condition than other compositions. This is due to the higher hardness value of S0 10 wt. % compositions than other compositions. The track width of Si 10 wt. % is measured to be 458  $\mu\text{m}$  and for Si 2, 5, and 20 wt. % it is measured to be 640, 464, and 817  $\mu\text{m}$  respectively after wear test at 60N load. This represents the more amount of materials removal from the surface for Si 2, 5, and 20 wt. % compositions. The material removal from a surface during sliding wear is consisting of smooth area, bright debris particles scattered on the surface and surface contains pits and surface fractures. As the contact surface is small, the strain at contact point is very high. The higher stress causes the change of the shape of the materials under applied load and plastic deformation takes place. Under repeated loading, the materials removed as wear debris and could be welded to the block surface. This process caused the surface delaminating and formation of cavities on the damaged surface shown in Fig 4.

### 3.5 Wear debris study

Fig. 6 (a-c) represents SEM micrographs of wear debris of SPS samples containing 10 wt. % Si tested at 20, 40, 60N applied load respectively. At low load, the wear debris produced is in the form of small particles but at higher load the particles are compacted and form flakes. Fig. 6 shows the changes in morphology and size of wear debris with load. The small particle shape

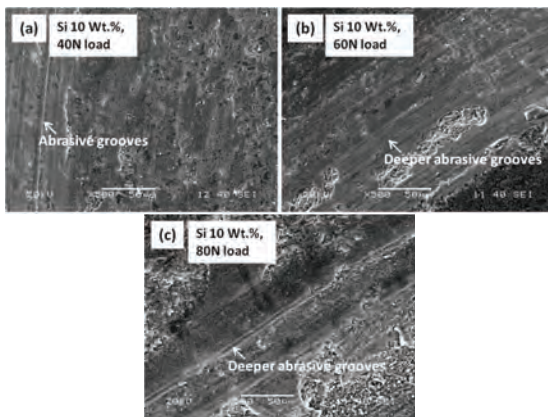


Fig. 5 SEM micrographs of worn surfaces of sample contain Si 10 wt. % at 40, 60, and 80N applied load showing abrasive grooves.

# NON-LUBRICATING SLIDING WEAR BEHAVIOUR STUDY OF SiC-B<sub>4</sub>C-Si CERMETS FABRICATED BY CONVENTIONAL AND SPARK PLASMA SINTERING TECHNIQUES

wear debris is evident at 20 N loads. At 40 and 60 N loads, the morphology of debris change from particle shape to flake shape. This is due to deformation of particles at higher applied loads.

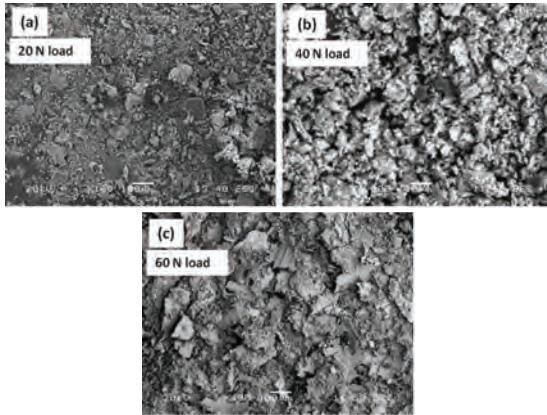


Fig. 6 (a-c) SEM images of wear debris of SPS samples contain Si 10 wt. % tested at 20, 40, 60N applied load respectively.

In the present study, XRD analysis confirmed the presence of SiC, B<sub>4</sub>C, B<sub>13</sub>C<sub>2</sub> and Si phases of the SPS sintered samples. The XRD of wear debris produced by 80N applied load for Si 20 wt. % sample sintered by SPS process is shown in Fig. 7. The peaks of SiC and B<sub>13</sub>C<sub>2</sub>

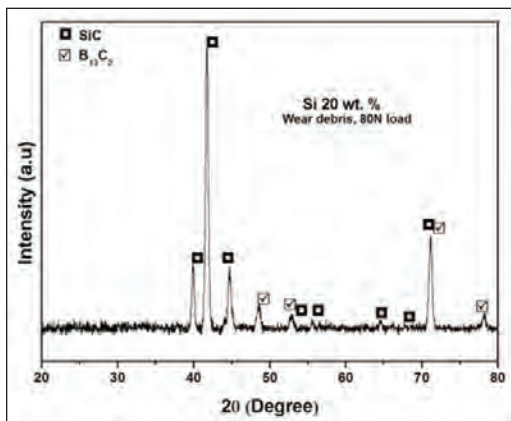


Fig. 7 XRD analysis of the wear debris produced for Si 20 wt. % sample sintered by SPS process at an applied load of 80N.

are observed. The existence of C-B-C chains in B<sub>13</sub>C<sub>2</sub>, instead of C-C-C chain in B<sub>4</sub>C is the only difference [22–24]. It has been reported that B<sub>4</sub>C phase is unstable above 327°C. With increasing sintering temperature, B<sub>4</sub>C changes to B<sub>13</sub>C<sub>2</sub> as C eliminates. There is no phase change until the melting point around 2527°C [25]. It can be deduced that the materials found in the debris completely come from composites. There was no oxidation peaks observed in the wear debris of Si 20 wt. % composition.

## 4. Conclusions

- The present investigation shows that there is an increase in density, hardness and wear resistance of SiC-B<sub>4</sub>C-Si based cermets when sintering method change from conventional sintering to spark plasma sintering.
- Wear depth increases with increase in applied load from 20 to 80N for all the SPS samples and also for conventional sintered samples tested at 20 and 40N.
- The wear resistance increases with Si content up to 10 wt. %. With further increase in Si content to 20 wt. % wear resistance decreases. The higher wear depth is found for SiC-B<sub>4</sub>C ceramic system as compared to SiC-B<sub>4</sub>C-Si cermets.
- The morphology and size of wear debris changes with change in applied load.
- The possible wear mechanisms are abrasion, de-lamination, ploughing and formation of crack.

## References

- [1] J.E. Zorzi, C.A. Perottoni, J.A.H. da Jornada, Hardness and wear resistance of B<sub>4</sub>C ceramics prepared with several additives, Mater. Let. 59 (2005) 2932 – 2935.
- [2] Y. Lv, G. Wen, T.Q. Lei, Friction and wear behavior of C-based composites in situ reinforced with W<sub>2</sub>B<sub>5</sub>, J. Euro. Cer. Soc. 26 (2006) 3477–3486.

## NON-LUBRICATING SLIDING WEAR BEHAVIOUR STUDY OF SiC-B<sub>4</sub>C-Si CERMETS FABRICATED BY CONVENTIONAL AND SPARK PLASMA SINTERING TECHNIQUES

- [3] Y. Song, G. Zhai, G. Li, J. Shi, Q. Guo, L. Liu, Carbon/graphite seal materials prepared from mesocarbon Microbeads, *Carbon* 42 (2004) 1427-1433.
- [4] S. Zhang, Titanium carbonitride-based cermets: processes and properties, *Mater. Sci. Eng. A.* 163 (1993) 141-148.
- [5] P.Q. Campbell, J.P. Celis, J.R. Roos, O.Van Der Biest, Fretting wear of selected ceramics and cermets, *Wear.* 274 (1994) 47-56.
- [6] D. Osset, M. Colin, Boron carbides of various compositions: An improved method for X-rays characterization, *J. Nuc. Mater.* 183 (1991)161-173.
- [7] A.W. Weimer, Carbide, Nitride and Boride materials synthesis and processing, London, Chapman & Hall,1997, pp. 10-14.
- [8] W.C. Johnson, Advanced Materials and powders, *Am. Ceram. Soc. Bull.* 80 (2001) 64-66.
- [9] F. Thevenot, Boron Carbide-A Comprehensive Review, *J. Eur. Ceram. Soc.* 6 (1990) 205.
- [10] R.J. Nelmes, J.S. Loveday, R.M. Wilson, W.G. Marshall, Observation of inverted-molecular compression in boron carbide, *Phys. Rev. Lett.* 29 (1995) 2268-2271.
- [11] H. Lee, R.F. Speyer, W.S. Hackenberger, Sintering of boron carbide heat treated with hydrogen, *J. Am. Ceram. Soc.* 85 (2002) 2131-2133.
- [12] H. Lee, R.F. Speyer, Pressureless sintering of boron carbide, *J. Am. Ceram. Soc.* 86 (2003) 1468-1473.
- [13] D. Jianxin, Z. Jun, F. Yihua, D. Zeliang, Microstructure and mechanical properties of hot-pressed B<sub>4</sub>C/(W, Ti)C ceramic composites, *Cer. Intern.* 28 (2002) 425-430.
- [14] L.S. Sigl, Processing and mechanical properties of boron carbide sintered with TiC, *J. Eur. Cer. Soc.* 18 (1998) 1521-1529.
- [15] A.K. Suri, C. Subramanian, J.K. Sonber, TSR Ch.Murthy, Synthesis and consolidation of boron carbide: a review *Int. Mater. Rev.* 55 (2010) 4-40.
- [16] X. Du, Y. Wang, Z. Zhang, F. Zhang, W. Wang, Z. Fu, Effects of silicon addition on the microstructure and properties of B<sub>4</sub>C-SiC composite prepared with polycarbosilane-coated B<sub>4</sub>C powder, *J. Mater. Sci. Eng. A.* 2015, Vol. 636, pp. 133-137.
- [17] I.S. Han, K.S. Lee, D.W. Seo, S.K. Woo, Improvement of mechanical properties in RBSC by boron carbide addition, *J. Mater. Sci. Lett.* 21 (2002) 703-706.
- [18] S. Hayun, N. Frage, M. P. Dariel, The morphology of ceramic phases in B<sub>x</sub>C-SiC-Si infiltrated composites *J. Solid State Chem.* 179 (2006) 2875-2879.
- [19] Y. Feng, W.Z. Hou, H. Zhang, L. Liu, Densification and Mechanical Properties of Spark Plasma Sintered B<sub>4</sub>C with Si as a Sintering Aid, *J. Am. Ceram. Soc.* 93 (2010) 2956-2959.
- [20] Advances in ceramic armor IX, ceramic engineering and science proceedings, Vol. 34, issue 5, 2013. Edited by: Jerry C. LaSalvia.
- [21] M.A. Farrokhzad, G.C. Saha, T.I. Khan, Wear performance of co-electrodeposited cermet coatings, *Surf. Coat. Tech.* 235 (2013) 75-85.
- [22] M. Widom, W.P. Huhn, Prediction of orientational phase transition in boron carbide, *Sol. Stat. Sci.* 14 (2012) 1648-1652.
- [23] G. Will, K.H. Kossobutzki, An X-ray structure analysis of boron carbide, B<sub>13</sub>C<sub>2</sub>, *J. Less Common Met.* 44 (1976) 87-97.
- [24] S. Zhang, W.Lu, C. Wang, Q. Shen, L. Zhang, Synthesis and characterization of B<sub>13</sub>C<sub>2</sub> boron carbide ceramic by pulsed electric current sintering, *Ceram. Int.* 38 (2012) 895-900.
- [25] H. Okamoto, Boron-Carbon phase diagram, in: H. Baker (Eds.) *ASM Handbook*, ASM International: Materials Park, OH, USA, 1992, pp. 422.

# FORGEABILITY OF ASTALOY AND ITS RESPONSE TO THERMAL PROCESSING

V. T. Thavale, N. B.Dhokey, S. Dhokale, P. Ghosh

Department of Metallurgy and Materials Science, College of Engineering, Pune, India

**Abstract:** Powder metallurgy is known to be a cost effective technology to manufacture components with narrow tolerances in combination with required mechanical properties, high strength to weight ratio. In the high performance gear applications, compaction and sintering are used as primary densification process while repressing, forging and heat treatment are used as the secondary densification process. In the present research work, forging is carried out as a secondary densification process on Astaloy (0.85% Mo+0.3% C) atomized powder. Cold compaction of the powder was done at 600MPa followed by sintering at 1120°C for 30min .Three forging temperatures (800°C, 900°C and 1000°C) and three strain rates(0.1s<sup>-1</sup>, 0.2s<sup>-1</sup>, 0.3s<sup>-1</sup>) were selected for forging parameters optimization . Two surface treatments viz. Carburizing and Carbonitriding were carried out on the optimized forged samples. Powder shape and size were characterized using SEM and sieve analysis. Cold compacted and sintered specimens were characterized for hardness, wear, density, tensile and transverse rupture strength (TRS). Microstructural characterizations of the differently treated specimens were carried out using optical microscope. The results indicated that forging at 1000°C and 0.3s<sup>-1</sup> strain rate gives approximately 98% density and 90 HRB Hardness. Carbonitriding gave improved hardness and wear resistance than carburized steel.

**Keywords:** Forging, Carburizing, Carbonitriding, TRS, Tensile Strength, Wear

## 1. Introduction

Powder metallurgy (PM) offers a versatile and efficient method for producing engineering parts and components especially for application in heavy duty components like gears, piston and connecting rod owing to attractive features such as good strength, easy formability, near net shape manufacturability and competitive cost [2]. Higher relative density is one of the most important factors for producing high quality PM parts since density strongly influences the physical and mechanical properties. Initially wrought steel gears were used but rapid development of automobile industries and focus on reducing production costs, present increase in the application of high performance powder metallurgy parts and exploit a great market of iron base powder.

A Powder forging is a process in which unsintered, presintered or sintered powder metal preforms are hot formed in confined dies. In powder metallurgy, gears are manufactured by pressing and sintering, selective densification, hardening and then sent for hard finishing in order acquiring the final geometrical quality. This manufacturing method eliminates waste of material as machining chips and acquires high gear strength, material and geometrical quality.

Powder forging technology has been introduced to manufacture the parts for vehicles. By containing 10-20% pore, the products manufactured by powder metallurgy have defects such as lower ductility, fatigue strength and impact strength. Therefore there is lot of limitation in the size and application of product. Powder forging technology has been introduced as an idea to overcome such defects.

## FORGEABILITY OF ASTALOY AND ITS RESPONSE TO THERMAL PROCESSING

In the powder forging process, the products manufactured by powder metallurgy are forged in order to remove the pores contained in them. Powder forging is a technology that can expand the limited application of powder metallurgy by minimized flash, reduced number of stages and possible grain refinement. Moreover, manufacturing cost and weight of product can be decreased by the net shape forging and less number of forming process compared to hot forging technology.

There are two basic forms of powder forging, (1) Hot Upsetting, in which the preform experiences a significant amount of lateral material flow and (2) Hot repressing, in which a material flow during densification is mainly in the direction of pressing commonly referred to as hot coining. Upsetting between flat dies is applicable as a model for initial stage of closed die forging until the lateral flow of the preform forces the material against the die wall. Dead zones created during initial deformation in which densification lags behind other regions may be difficult to compact later on, when they are enclosed by shell of denser and stronger material [8]. The densification process has been studied in terms of shape change and forging cracks. In the present paper, material properties such as density and strength are studied.

### 2. Experimental methods and Procedure

A prealloyed powder ASTALOY (Make: Hoganas India) was chosen for carrying out proposed work, having nominal chemical composition as 0.3%C, 0.85% Mo. The calculated theoretical density by rule of mixture is 7.8g/cc. The powder properties were having apparent density 4.1g/cc and particle mesh size 100 to 120 $\mu$ m. Cold compaction process was used to make green compact of the prealloyed powder using 50T hydraulic press. From prior work, 600MPa was

determined as optimized pressure for forging sample. Sintering was carried out in a tubular furnace having reducing atmosphere (mixture of N<sub>2</sub> and H<sub>2</sub>, 90:10 by volume) at 1120°C with controlled heating rate of 5°C/min and then soaked for 30min, as shown in Fig.1. Sintered specimens were cooled to the forging temperature. So in order to optimize forging temperature and strain rate, three different temperatures and strain rates i.e., 800°C, 900°C 1000°C and 0.1, 0.2, 0.3 respectively were chosen. Carburizing of specimens was carried out at Mothertech Heat Treatment Pvt. Ltd. The whole carburizing cycle is divided into three parts i.e. Carburizing, Diffusion, and Hardening. Carburizing was carried out at 900°C for 1hr followed by diffusion and hardening at 900°C and 820°C for 20min and 30min respectively. Quenching was carried out at 100 °C using oil as the quenching media and then tempered at 130°C for 2 hours to relieve the internal stresses. Carbonitriding was carried out at 840°C for 30min followed by hardening at 840°C for 5min. Quenching was carried out at 60°C using oil as the quenching media and then tempered at 120°C for 2 hours to relieve the internal stresses which developed after hardening.

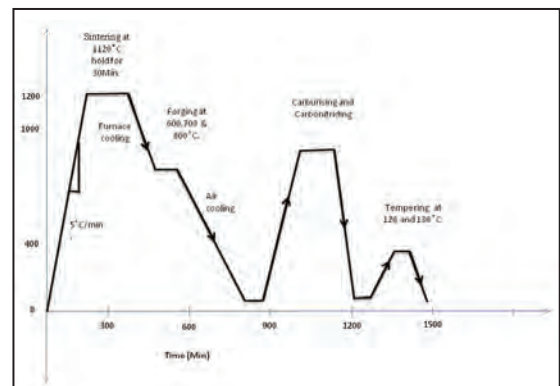


Fig. 1 Schematic T-T diagram showing processing steps of thermo mechanical processing cycle

Pin-on-disc test machine (Make: Magnum Engineers, Bangalore) was used for dry sliding wear test. Pin of 8.64 mm diameter and 20 mm height was slide on the circular rotating disc of SAE52100 having diameter 170 mm. The surface roughness of the counter face was maintained constant by polishing with 180 grit paper for 10 min. The loss in weight was measured using analytical digital weighing balance with measuring accuracy of 0.0001 g. TRS testing was carried out on 10 Tons UTM at COEP, Pune. During testing, the load was automatically applied by the machine and feed rate was set manually. Breaking Load was automatically recorded. TRS samples were manufactured according to MPIF 10.

### 3. Results and Discussions

#### 3.1 Particle shape and size

The particle size and shape has great importance in P/M because it affects properties such as green strength, density of compact as well as agglomeration, porosity, dimensional stability, flow and mixing characteristics. The powder material (Astaloy 0.85% Mo+0.3%C+1 % Zn stearate) has an irregular shaped powder particle which is confirmed as shown in Fig.2.

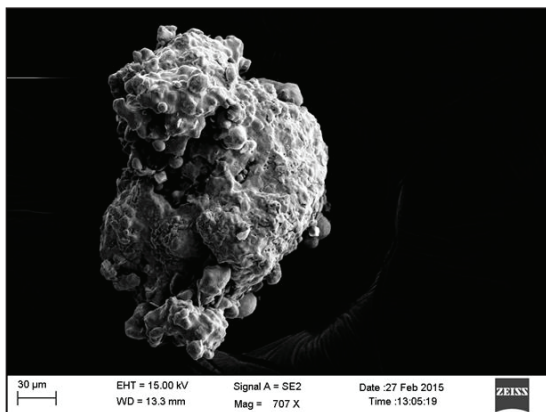


Fig. 2 SEM image of Astaloy 0.85% Mo+0.3%C+1 % Zn stearate powder.

#### 3.2 Effect of compaction pressure on density

Fig. 3 shows that, densities of the compacted specimens are lower than sintered specimens. Sintering process increases bonding between the powder particles due to mass transfer at atomic level and increases the strength of specimen as well as density. In case of green compact, 7.10 g/cc density was achieved at 600 MPa optimized pressure. Also density was raised to 7.24 g/cc after sintering of the same green compact. During sintering, mass transfer of atoms occurs due to higher temperature and thus bonding strength increases between powder particles and thus density increases.

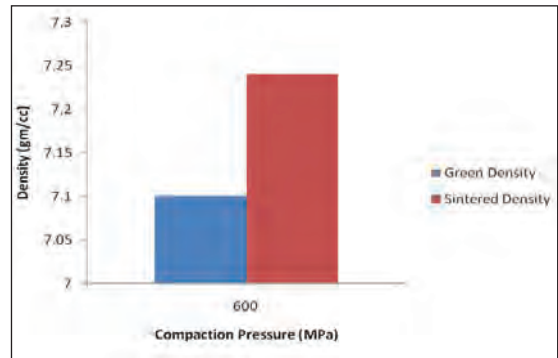


Fig.3 Effect of density difference after compaction and sintering

#### 3.3 Optical microscopy of cold compacted and sintered specimen

Fig.4 shows the optical microstructure of cold compacted specimen. Green compacted specimens have very low bonding between the particles. Fig.5 shows the optical microstructure of the sintered product. It is observed that sintering increases the densification and reduced porosity due to necking of particles. Sintering process was done on compacted specimens (600MPa) having average hardness 53HRB. It shows that with increase in compaction pressure, density as well as hardness increases.

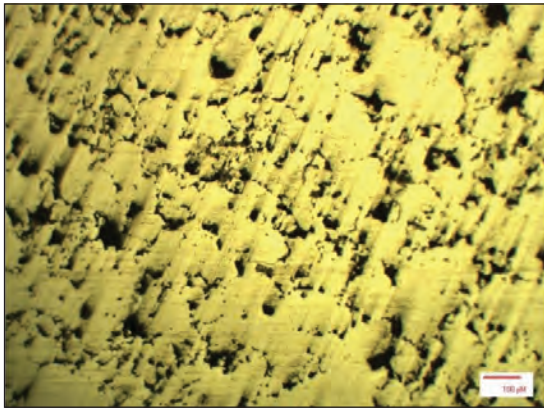


Fig. 4 Unetched microscopic image shows porosity population of 9% at 600 MPa

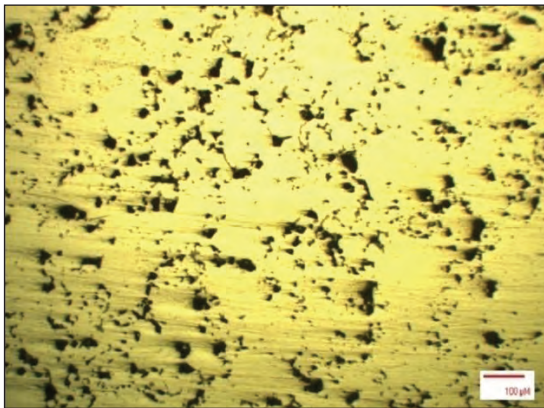


Fig. 5 Unetched microscopic image shows porosity distribution of 7%  $P_c = 600$  MPa and sintered at  $T_s = 1120^\circ\text{C}$  at 500X

### 3.4 Optimization of forging temperature and Strain rate

Generally for most metals, forging temperature is approximately 60% of the melting temperature in K. So in order to optimize temperature and strain rate, three different temperatures and strain rates i.e. 800°C, 900°C, 1000°C and 0.1, 0.2, 0.3 respectively were chosen which gave rise to maximum density. From the graphs, it is observed that as strain rate is increased, correspondingly density is also increased. This is

because with increased strain rate, time for heat dissipation from the specimens is also reduced while forging. Mode of heat flow is smoother in reaching full density. As interlocking between the particles gets stronger and denser and at the same time the pressure required for forging was also reduced. At same strain rates, density of closed die forged specimens was more than that of open die forged specimens because of less degree of plastic deformation and lateral flow. Density is a function of temperature and applied pressure. As temperature increases, density of specimen increases. Density was compared in open and closed die forging, lateral flow of material is lower in closed die at same height reduction due to restriction of die wall, interlocking of grains and porosity reduction was observed. Hence at 1000°C and closed die forging, we observe maximum 98% densification due to high forging temperature.

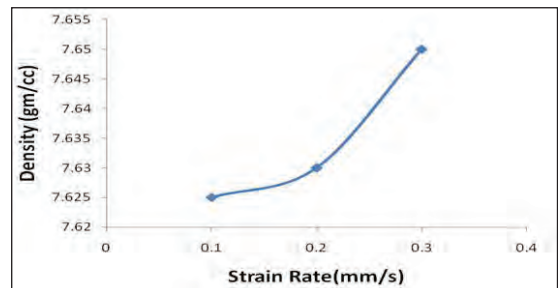


Fig. 6 Density vs. strain rate at 1000°C in closed die sintered hot forged specimen

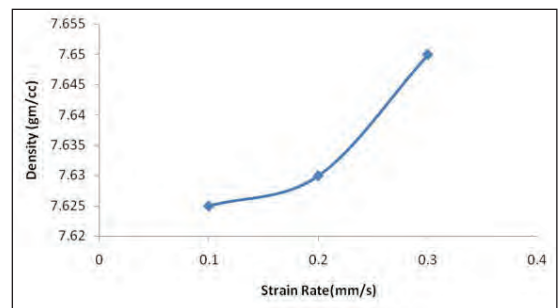


Fig. 7 Density vs. strain rate at 1000°C in open die sintered hot forged specimen

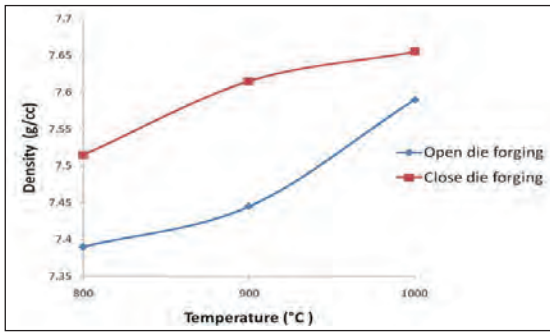


Fig. 8 Variation of densities with sintered forged temperature at 0.3mm/s strain rate

3.6 Hardness of sintered forged specimen

It is observed from the results that maximum hardness is achieved by closed die forging at 1000°C with strain rate of 0.3mm/s. The reason behind the maximum hardness was that with higher strain rate less time for forging was required. Because of higher strain rate, temperature drop was lower. Heat loss is inversely proportional to strain rate. Fig. 9 and 10 shows the hardness of the open die and close die sintered hot forged specimens at different temperatures. From the graph, it is observed that closed die forging at 1000°C gave highest hardness. This is due to the fact that material attains higher densities at higher temperatures. Porosity also gets reduced to a larger extent at higher temperature as compared to lower

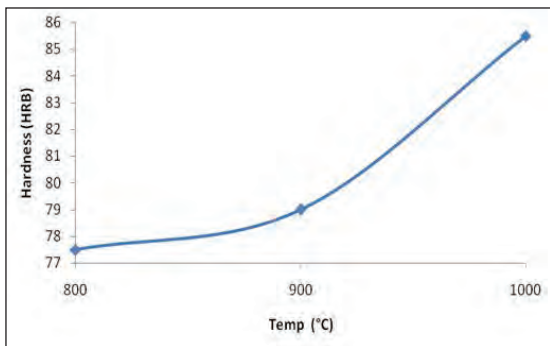


Fig. 9 Hardness of open die sintered hot forged specimen at three different temperatures

temperature. But in the case of open die forging, there is no control of machine’s parameters of forging. Hardness values obtained were dependent on strain rates.

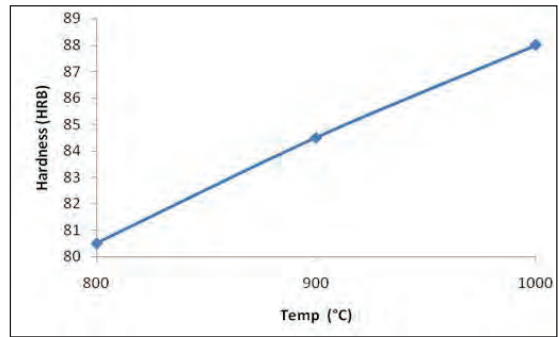


Fig.10 Hardness of closed die sintered hot forged specimen at three different temperatures

3.7 Microstructural Analysis of sintered hot forged specimen

The optical microstructure of open and closed sintered hot forged die specimen are shown in Fig. 11 and 12 respectively. It is observed that mainly ferrite is present in larger amount. Some amount of porosity is also present. As temperature of forging process was increased, amount of porosity also decreased. It can be predicted that forging process after sintering is beneficial to reduce the amount of porosity

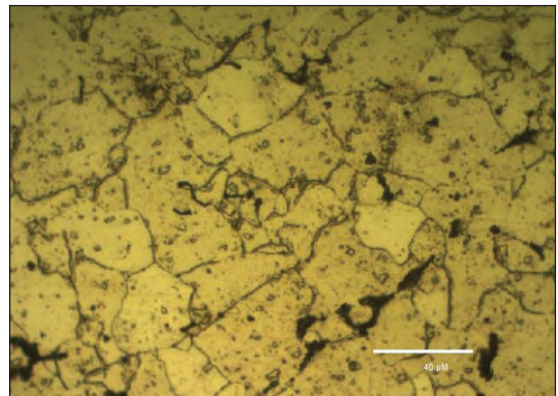


Fig.11 Optical microstructure of open die forged specimen at 1000°C showing ferrite grains at 500x

thereby increasing the density of the specimen which ultimately improves mechanical properties.

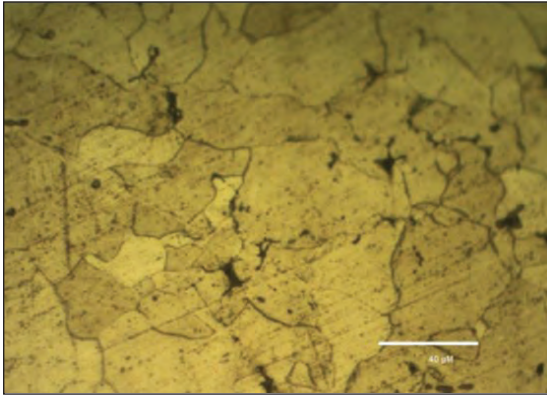


Fig.12 Optical microstructure of closed die forging at 1000°C showing ferrite grains at 500X

### 3.8 Wear Resistance

The wear volume loss of sintered specimens, sintered hot forged specimens, sintered hot forged carburized specimens and sintered hot forged carbonitrided specimens are shown in Fig.13. It is observed from the graphs that wear volume loss of sintered specimens were highest and that of sintered hot forged carbonitrided specimens were lowest. Less wear volume loss of sintered hot forged carbonitrided specimens were due to formation of carbonitrided layer on the surface of the specimen which is harder than

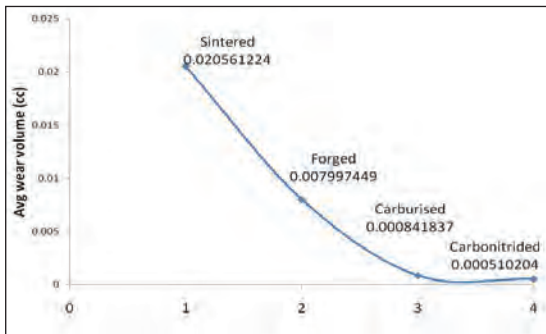


Fig.13 Comparison of wear volumes of sintered, forged, carburized and Carbonitrided specimens

that of the others. The microstructures consist of carbides and nitrides due to presence of carbon and nitrogen. (Fig. 14-16)

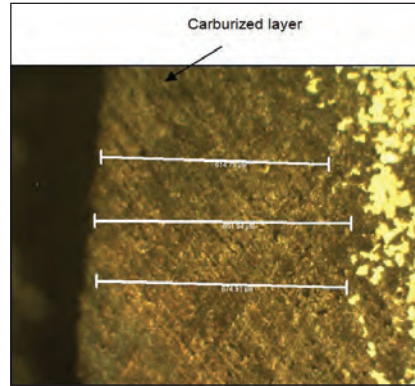


Fig.14 Carburized layer obtained after carburizing of the specimen showing carburising layer at 100X

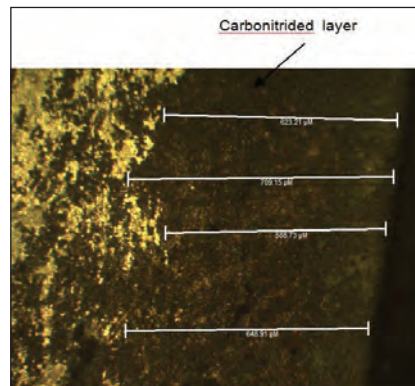


Fig.15 Layer obtained after carbonitriding of the specimen showing Carbonitrided layer at 100X

### 3.9 Case hardening

Surface hardness is mainly dependent on the carbon dissolved in austenite at carburizing temperature. Fig.16 shows the surface hardness of carburized and carbonitrided specimens. From the following data, it is observed that surface hardness of sintered hot forged carbonitrided specimen is more than that of sintered hot forged carburized specimen due to the presence of fine and equally distributed carbide-nitride on the surface.

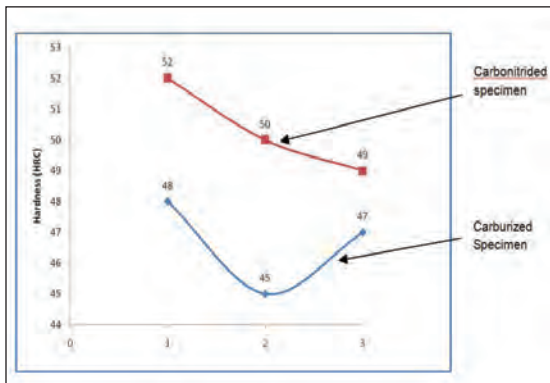


Fig.16 Surface hardness value of carburized and Carbonitrided specimens on the surface

### 3.10 Tensile Test and Transverse Rupture Strength

Cold compacted tensile and TRS samples were made conforming to MPIF 10 standard. Different pressures were used during making of tensile samples and TRS samples. Fig.17 and Fig.18 shows the cold compaction density of tensile samples and TRS samples at various pressures.

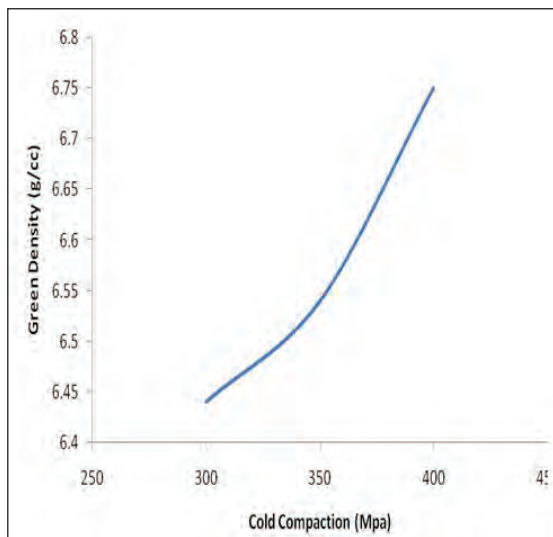


Fig.17 Cold compaction density of tensile sample at various pressures

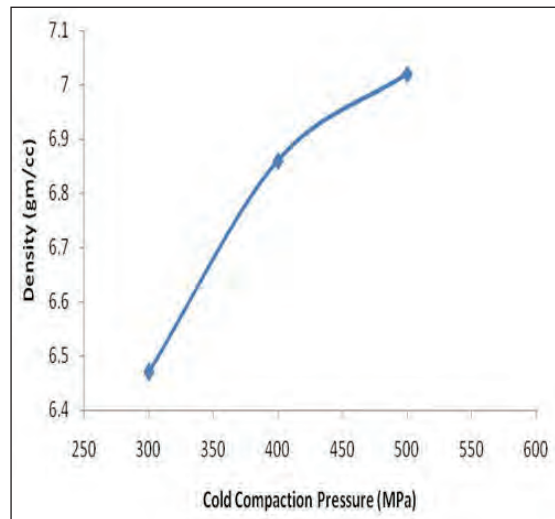


Fig.18 Cold compaction density of TRS sample at various pressures

At 300MPa, 83% densification was achieved. As pressure was increased to 350MPa the densification increases to 84% and good surface finish was observed but further increase in applied pressure formed crack on the specimen due to saturation of applied pressure so that 350MPa pressure is optimised for cold compaction. Cold compacted tensile specimens were sintered at 1120°C and hold for 30min in 90%N<sub>2</sub>+10% H<sub>2</sub> reduced atmosphere in tubular furnace. Sintered specimens were allowed to cool in water and the mechanical properties were evaluated.

Table 1 Properties of sintered samples after water quenching

Mechanical Properties	Values
Hardness	96HRB
Tensile Strength	711 MPa
Yield Strength	681MPa
Transverse rupture strength	597 MPa

For cold compaction of TRS samples, various pressures 300, 400, 500 MPa were used. At 200 MPa green strength was low so compaction pressure increased to 300MPa. At 300MPa 83% densification achieved and good surface observed during cold compaction. At 400MPa, 88% densification as well as good surface finish observed. At 500MPa, 90% densification is achieved but crack was observed on the sample. A 400MPa optimized pressure samples were used for sintering. During sintering at 1120°C temperature and 30 minutes holding time was used. 90% N<sub>2</sub>+10% H<sub>2</sub> reducing atmosphere were used for TRS samples. Samples were cooled in water and TRS was measured.

### 3.12 Conclusion

In the present context, the gear material Astaloy 85 Mo is studied to understand density improvement by forging and effect on it with applied heat treatment and its subsequent quantification by microstructure and hardness test. Based on the results, the following observations can be made-

1. Close die forging gives maximum density as compared to open die forging. Maximum density is achieved at 1000°C and 0.3mm/s strain rate because higher temperature gives ease of material flow during forging and less heat dissipation from the specimen.
2. Pressure required for forging is reduced as forging temperature increased. At 1000°C, during close die forging more pressure is required as compared with open die forging because of no restriction to material flow.
3. Higher hardness is observed at 1000°C and 0.3mm/s strain rate because of higher densification observed.
4. Close die forging gives maximum density as compared with open die forging.
5. Higher hardness 52HRC and less wear rate achieved in carbonitriding as compared with carburising.
6. Because of low percentage (~0.3%C) of the carbon in the material, and presence of molybdenum, heat treatment process has no significant effect on the material phase transformation even after forging.

### 3.13 References

1. A Rajeshkannan, K.S.pandey; "Some Studies on Sintered Cold Deformed Plain Carbon Steels", *Material and Design* 33(2012)115- 120.
2. V. Yu. Dorofeev, Yu. G. Dorofeev, "Powder Forging: Today and Tomorrow", *Powder Metallurgy and Metal Ceramics*, Vol. 52, Nos. 7- 8, November, 2013 (Russian Original Vol. 52, Nos. 7-8, July-August, 20 13)
3. A. Rajeshkannan, K.S Pandey, "Some Investigation on the Cold Deformation Behaviour of Sintered Iron 0.8% Carbon Alloy Powder Preform", *Journal of Material Processing Technology* 203(2008)542-547.
4. Abolfazl Babakhani, Ali Haerian, "On the Combined Effect of Lubrication and Compaction Temperature on Properties of Iron- Based P/M Parts", *Materials Science and Engineering A* 437 (2006) 360-365.
5. Bruce Lindsley and Howard Rutz, "Effect of Molybdenum Content in PM Steels", *Hoganas Corporation Cinnaminson, NJ 08077, USA*.
6. North American Hoganas, USA, "Properties of High Strength Powder Material Obtained by Different Compaction Method in Combination with High Temperature Sintering".
7. T.K. Kandavel, R. Chandramouli, "Experimental Study of the Plastic Deformation and Densification Behaviour of Some Sintered Low Alloy P/M Steels", *Materials and Design* 30 (2009) 1768-1776.

## FORGEABILITY OF ASTALOY AND ITS RESPONSE TO THERMAL PROCESSING

---

8. D.Shanmugasundaram, R Chanramouli, "Tensile and Impact Behaviour of Sinter forged Cr,Ni, and Mo Alloyed Powder Metallurgy Steels", *Materials and Design* 30 (2009) 3444-3449.
9. K Sheikhi Moghaddam, M Ghambari, "Effect of Sinter Hardening on Microstructure and Mechanical Properties of Astaloy 85 Mo", *Journal of Iron and Steel Research, International*.2012, 19(10): 43-46.
10. P. Nusskern, J. Hoffmeister, "Powder Metallurgical Components: Improvement of Surface Integrity by Deep Rolling and Case Hardening", *Procedia CIRP* 13 (2014) 192 - 197.
11. P.C.Angelo, R.Subramanian, "Powder Metallurgy", PHI Learning Pvt. Ltd. (50-84).
12. Jay Khatri, V.T.Thavale, N.B.Dhokey, "Study of Powder Forged Properties of Gear Material". PMAI 2015.

# ELECTROCHEMICAL PERFORMANCE EVALUATION OF $\text{Nd}_{1.7}\text{Sr}_{0.3}\text{NiO}_{4+\delta}$ AS A CATHODE FOR IT-SOFC APPLICATIONS

Vivek Patel<sup>a</sup>, R K Lenka<sup>b</sup>, P K Patro<sup>b</sup>, Amit Sinha<sup>b</sup>, L Muhmood<sup>a</sup>, T Mahata<sup>b</sup> and P K Sinha<sup>b</sup>

<sup>a</sup>K. J. Somaiya College of Engineering, Vidyavihar, Mumbai.

<sup>b</sup>Powder Metallurgy Division, Bhabha Atomic Research Centre, Mumbai, India

**Abstract :** A new cathode material,  $\text{Nd}_{1.7}\text{Sr}_{0.3}\text{NiO}_{4+\delta}$ , is synthesized by solid state route for intermediate temperature solid oxide fuel cell applications. Phase pure material is obtained after calcining the precursors at 1250°C. The electrical conductivity of the cathode material is above  $40\text{Scm}^{-1}$  in the operating temperature region of the fuel cell. From the symmetric cell measurement lower area specific resistance ( $0.2\Omega\cdot\text{cm}^2$ ) for the novel cathode material has been observed at 800°C. The performance of this cathode with a NiO-GDC anode supported SOFC is  $140\text{mW}/\text{cm}^2$  at 800°C. There is no appreciable change in the performance when operated at 0.6V for two hours. From the initial results this new cathode material can form a candidate cathode material for intermediate temperature SOFC.

**Key words:** IT-SOFC, Cathode,  $\text{Nd}_2\text{NiO}_4$

## Introduction

The journey towards the energy sustainability is closely associated with solid oxide fuel cells (SOFCs) having great potential to convert chemical energy of fuel (e.g. hydrogen) to electrical energy in an efficient and environment friendly manner [1]. The main advantages of Solid oxide fuel cells are absence of costly catalyst, internal reforming of fossil fuels, and higher electrical efficiency due to high quality waste heat for cogeneration, low activation losses and negligible pollution. In a fuel cell, high temperature operation leads to higher kinetics and higher performance. However, chemical compatibility of cell components, inter-diffusion of chemical species, and chemical stability of construction materials and usefulness of sealing are the issues associated with the high temperature operation [2,3]. Lowering the operating temperature suppresses the degradation of cell components and thereby increases the durability of the cell and widens the choice of materials in stack design. However, operation of SOFC at lower temperature implies lower electrode kinetics, resulting in large

interfacial polarization resistance especially the oxygen reduction reaction (ORR) at the cathode. Hence, over the last decades thrust has been given to develop SOFC that can be operated in the intermediate temperature range without sacrificing the performance. This challenge has been mitigated by various research groups worldwide through the development of new materials. Many mixed ionic and electronic (MIEC) conductors shown good performance as the dual ion and electron transfer capabilities extends the three-phase boundary away from the electrode-electrolyte interface. A wide variety of materials have been reported for use as cathode, and largely on perovskite based. Few cathode compositions like  $\text{Ba}_{0.5}\text{Sr}_{0.5}\text{Co}_{0.8}\text{Fe}_{0.2}\text{O}_{3-\delta}$  (BSCF),  $\text{Sm}_{0.5}\text{Sr}_{0.5}\text{CoO}_{3-\delta}$ ,  $\text{SrNb}_{0.1}\text{Co}_0\text{O}_{3-\delta}$  and  $\text{SrSc}_{0.2}\text{Co}_{0.8}\text{O}_{3-\delta}$  have proven to be a candidate cathode material for IT-SOFC applications[4-7]. There are still some advantages and disadvantages of these types of cathode materials with respect to the stability in the operating condition and compatibility with other cell components.

## ELECTROCHEMICAL PERFORMANCE EVALUATION OF $\text{Nd}_{1.7}\text{Sr}_{0.3}\text{NiO}_{4+\delta}$ AS A CATHODE FOR IT-SOFC APPLICATIONS

Apart from perovskites,  $\text{K}_2\text{NiF}_4$  type materials like Lanthanide Nickelates ( $\text{Ln}_2\text{NiO}_4$ ) have also been reported to be an effective cathode material for IT-SOFC [8]. Oxygen over stoichiometry in these types of materials lead to increase in the oxygen mobility compared to the perovskites [9]. Again dual valency of Ni in these types of material is responsible for the electronic conductivity. This MIEC behavior of  $\text{K}_2\text{NiO}_4$  structured materials proves as a candidate cathode material for fuel cell applications. Partial substitution of lanthanide site by alkaline earth metals (e.g. Sr, Ba, and Ca) has been reported to improve the electrochemical performance [10]. In the present investigation  $\text{Nd}_{1.7}\text{Sr}_{0.3}\text{NiO}_{4+\delta}$  composition has been prepared by solid state route and electrochemical performance has been evaluated.

### Experimental

#### *Powder Synthesis and characterization*

The composition,  $\text{Nd}_{1.7}\text{Sr}_{0.3}\text{NiO}_{4+\delta}$  (SrNNO) was prepared by solid state route by mixing required amounts of neodymium oxide ( $\text{Nd}_2\text{O}_3$ ) (IRE Limited, purity 99.9 %), nickel oxide (NiO) (SD Fine chemicals, Purity 99.9%) and strontium carbonate ( $\text{SrCO}_3$ ) (Sigma Aldrich, purity 99.98%) using a ball mill. The milling process was performed for 2hrs in ethanol medium in a zirconia pot. Mixed powder was calcined at  $1250^\circ\text{C}$  for 5h to obtain a single phase. Phase purity of the powder was confirmed from the X-ray diffraction pattern of the powder sample. Diffraction pattern was collected using an X-ray Diffractometer (INEL, France) using Cu K-alpha radiation from 20-80 degree. Particle size of the powder was measured using a laser diffraction particle size analyzer.

#### **Measurement of electrical conductivity:**

Bar shaped pellet of SrNNO was prepared by die pressing of the powder in a rectangular die followed by sintering at  $1350^\circ\text{C}$ . Two grooves were prepared at a distance of 1cm at the central part of the bar. Platinum paste was applied at the end faces and at the grooves prior to conductivity measurement. DC 4-probe electrical conductivity was measured using probostat test unit.

#### **Symmetric cell fabrication and measurement:**

Dense pellets of  $\text{Ce}_{0.9}\text{Gd}_{0.1}\text{O}_{1.95}$  (GDC) were prepared by uniaxial die pressing and sintering at  $1250^\circ\text{C}$ . Composite of SrNNO and GDC electrolyte in 50:50 wt ratio was ball milled for intimate mixing. Terpineol based slurry was prepared out of the composite and applied over the opposite faces of a dense GDC electrolyte pellet by screen printing method followed by sintering at  $1120^\circ\text{C}$ . Platinum paste was applied over the cathode coating for better current collection. Impedance of this symmetric cell was measured using an impedance analyzer (Solartron 1260) from 1MHz to 0.1Hz. Symmetric measurement was carried out up to  $800^\circ\text{C}$  in static air and area specific resistance (ASR) is calculated from it.

#### **Fabrication of planar cells and testing:**

Half cells of NiO-GDC//GDC were prepared by co-pressing of the two layers in a uniaxial die followed by sintering at  $1250^\circ\text{C}$ . The half cell diameter after sintering was 18mm and thickness of around 2mm. Cathode ink of SrNNO-GDC composite was prepared in terpineol medium as described earlier and applied over the dense electrolyte layer by screen printing method. The cell was fixed on an alumina tube using ceramic sealants as shown in Fig. 1. Platinum mesh with platinum wire was used for current collection.

## ELECTROCHEMICAL PERFORMANCE EVALUATION OF $\text{Nd}_{1.7}\text{Sr}_{0.3}\text{NiO}_{4+\delta}$ AS A CATHODE FOR IT-SOFC APPLICATIONS

Hydrogen and oxygen were passed at anode and cathode chamber respectively. Short term stability of the cell was measured at 0.6V for two hours to observe any degradation in the cell performance.

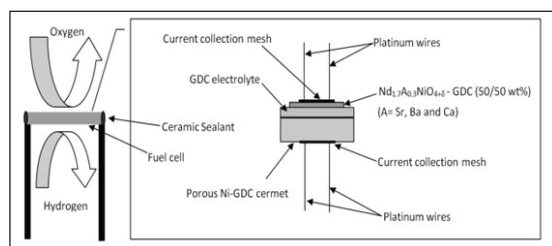


Fig.1. Schematic representation of fuel cell test rig

### Results and discussion:

#### Synthesis and characterization of cathode powder:

X-ray Diffraction pattern of  $\text{Nd}_{1.7}\text{Sr}_{0.3}\text{NiO}_{4+\delta}$  prepared through solid state route and calcined at 1250°C for 5hrs is shown in Fig.2. All the peaks in the X-ray diffraction pattern could be indexed to the  $\text{Nd}_2\text{NiO}_4$  type ruddlesden popper type phase as reported in the literature [xx]. No extra peak has been observed in the X-ray diffraction

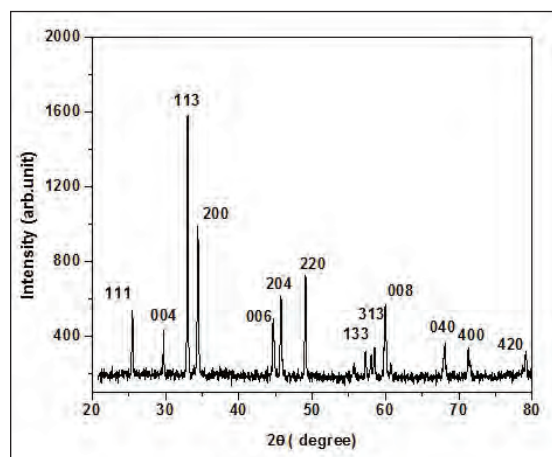


Fig.2. X-ray diffraction pattern of synthesized Sr-NNO powder

pattern showing phase purity of the material. As larger Strontium ion is substituted against small Nd ion, there is an increase in the volume of the unit cell is expected. The particle size of the powder as measured by laser diffraction particle size analyzer is in the range 0.5  $\mu\text{m}$  to 20 $\mu\text{m}$ . However the median particle size is 9.0  $\mu\text{m}$ .

#### Electrical conductivity:

DC- electrical conductivity of  $\text{Nd}_{1.7}\text{Sr}_{0.3}\text{NiO}_{4+\delta}$  in static air is shown in Fig.3. In this composition there is an increase in the conductivity value with temperature has been observed and this can be correlated to polaron hopping conduction associated with the variable valency of Ni. With further increase in temperature the conductivity value decreases. At higher temperature there is a loss of oxygen from the lattice and this decreases the total conductivity in the system.

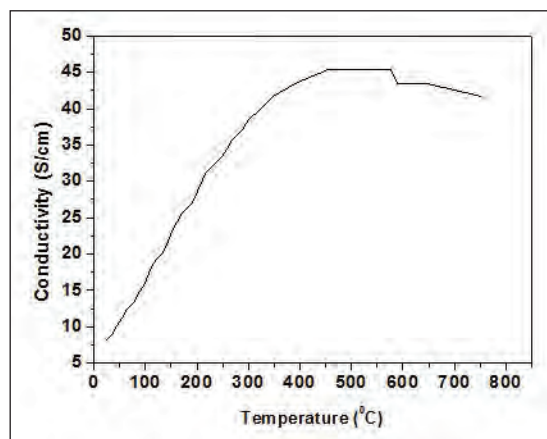


Fig.3. Electrical conductivity of Sr-NNO by DC 4-probe

#### ORR from the symmetric cell measurement:

The catalytic properties of a cathode material for the oxygen reduction reaction at the cathode electrolyte and cathode interface are expressed in term of area specific polarization resistance (ASR) or  $R_p$ . The polarization resistance is

## ELECTROCHEMICAL PERFORMANCE EVALUATION OF $\text{Nd}_{1.7}\text{Sr}_{0.3}\text{NiO}_{4+\delta}$ AS A CATHODE FOR IT-SOFC APPLICATIONS

obtained from impedance measurement of a symmetric cell with the same electrode at both sides of the electrolyte. This polarization resistance is obtained from the difference in intercepts of the impedance curve at the lower and higher frequency to the real axis. This result is corrected for each surface and the area of the cathode surface. Temperature dependant area specific polarization resistance (ASR) of  $\text{Nd}_{1.7}\text{Sr}_{0.3}\text{NiO}_{4+\delta}$  cathode is shown in Fig.4. ASR of  $\text{Nd}_{1.7}\text{Sr}_{0.3}\text{NiO}_{4+\delta}$  are  $0.2 \Omega \cdot \text{cm}^2$  and  $0.6 \Omega \cdot \text{cm}^2$  at  $800^\circ\text{C}$  and  $750^\circ\text{C}$ , respectively.

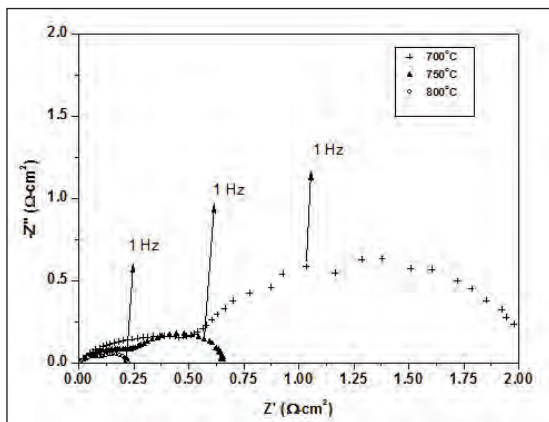


Fig.4. Area Specific Resistance of symmetric Sr-NNO with GDC electrolyte

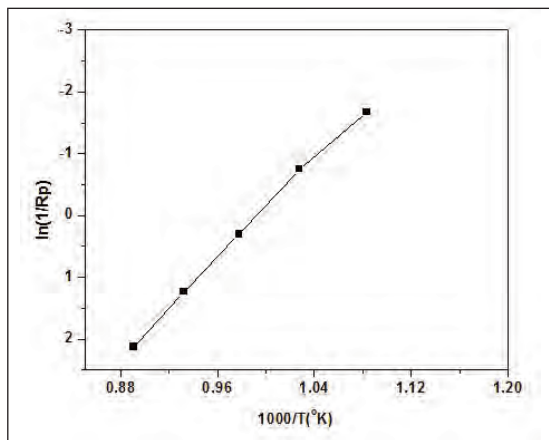


Fig.5. Thermal evolution of ASR with temperature

Thermal evolution of this SrNNO cathode has been represented in the form of Arrhenius plot and is shown in Fig.5. Activation energies for the oxygen reduction reactions have been calculated to be  $164 \text{ kJ mol}^{-1}$ . This shows that SrNNO cathode can perform well in the intermediate temperature region.

The electrochemical performance of  $\text{Nd}_{1.7}\text{A}_{0.3}\text{NiO}_{4+\delta}$  cathode was evaluated with a NiO-GDC//GDChalf-cell prepared through co-pressing method. The cell voltage and power density variation with current density is shown in Fig.6. The cell was characterized with humidified hydrogen as fuel and ambient air as oxidant. The highest power density of  $140 \text{ mW} \cdot \text{cm}^{-2}$  was obtained at  $800^\circ\text{C}$ . The power densities at  $700^\circ\text{C}$  and  $750^\circ\text{C}$  are  $20$  and  $90 \text{ mW} \cdot \text{cm}^{-2}$ , respectively.  $\text{Nd}_{1.7}\text{A}_{0.3}\text{NiO}_{4+\delta}$  have very high polarization resistance below  $750^\circ\text{C}$ . Hence the performance below  $750^\circ\text{C}$  is expected to be low.

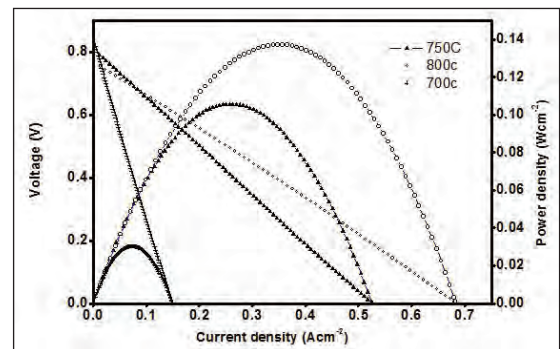


Fig. 6. I-V characterization of the cell with temperature

Again the microstructure at the electrode and electrolyte interface has significant effect to the total polarization resistance. SEM micrograph of the SOFC cell after testing is shown in Fig.7. An electrolyte layer of  $220 \mu\text{m}$  and a cathode layer of  $\sim 20 \mu\text{m}$  have been observed. The performance can be further improved by improving the

## ELECTROCHEMICAL PERFORMANCE EVALUATION OF $\text{Nd}_{1.7}\text{Sr}_{0.3}\text{NiO}_{4+\delta}$ AS A CATHODE FOR IT-SOFC APPLICATIONS

microstructure at the anode-electrolyte, cathode-electrolyte interface and decreasing the electrolyte thickness.

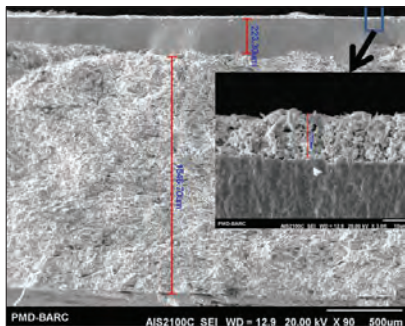


Fig.7. SEM micrograph of the cell and the cathode-electrolyte interface

Long term stability of the cell has been evaluated at 0.6V for 2hrs at 800°C. There is no appreciable decrease in the cell resistance during this period. This shows an appreciable fuel cell performance based on this novel cathode material.

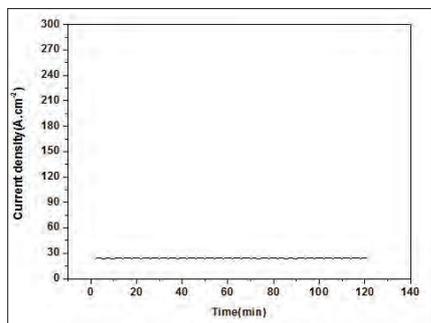


Fig.8. Stability of the cell at 0.6V

### Conclusion:

Single phase fine powders of  $\text{Nd}_{1.7}\text{Sr}_{0.3}\text{NiO}_{4+\delta}$  novel cathode material could be synthesized by solid state route. for intermediate temperature solid oxide fuel cell applications. Appreciable electrical conductivity above  $40\text{Scm}^{-1}$  has been obtained in the operating temperature region of the fuel cell. Area specific of the cathode material as low as  $0.2\text{--}0.2\Omega\cdot\text{cm}^2$  has been obtained for this types of cathode materials at 800°C. Fuel cell

performance of this cathode material was carried with a NiO-GDC anode supported cell. The peak power density of the cell was  $140\text{mW}/\text{cm}^2$  at 800°C. There is no appreciable change in the performance was observed even after operating for 2hrs at 0.6V. Electrochemical performance study reveals the better performance of this novel cathode material for intermediate temperature operation of the fuel cell.

### References:

1. W. Vielstich, H. A. Gasteiger, A. Lamm (Editors), Hand book of fuel cells, Fundamentals, Technology and applications, John Wally & sons Chichester, England, ISBN 0-471-49926-9, (2003).
2. Sun, C. W.; Hui, R.; Roller, J. J. Solid State Electrochem., 14, 1125–1144 (2010).
3. Hui, R.; Sun, C.; Yick, S.; Decès-Petit, C.; Zhang, X.; Maric, R.; Ghosh, D. Electrochim. Acta, 55, 4772–4775 (2010)
4. Z. P. Shao, S. M. Haile, Nature, 431, 170(2004).
5. T. Hibino, A. Hasimoto, T. Inoue, J.-I. Tokuno, S.-I. Yoshida, M.Sano, Science, 288, 2031(2000).
6. W. Zhou, Z. P. Shao, R. Ran, W. Q. Jin, N. P. Xu, Chem.Commun., 5791.20(2008).
7. W. Zhou, Z. P. Shao, R. Ran, R. Cai, Electrochem. Commun., 10, 1647(2008).
8. F. Mauvy, C. Lalanne, J.M. Bassat, J.C. Grenier, H. Zhao, P. Dordor, P. Stevens, J. Eur. Ceram. Soc. 25 2669-2672(2005).
9. Bassat, J. M., Boehm, E., Grenier, J. C., Mauvy, F., Dordor, P. and Pouchard, M., YSZ-supported cathodes of rare-earth nickelates  $\text{Ln}_2\text{NiO}_{4+\delta}$  for ITSOFC (650°C). In Proceedings of the 5th European Solid Oxide Fuel Cell Forum, ed. J. Huijsmans, pp. 586–593, (2002).
10. Y. Shen, H. Zhao, J. Xu and Łświerczek, International Journal of Hydrogen Energy 39[2] 1023–1029(2014).

# DRY SLIDING WEAR AND MICRO STRUCTURE OF STELLITE 6 COATING PROCESSED BY POWDER METALLURGY

D. Sathiya Narayanan<sup>1</sup>, S. Beer Mohammed<sup>1</sup>, K. Venkateswaran<sup>2</sup>

<sup>1</sup> B. S. Abdur Rahman University, Vandalur, Chennai, India

<sup>2</sup> Bimetal bearings Ltd, Chennai, India

**Abstract:** A major challenge for any industry is the design and processing of materials with improved tribology engineering application. Functional Graded Material (FGM) has great potential to improve tribological properties of the material. A FGM is a heterogeneous material which display a discrete or continuous variation of irreconcilable material properties depending on their processing techniques. In this paper, a FGM is developed with base iron powder coated with stellite6 powder on top to improve the hardness and micro structure by powder metallurgy to have discrete variation. A pre alloyed stellite6 powder has the properties of hardness and better corrosion resistance due to the presence of cobalt and chromium. On top of the Iron powder, the stellite powder was filled. The cold compaction of powders was done in hydraulic press and the green compact was sintered in the continuous furnace for 21 minutes. The sintered specimens were wire cut and tested as per ASTM G99 standards for dry wear test. The micro structural examination, wear and hardness were carried on the surface of the specimen. It was demonstrated that wear resistant of the FGM had been increased significantly.

**Key words:** Functionally Grade Material (FGM), Powder Metallurgy, Stellite 6 powder, Wear, Hardness

## 1. Introduction

For any engineering industry the major challenge is to improve operating performance of machinery, while maintaining or reducing the manufacturing costs. In most of the industrial machinery, surface damage generated by wear, limits the life of the component and therefore reduces durability and product reliability. Wear resistance of powder materials and coatings depends to a large extent on structural properties like heterogeneity of the composite structure, porosity of materials, state of stress of surface etc., and qualitative properties like hardness and toughness [1]. The conditions for obtaining wear-resistant materials with a clearly defined heterogeneous structure are most fully satisfied by the use of powder metallurgy techniques [2]. This drives the development

and implementation of providing intelligent deposition of harder material on the top surface with better compatibility to improve the performance of engineering components under contact loading, while retaining or reducing the material and manufacturing requirements for the base material. Macro scale Functionally Graded Materials (FGMs) offer a new method of surface engineering to produce tailored tribological properties.

FGM are the composite materials having non homogeneous microscopic micro structure. The variation in micro structure is due to the material properties are due to the continuous and synchronized distributions of the structure. The graded structure takes advantage of each base material without conventional material interfaces [3]. Constructive processes in which the gradient is produced by staking material

# DRY SLIDING WEAR AND MICRO STRUCTURE OF STELLITE 6 COATING PROCESSED BY POWDER METALLURGY

in a programmed fashion are attractive because there is essentially no limit on gradients that can be produced [4]. Stepwise constructive process advances in automation technology during the last decades have rendered constitutive gradation processes technologically and economically viable [5].

The Co-based alloys offer obvious potential for the current application as a result of their excellent high temperature wear resistance, retention of hardness at elevated temperature, oxidation resistance and anti-galling properties [6]. Co-base superalloys rely primarily on carbides formed in the Co matrix and at grain boundaries, for their strength and wear resistance. The distribution, size and shape of carbides depend on processing conditions. Currently, the use of Stellite alloys has extended into various industrial sectors [7]. Alloying with higher amounts of chromium and molybdenum additionally leads to corrosion resistance. This makes them excellent candidates for use in fluid flow systems with a high abrasive load [8]. Stellite are often used in lubrication-starved, high temperature, or corrosive environments [9]. Powder metallurgy (PM) provides great advantages for manufacturing large series of small size and relatively complex shape components [10]. As stellite display good resistance to corrosion in nitric acid environments, they are often used in the fabrication of valves that are to be used in such environments [11]. Powder metallurgy techniques as well as hot isostatic pressing can be used to consolidate Stellite alloy powders into solid components. Some alloys (e.g., Stellite alloys 1, 6, and 12) are derivatives of the original Co-Cr-W alloys developed by Haynes. These alloys are characterized by their carbon and tungsten/ molybdenum contents [12].

## 2. Experiment

### 2.1. Materials and Methods

The FGM is developed for wear resistance application with improved wear resistance on

the top surface, and maintaining the softness in the base to absorb the shock loads. Stellite 6 a cobalt base powder was selected as a top layer of the specimen due to its improved hardness, by the presence of harder complex carbides of chromium and tungsten and iron powder was chosen as the base material to withstand the load. The nominal composition and physical properties of stellite 6 powder are listed in the Table.1.

*Table 1. Nominal composition (mass %) and physical properties of stellite 6 powder.*

Co	Cr	W	C	Others	Hardness	Density	Melting Range
58	28.5	4.6	1.4	Ni,Fe,Si,Mn,Mo	40-46 HRC	8.44 g/cm <sup>3</sup>	1285-1410°C

The SEM image of the stellite6 powder before compaction shows the particle has spherical shape and has some projection in its outer structure as in Fig.1. The stellite powder not fixing to the iron powder in the bottom due to its spherical shape. So the stellite 6 powder blended with additional iron powder by 10% weight.

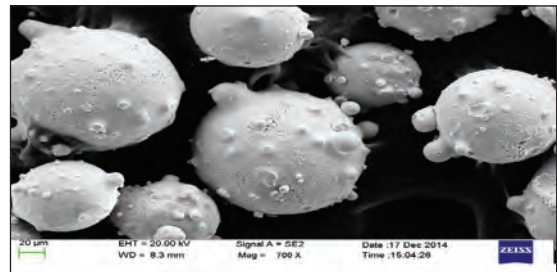


*Fig.1 SEM image of stellite 6 powder.(80 to 130 micro meter in size)*

The size of the stellite powder varies from 80 to 130 micro meter whereas the iron powder size is 325 mesh size (25 micro meter) Prior to the deposition of FGMs, deposition rates of both single powders were measured. Based on these measurements, powder feed rates were adjusted appropriately to achieve the required phase content and the thickness of each layer. The iron powder and stellite powder were taken

# DRY SLIDING WEAR AND MICRO STRUCTURE OF STELLITE 6 COATING PROCESSED BY POWDER METALLURGY

in different weight ratio as per Table 2 to suit the geometry of layer thickness of the standard specimen size 30 mm square. The powders were poured in the die cavity one after another for compaction. Compaction of powders was done in a single press with 50 Ton load in the hydraulic press.

*Table 2. Various weight ratios of iron and stellite 6 powders.*

Specimen	S1	S2	S3	S4
Composition of powder (in grams)	Iron powder 21 g + Stellite 6 09 g	Iron powder 24 g + Stellite 6 06 g	Iron powder 27 g + Stellite 6 03 g	Iron powder 30 g
Thickness of green compact (in mm)	5.0	5.0	5.0	5.0

The green compacts were sintered in the continuous furnace at the belt speed of 150 mm/minute. The furnace was maintained at the temperature  $1120 \pm 10^\circ\text{C}$  with a soaking time of 21 minutes. The sintering was carried at the inert gas atmosphere. All tests were repeated at least three times in order to have repeatability.

## 2.2. Dry wear test

The pin-on-disc test is a classical method commonly used for adhesive wear experiments. The wear rate was calculated from the weight loss measurement and expressed in terms of volume loss per unit sliding distance.

The specimens were wire cut to 10 mm diameter for conducting dry wear test as per ASTM G99 standards. The 10 mm specimen is fixed with a pin of 10 mm diameter and 30 mm long. The disk is a circular plate (5 mm thickness) prepared with High carbon high chromium steel of hardness 62HRC with surface roughness 1.6 Ra. Prior to wear testing, both the pin and disk surface are cleaned in alcohol solution and deionized water for 15 min at room temperature, then dried and stored under clean room condition. The wear resistance of S1, S2, S3 and S4 were evaluated using a Pin-on-Disk apparatus at room temperature,

During sliding, the load is applied on the specimen through cantilever mechanism and the specimens were brought into intimate contact with the rotating disk at a track radius of 50 mm. The disk was spinning at a rotational speed of 400 rpm, and the pin (specimen) was placed under a compressive force of 20 N without lubrication. The apparatus allowed running for 960 seconds (sliding distance of 1000 m). As a result of friction/wear, a circular wear track was created in the specimen surface. The wear loss was evaluated by calculating the weight loss of the specimen comparing before and after the test. In order to normalize the wear results in this paper, the commonly experiments were repeated and the weight loss before and after calculated by weighing in electronic analytical balance with 0.001 g precision.

## 2.3 Hardness & Micro structure

Samples were prepared by the same method as for SEM examination for micro hardness testing and taking pictures of micro structures. Micro hardness measurements were obtained from a series of indents along a line parallel to the coating on the stellite material coated side. A 100g load was generally used. Fifteen separate hardness measurements were taken for each sample and the average value and standard deviation determined. The micro structure was studied both on the surface of stellite coating and the cross section to study the bonding of iron powder with stellite powder.

## 3. Results

The micro structure of the specimen S2 and S3 in the cross section of the FGM which is perpendicular to the coating is given in the Fig 2 and Fig 3.

# DRY SLIDING WEAR AND MICRO STRUCTURE OF STELLITE 6 COATING PROCESSED BY POWDER METALLURGY



Fig. 2 Microstructure of cross section of FGM



Fig. 3 Microstructure of cross section of FGM

The micro structure of the specimen S1 and S3 in 100x on the coated surface on the specimen is given in Fig. 4 and Fig. 5.

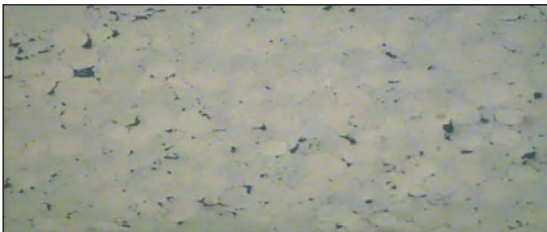


Fig. 4 Microstructure of FGM surface on stellite side

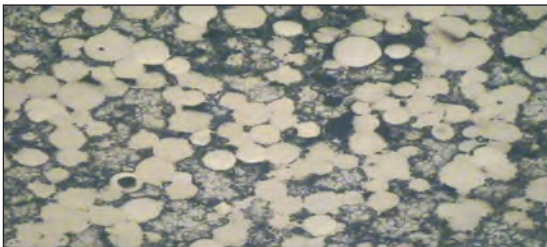


Fig 5 Microstructure of FGM surface on stellite side

The density, hardness and the wear loss occurred in the specimen after pin on wheel disc is given in the Table 3 with respect to different proportions of stellite and the iron powder.

Table 3. The Density, micro structure and weight loss of the samples after pin-on-wheel test.

S No	Proposition	Density (g/cc)	Micro Hardness	Weight loss in grams
S 1	Iron powder: 21 grams + Stellite : 9 grams	6.21	80	0.00126
S 2	Iron powder: 24 grams + Stellite : 6 grams	5.98	78	0.00180
S 3	Iron powder: 27 grams + Stellite : 3 grams	5.92	75	0.00254
S 4	Iron powder: 30 grams	6.12	50	0.00900

## 4. Discussion

It is widely accepted that the hardness property is a critical indicator when selecting a material for a designated application because it is closely associated with ductility, elasticity, toughness and strength properties of materials. It is commonly agreed that for most materials, the harder the material, the greater the wear resistance. To verify this relation on these Stellite alloys, micro hardness indentation test was conducted on them using a Micro hardness Tester Unit. For the Stellite 6 group, the hardness of solid solution of the three alloys was very close, which implies that the manufacturing or fabrication process of the alloys did not affect the hardness very much.

From the pin-on-disc wear test experimental results obtained, samples from the Stellite 6 group all had better wear resistance than the samples from the iron powder only which may be due to the crystallographic nature of the cobalt present in the stellite. But the micro structure of the FGM shows the powders has not sintered properly which may be due to the powder shape of the stellite. The sintering time may be increased to have better sintering.

## 5. Conclusion

It is very often that improvement in one attribute is accomplished at the expense of other desirable

## DRY SLIDING WEAR AND MICRO STRUCTURE OF STELLITE 6 COATING PROCESSED BY POWDER METALLURGY

properties of materials. For example, improving wear resistance of materials often results in reduced toughness, weldability and corrosion resistance. Therefore, a balance among various properties for a material should be concerned when it is selected for a designated application that involves a complex working environment such as high temperature, high stress, wear and corrosion, otherwise one property will be prior to the others in consideration for a material having a given application. Based on this discussion, the FGM was developed and the results from this research demonstrate that due to presence of cobalt and chromium in stellite FGM is the best candidate to use where better wear resistance with shock absorbing property is required.

### References

1. Ali Emamian, "A Study on Wear Resistance, Hardness and Impact Behaviour of Carburized Fe-Based Powder Metallurgy Parts for Automotive Applications" published in *Material Science and Applications*, 2012.
2. B. Kieback, A. Neubrand, H. Riedel, topic on "Processing Techniques for Functionally Graded Materials" published in Elsevier A 362 - 2003.
3. Wilfredo Mantialegro Rubio "Analysis, Manufacture and Characterization of Ni/Cu Functionally Graded Structures" April 2012.
4. A. Mortensen and S. Suresh "Functionally Graded Metals and Metal-Ceramic Composites: Part 1 Processing" 1995 Vol.40.
5. R. Ahmed H.L.deVilliers Lovelock "Influence of Re-HIPing on the Structure-Property Relationships of Cobalt-based Alloys" June 27- 2012.
6. L. C. Jones\*, R.J. Llewellyn "Sliding Abrasion Resistance Assessment of Metallic Materials for Elevated Temperature Mineral Processing Conditions" Elsevier doi: 10.1016. Journal .wear.2009.06.023.
7. F. Rosalbino, G. Scavino "Corrosion Behaviour Assessment of Cast and HIPed Stellite 6 Alloy in a Chloride-containing environment", *Electrochimica Acta* 111, pp.656- 662, 2013.
8. P. Niederhofer, S. Huth, W. Theisen "Cavitation Erosion and Hydro Abrasion Resistance of Cold Work Tool Steels produced by Powder Metallurgy" Elsevier .doi.org /10.1016/j.wear.2014.12.016.
9. B. Kieback, A. Neubrand, H. Riedel "Processing Techniques for Functionally Graded Materials" February 7, 2003.
10. F.Velasco, M. A.Martínez, R. Calabre's, A. Bautista, J. Abenojar "Friction of PM Ferritic Stainless Steels at Temperatures up to 300°C" April 1 2009.
11. M. Wong-Kian, L. A. Cornisht, and A. van Bennekom, "Comparison of Erosion-Corrosion Behaviour of Hot Isostatically Pressed and Eelded Dtellite Voatings" The South African Institute of Mining and Metallurgy, 1995.
12. J. B. C. Wu and J. E. Redman, Hardfacing with Cobalt and Nickel Alloys, *Weld. J.*, pp. 63-68, Sept 1994.

# INTERFACIAL DESIGN AND DEVELOPMENT OF Cu/SiC MMCs FOR THERMAL MANAGEMENT APPLICATIONS BY PM ROUTE

Rahul Shetty<sup>1</sup>, S. Kavithaa<sup>2</sup>, A. Udayakumar<sup>2</sup>, S. S. Avadhani<sup>2</sup>, B. Krishna Mohan<sup>2</sup>,  
A. Murugan<sup>2</sup> and S. Usha<sup>2</sup>

<sup>1</sup>Department of Mechanical Engineering, Siddaganga Institute of Technology, Tumkur, India

<sup>2</sup>Central Manufacturing Technology Institute, Bangalore, India

<sup>3</sup>National Aerospace Laboratories, Bangalore, India

**Abstract :** Micro and nano-electronics is to play a vital role in current and future electronics industry specifically for aerospace applications. Hence, the development of materials capable of handling improved power density, reliability and efficiency of existing semiconductors (Si, SiC and GaAs) and new semiconductors (GaN) capable of operation at higher temperatures is imperative to cater a broad range of future space, defence and telecom applications. The prime objective of the study presented is the development of novel interface tailored Cu/SiC MMCs by PM route. The paper describes in detail the development and optimization of suitable surface coatings on SiC<sub>p</sub> for use as reinforcement in Cu matrices. Optimization experiments carried out towards achieving a uniform dispersion of SiC<sub>p</sub> in Cu matrix, preliminary experiments on Cold Isostatic Pressing / sintering of green compacts and characterization of the compacts is outlined herein.

**Key words :** Metal Matrix Composites, Thermal Interface Material, Coefficient of Thermal Expansion, Cold Isostatic Pressing, Sintering

## Introduction

Nanotechnology has driven the need for miniature on-chip thermal management since the integrity of materials typically used for cooling structures breaks down leading to catastrophic failure of devices. The demand for advanced thermal management materials with higher thermal conductivity and low coefficients of thermal expansion (CTE) for maximizing heat dissipation and minimizing thermal stress and warping of electronic packages is critical to the continuing miniaturization, increased functionality and integration of electronic components.

Traditionally, heat dissipation in electronic devices was via passive strategies wherein, high thermal conductivity metals such as copper(Cu),

aluminium(Al) or silver(Ag) were employed as heat sinks and/or heat spreaders together with a Thermal Interface Material (TIMs) or thermal stress compensating material which attributed towards increase in thermal resistance resulting in significant design compromises. Moreover, maximum thermal dissipation requires direct attachment of device to a substrate or package. Al/Silicon Carbide(SiC) system with thermal conductivity of 190W/mK will not be able to provide the required thermal management performance in the near future with the exponential increase in electronic system heat flux [1].

## Overview

Cu and its alloys with a thermal conductivity around 396 W/mK with a CTE (17 ppm/°C)

lower than that of Al are an attractive option for high performance heat sink applications. Cu matrix composite materials are particularly useful for space/fusion applications wherein stringent requirement of high stiffness together with the ability to withstand high thermal loads are demanded. Studies of the Cu/SiC system indicate poor wettability and detrimental interfacial reactions at temperatures lower than 900°C [2]. Dissolved silicon reduces dramatically the thermal and electrical conductivities of Cu/SiC Metal Matrix Composites (MMCs). Therefore, diffusion barriers are necessary to prevent the interfacial reaction between copper and SiC [3]. Another effective way of improvising wetting between Cu and SiC is by alloying modification with a lower melting point metal. Few studies on barrier coatings on SiC, alloying additions to Cu for fabrication of Cu/SiC MMCs have been reported [4&5]. The compaction studies carried out for Cu/SiC MMCs in general comprised of hot compaction for higher volume percentage of the reinforcement [5]. Studies on fabrication of Cu/SiC MMCs on cold compaction and subsequent hot forging have been reported [6&7]. Some studies have been reported on CIPing of Cu/SiC MMCs followed by sintering with lower volume percentage of reinforcement have been reported [8].

### **Objective**

The present work involves the development of two Cu/SiC systems via Powder Metallurgy (PM) route with tailored interfaces namely; 1. barrier metal oxide coating [6] and 2. metallic coating envisaging better barrier and/or wetting properties of Cu on SiC. The present study aims the CIPing of the Cu/SiC MMCs and their subsequent sintering at approximately 1173 K.

### **Materials & Characterization methods**

Cu powder and green  $\alpha$ -SiC<sub>p</sub> (400 and 600 grit sizes) was locally procured from MEPCO and CUMI. The powders are blended, compacted and sintered. The characterization of the precursor materials, coated reinforcements, composite blends, compacted and sintered specimen were carried out employing Bruker D8 Advance X-ray Diffractometer and Zeiss NEON 40 EsB Cross Beam Scanning Electron Microscope. Density and porosity measurements of the compacted samples were carried out using Archimedes method.

### **Experimental methodology**

#### **Electroless nickel phosphide coatings on SiC<sub>p</sub>**

Surface cleaning of SiC<sub>p</sub> was initially carried out using a mixture of isopropanol and toluene followed by surface activation using 0.005% palladium chloride solution. Electroless nickel plating is a chemical process which reduces nickel ions in solution to nickel metal by chemical reduction. The most common reducing agent used is sodium hypophosphite. The surface treated SiC<sub>p</sub> is then magnetically stirred at 363K in a mixture of electroless nickel process precursor solutions GINPLATE NI 418 A and GINPLATE NI 418 B for a duration of 30 minutes. The SiC<sub>p</sub> were vacuum filtered and dried in an air oven at 373 K for one hour. Sol-gel metal oxide coatings on SiC<sub>p</sub> as reported [6] and experiments were taken up to optimize the duration of the coating process to achieve a uniform adherent coating of metal oxide on SiC<sub>p</sub>. Electroless Ni-P coated and Sol-gel metal oxide coated SiC<sub>p</sub> were characterized using X-ray diffraction (XRD), Scanning Electron Microscopy (SEM) and Energy Dispersive Analysis of

## INTERFACIAL DESIGN AND DEVELOPMENT OF Cu/SiC MMCs FOR THERMAL MANAGEMENT APPLICATIONS BY PM ROUTE

X-rays (EDAX). The parameters for the coating process were optimized based on the analysis of characterization results.

### Preparation of Cu/SiC<sub>p</sub> MMC blends

Cu(60 vol%) and SiC(40 vol%) were blended in a Double-cone blender with hardened steel balls(~8 mm in diameter). The ball to charge ratio was maintained as 10:1. Cu/As-received SiC<sub>p</sub> MMC blends were prepared taken up initially using the Double cone blender to optimize the blending duration so as to achieve a uniform dispersion of the reinforcement particles in the matrix. The mixtures were blended for different durations (10, 15, 20 and 30 minutes). The milling duration was optimized based on the chemical estimation of Cu content in the composite mixture blended for different durations. Representative samples (2 No.s) were randomly picked from the each of the above mixtures, dissolved in con. HNO<sub>3</sub> and copper was electrolysed using electroplating method. The difference in weight of the empty electrode and after completion of electrolysis indicated the weight of copper in one gram of sample. The prepared composite powders were characterized using SEM to ascertain and validate the concurrence of experimental and chemical analysis results. XRD of the blended mixtures was also taken up to ascertain the absence of any contaminant pick-up from the milling media. Cu/NiP coated SiC<sub>p</sub> and Cu/metal oxide coated SiC<sub>p</sub> composites were prepared employing the optimized process parameters.

### Cold Isostatic Pressing (CIP) and sintering of the Cu/SiC MMCs

The Cu / as-received SiC(600 grit) composite powders were mixed with 3wt% of PEG(Poly Ethylene Glycol) using a mortar and pestle and intermittently dried in a microwave oven and subsequently sieved before filling into rubber

moulds. The moulds were CIPed at 3000 bar for 2 minutes using a EPSI Cold Isostatic Press (Fig.1a). CIPing of Cu/As-received SiC(400 grit) was also taken up using 5% PVA(Poly Vinyl Alcohol) as the binder material at pressure of 800 bar for 6 minutes. The green compacts [Fig. 1b] were sintered in flowing N<sub>2</sub> at 1173 K for 2 hours using a sintering furnace to obtain a dense component (Fig. 1c). The ramp up was maintained at 4°C/minute. Density measurements of the sintered compacts were taken up followed by Image analysis using Nikon ECLIPSE LV150 microscope and SEM.

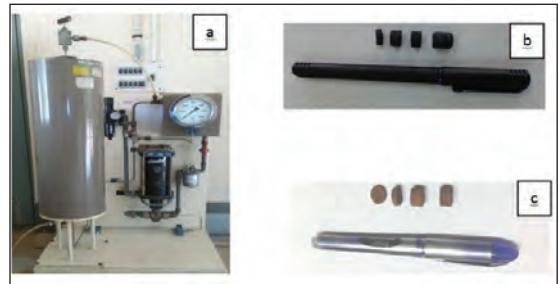


Fig.1 a. EPSI Cold Isostatic Press b. Green Cu/SiC compacts and c. Sintered compacts

### Density and porosity measurements

The dry weight (W<sub>1</sub>) of the sample was measured after sintering. The specimen was then placed in vacuum in-order to clean the pores and subsequently immersed in distilled water. The sample was removed from vacuum and its weight (W<sub>2</sub>) was measured when immersed in deionized water and. Further, the sample was weighed (W<sub>3</sub>) after removal of deionized water. The percentage porosity is given by equation (1). The actual density was arrived on calculation of the percentage porosity.

$$\% \text{porosity} = (W_3 - W_1 / W_3 - W_2) \times 100\% \text{-----(1)}$$

Results & Discussion

The SEM micrographs and corresponding EDAX results (insets) of yttrium oxide and NiP coated SiC<sub>p</sub> are shown in Figs. 2 and 3 respectively.

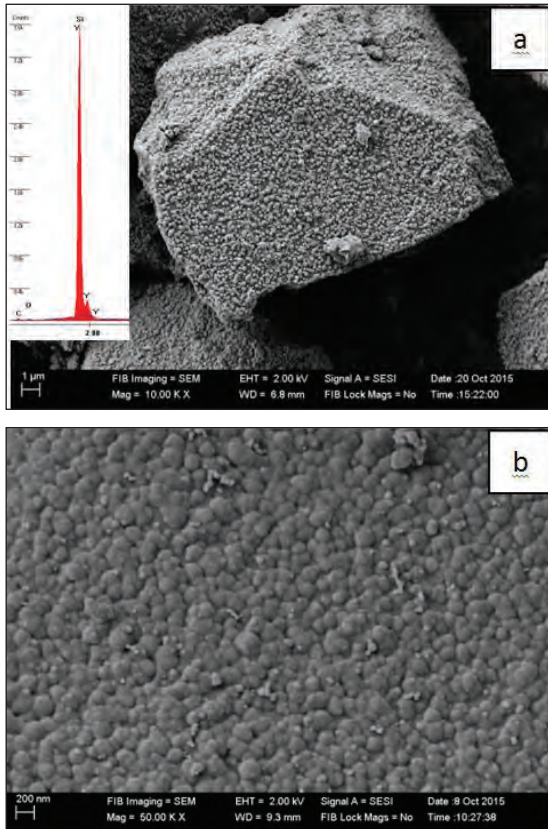


Fig. 2 a. Metal oxide coatings on SiC<sub>p</sub> b. Morphology and size distribution of the metal oxide coating

SEM studies reveal the adherent, continuous and substantially uniform deposition of electroless nickel phosphide and Sol-gel yttrium oxide coatings on SiC<sub>p</sub>. XRD and EDAX analysis of the coated SiC<sub>p</sub> evidenced the purity of the deposited coatings. The XRD analysis of coated SiC<sub>p</sub> indicated the phase purity of the coatings. The presence of monoclinic base-centred NiP<sub>2</sub>

and cubic yttrium oxide phases were observed as given in Figs. 4 and 5. The absence of any impure phases associated with the coating methodologies employed is evident from the reported results. This emphasizes the quality of the process methodologies established and reported. The parameters of the Sol-gel coating process for deposition of yttrium oxide on 400 grit size SiC was optimized in addition to the earlier reports on 600 grit size SiC. The coating was uniform and continuous in comparison to the substantially uniform deposition of yttrium oxide as reported earlier [9].

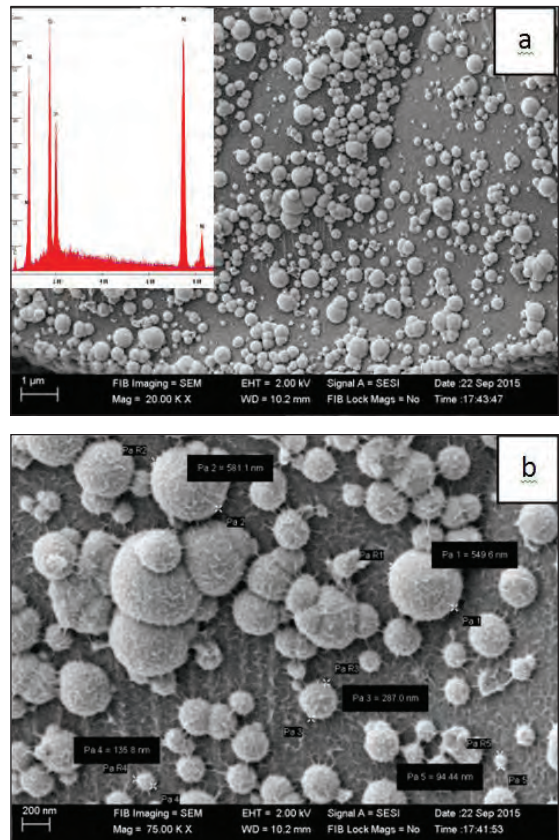


Fig. 3 a. NiP coatings on SiC<sub>p</sub> b. HRSEM image showing typical size distribution and morphology of NiP coating

# INTERFACIAL DESIGN AND DEVELOPMENT OF Cu/SiC MMCs FOR THERMAL MANAGEMENT APPLICATIONS BY PM ROUTE

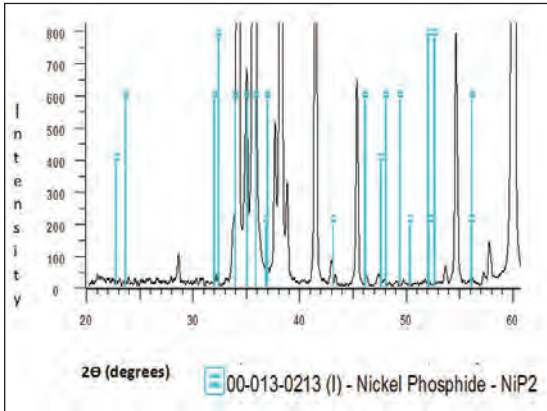


Fig. 4 XRD analysis of NIP coated SiC<sub>p</sub>

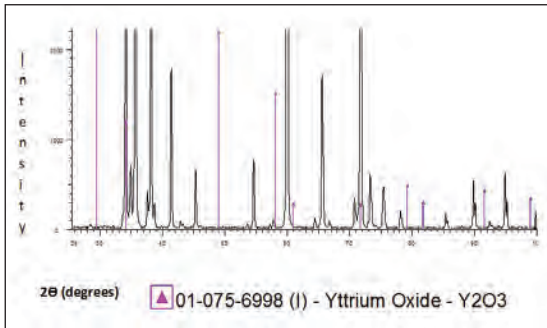


Fig. 5 XRD analysis of yttrium oxide coated SiC<sub>p</sub>

The duration of the blending process was optimized as 15 minutes based on the results of chemical estimation results tabulated in table 1.

Table 1: Cu estimation in Cu/SiC composite blends

Blending duration (minutes)	Amount of copper present in 1 gm of composite mixture (grams)	
	Sample 1	Sample 2
10	0.8050	0.8412
15	0.8052	0.8072
20	0.8635	0.8084
30	0.8142	0.7882

SEM of the composite blends shown in Fig. 6 restate that composites blended for 15 minutes resulted in uniform dispersion of the reinforcement and the matrix components in the

composite blend. XRD analysis indicated (Fig. 7) no contamination pick-up from the high carbon steel balls during the blending operations.

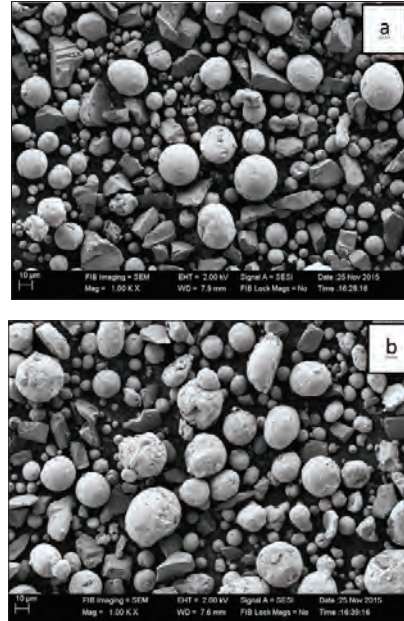


Fig. 6 SEM image showing a. uniform distribution of matrix and reinforcement after 15 minutes of blending and b. Non-uniform distribution of matrix and reinforcement after 30 minutes of blending

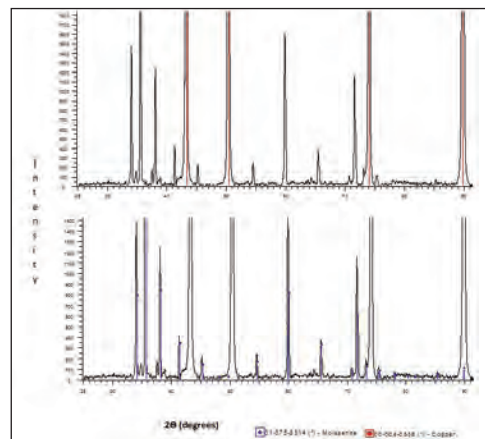
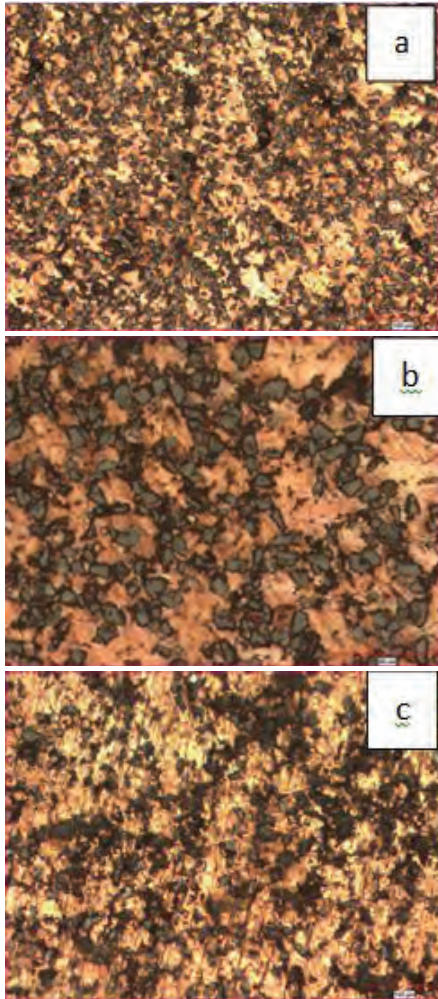


Fig. 7 XRD analysis of composite blends showing presence of copper and SiC

Optical microscopy of the CIPed/sintered specimens as shown in Fig. 8 revealed the uniform distribution of the second phase in the matrix.



*Fig. 8 Optical microscopy of sintered MMCs a & b. Cu/As-received SiC(600 grit) c. Cu/As-received SiC(400 grit)*

The Cu/As-received SiC 600 grit size MMCs using PEG as the binder material recorded a density of 55% TD. The distribution of the reinforcement was substantially uniform and

the dark regions (Fig. 8a) in the micrographs indicate the presence of pores. Prior to CIPing pot milling was taken up using alumina balls with ball to charge ratio as 3:1 for a duration of 2 h to achieve good distribution of binder material in the composite blend. SEM images (Fig. 9) reveal the recrystallization of Cu matrix after sintering. The effect of the absence of pot milling prior to CIPing of Cu/as-received SiC 400 grit size MMCs is evident from the presence of reinforcement agglomeration in the micrographs. Hence, pot milling of the composite blends is considered to be an essential aspect for uniform agglomerate free distribution of the second phase in the matrix. The binder is expected to be well distributed as a result of pot milling prior to CIPing. 80% TD was attained for 400 grit sized SiC<sub>p</sub> reinforced Cu composites.

SEM images of the Cu/As-received SiC 600 grit size sintered composites reveal the uniform distribution of the second phase and the presence of porosity in support to the image analysis results reported. SEM of Cu/As-received SiC 400 grit sizes were also in agreement with the earlier microscopic studies. The presence of porosity in this case could be attributed towards the formation of agglomerates of reinforcement in the Cu matrix. This may be due to the absence of pot milling prior to CIPing of the composite blends.

#### **Future scope**

Further experiments are underway to optimize the compaction process parameters by varying the percentage of binder material and increasing the hold time during CIPing and sintering. The influence of the metal oxide and nickel phosphide

# INTERFACIAL DESIGN AND DEVELOPMENT OF Cu/SiC MMCs FOR THERMAL MANAGEMENT APPLICATIONS BY PM ROUTE

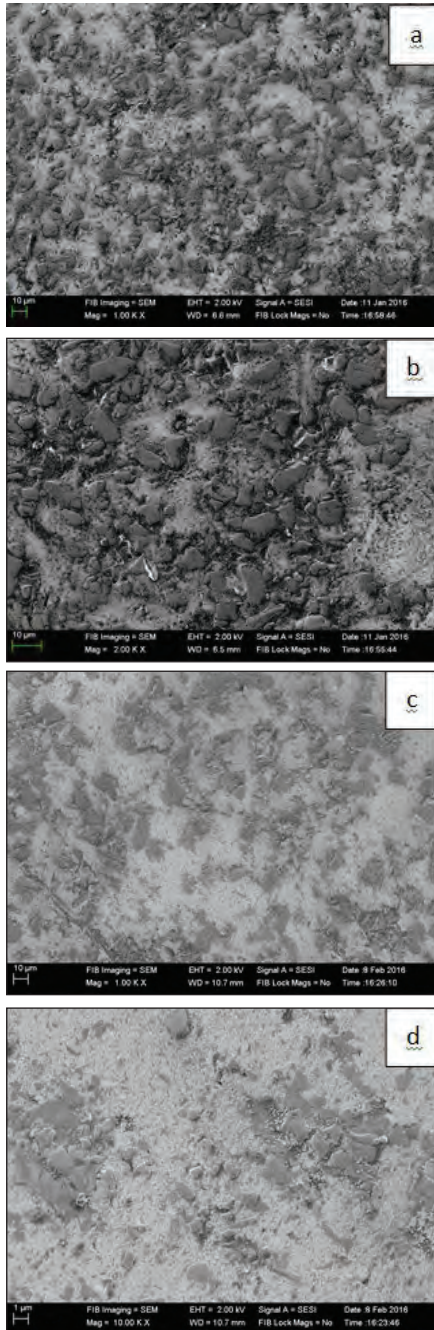


Fig. 9 SEM images of sintered composites a & b. Cu/As-received SiC 600 grit size ; c & d. Cu/As-received SiC 400 grit size

barrier coatings on the thermal conductivity of the proposed interface tailored Cu/SiC MMCs will be taken up after optimization of the compaction process.

## Acknowledgement

SK wishes to thank Directors, CMTI and NAL for the infrastructural support extended. SK wishes to acknowledge Shri. S. Arumugasamy and Dr. C. K. Srinivasa, CMTI for the continuous encouragement and support received. RS would like to acknowledge Principal, SIT-Tumkur and Director, CMTI for providing the opportunity for carrying out this M.Tech. project work.

## References

- [1] M.Z. Bukhari, M.S.J. Hashmi and D. Brabazon, "Application of Metal Matrix Composite of CuSiC and AlSiC as Electronics Packaging Materials", The 28th International Manufacturing Conference, 2011
- [2] Harrigan Jr WC, " Commercial processing of metal matrix composites", Mater. Sci. Eng. No 224(1998) 75-82
- [3] G. Sundberg, P. Paul, C. Sung and T. Vasilos, Identification and characterization of diffusion barriers for Cu/SiC systems, Journal of Materials Science, 40(2005) 3383-3393
- [4] Th. Schubert, B. Trindade, T. Weißgärber and B. Kieback, "Interfacial design of Cu-based composites prepared by powder metallurgy for heat sink applications", Mater. Sci. Eng. A 475(2008) 39-44
- [5] Glenn Sundberg, Pradeep Paul, Changmo Sung and Thomas Vasilos, "Fabrication of CuSiC metal matrix composites", Journal of Materials Science (2006) 41, Issue 2, 485-504

## INTERFACIAL DESIGN AND DEVELOPMENT OF Cu/SiC MMCs FOR THERMAL MANAGEMENT APPLICATIONS BY PM ROUTE

---

- [6] G. Celebi Efe, I. Altinsoy, M. Ipek, S. Zeytin and C. Bindal, "Effect of SiC particle size on properties of CuSiC metal matrix composites", Proc. Of the Intl. Congress on Advances in Appl. Phy. & Materials Science, 2011
- [7] Kuen - Ming Shu and G. C. Tu, "The microstructural and thermal expansion characteristics of Cu/SiCp composites", Mat. Sci. & Engg. A, 349,(2003), 236-247
- [8] M.Z. Bukhari, M.S.J. Hashmi and D. Brabazon, "The effects of sintering parameters study to the microstructure and thermal properties of Cu/SiC composite for electronics packaging application", 3rd Intl Malaysia-Ireland Joint Symposium on Engg., Science and Business, 2013
- [9] S. Kavithaa, B.C. Pai, R.M. Pillai, K.G. Satyanarayana and S. Banerjee, "An improved sol gel processfor coating ceramic reinforcements with rare earth oxides", PAN0370/DEL/2008

# DEVELOPMENT OF DRY RECYCLING PROCESS FOR (Th,U)O<sub>2</sub> CLEAN REJECTED OXIDE SINTERED PELLETS

P. M. Khot\*, S. K. Shotriya, K. Subbarayal, Niraj Kumar, B. Singh, B. Surendra, A. K. Mishra, P. G. Behere, Mohd Afzal

Advanced Fuel Fabrication Facility, Bhabha Atomic Research Centre, Tarapur, India

**Abstract :** Thorium utilization is an important aspect of Indian three stage nuclear power program. Construction of thorium based 300 MWe Advanced Heavy Water Reactor (AHWR) is an important step for this purpose. (Th-LEU) MOX fuel is the proposed fuel AHWR LEU-300. The fuel composition for AHWR LEU-300 is ThO<sub>2</sub> containing nearly 13 to 30 % UO<sub>2</sub> (composition in wt. %).

The (Th,U)O<sub>2</sub> mixed oxide pellets are generally prepared by the conventional powder metallurgy route. During fabrication of (Th,U)O<sub>2</sub> MOX fuel, a small percentage (10–15%) of pellets gets rejected at various stages. The sintered rejects are broadly divided into two categories; clean reject oxide (CRO) and dirty reject oxide (DRO) depending on the chemical and physical characteristics of the pellets. The CRO consist of sintered MOX pellets rejected either due to low density, physical defects such as cracks, chips, blisters etc. or not meeting the physical specifications.

Dry recycling of sintered (Th,U)O<sub>2</sub> MOX CRO using thermal pulverization technique involving oxidation and reduction is difficult since ThO<sub>2</sub> is stable stoichiometric compound and does not oxidize unlike UO<sub>2</sub>, which oxidizes easily to U<sub>3</sub>O<sub>8</sub> and UO<sub>3</sub>. Wet recycling of (Th,U)O<sub>2</sub> MOX CRO also pose problem due to difficulty in nitric acid dissolution without addition of HF. The presence of UO<sub>2</sub> in (Th,U)O<sub>2</sub> MOX CRO makes it somewhat easier recycling as it is amenable to oxidation treatment. In dry recycling of (Th,U)O<sub>2</sub> MOX CRO, mechanical pulverization comprising of jaw crushing, attritor milling and sieving has been coupled with thermal pulverization involving oxidation. In this study dry recycling of (Th, 14% U)O<sub>2</sub> MOX pellets were carried out with varying content of % CRO. From the study it has been observed that CRO upto 20-30% can be easily recycled with acceptable density (90-95% TD) and quality of pellets.

This paper describes the fabrication process developed for dry recycling of (Th,U)O<sub>2</sub> MOX CRO. In this study dry recycling of (Th, 14% U)O<sub>2</sub> MOX pellets were carried out with varying content of % CRO. Effect of % CRO addition on powder characteristics and pellet density were studied. Characteristics of the virgin powder and powder prepared by dry recycling technique were compared. The (Th, 14% U)O<sub>2</sub> pellets fabricated from virgin powder and dry recycling were characterized for density, metallic impurities,  $\alpha$ -autoradiography and the results obtained were compared.

**Keywords:** AHWR,(Th,Pu)O<sub>2</sub> MOX , CRO, Recycling

## 1. Introduction

The Indian power program has been framed bearing in mind optimum utilization of domestic uranium and thorium reserves with the objective of proving long term energy security

to the country. Thorium utilization is important aspect in third stage of nuclear power program. Thorium will be utilized in closed cycle in this stage where Advanced Heavy Water Reactor of 300MW is going to be constructed. (Th-LEU)

## DEVELOPMENT OF DRY RECYCLING PROCESS FOR (Th,U)O<sub>2</sub> CLEAN REJECTED OXIDE SINTERED PELLETS

MOX fuel is the proposed fuel AHWR LEU-300[1]. The fuel composition for AHWR LEU-300 is ThO<sub>2</sub> containing nearly 13 to 30 % UO<sub>2</sub> (composition in wt. %).

The (Th,U)O<sub>2</sub> mixed oxide pellets are generally prepared by the conventional powder metallurgy route involving cold compaction and sintering. (Th,U)O<sub>2</sub> mixed oxide pellets containing nearly 13 to 30 % UO<sub>2</sub> will be fabricated for AHWR LEU-300. During fabrication of (Th, U)O<sub>2</sub> MOX fuel, a small percentage of pellets gets rejected at various stages. These process rejects comprises of green rejects formed during the cold pressing and rejected sintered pellets. Dust produced during grinding of oversize sintered pellets also contributes to process rejects. Sintered rejects are broadly divided into two categories; clean reject oxide (CRO) and dirty reject oxide (DRO) depending on the chemical and physical characteristics of the pellets. An attempt has been made to recycle the rejected pellets which do not meet the specification of physical characteristics.

Various dry and wet techniques has been developed for recycling of sintered (U,Pu) O<sub>2</sub> MOX CRO [2-5]. However, no study has been reported in literature for recycling of sintered (Th,U)O<sub>2</sub> MOX CRO. Dry recycling of sintered (Th,U)O<sub>2</sub> MOX CRO is challenging task since ThO<sub>2</sub> is relatively inert due to its stable oxidation state and does not oxidize unlike UO<sub>2</sub>, which oxidizes easily to U<sub>3</sub>O<sub>8</sub> and UO<sub>3</sub> [6]. ThO<sub>2</sub> and ThO<sub>2</sub> based mixed oxide fuels are relatively inert and, unlike UO<sub>2</sub> and (U,Pu) O<sub>2</sub> fuels, do not dissolve easily in concentrated nitric acid without addition of HF. Addition of small quantities of HF in concentrated HNO<sub>3</sub> is essential which cause corrosion of stainless equipment and pipings in reprocessing plants [5].

This paper describes the fabrication process developed for dry recycling of (Th,U)O<sub>2</sub> MOX

CRO. In this study dry recycling of (Th, 14% U) O<sub>2</sub> MOX pellets were carried out with varying content of % CRO. Effect of % CRO addition on powder characteristics and pellet density were studied. Characteristics of the virgin powder and powder prepared by dry recycling technique were compared. The (Th, 14% U) O<sub>2</sub> pellets fabricated from virgin powder and dry recycling were characterized for density,  $\alpha$ -autoradiography and the results obtained were compared.

### 2. Fabrication

ThO<sub>2</sub> and UO<sub>2</sub> powders of specified characteristics given in Table 1 and used for fabrication of mixed (Th-U)O<sub>2</sub> fuel pellet. The flowsheet for fabrication of (Th,14%U)O<sub>2</sub> MOX fuel along with dry recycling routes for recycling of CRO is shown in Fig. 1. As received thorium dioxide powder from oxalate route is milled in attritor for 20 min to break its platelet morphology. Milled thorium dioxide and uranium dioxide were first weighed and then milled together in attritor to get the required enrichment and homogeneity. The milled material was pre-compacted and the pre-compacts were granulated in the size range of 400-2000  $\mu$ m. These granules were used in final compaction to make the green pellets. Final compaction of (Th, 14%U)O<sub>2</sub> MOX pellets was carried out in a hydraulic press. Sintering of green pellets was done in a batch type resistance heating furnace under reducing atmosphere (mixed N<sub>2</sub>-7% H<sub>2</sub> gas) at 1650°C for 4-6 h. Physical specifications of sintered pellets for AHWR are given in Table 2. The inspected pellets were loaded into clad tubes for encapsulation.

*Table 1: Characteristic ThO<sub>2</sub> and UO<sub>2</sub> powders*

Sr. No	Characteristics	ThO <sub>2</sub> Powder	UO <sub>2</sub> Powder
i)	Apparent density (gm/cm <sup>3</sup> )	0.70	2.0
ii)	Specific Surface Area (m <sup>2</sup> /gm)	1.53	2-3
iii)	Theoretical density (gm/cm <sup>3</sup> )	10.00	10.96
iv)	Oxygen to Metal Ratio	2.00	≤2.15
v)	Total impurities (ppm)	<1200	< 800

## DEVELOPMENT OF DRY RECYCLING PROCESS FOR (Th,U)O<sub>2</sub> CLEAN REJECTED OXIDE SINTERED PELLETS

Table 2: Physical specifications of (Th-U)O<sub>2</sub> MOX fuel pellets.

Sr.No	Characteristics	Specifications
i)	Density of the pellet	90-95 % of T.D
ii)	Diameter of the pellet	9.7± 0.10 mm
iii)	L/D Ratio	0.5 to 1.0
iv)	Grain Size	5 to 50 μ

### 3. Development of Dry method for recycling of MOX (Th,14%U)O<sub>2</sub> CRO

During fabrication of (Th,U)O<sub>2</sub> MOX fuel, a small percentage (10–15%) of pellets gets rejected after quality control inspection and during various stages of encapsulation. The CRO consist of sintered MOX pellets rejected either due to low density, physical defects such as cracks, chips, blisters etc. or not meeting the physical specifications as per Table 2. This CRO contain significant amount of uranium which has to be recovered and recycled back into production line.

It was difficult to recycle (Th,U)O<sub>2</sub> MOX CRO due to stable oxidation state of thorium oxide which limits thermal pulverization involving oxidation and reduction. The presence of UO<sub>2</sub> in (Th,U)O<sub>2</sub> MOX CRO makes it somewhat easier recycling as it is amenable to oxidation treatment. Direct thermal pulverization of (Th,U)O<sub>2</sub> MOX CRO was unable to disintegrate rejected pellets into powder even at higher oxygen potential due to its higher thorium content with stable oxidation state. The stresses generated from the phase change of UO<sub>2</sub> to U<sub>3</sub>O<sub>8</sub> were less due to presence of 14% UO<sub>2</sub> only. It was observed that only a few pellets of CRO showed cracking in pellet. Therefore, in dry recycling of (Th,14%U)O<sub>2</sub> MOX CRO, mechanical pulverization comprising of jaw crushing, attritor milling and sieving has been coupled with thermal pulverization involving oxidation.

### 3.1 Powder conditioning treatments

#### 3.1.1 Jaw crushing

Initially, Mechanical pulverization of (Th,14%U)O<sub>2</sub> MOX CRO was carried out using a jaw crusher. Modification in the feeding hopper of the jaw crusher was carried out to minimize dust generated during mechanical pulverization of MOX pellets. The feed material was passed through the no-rebound hopper before entering the crushing chamber. The size reduction takes place in the wedge shaped area between the fixed crushing arm and the one moved by an eccentric drive shaft. The elliptical motion crushed the pellets which then fell under gravity into a removable collector. The sintered MOX pellets with a large feed size of 11 mm were crushed down to < 1 mm in a multiple step.

#### 3.1.2 Oxidation and Reduction

The fine MOX CRO powder obtained after jaw crushing provided more reaction site for oxidation of UO<sub>2</sub>. The crushed CRO was oxidized at 700°C for 4 h in air atmosphere. In case of CRO addition more than 30% in batch preparation, the oxidized CRO was then reduced at 700°C for 4 h in presence of N<sub>2</sub>-7% H<sub>2</sub> atmosphere to eliminate the excess oxygen present.

#### 3.1.3 Attritor milling

The oxidized CRO was further milled in attritor for about 40 min for particle size reduction which in turn improve the sinterability of the powder.

#### 3.1.4 Sieving

The milled powder was further sieved though #100 mesh sieve. The -100# fraction obtained after sieving was used for batch making. On the other hand, + 100# fraction of powder obtained after sieving was recycled back to oxidation step of recycling and further processed as per flowsheet showed in Fig.1.

# DEVELOPMENT OF DRY RECYCLING PROCESS FOR (Th,U)O<sub>2</sub> CLEAN REJECTED OXIDE SINTERED PELLETS

## 3.1.5 Batch preparation

In order to study the effect of % CRO addition on green and sintered density, batches of about 500 g were fabricated with varying content of CRO. Batches of MOX powder of 5 Kg was prepared from virgin powder as well as from varying % CRO powder and further processed as per flowsheet shown in Fig.1. Details of all batches made are as follows:

1. Virgin batch
2. 30% CRO + Virgin ThO<sub>2</sub> + virgin UO<sub>2</sub> p/w
3. 50% CRO + Virgin ThO<sub>2</sub> + virgin UO<sub>2</sub> p/w
4. 100% CRO p/w

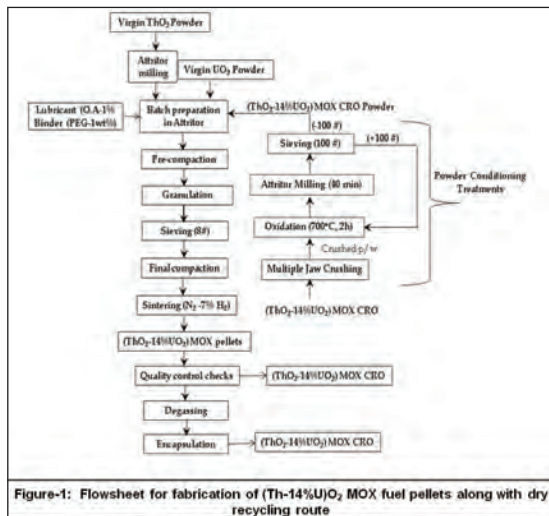


Figure-1: Flowsheet for fabrication of (Th-14%U)O<sub>2</sub> MOX fuel pellets along with dry recycling route

## 4. Results & Discussion

### 4.1 Density

The green and sintered density was measured geometrically. The green and sintered densities along with their powder characteristics are shown in Table 3. The green density of the batches fabricated from recycled CRO was higher than that of virgin batches. This was

due to higher apparent and tap density of MOX powder obtained from CRO batches (Table 3). However, the sintered densities of CRO batches were found to be less than that of virgin batches. The shrinkage of CRO batches (10 %) was lower compared to virgin batches (13%) due to lower surface area and higher particle size compared to virgin powder which in turn affected the sinterability of the powder. Tooling of lower size was required for CRO batches to achieve sintered to size pellet because of less diametrical shrinkage in green pellets fabricated. The percentage of acceptance was marginally higher in CRO batches compared to that of virgin batches may be due to higher green density which in turn reduces the handling defect in the green pellets.

Table 3: Physical characteristics of powder and pellets obtained via dry route

Sr. NO	Batch details	Powder characteristics		Pellet data		Yield %
		Apparent density (g/cc)	Tap density (g/cc)	Green density (% TD)	Sintered density (% TD)	
1	Virgin batch	3.4-3.5	3.65-3.78	66-67	93-95	89-90
2	30% CRO	3.6-3.75	3.95-4.12	72-73	91-93	91-92
3	50% CRO	3.80-3.91	4.15-4.26	73.5-74	88-90	92-95
4	100% CRO	4.17-4.25	4.31-4.42	79-80	85-87	92-95

### 4.2 Effect of % CRO addition

The effect of addition of % CRO on green and sintered density of (Th,U)O<sub>2</sub> MOX pellets is shown in Table 3. Addition of CRO upto 50 % showed significant improvement in green density from 66 to 74 % TD due to increased apparent and tap density of the MOX powder. However, the addition of CRO above 50 % showed least improvement in green density of MOX pellets. Sintered density showed decreasing trend from 0-100 % CRO addition. The decrease in sintered density with CRO addition may be attributed to significant reduction in sinterability of powder due to its lower surface area and larger particle size.

From the study it has been observed that (Th,14%U)O<sub>2</sub> MOX CRO upto 20-30% can be

## DEVELOPMENT OF DRY RECYCLING PROCESS FOR (Th,U)O<sub>2</sub> CLEAN REJECTED OXIDE SINTERED PELLETS

easily recycled with acceptable density (>90% TD) and quality of pellets.

### 4.3 Metallic impurities:

The metallic impurities of sintered (Th,14%U)O<sub>2</sub> MOX pellet obtained from virgin and CRO powder (dry recycling route) determined by atomic emission spectroscopy (AES) using DC arc as an excitation source are shown in Table 4.

*Table 4: Metallic impurities in a typical sintered (Th,14%U)O<sub>2</sub> MOX pellet obtained via dry recycling method*

Sr. No	Element	Specification in ppm	(Th,14%U)O <sub>2</sub> sintered pellet from virgin batch	(Th,14%U)O <sub>2</sub> sintered pellet from dry recycling CRO batch
1	B	1	0.5	0.4
2	Cd	1	0.5	0.5
3	Cr	400	31	71
4	Cu	400	37	38
5	Fe	800	197	331
6	Mg	400	70	85
7	Mo	400	47	58
8	Na	400	< 10	< 10
9	Ni	400	< 10	< 10
10	Pb	400	< 10	< 10
11	V	400	46	43
12	Zn	400	126	138
13	Ca	500	239	264
14	Si	400	165	191

The CRO batches showed more pick up of Fe, Cr impurities compared to virgin batches may be due to additional processing steps such as jaw crushing, attritor milling and sieving. (Th,14%U)O<sub>2</sub> MOX pellets from virgin and CRO batches showed all the metallic elements including critical elements B and Cd within specification limits.

### 4.4 $\alpha$ -autoradiography:

Homogeneity of (Th,14%U)O<sub>2</sub> fuel pellet from CRO batches was evaluated by  $\alpha$ -autoradiography. The presence of fissile rich zone in mixed oxide fuel pellet leads to higher fission gas release and fuel failure [7,8]. So it was necessary that size of agglomerate should be as low as possible and its distribution through the matrix should be uniform.

Fig 2 shows  $\alpha$ - autoradiograph of (Th,14%U)O<sub>2</sub> sintered MOX pellet from dry recycling CRO batches. From the  $\alpha$ - autoradiograph it has been observed that distribution of uranium in thorium matrix was uniform. The maximum size of uranium agglomerate was less than the specified value (<400  $\mu$ m).



*Fig. 2:  $\alpha$ -autoradiograph of (Th,14%U)O<sub>2</sub> pellet fabricated by dry recycling route sintered in N<sub>2</sub>-7%H<sub>2</sub> at 1650°C for 4 Hr*

## 5. Conclusion

- Flowsheet for dry recycling of (Th,14%U)O<sub>2</sub> MOX CRO has been successfully developed and considerable quantity of CRO recycled using existing facility of AFFF, Tarapur.
- (Th,14%U)O<sub>2</sub> MOX pellets from recycled batches containing 20-30% CRO meets all desired physical and chemical specifications.
- All CRO batches showed higher green density and lower sintered density as compared to virgin batches.
- Homogeneity evaluation of (Th,14% U)O<sub>2</sub> fuel pellet fabricated via dry recycling route showed uniform distribution of uranium in thorium matrix.

## Acknowledgments

Authors are very thankful to all the staff members of Oxide Fuel Section (OFS) for their active support in carrying out this work.

## DEVELOPMENT OF DRY RECYCLING PROCESS FOR (Th,U)O<sub>2</sub> CLEAN REJECTED OXIDE SINTERED PELLETS

---

### References

- [1] Neelima Prasad et. al., "Advanced Heavy Water Reactor-LEU (AHWR-LEU): A Reactor Safeguard by Design", IAEA-CN-184/207.
- [2] P.M. Khot et. al., "Development of recycling processes for clean rejected MOX fuel pellets, Nuclear Engineering and Design", 270 (2014) 227-237,
- [3] Larson et. al., "Dry recycle process for recovering UO<sub>2</sub> scrap material", United State patent (US2002/0005597 A1), 17 Jan 2002.
- [4] Vandergheynst et. al., "Method for dry process recycling of mixed (U,Pu)O<sub>2</sub> oxide nuclear fuel waste", United State Patent (US6,783, 706B1), 13 Aug 2004.
- [5] Masumichi KOIZUMI et. al., Journal of Nuclear Science and Technology, 20 (7), 1983, pp. 529-536.
- [6] Thorium fuel cycle – Potential benefits and challenges IAEA-TECDOC-1450, May 2005.
- [7] A.G.Leyva, D.Vega, V.Trimacor, D. Mar, J.Nucl. Mater. 303 (2002)29.
- [8] Status and advances in MOX technology, technical report series no. 415, IAEA Vienna-2003.

# AUTOMATION OF SINTERED BUSH SECONDARY OPERATION - SIZING

Disha Nikam

Nikam Iron Sintered Products Private Limited, Kolhapur, India

**Abstract :** With the growing market of automobiles and home appliances in India, demand for self-lubricating sintered bushes is also growing rapidly. One of the prominent operations involved in manufacturing these sintered bushes is Sizing – a secondary operation done to increase density, to achieve dimensional accuracy and surface finish for bush. However this operation has become a major bottleneck while manufacturing large volumes. Each bush is sized manually one by one on conventional presses that reduces production speed, increases time and cost, becomes operator dependent and mainly involves major operator accidents. Due to these limitations, efforts were directed if this entire sizing operation of bushes can be automated. A mechanism of rotating disc with a vibratory bowl feeder was designed that made sizing operation independent of operator. A pneumatic embossing unit was also included enabling both sizing and embossing operations together in one machine. Bushes are put in to vibratory bowl feeder after which they get embossed, sized and get collected in the container automatically. This effort increased production (two and a half times) of bushes, eliminated operator accidents, reduced electricity (energy) requirement, required less space and reduced cost. The bottleneck in the manufacturing of bushes got removed and operator safety was also ensured. This automation has been extended to all other types of bushes such as spherical, bushes with flange or orientation and 198 type bushes. The same technique can be used for high tonnage machines with relevant changes in the same. Thus Sizing operation and embossing operation were merged in one machine with improved design, production and safety.

**Keywords :** Sizing, sintered bush, accidents, automated, operator independent, increased productivity, safety,

## 1. Introduction

Self-lubricating metal bearings are used extensively in the industries of automobile, textile, agricultural and home appliances manufacturing and also to a small extent in small motors of fractional HP capacities. With India growing at a rapid pace of approximate growth rate of 7.4% in Q2 2015-16 and with the increasing application of sintered metal bushes in automobile sectors and home appliances such as washing machines, refrigerators, electric clocks manufacturing industry, the demand is steadily increasing for this item.

The processes involved in manufacturing these bushes are – powder blending, forming,

sintering, embossing and secondary operation performed as per requirement. One of the prominent secondary operation involved in manufacturing these bushes is Sizing – an operation done to increase density, to achieve dimensional accuracy and to improve surface finish. However this operation has become a major bottleneck while manufacturing large volumes. Currently each bush is sized manually one by one over large mechanical conventional presses that require more space, more power and reduce production speed drastically. Embossing done before sizing operation is also an important but another time consuming operation. Such manual sizing and embossing not only reduces productivity but also involves major operator

accidents. Due to all these limitations of mainly operator dependency involving operator fatigue and accidents along with slow speed sizing, increasing cost and energy requirements, efforts were directed if this entire sizing operation of bushes can be automated. In this paper we present completely automated sizing press AUTOSIZER that combines both embossing and sizing operation, increases speed, reduces cost-energy-space requirements and makes sizing operation independent of operator enhancing safety. A simple rotary mechanism is designed that uses indexing plate and vibratory feeder bowl to size each bush and forwards them to get collected in bin automatically. This automation is found applicable for all types of bushes such as plain, spherical, flange or with orientation bushes and more. Also same technique can be used for high tonnage sizing presses with relevant changes in the same.

Paper is organized as follows: Section 2 explains the detailed mechanism of automation of sizing press. Section 3 points out all the precautions taken while designing the machine after successive trials on it. Section 4 lists all unique features of AUTOSIZER. Section 5 elaborates on positive results achieved with AUTOSIZER over conventional press. Some related work is discussed in Section 6. We outline conclusions and future work in Section 7.

### 2. AUTOSIZER mechanism

A basic sizing press design was initiated based on tonnage needed at the output. We designed AUTOSIZER for 30 tons load with 5 HP motor used to rotate the flywheel to achieve the desired load. Flywheel further uses a gear box transmission to rotate the main shaft. Cam-follower mechanism is used to press top punch and to eject the item from bottom punch. Thus two cams are incorporated on the main shaft – one for pressing top punch and other for ejection

from bottom punch. Fig. 1 shows complete machine AUTOSIZER with motor at the top and flywheel at the rear portion of the machine. Main shaft along with cams and chain sprocket pair are on the top part of the machine behind the name written on the machine shown in Fig.1. Since this basic 30 tons sizing press places flywheel at the back of the machine and uses cam follower mechanism for sizing, the design becomes sleek and simple and requires less space as compared to conventional presses. 5 HP motor uses a star-delta connection that starts motor softly with low speed and later increasing it slowly. Such soft start elongates belt life and avoids abrupt start of motor. Die-set with top and bottom punch are set for the required bush to obtain its desired dimensions. When the bush is at the sizing location, top punch moves down



*Fig. 1 Autosizer*

## AUTOMATION OF SINTERED BUSH SECONDARY OPERATION - SIZING

and pushes the bush into the die pressing it. Then bottom punch ejects the bush up to the die level. This is same as normal sizing operation where operator places each bush on the sizing location and presses clutch to complete one cycle of sizing and then collects the bush from the location to the bin.

With AUTOSIZER, some additional design features are incorporated to remove this manual dependency.



*Fig. 2 An Indexing Plate*

An indexing plate as shown in Fig. 2 is designed that has 18 pockets in it where each pocket can hold one bush. The diameter of the pocket is same as the diameter of the bush with entry chamfer given to each pocket so that bush can fall into the pocket easily. This indexing plate has a center hole to position and place it on the sizing table with semi arc type teeth on the circumference. These arcs are designed to rotate the plate for a certain degree after sizing of each bush and to bring the next pocket to the sizing location. This plate is rotated with the help of a pin located on sizing table which in turn is rotated by chain sprocket pair connected to the main shaft. Thus the main shaft rotates chain sprocket which rotates the pin which further transfers this motion to indexing plate.

Bush enters into the pocket of indexing plate through the pipe that comes from pneumatic embossing unit. Embossing unit contains an air cylinder that pushes the bush against numbering letters thus embossing each bush one by one. After embossing, the bush gets forwarded to the pipe through which they fall into pocket of indexing plate. When one bush falls into the pocket, the disc rotates that then the next bush in line in the pipe falls in the next pocket and this continues on.



*Fig. 3 Vibratory Feeder Bowl*

Bush enters into the embossing unit through a pipe connected to vibratory feeder bowl shown in Fig. 3. This circular vibratory feeder bowl is designed in such a way that due to vibration and convex base, bush gets arranged in line one after the another on the periphery of the bowl and get transferred slowly to the rim of the bowl. Here all dis-oriented bushes fall back to the center of the bowl. Only bush with required orientation are allowed to pass forward through the pipe. This pipe is connected further to the pneumatic embossing unit.

Thus complete operation of AUTOSIZER is all bushes are poured into the vibratory bowl that vibrates and forwards them in a specific orientation in line into a pipe that is connected further to the pneumatic embossing unit. This

unit pushes each bush received from the pipe against embossing letters and forwards the numbered bush. These bushes then further go into a vertical pipe that ends at the pocket of indexing plate. Once a bush falls into pocket, the disc rotates and next bush falls in the next pocket. The rotating disc carries each bush placed in pocket to the sizing location for sizing. Once the bush reaches the sizing location, sizing cycle starts. Top punch moves down and sizes the bush. When the bush is sized, the top punch moves upwards and after certain delay, the bottom punch moves up to eject the bush. Once the bush reaches to the top level of the die, the indexing plate rotates moving the sized bush forward and bringing in the next bush for sizing.

A hole is given to the sizing table below the pocket of indexing plate. The sized bush falls off through this hole and gets collected in the bin kept below.

Thus in AUTOSIZER, an operator does initial die-set setting, pours the bush into vibratory bowl and collects them in the bin in the end. A close up snap shot is shown below in Fig. 4.

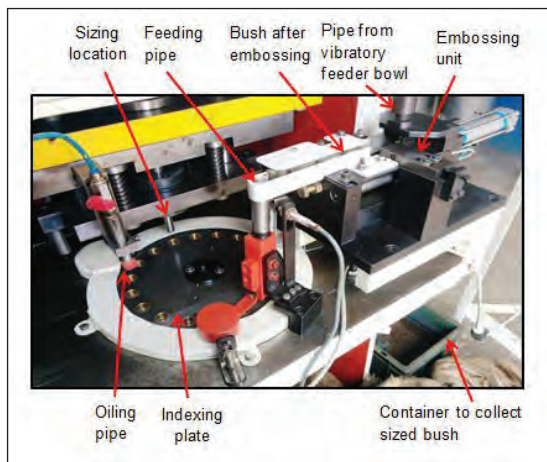


*Fig. 4 Close up snap shot of Autosizer*

### 3. Special precautions incorporated based on trials on AUTOSIZER

- Bushes put into vibratory bowl are forwarded through the pipe to embossing unit. Only those bushes with required orientation can enter the pipe. Rest all bushes fall back into the bowl.
- After embossing, the bushes are forwarded in straight line to fall in vertical pipe that is used to fill pocket of indexing plate. These bushes when being forwarded into the pipe follow a straight path and are covered from above with a rectangular plate so that they cannot move anywhere but to fall directly into the pipe.
- A sensor is placed near the place where the bush falls into the pocket. If the bush does not fall properly into the pocket or is still lifted above the pocket or is in any other position than desired, the proximity sensor senses it and stops the machine immediately.
- When the bush gets sized at the sizing location, if the bush does not eject positively from the top punch, positions of core rod and top punch are such adjusted that it throws back the bush into the pocket ensuring positive ejection.
- The sized bush moves forward to fall from the pocket below to get collected into the bin. If the bush doesn't fall off from the pocket then another proximity sensor is given to stop the machine in such case.
- Precautions are taken to prevent top punch pressing into the die beyond desired limit.
- Air cylinders are provided at the top of the machine to hold the load when top punch moves up at the end of each cycle.
- Drive motor is given a soft start during the start of the machine that enhances belt life significantly.

## AUTOMATION OF SINTERED BUSH SECONDARY OPERATION - SIZING

### 4. Table 1. Enlists all the salient features of AUTOSIZER-30

*Table 1*

Parameter	Details
No of strokes per min	40/41
Auto Embossing	Yes
Max OD × Length	φ25 × 30 L
Auto Parts lubrication	Yes
Counter to count productivity	Yes
Mode of operation	Auto/Manual

### 5. Table 2. Shows positive results achieved with AUTOSIZER over conventional sizing press

*Table 2*

	Conventional Sizing press (CS)	AUTOSIZER 30	Assumptions
<b>Production</b>	850*21 = 17850	2000*21 = 42000	CS produces 850 bush per hour as against 2000 in AUTOSIZER
<b>Cost incurred</b>			
1. Operator cost	500*3 = 1500	500*3 = 1500	Operator cost =Rs. 500 per shift.
2. Electricity cost	3.75*21*10 = 750	3.75*21*10 = 750	3.75kW electricity per hour consumed. Electricity rate = Rs10 per unit
3. Space	Requires more space	Sleek design that utilizes less space	
<b>Total</b>	<b>17850 components produced with cost Rs 2250 and more space</b>	<b>42000 components produced with cost Rs 2250 and less space</b>	

Productivity of AUTOSIZER-30 is seen to be more than double than that of conventional Sizing press using the same amount of time and cost.

An economical study was done to verify the same as shown in Table 2.

Calculations are made for one day with 3 shifts of 7 hours each. Hence No. of working hours in 3 shifts (3\*7) = 21 hours (\*worker productivity considered 7 hours in a shift)

Thus to summarize,

- Increased (more than twice) Productivity in same time and cost.
- Reduced dependency on labor. Labor required only for die-set setting and monitoring.
- Substantial reduction in operator related accidents.
- Reduction in space required.
- Clutch remains ON in Auto mode. This avoids continuous on-off of clutch that happens in manual mode. Thus wear and tear reduces ensuring long life.
- Gear box power transmission used instead of V-belt. This avoids belt slippage and ensuring longer life.
- Less maintenance required.
- Substantial reduction in cost due to above listed factors.

### 6. Related work

Efforts have been made earlier to automate sizing of bushes. Pick and Place robots are used to pick up a bush and place at sizing location. These robots are pneumatic and act as clamping device. This design is useful and automates

sizing operation. However pneumatic robots limit the number of strokes in a minute and also these machines do not ensure complete ejection of bush from top punch after sizing. Another design made in this area is two opposite rotating wheels placed vertically that carry the bush in a line on their periphery to the sizing location. This design requires operator to place the bush on the wheels and is not completely automatic. Also the speed is far less as compared to AUTOSIZER.

### 7. Conclusion and Future work

Currently AUTOSIZER can size 2500 bushes - plain, spherical, flanged in an hour and is a 30 Ton capacity press. It minimizes operator dependence and proves to be more economical and safe compared to any other conventional sizing press. We are working towards applying this mechanism to a high tonnage presses also. Also AUTOSIZER is being re-designed to increase the sizing speed to 5000 bush per hour. At such speed sintered bushes will become very economical and will be produced in minimal time.

### Acknowledgements

- Rajan Bapurao Nikam (Managing Director at Krushnal Agro Engineers and Nikam Iron Sintered Products Pvt. Ltd.)
- Kunal Rajan Nikam (Nikam Iron Sintered Products Pvt. Ltd.)
- Shivaji Kumbhar ( Krushnal Agro Engineers)
- Sanjay Pawar (Krushnal Agro Engineers)
- Working staff at Krushnal Agro Engineers

### References

- Machine Design - S. G. Kulkarni
- Powder Metallurgy - A. K. Sinha
- Fundamentals of Metal Machining and Machine Tools, Third Edition (Mechanical Engineering) - by Winston A. Knight (Author), Geoffrey Boothroyd (Author)